



UNIVERSIDAD DE LAS PALMAS DE GRAN CANARIA  
Instituto Universitario de Microelectrónica Aplicada



# CONTRIBUTIONS TO THE DESIGN AND IMPLEMENTATION OF ALGORITHMS FOR THE CLASSIFICATION OF HYPERSENSPECTRAL IMAGES OF BRAIN TUMORS IN REAL-TIME DURING SURGICAL PROCEDURES

Doctorado en Tecnologías de Telecomunicación e Ingeniería Computacional



Tesis Doctoral  
Himar Fabelo Gómez  
Las Palmas de Gran Canaria, Abril 2019





**D. GUSTAVO MARRERO CALLICÓ, COORDINADOR/A DEL PROGRAMA DE DOCTORADO EN TECNOLOGÍAS DE TELECOMUNICACIÓN E INGENIERÍA COMPUTACIONAL DE LA UNIVERSIDAD DE LAS PALMAS DE GRAN CANARIA, INFORMA,**

Que la Comisión Académica del Programa de Doctorado, en su sesión de fecha **diez de abril de 2019** tomó el acuerdo de dar el consentimiento para su tramitación, a la tesis doctoral titulada ***“Contributions to the design and implementation of algorithms for the classification of hyperspectral images of brain tumors in real-time during surgical procedures”*** presentada por el doctorando D. Himar Fabelo Gómez y dirigida por los Doctores D. Gustavo Marrero Callicó y D. Roberto Sarmiento Rodríguez. Además, se ha acordado que la tesis **reúne todos los requisitos para optar a la mención de DOCTORADO INTERNACIONAL.**

Y para que así conste, y a efectos de lo previsto en el Artº 11 del Reglamento de Estudios de Doctorado (BOULPGC 7/10/2016) de la Universidad de Las Palmas de Gran Canaria, firmo la presente en Las Palmas de Gran Canaria, a **diez de abril de 2019.**





**UNIVERSIDAD DE LAS PALMAS DE GRAN CANARIA  
ESCUELA DE DOCTORADO**

Programa de doctorado en Tecnologías de Telecomunicación e Ingeniería  
Computacional

**Título de la Tesis**

**CONTRIBUTIONS TO THE DESIGN AND IMPLEMENTATION OF ALGORITHMS  
FOR THE CLASSIFICATION OF HYPERSPECTRAL IMAGES OF BRAIN TUMORS  
IN REAL-TIME DURING SURGICAL PROCEDURES**

Tesis Doctoral presentada por **D. Himar Fabelo Gómez**

Dirigida por el **Dr. D. Gustavo Marrero Callicó**

Codirigida por el **Dr. D. Roberto Sarmiento Rodríguez**

**El Director,**

(firma)

**El Codirector,**

(firma)

**El Doctorando,**

(firma)

Las Palmas de Gran Canaria, a 10 de abril de 2019





UNIVERSIDAD DE LAS PALMAS DE GRAN CANARIA  
Instituto Universitario de Microelectrónica Aplicada

DIVISIÓN DE DISEÑO DE SISTEMAS INTEGRADOS

## **TESIS DOCTORAL**

# **CONTRIBUTIONS TO THE DESIGN AND IMPLEMENTATION OF ALGORITHMS FOR THE CLASSIFICATION OF HYPERSPECTRAL IMAGES OF BRAIN TUMORS IN REAL-TIME DURING SURGICAL PROCEDURES**

Himar Fabelo Gómez



# *Abstract*

Hyperspectral imaging allows the acquisition of large numbers of spectral bands throughout the electromagnetic spectrum (within and beyond the visual range) with respect to the surface of scenes captured by sensors. Using this information and a set of complex classification algorithms, it is possible to determine which material or substance is located in each pixel. One of the major benefits of this technology is that it can be used as a guidance tool during brain tumor resections. Unlike other tumors, brain tumor infiltrates the surrounding normal brain tissue and thus their borders are indistinct and extremely difficult to identify to the surgeon's naked eye. The surrounding normal brain tissue is critical and there is no redundancy, as in many other organs, where the tumor is commonly resected together with an ample surrounding block of normal tissue. This is not possible in the brain, where it is essential to accurately identify the margins of the tumor to resect as less healthy tissue as possible. In this sense, the work performed in this thesis aims to exploit the characteristics of hyperspectral imaging to develop an intraoperative demonstrator capable of performing a precise localization of malignant tumors during brain surgical procedures. A precise delineation of tumor boundaries is expected to improve the outcomes of surgery.

As a proof-of-concept, the demonstrator developed in this work was able to generate thematic maps of the exposed brain surface using spectral information of the range comprised between 400 and 1000 nm. These thematic maps distinguish between four different classes previously established: normal tissue, tumor tissue, blood vessels/hypervascularized tissue, and background. In these maps, the tumor boundaries can be easily identifiable. A hyperspectral brain cancer detection algorithm, based on a mix of unsupervised and supervised machine learning approaches, was developed and implemented in the system. The supervised algorithm was trained by employing a labeled dataset composed of more than 300,000 spectral signatures, extracted by medical doctors from 36 different hyperspectral cubes captured with the acquisition system from 22 different patients from Spain and United Kingdom. The implementation of the algorithm was partitioned between the control unit and a hardware accelerator, where the higher computational tasks were implemented in a many-core platform to achieve intraoperative processing time (~1 min).

The intraoperative demonstrator was validated using seven hyperspectral images obtained in four neurosurgical operations. The thematic maps demonstrate that the system did not introduce false positives in the parenchymal area when no tumor was present and it was able to identify low grade tumors that were not used to train the brain cancer detection algorithm, resulting in a robust and generalized classification algorithm. Additionally, a preliminary study to improve the accuracy results of the hyperspectral brain cancer detection algorithm using deep learning techniques was performed. This study achieved promising results in the discrimination between tumor and normal brain tissue, being a suitable method to further improve the outcomes of the intraoperative demonstrator and, hence, the outcomes of the neurosurgical procedures.





# Resumen

Las imágenes hiperespectrales permiten la adquisición de un gran número de bandas espectrales en todo el espectro electromagnético (dentro y más allá del alcance visual del ojo humano) conteniendo información sobre la superficie de las escenas capturadas por los sensores. Usando esta información y un conjunto de complejos algoritmos de clasificación, es posible determinar qué material o sustancia se encuentra en cada píxel. Uno de los principales beneficios de esta tecnología es que puede utilizarse como una herramienta de asistencia visual durante las resecciones de tumores cerebrales. A diferencia de otros tumores, el tumor cerebral se infiltra en el tejido normal circundante y, por lo tanto, sus bordes son indistinguibles y extremadamente difíciles de identificar mediante simple inspección visual del cirujano. El tejido cerebral normal circundante es crítico y no hay redundancia, como en muchos otros órganos donde el tumor se reseca normalmente junto con un amplio bloque circundante de tejido normal. Esto no es posible en el cerebro, donde es esencial identificar con precisión los márgenes del tumor para reseca la menor cantidad posible de tejido sano. En este sentido, el trabajo realizado en esta tesis pretende explotar las características de las imágenes hiperespectrales para desarrollar un demostrador intraoperatorio capaz de proporcionar una localización precisa del tumor durante los procedimientos neuroquirúrgicos. Se espera que una delimitación precisa de los límites del tumor mejore los resultados de la cirugía.

Como prueba de concepto, el demostrador desarrollado en este trabajo es capaz de generar mapas temáticos de la superficie del cerebro expuesta utilizando información espectral del rango comprendido entre 400 y 1000 nm. Estos mapas temáticos distinguen entre cuatro clases diferentes previamente establecidas: tejido normal, tejido tumoral, tejido hipervascularizado y fondo. En estos mapas, los límites del tumor pueden ser fácilmente identificados. Para este fin se desarrolló e implementó en el sistema un algoritmo para la detección de cáncer cerebral basado en tecnología hiperespectral, usando técnicas de aprendizaje automático no supervisado y supervisado. El algoritmo supervisado se entrenó empleando un conjunto de datos etiquetados compuesto por más de 300,000 firmas espectrales, extraídas por los médicos involucrados en el proyecto a partir de 36 cubos hiperespectrales capturados con el sistema de adquisición en 22 operaciones neuroquirúrgicas realizadas en España y el Reino Unido. La implementación del algoritmo se dividió entre la unidad de control del sistema y un acelerador de hardware, donde las tareas con mayor carga computacional se implementaron en una plataforma multi-núcleo para lograr el procesamiento intraoperativo de las imágenes (~ 1 min).

El demostrador intraoperatorio desarrollado se validó utilizando siete imágenes hiperespectrales obtenidas en cuatro operaciones neuroquirúrgicas. Los mapas temáticos demuestran que el sistema no introduce falsos positivos en el área parenquimatosa cuando no existe tumor y que es capaz de identificar diferentes tipos de tumores que no estaban presentes en la base de datos de entrenamiento. Además, se realizó un estudio preliminar para mejorar los resultados de precisión del algoritmo de utilizando técnicas de aprendizaje profundo. Este estudio logró resultados prometedores en la discriminación entre el tumor y el tejido cerebral normal, siendo un método adecuado para mejorar aún más los resultados del demostrador intraoperatorio y, por lo tanto, los resultados de los procedimientos neuroquirúrgicos.



# Acknowledgements

The work performed during the development of this thesis has been carried out thanks to numerous collaborations between different institutions, where I had the opportunity to work with experts and researchers from several disciplinary areas. First of all, I would like to thank my first supervisor Dr. Gustavo M. Callicó, who had the confidence for putting me in charge of the HELICoiD European project, offering me the possibility of learning all the aspects related with the management and execution of a European project (technical, scientific and management tasks). Furthermore, his support and advice in all the matters related with the execution and development of the thesis provide me very useful tools for the successful finalization of this work and also for future steps in my career. Secondly, I would like also to thank my co-supervisor Prof. Roberto Sarmiento for his exceptional advices during the development of this thesis, guiding wisely my steps during these years. On the other hand, I want to especially thank my co-worker Samuel Ortega for his participation in the project, since without his highly useful help this thesis could not be possible or at least not with the quality that I think it was performed. In addition, I would like to thank all my laboratory co-workers since, although we worked in different projects, we spent a lot of time together during these years (Abelardo Báez, Lucana Santos, Ana Gómez, María Díaz, Raúl Guerra and also the new ones Antonio Sánchez, Yúbal Barrios, Pablo Horstrand and Raquel León) and also my master thesis students (Alfredo Pérez, Abián Hernández and Ruymán Hernández).

Furthermore, I would like to thank all the research institutions that participated in the HELICoiD project and his researchers. First of all, I would like to thank Daniel Madroñal and Raquel Lazcano for their exceptional teamwork, being at the end great friends, applied this also to their supervisors Dr. Eduardo Juárez, Dr. Ruben Salvador and Prof. César Sanz from the *Universidad Politécnica de Madrid* (UPM). Secondly, I would like to thank all the staff from the neurosurgery department of the University Hospital Doctor Negrín (Jesús Morera, Adam Szolna, Juan F. Piñeiro, Aruma J-O'Shanahan, Sara Bisshopp, Coralia Sosa, María Hernández, Carlos Espino, Mariano Márquez and David Carrera) for their remarkable and outstanding collaboration during the project execution. Additionally, I would like to thank the other researchers that participate in the HELICoiD project: Dr. Daniele Ravi and Prof. Guang-Zhong Yang from the Hamlyn Centre of the Imperial College of London; Dr. Diederik Bulters, Dr. Harry Bulstrode and Silvester Kabwama from the Wessex Neurological Centre of the University Hospital of Southampton; Dr. B. Ravi Kiran and Dr. Bogdan Stanciulescu from the Ecole Nationale Supérieure des Mines de Paris.

Moreover, I would like to give special thanks to Martin Halíček and his supervisor Prof. Baowei Fei from the Department of Bioengineering of the University of Texas at Dallas for their valuable support and collaboration during my research stay in their laboratory, being at the end a highly fruitful collaboration. These thanks are extended also to James Dorner and Dr. Maysam Shahedi for their help during my stay. I would like also to thank Dr. Giordana Florimbi, Dr. Emanuele Torti and their supervisor Prof. Francesco Leporati for their exceptional collaboration achieved in the final stage of this project, being a promising continuous collaboration and friendship in the next years.

Last, but not least, I am deeply grateful to my parents for working so hard during all their life, providing me the resources and the opportunity to have access to this stage, always encouraging me to fulfil my goals; to my brother for teaching me to be always curious, discovering new things; and to Aitor and Abián for give me the possibility to disconnect sometimes from the research work, having fun playing music with the band. Finally, I would like to give a very special thanks to Elena: first, for her exceptional managing of the acquisition system shipment from Spain to United Kingdom, returning the system safe and sound (not without some difficulties...); and second, for deciding to share her life with me and for offering me her support during the last stage of this thesis.

# Contents

<i>Abstract</i> .....	i
<i>Resumen</i> .....	iii
<i>Acknowledgements</i> .....	v
List of Figures .....	ix
List of Tables.....	xiii
List of Acronyms.....	xv
Chapter 1: Introduction.....	1
1.1 Motivations.....	1
1.2 Objectives .....	3
1.3 Thesis organization.....	4
Chapter 2: State-of-the-art in cancer detection using hyperspectral images.....	7
2.1 Introduction .....	7
2.2 Intraoperative brain surgical guidance tools .....	7
2.3 Introduction to hyperspectral imaging.....	10
2.3.1 Hyperspectral imaging cameras.....	11
2.3.2 Hyperspectral imaging processing algorithms.....	13
2.4 Medical hyperspectral imaging for cancer analysis.....	15
2.4.1 Ex-vivo cancer HSI analysis .....	17
2.4.2 In-vivo cancer HSI analysis .....	20
2.4.3 Summary .....	24
2.5 Conclusions.....	24
Chapter 3: Intraoperative hyperspectral acquisition and processing system .....	27
3.1 Introduction .....	27
3.2 Development of the intraoperative demonstrator.....	28
3.2.1 Acquisition platform.....	28
3.2.2 Electromechanical elements.....	31
3.2.3 Control unit .....	32
3.2.4 Hyperspectral image acquisition software .....	32
3.2.5 Hardware accelerator .....	33
3.3 Repeatability analysis of the HS acquisition system .....	34
3.3.1 Repeatability dataset .....	35
3.3.2 Repeatability metrics .....	35
3.3.3 Spectral repeatability .....	37
3.3.4 Spatial repeatability .....	42
3.4 Conclusions.....	43
Chapter 4: In-vivo hyperspectral human brain image database .....	45
4.1 Introduction .....	45
4.2 Participants.....	46
4.3 Intraoperative HS image acquisition procedure.....	46
4.3.1 Patient preparation.....	46
4.3.2 HS image acquisition .....	46
4.3.3 Tissue resection .....	48
4.3.4 Neuropathology evaluation.....	48
4.3.5 Sample labeling .....	48
4.4 HS gold standard generation .....	49
4.4.1 Definition of the of the labeling classes.....	52
4.4.2 Gold standard dataset .....	52
4.5 Conclusions.....	59
Chapter 5: Hyperspectral brain cancer detection algorithm .....	61
5.1 Introduction .....	61
5.2 Brain cancer detection algorithm.....	61
5.2.1 Data pre-processing.....	62
5.2.2 Dimensional reduction algorithms .....	63
5.2.3 Spatial-spectral supervised classification .....	65
5.2.4 Unsupervised clustering segmentation .....	68
5.2.5 Hybrid classification.....	69

5.3 Evaluation metrics.....	70
5.4 HS brain cancer detection algorithm results .....	71
5.4.1 Hyperspectral imaging can distinguish tissues by their spectra .....	71
5.4.2 Improving the spatial coherence of the classification maps .....	74
5.4.3 Unsupervised clustering for accurate boundaries delineation.....	75
5.4.4 Delimiting and identifying the brain area affected by cancer .....	76
5.5 Conclusions.....	78
Chapter 6: HS brain cancer detection algorithm fine-tuning and acceleration .....	81
6.1 Introduction .....	81
6.2 Evaluation methodology .....	81
6.3 Fine-tuning for surgical-time processing.....	82
6.3.1 Data pre-processing fine-tuning .....	82
6.3.2 Dimensional reduction fine-tuning .....	85
6.3.3 Dimensional reduction input fine-tuning.....	85
6.3.4 Fine-tuning for real-time processing summary.....	87
6.4 Fine-tuning for accurate classification results.....	87
6.4.1 SVM training samples percentage evaluation.....	87
6.4.2 SVM model generation study.....	88
6.5 HS brain cancer algorithm implementation .....	89
6.6 Intraoperative demonstrator validation .....	91
6.7 Conclusions.....	93
Chapter 7: Improvement of the classification results using Deep Learning techniques .....	95
7.1 Introduction .....	95
7.2 Deep learning techniques .....	95
7.2.1 Proposed deep learning pipeline .....	96
7.2.2 DL surgical aid visualization system .....	98
7.3 Quantitative evaluation .....	99
7.4 Qualitative evaluation.....	104
7.5 Conclusions.....	106
Chapter 8: Conclusions & Future Lines .....	109
8.1 Conclusions.....	109
8.2 Future lines.....	112
Annex A: Brain cancer detection algorithm implementation and acceleration using GPUs.....	117
Annex B: Publications .....	123
Journal publications.....	123
Patents .....	125
Conferences .....	125
Annex C: Sinopsis en español .....	129
Bibliography .....	135

# List of Figures

<b>Figure 1-1: Thesis organization and interrelation between chapters.</b> .....	5
<b>Figure 2-1: Estimated incidence and mortality from brain cancer and central nervous system</b> per 100,000 inhabitants in (a) men and (b) women in 2012 in Europe.....	8
<b>Figure 2-2: Image-guided stereotaxis (IGS) (also called neuronavigation) system used to locate the position of a tumor in a MRI.</b> (a) Pointer over the exposed brain; (b) Screen capture of the neuronavigation system where the green cross indicates the position of the pointer in the MRI.....	9
<b>Figure 2-3: Intraoperative magnetic resonance imaging system.</b> .....	9
<b>Figure 2-4: Fluorescence-guided surgery using 5-Ala system.</b> .....	10
<b>Figure 2-5: HSI basis.</b> Basic structure of a HS cube, single band representation at a certain wavelength and spectral signature of a single pixel. ....	10
<b>Figure 2-6: Electromagnetic spectrum.</b> Hyperspectral imaging is commonly employed between the visible and the medium-infrared range. ....	11
<b>Figure 2-7: HS camera types and their respective acquisition and storage data methods.</b> (a) Whiskbroom camera; (b) Pushbroom camera; (c) HS camera based on spectral scanning; (d) Snapshot camera. ....	12
<b>Figure 2-8: HS data storage structure types.</b> (a) Band sequential (BSQ) format; (b) Band-interleaved-by-line (BIL) format; (c) Band-interleaved-by-pixel (BIP) format. ....	13
<b>Figure 2-9: Number of publications per year related with the use of HSI for cancer analysis.</b> Source: Scopus. ....	16
<b>Figure 2-10: Number of publications per author (a) and per institution (b) related with the use of HSI for brain cancer analysis.</b> Source: Scopus.....	16
<b>Figure 2-11: Taxonomy of the state-of-the-art of medical HSI for cancer detection.</b> .....	17
<b>Figure 2-12: Acquisition system employed, cancer detection results using the NDCI and integral filter and comparison with pathological results obtained in [114].</b> (a) HS acquisition system setup; (b) RGB representation of the <i>ex-vivo</i> sample; (c) Cancer enhanced regions using integral filter in the hyperspectral image (1057–2440 nm), the tissues are shown in a blue to red spectrum, where the red regions represent the tumor; (d) Cancer enhanced regions using NDCI; (e) Pathological results; (f) Detected tumor using integral filter; (g) Detected tumor using NDCI.....	18
<b>Figure 2-13: Preliminary results obtained in the tumor margin delineation for head &amp; neck cancer [119].</b> After hyperspectral image acquisitions (top-left), the tissue was processed histologically, and tumor margins were outlined on the pathology image (bottom right) by a pathologist, which was used to validate the results of the classification (top-right). The average spectral curves are shown at the bottom left for each type of tissue, i.e., tumor, normal, and tumor with adjacent normal tissue. ....	20
<b>Figure 2-14: Result of the tumor identification using the Minimum-Spanning Forest method developed in [131].</b> (a) RGB image of the original mouse; (b) Corresponding gold standard image; (c) Classification result obtained. ....	22
<b>Figure 2-15: HS image example of the lower lip of a normal human acquired with the image mapping spectroscopy (IMS) endoscope developed in [132].</b> (a) RGB representation; (b) Spectral signature of the normal tissue pixel and a vein pixel; (c) Clinical setup of the IMS endoscope; (d) Miniature imaging end of the IMS endoscope; (e) Fiber optics of the IMS endoscope inserted into the instrument channel. .	23
<b>Figure 2-16: System and preliminary results obtained in [136].</b> (a) The optical filter wheel used in the HSI system; (b) Color image of a malignant colorectal tumor and a graph showing the spectral signature of the tumor and normal mucosa in the wavelength range of 405 to 655 nm. ....	23
<b>Figure 2-17: Delineation of the tongue tumor region in [137].</b> Expert labeling (left) and classifier prediction of tumor regions (right) .....	24
<b>Figure 3-1: Block diagram of the intraoperative demonstrator.</b> .....	27
<b>Figure 3-2: The intraoperative demonstrator acquisition platform.</b> (a) and (b) VNIR and NIR HS cameras mounted on the scanning platform; (c), (d), and (e) QTH light source connected to the fiber optic system for the light transmission to obtain cold light emission in the scanning platform; (f) and (g) Stepper motor coupled to the spindle and connected to the stepper-motor controller to perform the linear movement of the cameras; (h) Positioning of the RGB camera used to identify the position of the cameras' FOV; (i) The	



Up&Down system used to focus the HS cameras; (j) and (k) Tilt and manual panning systems employed to correctly orientate the scanning platform.....	28
<b>Figure 3-3: Calibration process of a certain pixel of the VNIR and NIR cameras.</b> (a) The VNIR white reference spectrum; (b) and (c) The VNIR raw and calibrated spectra of a pixel of normal brain tissue; (d) The NIR white reference spectrum; (e and f) The NIR raw and calibrated spectra of a pixel of normal brain tissue. ....	30
<b>Figure 3-4: HS image acquisition interface.</b> (a) HS image acquisition software flow diagram; (b) HS image acquisition user interface (and the RGB representations of each HS cube) being used during a neurosurgical intervention at the University Hospital Doctor Negrin of Las Palmas de Gran Canaria (Spain).....	33
<b>Figure 3-5: The Kalray MPPA® EMBO1 Platform.</b> (a) Developer environment; (b) EMBO1 top view where the host module is located; (c) EMBO1 bottom view where the carrier board is placed. ....	34
<b>Figure 3-6: HS images of the repeatability dataset.</b> (a) White reference tile; (b) Chessboard pattern; (c) Book cover fragment. ....	35
<b>Figure 3-7: HS images of the repeatability dataset and their correspondent scatterplot of the voxel values of an example section of 200x200 pixels obtained from two HS cubes of the same scene.</b> (a) and (b) White reference tile; (c) and (d) Chessboard pattern; (e) and (f) Book cover fragment.	36
<b>Figure 3-8: Pushbroom technique block diagram example</b> .....	38
<b>Figure 3-9: Spectral repeatability indexes in line scans of the three different HS cube pairs.</b> (a) White reference tile; (b) Chessboard pattern; (c) Book cover fragment. ....	39
<b>Figure 3-10: Spectral repeatability indexes in CCD bins of the three different HS cube pairs.</b> (a) White reference tile; (b) Chessboard pattern; (c) Book cover fragment. ....	40
<b>Figure 3-11: Spatial representation of the spectral repeatability indexes of N/S and <math>RD_{mean}</math> of the three different HS cube pairs at a certain wavelength (<math>\lambda = 690.78</math> nm).</b> (a) White reference tile; (b) Chessboard pattern; (c) Book cover fragment. ....	41
<b>Figure 3-12: Spatial repeatability indexes of the three different HS cube pairs.</b> (a) White reference tile; (b) Chessboard pattern; (c) Book cover fragment. ....	42
<b>Figure 4-1: <i>In-vivo</i> HS brain surface acquisition procedure.</b> (a) Hyperspectral acquisition system being used during the acquisition process in a neurosurgical operation; (b) Hyperspectral images acquired with the acquisition system at different wavelengths from a patient affected by a glioblastoma tumor; (c) HSI data cube; (d) RGB image generated from the HS cube with the tumor tissue marker (left) and the normal tissue marker (right) placed on the brain surface; (e) and (f) Histopathological images of the tumor tissue sample (glioblastoma) and normal tissue sample respectively; (g) Gold standard map where certain pixels have been labeled in four different classes: normal brain tissue (green), tumor tissue (red), blood vessel (blue) and background (black); (h) Average and standard deviation (Std) of the pre-processed spectral signatures of tumor tissue, normal tissue and blood vessel labeled pixels, represented in red, green and blue color respectively. ....	47
<b>Figure 4-2: MRI markers registration.</b> (a) IGS system pointer over the tumor marker located on the exposed brain surface; (b) IGS system screen snapshot with the coordinates of the tumor marker in the MRI.....	48
<b>Figure 4-3: Semi-automatic labeling process flowchart.</b> (a) Pre-Processed HS cube; (b) Synthetic RGB image extracted from the HS cube; (c) SAM mask over the synthetic RGB image; (d) Final gold standard map...	51
<b>Figure 4-4: Threshold values selected for each reference pixel in each image for each class.</b> (a) Normal class. (b) Tumor class. (c) Hypervascularized class. (d) Background class.....	51
<b>Figure 4-5: Screenshot of the semi-automatic labeling tool interactive interface.</b> (a) Synthetic RGB image; (b) SAM masked image; (c) Final gold standard map. ....	52
<b>Figure 4-6: Average and standard deviation (Std) across all the patients of the different types of spectral signatures in the labeled database.</b> (a) Normal tissue. (b) Blood vessels. (c) GBM tumor. (d) Anaplastic oligodendroglioma tumor. (e) Secondary breast tumor. (f) Secondary lung tumor. ....	55
<b>Figure 4-7: RGB representations and gold standard maps of the HS images that compose the <i>in-vivo</i> HS human brain image database.</b> The numeric code shown above each image represents the Patient ID and Image ID (PatientID-ImageID) that are detailed in <b>Table 4-3</b> .....	58
<b>Figure 5-1: Brain cancer detection and delimitation algorithm framework overview diagram.</b> (a) HS cube of <i>in-vivo</i> brain surface; (b) Pre-processing stage of the algorithm; (c) Database of labeling samples generation; (d) SVM model training process employing the labeled samples dataset; (e), (f) and (g) Algorithms that conform the spatial-spectral supervised classification stage; (h) and (i) Algorithms that generate the unsupervised segmentation map and the final HELICoID TMD map, respectively. ....	62

<b>Figure 5-2: Spectral signature of a grade IV GBM tumor tissue.</b> (a) Raw spectral signature; (b) Calibrated spectral signature; (c) HySIME filtered spectral signature; (d) Final pre-processed spectral signature. ....	63
<b>Figure 5-3: Taxonomy of dimensionality reduction techniques [155].</b> .....	64
<b>Figure 5-4: KNN filtered maps obtained with different K and <math>\lambda</math> values.</b> (a), (b), (c), (d) and (e) filtered maps obtained with K equal to 5, 10, 20, 40, and 60, while keeping $\lambda$ value fixed to 1; (f), (g), (h), (i) and (j) filtered maps obtained with $\lambda$ equal to 0, 1, 5, 10, and 100, while keeping K value fixed to 40. ....	68
<b>Figure 5-5: Hybrid classification example based on a majority voting technique.</b> The unsupervised segmentation map and the supervised classification maps are merged using the majority voting method.	70
<b>Figure 5-6: Mean and variances of the pre-processed spectral signatures.</b> Tumor, normal and blood vessel classes of the labeled pixels from patient 8 (a) and patient 12 (b) are represented in red, black and blue color respectively. ....	72
<b>Figure 5-7: Quantitative results of the supervised classification performed with the SVM classifier applied to the labeled data of each patient.</b> (a) Overall accuracy results of supervised classification per SVM kernel type and patient; (b) and (c) Specificity and sensitivity results obtained using the SVM classifier with linear kernel for each patient and class employing the one-vs.-all evaluation method. ....	73
<b>Figure 5-8: Results of each step of the optimized spatial-spectral supervised classification of the five different patients.</b> (a), (b), (c), (d) and (e) Synthetic RGB images generated from the HS cubes; (f), (g), (h), (i) and (j) Gold standard maps used for the supervised classification training; (k), (l), (m), (n) and (o) Supervised classification maps generated using the SVM algorithm; (p), (q), (r), (s) and (t) FR-t-SNE one band representation of the HS cubes; (u), (v), (x), (y) and (z) Spatially optimized classification maps obtained after the KNN filtering. ....	75
<b>Figure 5-9: Results of each step of the proposed cancer detection algorithm applied to the five different patients.</b> (a), (b), (c), (d) and (e) Segmentation maps generated using the HKM algorithm; (f), (g), (h), (i) and (j) MV classification maps; (k), (l), (m), (n) and (o) OMD maps that take into account only the major probability per class obtained from the MV algorithm; (p), (q), (r), (s) and (t) TMD maps that take into account the first three major probabilities per class obtained from the MV algorithm. ....	77
<b>Figure 6-1: Different data pre-processing chains.</b> a) CP129 pre-processing chain; b) CP128 pre-processing chain; c) SP128 pre-processing chain. ....	83
<b>Figure 6-2: Fine-tuned brain cancer detection algorithm for real-time processing.</b> .....	87
<b>Figure 6-3: Overall accuracy evolution depending on the percentage of training samples employed to generate the supervised classification model of the HS brain cancer detection algorithm.</b> .	88
<b>Figure 6-4: Implementation of the HS brain cancer detection algorithm onto the intraoperative demonstrator.</b> (a) HS brain cancer detection algorithm implementation flow diagram and the RGB representation of the output of each step; (b) Different parts related to the HS data processing of the intraoperative demonstrator. ....	90
<b>Figure 6-5: Normal brain image results obtained from the validation database employing the HELICoiD demonstrator.</b> (a) and (b) Synthetic RGB image and TMD map of the Op35C1 HS image; (c) and (d) Synthetic RGB image and TMD map of the Op36C1 HS image; (e) and (f) synthetic RGB image and TMD map of the Op37C1 HS image. ....	92
<b>Figure 6-6: Tumor tissue identification results obtained from the validation database employing the HELICoiD demonstrator.</b> (a) and (b) synthetic RGB image and TMD map of the Op36C2 HS image; (c) and (d) synthetic RGB image and TMD map of the Op38C1 HS image; (e) and (f) synthetic RGB image and TMD map of the Op35C2 HS image; (g) and (h) synthetic RGB image and TMD map of the Op37C2 HS image. ....	92
<b>Figure 7-1: Block diagram of the proposed DL framework.</b> .....	98
<b>Figure 7-2: Gray-scale representation image examples and the correspondent three selected spectral channels employed in the three-band combination for the parenchymal and blood vessel detection.</b> .....	98
<b>Figure 7-3: Block diagram of the proposed surgical aid visualization algorithm to generate the three class density map.</b> A hierarchical K-Means (HKM) algorithm and the proposed DL framework were used to generate the maps for majority voting algorithm. ....	99
<b>Figure 7-4: Average results of the leave-one-out cross-validation of the binary dataset obtained for each classification approach using the class-balancing and bootstrapping method with the 95% confidence interval.</b> .....	101
<b>Figure 7-5: Average results of the leave-one-out cross-validation of the four-class dataset obtained for each classification approach using the class-balancing and bootstrapping method with the</b>	

**95% confidence interval.** (a) Overall accuracy and accuracy per class results. (b) Boxplot of the overall accuracy results. (c) AUC results per class. [NT] Normal tissue; [TT] Tumor tissue; [HT] Hypervascularized tissue; [BG] Background. ....103

**Figure 7-6: Classification maps of four of the test HS images and their respective tumor accuracy below each map.** (a) Synthetic RGB image with the tumor area surrounded by the yellow lines; (b), (c), (d), (e) and (f) Multiclass classification maps obtained with the SVM, PCA+SVM+KNN, 2D-CNN, 1D-DNN and the proposed pipeline, respectively. Normal, tumor, and hypervascularized tissue are represented in green, red and blue colors, respectively, while the background is represented in black color; (g) Density maps generated using the surgical aid visualization algorithm with the optimal threshold established for the tumor class. In these maps the colors have been adjusted depending on the probability values obtained after the majority voting algorithm. ....105

**Figure 7-7: Surgical aid visualization with manual adjustable threshold values.** (a) Synthetic RGB image generated from the HSI cube; (b) 1D-DNN classification map generated with the established threshold; (c) Density map generated with the new classification map. ....106

# List of Tables

<b>Table 2-1: Summary of the state-of-the-art in the use of HSI for cancer analysis</b> .....	25
<b>Table 4-1: Labeling class list</b> .....	53
<b>Table 4-2: Final labeling class list</b> .....	54
<b>Table 4-3: Summary of the <i>in-vivo</i> HS human brain image database</b> .....	54
<b>Table 4-4: Summary of the labeled dataset</b> .....	55
<b>Table 5-1: Comparison of the dimensional reduction algorithms sorted according to the proposed quality score [83]</b> .....	66
<b>Table 5-2: Gold standard dataset for the preliminary evaluation of the developed brain cancer detection algorithm</b> .....	71
<b>Table 6-1: Pre-processing chains comparison</b> .....	84
<b>Table 6-2: Dimensional reduction fine-tuning comparison</b> .....	85
<b>Table 6-3: Dimensional reduction input fine-tuning comparison</b> .....	86
<b>Table 6-4: Comparison of the TMD maps obtained with each SVM model generated with a leave-one-patient-out cross-validation method.</b> .....	89
<b>Table 6-5: Validation HS image dataset characteristics.</b> .....	91
<b>Table 6-6: Execution time comparison between the sequential (Seq.) and accelerated (Acc.) implementations.</b> .....	93
<b>Table 7-1: Schematic of the proposed 2D-CNN architecture.</b> The input size is given in each row. The output size is the input size of the next row. All convolutions were performed with sigmoid activation and 40% dropout .....	96
<b>Table 7-2: Summary of the test dataset employed for the quantitative evaluation.</b> .....	100
<b>Table 7-3: Average results of the leave-one-out cross-validation of the binary dataset obtained for each classification approach using the bootstrapping method with the 95% confidence interval.</b> .....	101
<b>Table 7-4: Average accuracy results of the leave-one-out cross-validation of the four-class dataset obtained for each classification approach using the bootstrapping method with the 95% confidence interval.</b> .....	103
<b>Table 7-5: Average AUC results of the leave-one-out cross-validation of the four-class dataset obtained for each classification approach using the bootstrapping method with the 95% confidence interval.</b> .....	103



# List of Acronyms

Acronym	Meaning
<b>5-ALA</b>	5-Aminolevulinic Acid
<b>ACIISI</b>	Canarian Agency for Research, Innovation and the Information Society
<b>ANN</b>	Artificial Neural Networks
<b>AOTF</b>	Acousto-Optic Tunable Filter
<b>AUC</b>	Area Under the Curve
<b>BIL</b>	Band-Interleaved-by-Line
<b>BIP</b>	Band-Interleaved-by-Pixel
<b>BSQ</b>	Band Sequential
<b>CCD</b>	Charge-Coupled Device
<b>CEIC/CEI</b>	<i>Comité Ético de Investigación Clínica-Comité de Ética en la Investigación</i>
<b>CITSEM</b>	Centre of Software Technologies and Multimedia Systems
<b>CNN</b>	Convolutional Neural Network
<b>CS</b>	Case Study
<b>CT</b>	Computed Tomography
<b>CU</b>	Control Unit
<b>DBN</b>	Deep Belief Networks
<b>DL</b>	Deep Learning
<b>DMA</b>	Direct Memory Access
<b>DNN</b>	Deep Neural Network
<b>DTC</b>	Decision Tree Classifier
<b>ENSM</b>	Ecole Nationale Supérieure des Mines de Paris
<b>ES</b>	Electromagnetic Spectrum
<b>FFD</b>	B-spline free-form deformation
<b>FNR</b>	False Negative Rate
<b>FOV</b>	Field-Of-View
<b>FPGA</b>	Field Programmable Gate Arrays
<b>FPR</b>	False Positive Rate
<b>FR-tSNE</b>	Fixed Reference t-Stochastic Neighbors Embedding
<b>GBM</b>	Glioblastoma Multiforme
<b>GCF</b>	Global Contrast Factor
<b>GPU</b>	Graphic Processor Unit
<b>GUI</b>	Graphical User Interface
<b>H&amp;E</b>	Hematoxylin and Eosin
<b>H2NMF</b>	Hierarchical rank-2 non-Negative Matrix Factorization
<b>HA</b>	Hardware Accelerator
<b>HELICoiD</b>	HypErspectraL Imaging Cancer Detection
<b>HG</b>	High Grade
<b>HKM</b>	Hierarchical K-Means
<b>HS</b>	Hyperspectral
<b>HSI</b>	Hyperspectral Imaging
<b>HSKM</b>	Hierarchical Spherical K-Means
<b>I/O</b>	Input/Output
<b>ICL</b>	Imperial College London
<b>ID</b>	Identification number
<b>IGS</b>	Image-Guided Stereotaxis
<b>iMRI</b>	Intra-Operative Magnetic Resonance Imaging
<b>InGaAs</b>	Indium Gallium Arsenide
<b>ISODATA</b>	Iterative Self-Organizing Data Analysis
<b>ITHACA</b>	Hyperspectral Identification of Brain Tumors
<b>IUMA</b>	Institute for Applied Microelectronics
<b>JCR</b>	Journal Citation Reports
<b>KNN</b>	K-Nearest Neighbors
<b>LCTF</b>	Liquid Crystal Tunable Filter
<b>LDA</b>	Linear Discriminant Analysis
<b>LED</b>	Light-Emitting Diode
<b>LG</b>	Low Grade
<b>LLE</b>	Locally Linear Embedding
<b>LR</b>	Logistic Regression
<b>LS-SVM</b>	Least Squares Support Vector Machine
<b>MCT</b>	Mercury Cadmium Telluride
<b>MIMD</b>	Multiple Instruction, Multiple Data
<b>ML</b>	Machine Learning
<b>MNF</b>	Minimum Noise Fraction
<b>MPPA</b>	Massively Parallel Processor Array
<b>MRI</b>	Magnetic Resonance Imaging

<b>Acronym</b>	<b>Meaning</b>
<b>mRMR</b>	maximal Relevance and Minimal Redundancy
<b>MS</b>	Multispectral
<b>MSF</b>	Minimum-Spanning Forest
<b>MV</b>	Majority Voting
<b>N/S</b>	Noise-to-Signal ratio
<b>NCC</b>	Normalized Cross-Correlation
<b>NDCI</b>	Normalized Cancer Index
<b>NIR</b>	Near-InfraRed
<b>NoC</b>	Network-on-a-Chip
<b>NRES</b>	National Research Ethics Service
<b>OMD</b>	One Maximum Density
<b>OS</b>	Operative System
<b>PCA</b>	Principal Component Analysis
<b>PCIe</b>	Peripheral Component Interconnect Express
<b>POSIX</b>	Portable Operating System Interface
<b>QDA</b>	Quadratic Discriminant Analysis
<b>QTH</b>	Quartz Tungsten Halogen
<b>RAM</b>	Random Access Memory
<b>RD</b>	absolute Relative Difference percentage
<b>RE</b>	Repeatability Error
<b>RF</b>	Random Forest
<b>RGB</b>	Red, Green and Blue
<b>RM</b>	Resource Management
<b>rms</b>	root mean square
<b>ROC</b>	Receiver Operating Characteristic
<b>ROI</b>	Region of Interest
<b>RVM</b>	Relevance Vector Machine
<b>S/N</b>	Signal-to-Noise ratio
<b>SAM</b>	Spectral Angle Mapper
<b>SCC</b>	Squamous Cell Carcinoma
<b>SDK</b>	Software Development Kit
<b>SR</b>	Sparse Representation
<b>SSD</b>	Solid-State Drive
<b>STD</b>	Standard Deviation
<b>Std</b>	Standard Deviation
<b>SVMs</b>	Support Vector Machines
<b>SWIR</b>	Short-Wavelength InfraRed
<b>TMD</b>	Three Maximum Density
<b>TNR</b>	True Negative Rate
<b>TPR</b>	True Positive Rate
<b>t-SNE</b>	t-Distributed Stochastic Neighbors Embedding
<b>UHDRN</b>	University Hospital Doctor Negrin
<b>UHS</b>	University Hospital of Southampton
<b>ULPGC</b>	University of Las Palmas de Gran Canaria
<b>UPM</b>	Universidad Politécnica de Madrid
<b>UTD</b>	University of Texas at Dallas
<b>VDC</b>	Volts of Direct Current
<b>VLIW</b>	Very Long Instruction Word
<b>VNIR</b>	Visible and Near-InfraRed
<b>WHO</b>	World Organization Health



*Dedicated to Malié*



# Chapter 1: Introduction

## 1.1 Motivations

Currently, patients with brain cancer continue to have very poor survival rates, being surgery one of the mainstays of treatment, together with radiotherapy and chemotherapy [1]. Brain tumors are classified based on their histology and molecular parameters [2], where malignant gliomas are the most common form of primary brain tumors in adults, causing between 2 and 3% of cancer deaths worldwide [3]. Since brain tumors diffusely infiltrate into the surrounding normal brain tissue (especially gliomas), it is extremely difficult for the surgeon to accurately differentiate between tumor and normal brain tissue with the naked eye. In some cases, unintentionally leaving behind tumor tissue after the resection is unavoidable, and in other cases, too much normal brain tissue is resected in an effort to ensure complete excision. In this last case, over-resection can produce permanent neurological deficits that affect patient quality of life [4]. In contrast, several studies have demonstrated that tumor tissue left behind during surgery is a major cause of morbidity and mortality and represents the most common cause of tumor progression [5]–[7].

Several image guidance tools, such as intraoperative neuronavigation, intraoperative magnetic resonance imaging (iMRI), and fluorescent tumor markers (for example 5-aminolevulinic acid, 5-ALA), have been commonly used to assist surgeons in the identification of brain tumor boundaries. However, these technologies have several limitations. One limitation is related to the brain shift phenomenon [8], which is produced due to the craniotomy. In this process, the opening of the skull and dura inevitably leads to movement of the brain. This typically manifests as herniation of the brain into the craniotomy defect under pressure from the underlying tumor, or the slump of the brain due to drainage of cerebrospinal fluid and the administration of mannitol. Similarly, following resection of the tumor, the residual brain tissue may slump towards the surgical cavity. This brain deformation invalidates the patient-to-image mapping and reduces the effectiveness of using pre-operative images for intraoperative surgical guidance. Thus, neuronavigation systems relying on preoperative image data are decreasing accuracy as the surgical procedure progresses [9]–[11]. On the contrary, iMRI solves the problem of brain shift mapping the tumor margins intraoperatively. However, this method has poor spatial resolution and significantly extends the duration of the surgery, obtaining a limited number of images during the surgical procedure [12]. Finally, although 5-ALA can identify the tumor boundaries, it produces relevant knock-on effects for the patient and can only be used

for high-grade tumors [13], [14]. Thus, there is no current device that can help in the accurate definition of brain tumor boundaries during surgical procedures. A label-free and non-ionizing imaging modality would be an ideal solution to this problem.

In this sense, hyperspectral imaging (HSI) is an imaging modality that integrates conventional imaging and spectroscopy methods to obtain both spatial and spectral information of a scene [15]. Unlike conventional RGB (red, green and blue) image, which only captures three diffuse Gaussian spectral bands in the visible spectrum (from 400 to 700 nm), HSI increases the amount of data acquired beyond the capabilities of the human eye [16]. Hyperspectral (HS) sensors measure the aggregate signal of reflected, absorbed and emitted radiance at specific wavelengths of the material that is being observed. These sensors are capable of capturing a very large number of contiguous spectral bands (also called *spectral wavelengths* or *spectral channels*) across the electromagnetic spectrum (ES), obtaining a vector of radiance values for each pixel of the image that is commonly called *spectral signature* [15]. Image processing algorithms utilize these spectral signatures to automatically differentiate the materials observed by the sensor at each pixel [17]. These methods rely on the basis that different molecular compositions of each material present in the nature or artificially generated have different responses to the incident light [15].

HSI has shown considerable early promise as a non-invasive and non-ionizing technique, supporting rapid acquisition and analysis of diagnostic information in several fields, such as remote sensing [18], [19], archeology [20], [21], drug identification [22], [23], forensics [24]–[26], defense and security [27], [28], agriculture [29], [30], food safety inspection and control [31]–[33], among many others. Particularly, several studies can be found in the literature where HSI is applied to different medical applications [34], [35]. It has been proven that the interaction between the electromagnetic radiation and matter carries useful information for medical diagnostic proposes [34]. Alternatively to other existing technologies for assessing the diagnosis, one of the strengths offered by HSI is being completely non-invasive, non-contact and label-free sensing technique. In medical applications, this technology has been employed in several different areas like blood vessel visualization enhancement [36], [37], intestinal ischemia identification [38], oximetry of the retina [39]–[41], estimation of the cholesterol levels [42], chronic Cholecystitis detection [43], diabetic foot [44], etc. In recent years, medical HSI has started to achieve promising results with respect to cancer detection through the utilization of cutting-edge machine learning algorithms and modern computational power. Thus, the main motivation of this thesis is the application of HSI techniques for the development of a non-invasive, non-ionizing and non-contact surgical aid visualization tool able to assist neurosurgeons during the brain tumor resection, identifying and delineating the tumor boundaries in real-time throughout the surgical procedure.

Concretely, the work performed in this thesis describes the main outcomes achieved during the collaboration between the Institute for Applied Microelectronics (IUMA) of the University of Las Palmas de Gran Canaria (ULPGC) with several relevant research institutions, such as the Centre of Software Technologies and Multimedia Systems (CITSEM) of the *Universidad Politécnica de Madrid* (UPM), the Hamlyn Centre of the Imperial College London (ICL), the *Ecole Nationale Supérieure des Mines de Paris* (ENSMP), the Wessex Neurological Centre of the University Hospital of Southampton (UHS) and the Department of Neurosurgery of the University Hospital Doctor Negrin

of Las Palmas de Gran Canaria. These collaborations were framed within the European project HELICoiD (*HypErspectraL Imaging Cancer Detection*) by the Research Executive Agency, under Grant Agreement 618080, through the Future and Emerging Technologies (FET-Open) Programme, under the 7th Framework Programme of the European Union. HELICoiD was a collaborative project between four universities, three industrial partners and two hospitals, whose main goal was to use HSI to generalize a methodology to discriminate between normal and malignant tissues in real-time during neurosurgical procedures. For this purpose, an intraoperative demonstrator was designed and built capable of acquiring hyperspectral (HS) intraoperatively and process them in order to assist neurosurgeons during the hard task of brain tumor resection. Through the development of a complex HS classification algorithm, neurosurgeons were able to visualize a thematic map where the tumor boundaries were accurately delineated. This new methodology will allow surgeons to avoid the excessive extraction of normal brain tissue, preventing small remnants of tumors from being left behind. Such precise delimitation of the tumors boundaries will improve the results of the surgery and is expected to improve patient outcomes in the future.

In addition, thanks a collaboration carried out between the IUMA and the Department of Bioengineering of the University of Texas at Dallas (UTD), complex deep learning (DL) algorithms were studied and employed to accelerate and improve the accuracy of the results obtained within the HELICoiD project. This research was framed in the ITHaCA (*Hyperspectral Identification of Brain Tumors*) project funded by the Canary Islands Government through the ACIISI (Canarian Agency for Research, Innovation and the Information Society) under Grant Agreement ProID2017010164.

## 1.2 Objectives

The main objective of this thesis is to demonstrate that HSI is capable of accurately delineate the boundaries between normal brain and tumor tissue during surgical procedures, providing the results in real-time to help neurosurgeons during the tumor resection decision and, thus, improving the outcomes of the surgery. In order to achieve this main goal, several specific objectives were raised at the beginning of this thesis:

- **To acquire the required knowledge about the existing different algorithms** for the pre and post-processing of HS images, analyzing their advantages and disadvantages as well as their computational requirements and focusing the analysis in medical applications.
- **To design and develop an intraoperative HS acquisition system** adequate for surgical environments, which allows the generation of an *in-vivo* **HS human brain image database** that will be used for the development of the HS brain cancer detection algorithms.
- **To design and develop a high-level HS classification algorithm** capable of discriminate and delineate the boundaries between tumor and normal tissues using the acquired *in-vivo* HS human brain image database, taking into account the computational requirements of the developed algorithm for its subsequent implementation and acceleration.

- **To integrate the developed algorithm within the intraoperative HS acquisition system** to achieve the fully operational intraoperative HS demonstrator, performing an exhaustive quantitative and qualitative assessment and validation of the results obtained during surgical procedures.

### 1.3 Thesis organization

This thesis has been structured in 8 chapters that are interrelated as presented in **Figure 1-1**. A brief explanation of each chapter is presented next.

- Chapter 1: Introduction.** In the present chapter, the main motivations and objectives that have led to the development of the thesis are described. In addition, the structure of the document is presented.
- Chapter 2: State-of-the-art in cancer detection using hyperspectral images.** In this chapter, the current intraoperative surgical guidance tools employed in brain surgeries are described. Additionally, the HSI concept and a brief description of the main algorithms employed process this type of data, are presented. Finally, a brief review of the literature in the use of HSI in the medical field for cancer analysis is detailed.
- Chapter 3: Intraoperative hyperspectral acquisition and processing system.** This chapter provides an overview of the HSI instrumentation employed in order to develop the intraoperative demonstrator for brain cancer detection as well as a detailed description of the developed system. In addition, the results of a repeatability analysis performed to the HS acquisition system are presented.
- Chapter 4: *In-vivo* hyperspectral human brain image database.** This chapter presents the procedure carried out to obtain the HS images of the human brain surface that were stored in the *in-vivo* HS human brain image database. Furthermore, the process to label the samples as tumor or normal tissue for the supervised algorithm development is described. Finally, a detailed description of the entire database is provided.
- Chapter 5: Hyperspectral brain cancer detection algorithm.** In this chapter, a detailed description of each part of the HS brain cancer detection algorithm developed in this thesis is presented. Furthermore, an intra-patient quantitative and qualitative assessment of the algorithm is provided.
- Chapter 6: HS brain cancer detection algorithm fine-tuning and acceleration.** In this chapter, the optimizations performed to the HS brain cancer detection algorithm to reduce the execution time and to achieve more accurate results during surgical procedures are described. Furthermore, a brief explanation of the algorithm implementation and acceleration onto the intraoperative demonstrator is provided. Finally, the validation results of the final intraoperative demonstrator performed during surgical operations are presented.

**Chapter 7: Improvement of the classification results using Deep Learning techniques.** This chapter presents the development of an improved HS brain cancer detection algorithm that employs deep learning architectures to increase the accuracy of the classification results previously obtained with traditional machine learning techniques. Moreover, an exhaustive quantitative comparison between the different approaches is provided as well as new method to adjust the classification results taking into account the operating surgeon criteria.

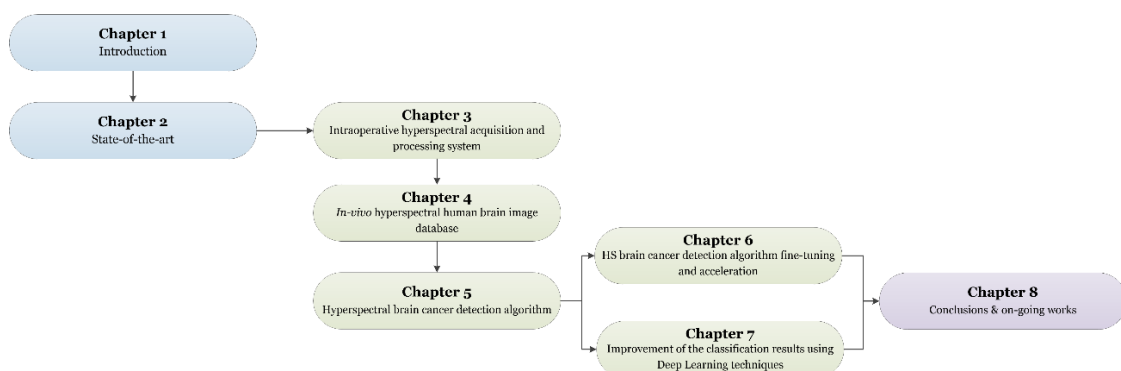
**Chapter 8: Conclusions & future lines.** This chapter concludes the work presented in this thesis by summarizing the advantages, disadvantages and main contributions of the methods developed in this work as well as presenting the current works that indicates future research lines of this thesis.

**Annex A: HS Brain cancer detection algorithm implementation and acceleration using GPUs.** In this annex, the work performed in collaboration between the ULPGC and the University of Pavia for the implementation and acceleration of the HS brain cancer detection algorithm onto GPU-based architectures is explained.

**Annex B: Publications.** In this annex, all the scientific communications performed during the development of the work described in this thesis and the different collaborations performed with other institutions and research groups are detailed. Specifically, 17 articles published in journals indexed in the JCR (Journal Citation Reports) (two of them submitted and the rest already published), 18 peer-reviewed conference papers (two of them submitted and the rest already published) and 1 patent have been achieved during the course of this thesis. In total, 36 scientific contributions have been accomplished.

**Annex C: Sinopsis en español.** In this annex, a brief summary of the thesis is presented in Spanish.

**Bibliography:** This thesis manuscript concludes with the list of references employed during the elaboration of this document.



**Figure 1-1: Thesis organization and interrelation between chapters.**





# Chapter 2: State-of-the-art in cancer detection using hyperspectral images

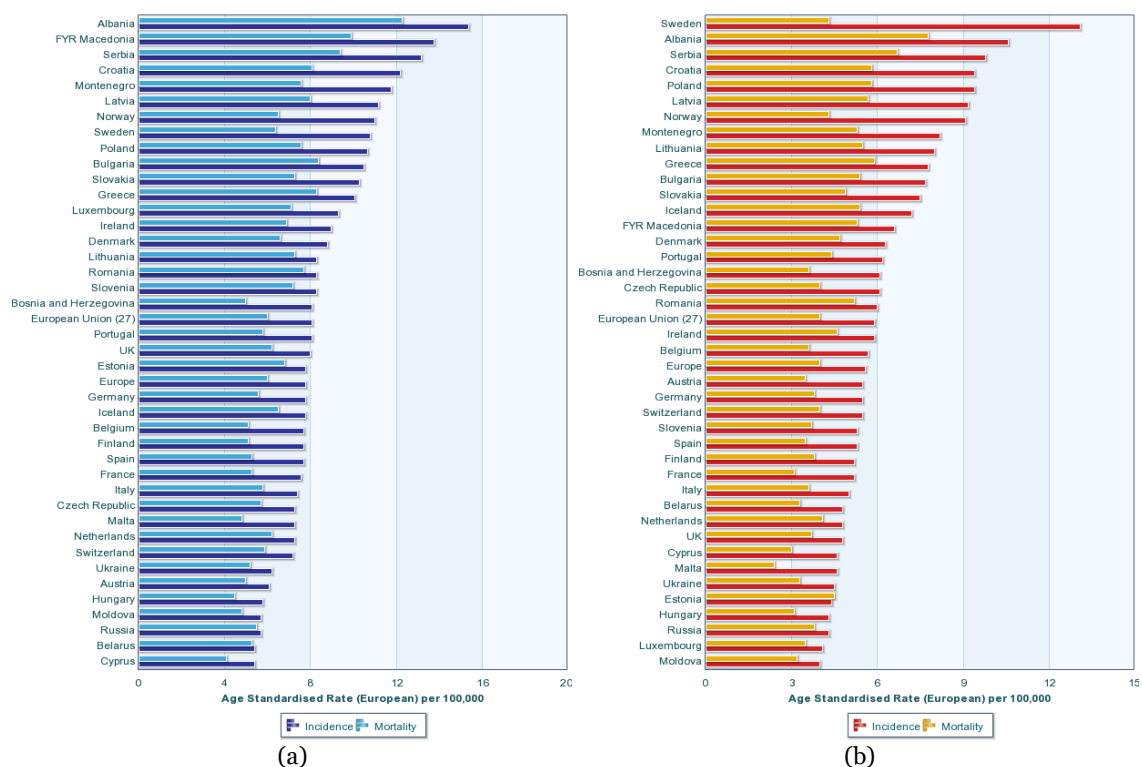
## 2.1 Introduction

This chapter provides an overview of the current state-of-the-art on the areas related with the development of this thesis. First, the current intraoperative surgical guidance tools that are commonly used during brain surgeries to assist neurosurgeons in the resection of brain tumors are described. Secondly, an introduction of the HSI concept and a brief description of the main algorithms employed process this type of data are presented. Finally, a brief review of the studies that can be found in the literature related with the use of HSI in the medical field for cancer analysis is detailed.

## 2.2 Intraoperative brain surgical guidance tools

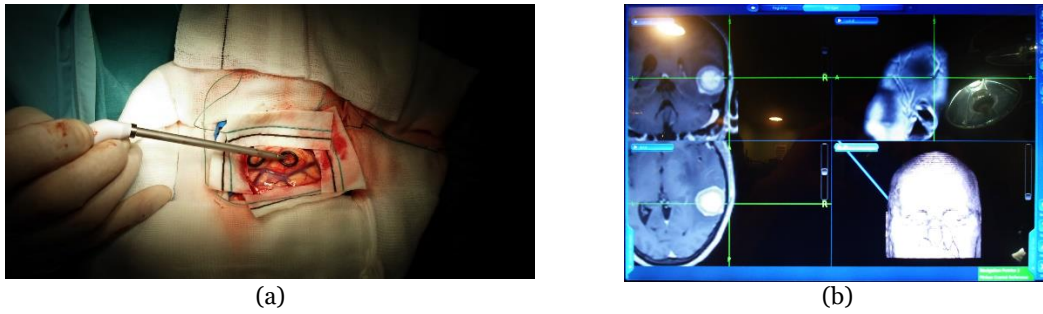
Currently, patients with brain cancer continue to have very poor survival rates. Brain tumors are classified based on their histology and molecular parameters [2]. Malignant gliomas are the most common form of primary brain tumors in adults and cause between 2 and 3% of cancer deaths worldwide [3]. **Figure 2-1** shows the estimated standardized rate per 100,000 habitants of incidence and mortality of people affected by brain cancer and central nervous cancer in Europe in 2012. It seems that both incidence and mortality is higher in men (**Figure 2-1.a**), having a total rate of 7.8 and 6.0 per 100,000 habitants respectively in the entire Europe. Women have also a relative high rate (**Figure 2-1.b**), reaching a total rate of incidence and mortality of 5.6 and 4.0 per 100,000 habitants respectively also in the entire Europe. In addition to radiotherapy and chemotherapy, surgery is one of the major treatment options for brain tumors [1]. However, because brain tumors infiltrate and diffuse into the surrounding normal brain, the surgeon's naked eye is often unable to accurately distinguish between tumor and normal brain tissue. Often, tumor tissue is either unintentionally left behind during surgery or too much normal brain tissue is taken out. Studies have shown that tumor tissue left behind during surgery is the most common cause of tumor recurrence and is a major cause of morbidity and mortality [5]–[7]. On the other hand, over-resection of brain tumor tissues has also been shown to cause permanent neurological damages that affect patients' quality of life [4].

Several image guidance tools, such as intraoperative neuronavigation, intraoperative magnetic resonance imaging (iMRI), ultrasound and fluorescent tumor markers (for example 5-aminolevulinic acid, 5-ALA), have been commonly used to assist surgeons in the identification of brain tumor boundaries. However, these technologies have several limitations. One limitation is related to the brain shift phenomenon [8]. During craniotomy, the opening of the skull and dura inevitably leads to movements of the brain. This typically manifests as herniation of the brain into the craniotomy defect under pressure from the underlying tumor, or the slump of the brain due to drainage of cerebrospinal fluid and the administration of mannitol. Similarly, following resection of the tumor, the residual brain tissue may slump towards the surgical cavity. This brain deformation invalidates the patient-to-image link and reduces the effectiveness of using pre-operative images for intraoperative surgical guidance. Thus, neuronavigation systems (**Figure 2-2**) enable the correlation of preoperative imaging (computed tomography, CT, or magnetic resonance image, MRI) with landmarks before and during surgery, doubling the complete-removal success rate but just in only around one third of patients [45]. Since neuronavigation systems rely on preoperative image data, the accuracy decreases as the surgical procedure progresses due to the brain shift [9]–[11].



**Figure 2-1: Estimated incidence and mortality from brain cancer and central nervous system per 100,000 inhabitants in (a) men and (b) women in 2012 in Europe.**

iMRI (**Figure 2-3**) solves the problem of brain shift, mapping the tumor margins intraoperatively, but this method has poor spatial resolution and significantly extends the duration of the surgery (between 20 and 75 minutes per image [46]), with a limited number of images that can be obtained [12]. It is also unclear how the contrast-enhancing portion of the tumor is related to pathology and, taking into account the infiltrating nature of brain tumors, if this represents the ideal target for resection. Furthermore, MRI cannot distinguish between electro-cauterized tissue and the contrast-enhancing areas [45], and its ability to demarcate borders is debated.



**Figure 2-2: Image-guided stereotaxis (IGS) (also called neuronavigation) system used to locate the position of a tumor in a MRI.** (a) Pointer over the exposed brain; (b) Screen capture of the neuronavigation system where the green cross indicates the position of the pointer in the MRI.



**Figure 2-3: Intraoperative magnetic resonance imaging system.**

On the other hand, ultrasound is inexpensive, real-time, unaffected by brain shift, and for most gliomas it can identify the contrast-enhancing portion seen on MRI, reliably identifying tumor margins [47]–[50]. However, it has been reported that the use of intraoperative ultrasound can cause the resection of histologically-normal parenchyma [48]. Furthermore, radiotherapy leaves borders difficult to demarcate [49] and it is also time-consuming, operator-dependent [50], requiring large experience by the user to interpret the ultrasound images, and lacks image resolution [51].

Finally, the hitherto discussed imaging technologies focus on the tumor morphology, not on its physiological function. This physiological function may show active tumor areas within the apparent normal morphology of the brain, especially in the infiltrating margins of a glioma. Fluorescence imaging with 5-ALA exogenous addresses this problem to a certain extent (**Figure 2-4**). 5-ALA is a naturally-found precursor to hemoglobin that results in intra-tumor synthesis of fluorescent porphyrins in high-grade gliomas [52], [53], which under ultraviolet light (between 375 and 440 nm) produce the tumor tissue to emit red light. Although 5-ALA can identify the tumor boundaries, it produces relevant knock-on effects for the patient and can only be used for high-grade tumors [14], [52]. Thus, there is no current a device that can help in the accurate definition of brain tumor boundaries during surgical procedures. Label free, non-ionizing imaging modalities that rely on intrinsic properties of tumors or normal brain could be a potential solution to the above problem.

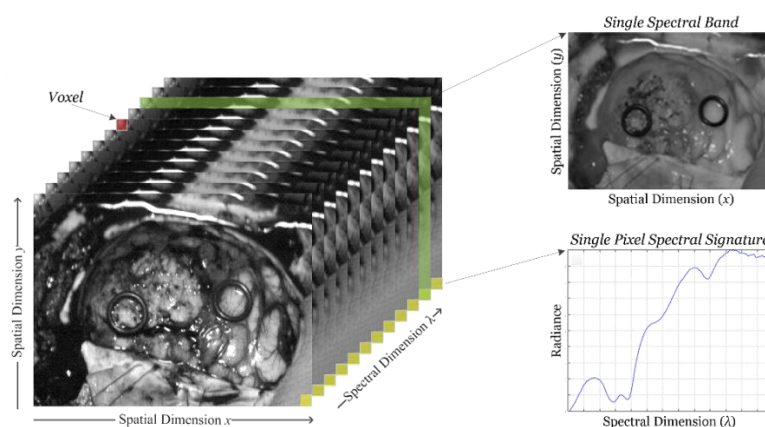


**Figure 2-4: Fluorescence-guided surgery using 5-Ala system.**

## 2.3 Introduction to hyperspectral imaging

Hyperspectral imaging, also known as imaging spectroscopy, is the term designated to the technology that integrates conventional imaging and spectroscopy methods to obtain both spatial and spectral information of an object. HSI sensors measure the reflected, absorbed or emitted radiance at specific wavelengths of the material that is being observed. These sensors are capable of capturing a very large number of contiguous spectral bands (spectral wavelengths) within the electromagnetic spectrum (ES), obtaining a vector of radiance values for each pixel of the image that is commonly called *spectral signature* [15]. Employing these spectral signatures, specific image processing algorithms are able to automatically differentiate the materials observed by the sensor at each pixel [17]. These methods rely on the basis that different molecular compositions of each material present in the nature or artificially generated have different responses to the incident light [15].

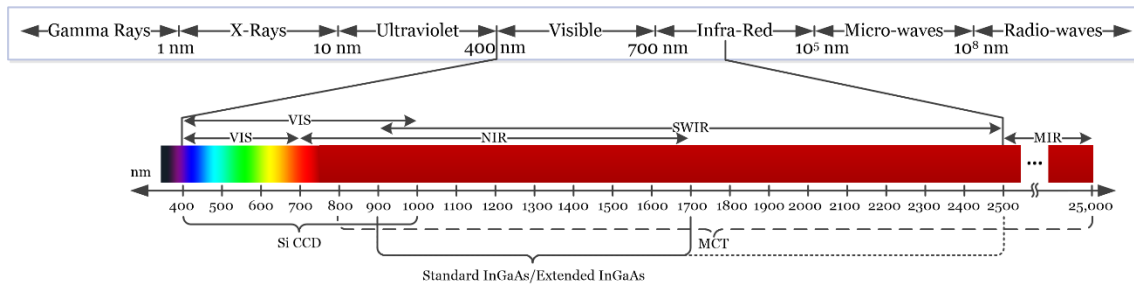
HSI sensors generates a three dimensional (3D) data structure, where the spatial information is contained in the first two dimensions, while the third dimension stores the spectral information of the scene. This 3D data structure is called *hyperspectral cube*. **Figure 2-5** shows the information structure of a HS cube. Each radiance value that conforms the HS cube is called *voxel* and each pixel of the image is formed by a certain number of voxels equal to the number of spectral bands (also called *spectral channels*) of the HS cube. Therefore, from each pixel of the image, it is possible to obtain one spectral signature (containing all the spectral information provided by the HS sensor) and at a certain wavelength, it is possible to obtain a gray scale image of the captured scene (containing the spatial information provided by the image sensor).



**Figure 2-5: HSI basis.** Basic structure of a HS cube, single band representation at a certain wavelength and spectral signature of a single pixel.

### 2.3.1 Hyperspectral imaging cameras

Since HS sensors have not the human eye limitations, they are able to collect information across the ES, beyond the human eye capabilities that covers on average the range from 400 to 700 nm [16]. Consequently, HSI increases the amount of information acquired from a certain scene compared with a conventional RGB (Red, Green and Blue) image that only captures three spectral bands in the visual spectrum. Depending on the type of sensor employed, HS cameras will cover different spectral ranges. **Figure 2-6** shows the partition of the entire ES and the range where HS images are commonly captured depending on the sensor type. Charge-coupled device (CCD) silicon based sensors cover the visible and near-infrared (VNIR) spectrum that conforms the range comprised between 400 and 1000 nm. The standard indium gallium arsenide (InGaAs) sensors are able to capture HS images in the near-infrared (NIR) range, between 900 and 1700 nm, while the extended InGaAs sensors can spread the range to 2500 nm. Other types of sensors can reach larger spectral ranges. For example, the mercury cadmium telluride (MCT) sensors are able to acquire HS images in the short-wavelength infrared (SWIR) range, from 1000 to 2500 nm, being able also to reach 25,000 nm in some specific systems [54].



**Figure 2-6: Electromagnetic spectrum.** Hyperspectral imaging is commonly employed between the visible and the medium-infrared range.

HS cameras are mainly classified into four different types (**Figure 2-7**) depending on the method employed to obtain the HS cube: *whiskbroom* (point-scanning) cameras, *pushbroom* (line-scanning) cameras, cameras based on spectral scanning (area-scanning or plane-scanning), and *snapshot* (single shot) cameras [31]. Each type of camera stores the HS data in a different way. **Figure 2-8** shows the three most commonly used types of HS data storage formats. Depending on the specifications and requirements of the application where the system is going to be used, some HS systems are more suitable than others.

Whiskbroom cameras (**Figure 2-7.a**) are characterized by capturing one single pixel at one time containing all its spectral information. The rest of the pixels of the scene are captured by scanning both spatial dimensions ( $x$  and  $y$ ). This type of cameras usually stores the HS data in the band-interleaved-by-pixel (BIP) format (**Figure 2-8.c**), being the suitable format to quickly access the spectral information of each pixel. Whiskbroom cameras have the main disadvantage of being very time-consuming during the image acquisition. However, they can achieve very high spectral resolutions.

Related with the previous camera type, pushbroom cameras (**Figure 2-7.b**) offer a faster scanning solution, obtaining also high spectral resolution. In this case, the camera captures one line of pixels of the scene ( $y$ ) at one time. The other spatial dimension ( $x$  axis) is obtained moving the field-of-view (FOV) of the camera in that direction. In this case, the HS data are normally stored following the band-interleaved-

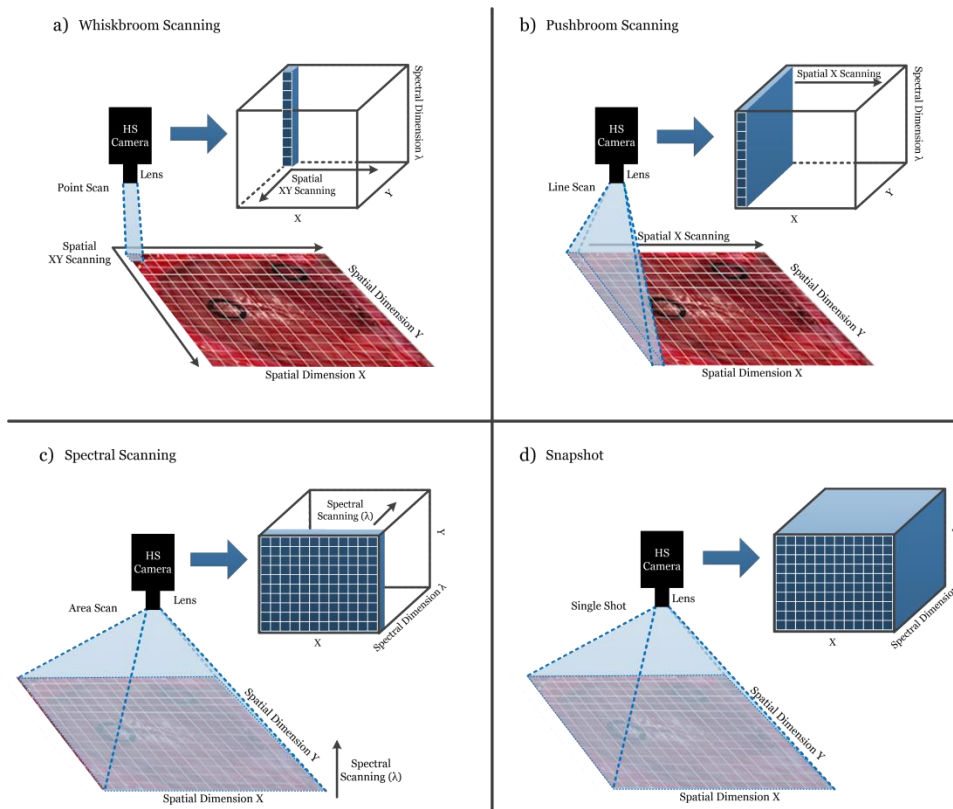


by-line (BIL) format (**Figure 2-8.b**), since the pixels are captured line by line with their entire spectral information. Pushbroom cameras are the most common systems in remote sensing field and other industrial sectors due to their high spectral resolution, having reduced capturing times with respect to the whiskbroom cameras.

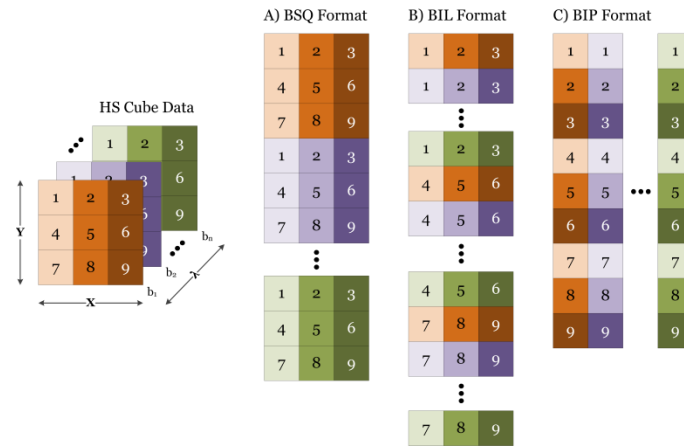
On the other hand, HS cameras based on spectral scanning (**Figure 2-7.c**) are able to obtain the entire spatial information ( $x$  and  $y$ ) of the scene for a certain wavelength at one time, performing a scanning in the spectral dimension ( $\lambda$ ). This type of cameras usually stores the HS data in the band sequential (BSQ) format (**Figure 2-8.a**), staking every single band captured by the sensor. These cameras can achieve high spatial resolutions and fast acquisition times; however, the spectral resolution use to be lower compared to the spatial scanning (whiskbroom and pushbroom) cameras. One of the main disadvantages of this type of cameras is that they are not suitable for capturing moving objects due to the time required to perform the spectral scanning.

Finally, there is an emerging type of HS cameras that are able to provide hyperspectral video, having the lowest acquisition time and allowing acquiring moving objects without performing any spatial or spectral scanning. Snapshot cameras (**Figure 2-7.d**) capture the entire scene in a single shot that contains both the spectral and spatial information [55]. In the same way as the cameras based on spectral scanning, snapshot cameras usually store the HS data in BSQ format. The main disadvantage of snapshot cameras is that the spectral and spatial resolutions are much lower with respect to the other camera types.

In conclusion, the HS camera type selected to shape the acquisition system is closely related with the application where the system is going to be used.



**Figure 2-7: HS camera types and their respective acquisition and storage data methods.** (a) Whiskbroom camera; (b) Pushbroom camera; (c) HS camera based on spectral scanning; (d) Snapshot camera.



**Figure 2-8: HS data storage structure types.** (a) Band sequential (BSQ) format; (b) Band-interleaved-by-line (BIL) format; (c) Band-interleaved-by-pixel (BIP) format.

### 2.3.2 Hyperspectral imaging processing algorithms

An extensive literature is available on classification of HS images [56]. Traditionally, HSI has been widely employed in the remote sensing field and, for that reason, the majority of algorithms developed to classify HS images are related with this field [57]. However, more recently, HSI is progressively being used in other fields, such as drug analysis [58], [59], food quality inspection [31]–[33], [60] or defense and security [27], [61] among many others. That is why the algorithms that were developed targeting remote sensing application have been adapted to classify different types of scenes.

Pixel-wise classification methods assume that each pixel is pure or a mix of pure pixels and can be assigned to a certain material based on its spectral information [62]–[64]. Pixel-wise classification algorithms can be divided in two types: *supervised* classifiers and *unsupervised* classifiers (also called *clustering* or *segmentation* algorithms). Furthermore, in the recent years, the use of deep learning (DL) approaches to classify HS data has become increasingly common, achieving excellent results when compared with traditional machine learning (ML) algorithms [65]. All these algorithms have to face two main problems when they are applied to HS data: the high dimensionality and the limited size of samples.

The basis of the supervised classification algorithms relies on assigning to each pixel of the HS image one of the previously established classes based on its spectral values. In order to perform this assignation, the algorithm must be previously trained employing a spectral signature library where each type of signature has been identified with a certain class. For this purpose, ML methods based on decision trees, such as Random Forest (RF) [66], [67], neural networks, such as Artificial Neural Networks (ANN) [68]–[70], and kernel-based methods have been widely used to classify HS images. In particular, there are several types of kernel-based methods in the literature [71], where support vector machine (SVM) classifier is the most commonly used algorithm. In the HSI field, SVMs provide good performance for classifying this type of data when a limited number of training samples is available [71]. Due to its strong theoretical foundations, good generalization capabilities, low sensitivity to the problem of dimensionality and the ability to find optimal solutions, SVMs are usually selected by many researchers over other classification paradigms for classifying HS images [34]. As a relevant example, a variant of the SVM classifier, called Fuzzy SVM classifier, was employed in the development of an emotion recognition system based on facial

expression images, obtaining overall accuracy results of  $96.77 \pm 0.10\%$  [72]. In the medical field, SVMs have been used to detect multiple sclerosis subjects employing stationary wavelet entropy to extract features from magnetic resonance images used as inputs of the SVM classifier [73]. Furthermore, the same technique combined with a directed acyclic graph method has been used to diagnose unilateral hearing loss in structural MRI [74], demonstrating that the SVM algorithm is a reliable candidate to work with medical images.

On the other hand, the goal of the unsupervised classifiers is to divide an image into a certain number of similar groups (also called *clusters*), where each group shares approximately the same spectral information and provides the correspondent cluster centroid [75], [76]. Each cluster centroid represents a spectra corresponding to a material in the scene, while the membership functions provide the weights for these spectra. Unlike the supervised classifiers, unsupervised methods do not require a training process using labeled samples. For that reason, they cannot provide the identification of the class that each pixel belong to. They only provide a certain number of clusters with no information about the material nature. Although unsupervised clustering does not provide any discriminant feature by itself, it could be used to delineate the boundaries of the different spectral regions presented in a HS image. ML unsupervised algorithms such as K-means algorithm [77], [78] and the Iterative Self-Organizing Data Analysis (ISODATA) technique [79]–[81] are the most common clustering algorithms employed in the literature using HS data [56]. In particular, within the unsupervised classification algorithms, hierarchical clustering is a method of cluster analysis that seeks to obtain a hierarchy of clusters [82], [83]. Several hierarchical clustering algorithms have been employed to classify HS images, such as Hierarchical rank-2 non-Negative Matrix Factorization (H2NMF) [84], Hierarchical K-Means (HKM) [84], [85] and Hierarchical Spherical K-Means (HSKM) [86]. Some works based on HS analysis for medical applications use unsupervised clustering as part of the classification algorithm, such as for colon tissue cell classification [87] or laryngeal cancer detection [88].

In the field of deep learning, these techniques have recently become a hotspot to process HS data, being introduced in the field of remote sensing big data analysis. DL techniques have been used in many sectors of remote sensing data analysis, such as image processing, pixel-wise classification, target detection and also other recent challenging tasks of high-level semantic feature extraction and scene understanding [65]. As basis, DL generates computational models that are formed by several processing layers to learn different representations of data with multiple levels of abstraction. DL architectures can discover intricate structures in large datasets employing backpropagation algorithms to determine the changes that a machine should perform in its internal parameters to compute the representation at each layer from the representation in the previous layer [89]. Conventional ML techniques are limited in their ability to process original data on their raw form. However, DL methods are composed of a set of methods that allows a machine to be fed with raw data and to automatically discover the representations required for detection or classification. These multiple levels of representation are obtained by composing single but non-linear modules that modify the representation at one level (starting with the raw input) into a representation at a higher, slightly more abstract, level. With the composition of enough such transformations, very complex functions can be learned [89].



Many DL frameworks have been applied to HS images in the literature. Deep belief networks (DBNs) [90] and convolutional neural networks (CNNs) [91], [92] have been employed to process and classify HS remote sensing data, improving the results obtained with conventional SVM-based algorithms [93]–[96]. CNNs have been also employed to extract high-level spatial features from HS data in a spectral-spatial feature extraction algorithm for HS image classification [97]. In the medical field, DL is emerging in the recent years as a powerful tool in the field of translational bioinformatics, medical imaging, pervasive sensing and medical informatics [98]. As an example, deep neural networks (DNNs) and CNNs have been employed to classify electrocardiogram signals [99]–[101], detect retinal vessels [102]–[105], classify colorectal polyps [106]–[108] and several types of cancer analysis [109]–[113]. On the other hand, the use of DL techniques in the medical field related with HSI is quite reduced until now. The main reason that can cause this fact is that deep learning requires of high amount of data to train the networks and currently there are not such high quantity of medical HSI databases available as the capturing process is quite expensive and complex. In general, other techniques commonly used in HSI applied to remote sensing, such as unmixing or anomaly detection, are not normally used for medical HSI mainly due to the spatial resolution of the HS images are quite high due to the distance between the camera and the sample it is much more lower in comparison with remote sensing applications.

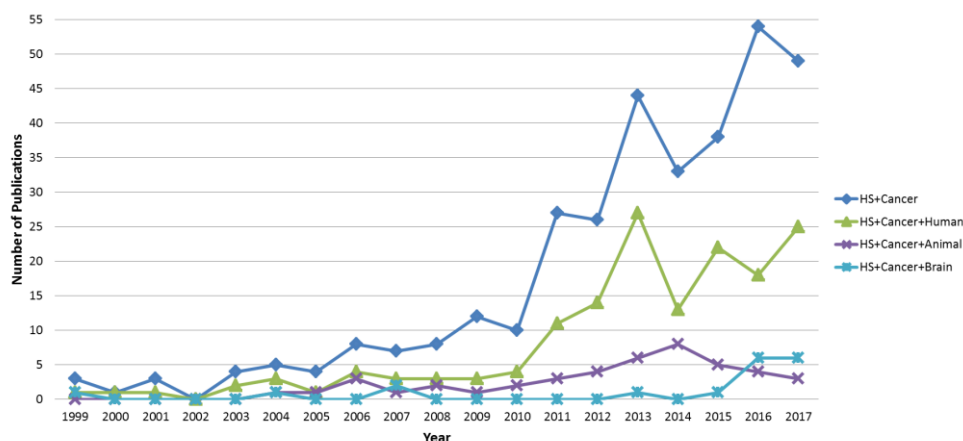
At this point, it is required to analyze the different studies available in the literature where HSI is employed for cancer analysis, potentially providing useful information to the operating surgeon in the identification of different types of tissues.

## 2.4 Medical hyperspectral imaging for cancer analysis

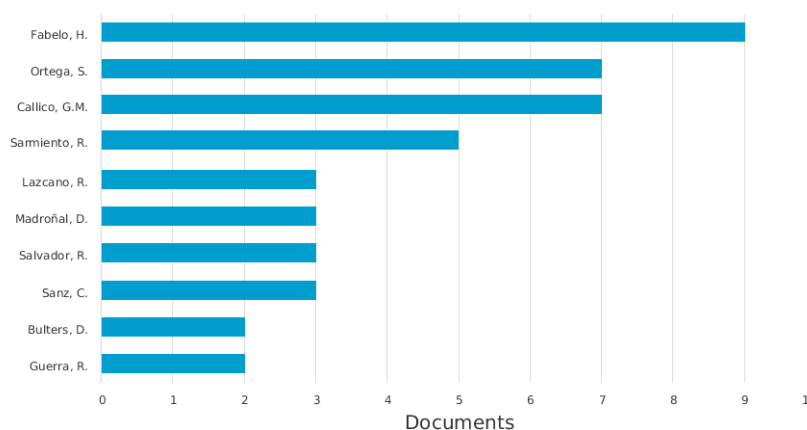
In the previous sections, the current devices that surgeons have available to assist them during surgical procedures and the problems that must still to be solved have been presented. In addition, the basis of the HSI technology and the main algorithms employed to process this type of data have been described. In this section, the state-of-the-art in the use of HSI within the medical field, particularly in the cancer analysis, is presented. This imaging modality is a non-invasive sensing technique that has been used in medical applications for more than two decades [34], [35]. However, it has been in the recent years when medical HSI has started to achieve promising results with respect to cancer detection. **Figure 2-9** shows the statistics obtained from Scopus<sup>1</sup>, where the number of documents published per year related with the use of HSI to study different types of cancer is presented. The exploration was performed searching the terms presented in the legend (HS was searched as hyperspectral) in the title, abstract and keywords of each document. As it can be seen, the studies that mention brain cancer are only a few in the past years and they started to grow from 2016 mainly due to the research works published by the HELICoiD group, positioning the University of Las Palmas de Gran Canaria as the main institution working in this field (**Figure 2-10**).

---

<sup>1</sup> <https://www.scopus.com/>

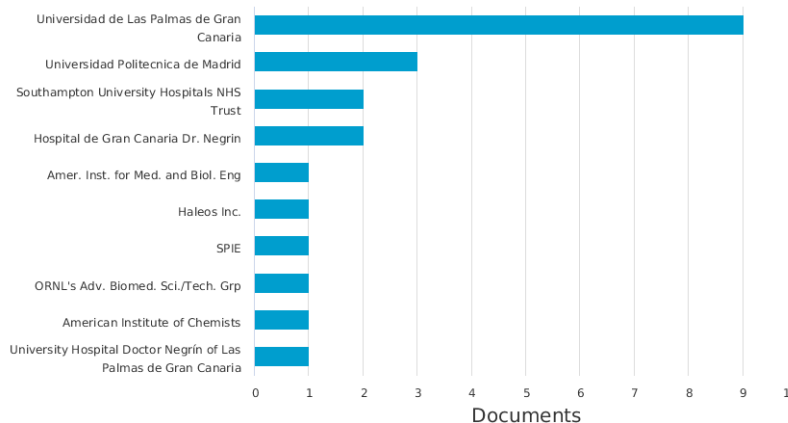


**Figure 2-9: Number of publications per year related with the use of HSI for cancer analysis.** Source: Scopus.



Copyright © 2018 Elsevier B.V. All rights reserved. Scopus® is a registered trademark of Elsevier B.V.

(a)



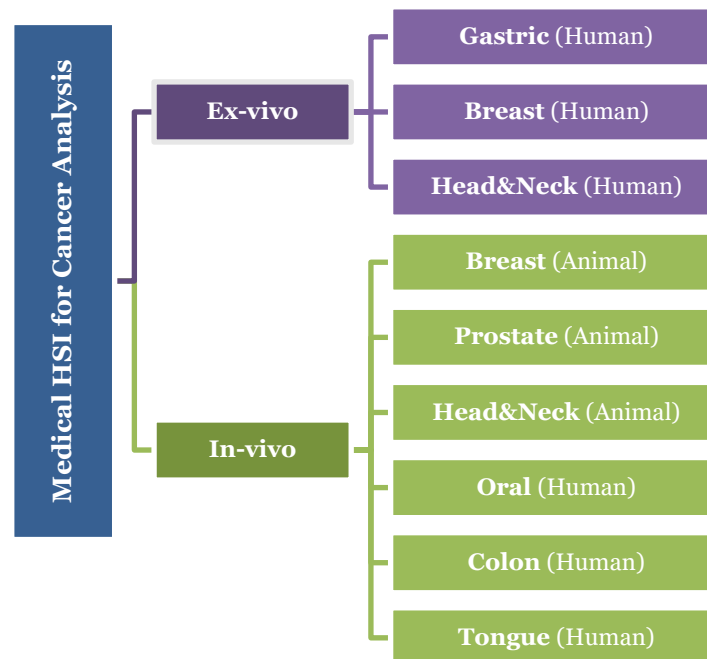
Copyright © 2018 Elsevier B.V. All rights reserved. Scopus® is a registered trademark of Elsevier B.V.

(b)

**Figure 2-10: Number of publications per author (a) and per institution (b) related with the use of HSI for brain cancer analysis.** Source: Scopus.

These studies performed in the literature related with the use of HSI for cancer analysis can be categorized depending on the type of tissue sample (*ex-vivo*, *in-vivo*), the type of organ studied (brain, breast, colon, prostate, etc.) or the type of subject (human, animal). The *in-vitro* studies will not be included in this state-of-the-art as they have not been used in this work. Considering this, a specific taxonomy has been established to present the studies performed in this area (**Figure 2-11**).

On the other hand, HSI systems are not standardized, as different technologies were used in these studies. As explained in Section 2.1, HS cameras generally use CCD sensors for VNIR applications (covering the range between 400 and 1000 nm) while InGaAs sensors are used for NIR applications (covering the range between 1000 and 1700 nm), since the quantum efficiency of the CCD sensors is very low above 1000 nm. As will be detailed in **Table 2-1**, most of the studies work in the VNIR spectral region, employing CCD sensors. However, in some studies, the NIR region is also explored, requiring the use of InGaAs sensors. Regarding to the illumination systems used in HSI applications, they are mainly based on halogen or xenon lamps, and sometimes, optical fibers are used for light transmission in order to avoid the high temperatures produced by these types of light sources or to concentrate the light into a certain area. The main characteristics of the systems employed in each study presented in this literature review will be detailed in the summary table shown at the end of this section (**Table 2-1**).



**Figure 2-11: Taxonomy of the state-of-the-art of medical HSI for cancer detection.**

### 2.4.1 Ex-vivo cancer HSI analysis

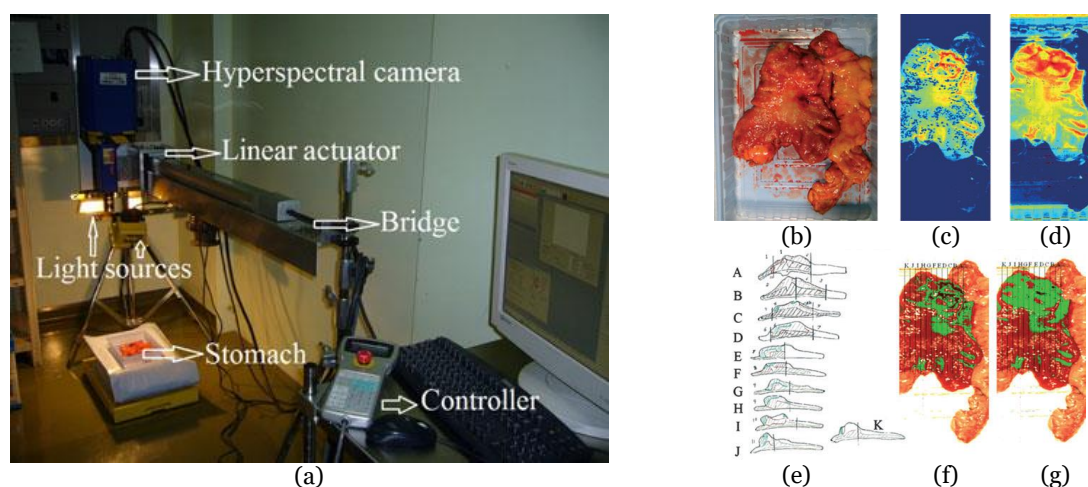
Several studies have been performed related to the analysis of *ex-vivo* cancerous tissue employing HSI. Due to the complexity of the procedures to capture *in-vivo* samples from human beings, *ex-vivo* cancer analysis has been performed during many years in human tissue. Gastric, breast and head & neck tumors have been mainly analyzed. Next, the more relevant studies that can be found in the literature in this area are exposed.

#### 2.4.1.1 Gastric human cancer

In 2011, Akbari *et al.* performed a study to identify gastric tumors in human *ex-vivo* tissues employing an HS system capable of capturing images in the range between 1000 and 2500 nm, obtaining 239 spectral bands [114]. They used an integral filter and the normalized cancer index (NDCI) to perform an automatic classification of the tumor

tissue determining the boundaries between tumor and normal tissue using the pathological analysis to validate their results (**Figure 2-12**). From their experiments, they determined that the spectral regions between 1226 and 1251 nm and 1288 and 1370 nm are the most suitable ranges for distinguishing between non-cancerous and cancerous gastric tissue.

In 2013, Kiyotoki *et al.* collected HS images in the spectral range comprised between 400 and 800 nm from *ex-vivo* tissue gastric samples to perform a preliminary study of gastroduodenal tumors removed by endoscopic resection or surgery from 14 different patients [115]. The system was able to obtain HS images composed by 72 spectral bands with a spatial dimension of 640 x 480 pixels. Using these images, they were able to determine the optimal wavelength that allowed the most accurate classification between tumor and normal mucosa using the cutoff point method in the 726 nm wavelength. The sensitivity, specificity, and accuracy obtained in the test samples were 78.8%, 92.5% and 85.6%, respectively. This work was improved in 2015 by the same group, increasing the number of patients to 96 and performing the selection of the optimal wavelength using the Mahalanobis distance, which in this case was 770 nm [116]. Sensitivity, specificity, and accuracy results obtained were 71%, 98%, and 85%, respectively, demonstrating that the increment in the number of patients to analyze did not decrease the accuracy of the method. Although the classification method employed to distinguish the different types of samples was quite basic, the studies revealed promising results in the use of HSI as a diagnostic tool for gastric cancer.



**Figure 2-12: Acquisition system employed, cancer detection results using the NDCI and integral filter and comparison with pathological results obtained in [114].** (a) HS acquisition system setup; (b) RGB representation of the *ex-vivo* sample; (c) Cancer enhanced regions using integral filter in the hyperspectral image (1057–2440 nm), the tissues are shown in a blue to red spectrum, where the red regions represent the tumor; (d) Cancer enhanced regions using NDCI; (e) Pathological results; (f) Detected tumor using integral filter; (g) Detected tumor using NDCI.

#### 2.4.1.2 Breast human cancer

Breast cancer has been also studied using *ex-vivo* samples with the goal of automatically delineate the regions of interest (ROI) in the samples and classify the tumor and normal tissue samples. In 2013, two studies were published with both previous mentioned goals using a HS system capable of obtaining images in the spectral range between 380 and 780 nm. The study accomplished by Kim *et al.* performed an automatic ROI detection based on contrast and texture information

achieving a true positive rate (TPR) and a true negative rate (TNR) of 97.3% and 95.9%, respectively, similar to the results obtained in a manual segmentation (98.7% and 96.4%) [117]. In the study performed by Pourreza-Shahri *et al.*, authors performed a feature extraction (using the Fourier coefficient selection features method) and a dimensional reduction (using the Minimum Redundancy Maximum Relevance method) to the HS images and then performing an automatic classification (using the SVM classifier with the RBF kernel) of the tissue samples, differentiating between cancerous and non-cancerous tissue [118]. Sensitivity and specificity results of 98% and 99%, respectively were obtained, demonstrating that HSI is a powerful imaging modality that can be used for the diagnostic of breast cancer.

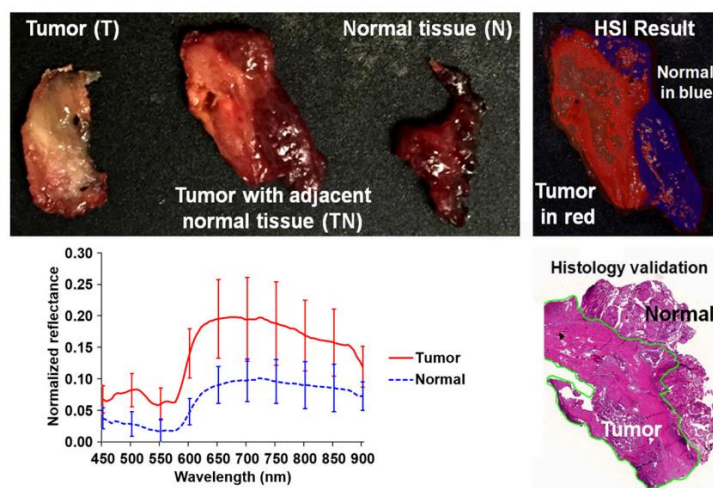
#### 2.4.1.3 Head & neck human cancer

One of the most active research groups in biomedical applications of HSI is led by Professor Baowei Fei, who is currently affiliated to the Department of Bioengineering of The University of Texas at Dallas. Mainly, their experiments explore cancer diseases in animal subjects, although some studies have been carried out using *ex-vivo* human head & neck tumor samples. They usually work using an acquisition system based on LCTFs (Liquid Crystal Tunable Filters) in the VNIR spectral range, from 450 to 950 nm, with a spatial resolution of 1392 x 1040 pixels, capturing 91 spectral bands.

In 2017, several works were published in this area with the goal of discriminating cancerous and non-cancerous tissue. Fei *et al.* achieved an accurate delineation of the boundaries between the normal and cancerous tissue using head & neck *ex-vivo* samples contrasted with the histopathological results (**Figure 2-13**) [119]. The ensemble linear discriminant analysis (LDA) was employed to perform the classification, achieving an average accuracy, sensitivity and specificity of 90%, 89% and 91%, respectively, using oral cavity samples and an average accuracy, sensitivity and specificity of 94%, 94% and 95%, respectively, using thyroid samples. Autofluorescence, fluorescence with 2-deoxy-2-[(7-nitro-2,1,3-benzoxadiazol-4-yl)amino]-D-glucose (2-NBDG) and proflavine images were also classified and compared with the HSI results demonstrating that HSI offered better results over the other alternative imaging modalities (an increment of more than 7% of accuracy).

In addition, Lu *et al.* increased the number of patients ( $N = 36$ ) and accomplished an extensive comparison using different machine learning classification approaches, reinforcing the conclusion obtained from the other study, where the ensemble LDA outperformed other traditional machine learning algorithms [120]. In this study, intra-patient and inter-patient classifications were performed, as well as different classifications using different spectral regions within the VNIR range (450-600 nm, 605-850 nm, 855-900 nm and 450-900 nm). Finally, they concluded that the use of the entire spectral range (from 450 to 900 nm) provides the best accuracy results.

Finally, one of the few studies performed in the literature regarding to the use of deep learning methods to classify HS images with the goal of distinguishing cancerous and non-cancerous tissue was performed by Halicek *et al.* [121]. Authors developed a CNN classifier to process the *ex-vivo* tissues from 50 different patients and compared the deep learning method with traditional machine learning approaches, demonstrating that CNNs outperforms the traditional classifiers in this case.



**Figure 2-13: Preliminary results obtained in the tumor margin delineation for head & neck cancer** [119]. After hyperspectral image acquisitions (top-left), the tissue was processed histologically, and tumor margins were outlined on the pathology image (bottom right) by a pathologist, which was used to validate the results of the classification (top-right). The average spectral curves are shown at the bottom left for each type of tissue, i.e., tumor, normal, and tumor with adjacent normal tissue.

## 2.4.2 In-vivo cancer HSI analysis

One of the most important applications of HSI in the field of cancer detection and classification is regarding to the intraoperative use of this image modality. Taking into account its non-invasive and non-ionizing nature, HSI is suitable to be used as an aid guidance tool for the resection of tumors during surgical operations. In this sense, several studies have been focused during many years in the application of this technology for *in-vivo* tissue analysis. However, due to the complexity of the surgical procedures and the ethical implications regarding to human beings, the majority of the HSI studies using *in-vivo* tumor samples employs animal subjects. Only works related with endoscopic systems attached to HSI or spectrograph apparatus that uses *in-vivo* tumor human samples are presented in the literature. In the following sections, some of these studies will be presented.

### 2.4.2.1 Breast animal cancer

One of the first and most relevant works performed using HSI to study breast cancer was performed in 2007 by Panasyuk *et al.* [122]. In this work, authors employed a HS system based on LCTFs to acquire HS images in the visual spectral range (comprised between 450 and 700 nm and composed by 34 bands) during intraoperative surgery of 60 rats affected by an induced breast cancer. They generated thematic maps, where different types of tissue including tumor, blood vessels, muscle, and connective tissue were clearly identified and differentiated. Furthermore, a sensitivity of 89% and a specificity of 94% for the detection of the residual tumor were obtained and compared to the histopathological examination of the tumor bed. One of the lacks of this work was the use of LED (light-emitting diode) illumination in the HS acquisition system, which produced a non-standard spectral signature due to LED light does not provides a broadband and uniform spectrum compared to the halogen of xenon light.

In addition, in 2014, McCormack *et al.* accomplished an study where mouse models of breast cancer were employed to evaluate the use of *in-vivo* HSI for microvessel sO<sub>2</sub>

segmentation and classification during surgical procedures, studying also the response of the microvessels to different types of treatments [123]. In order to obtain the HS images it was employed an acquisition system based on LCTFs and a halogen lamp, capturing images in the spectral range between 500 and 600 nm and composed by 26 bands.

#### 2.4.2.2 Prostate animal cancer

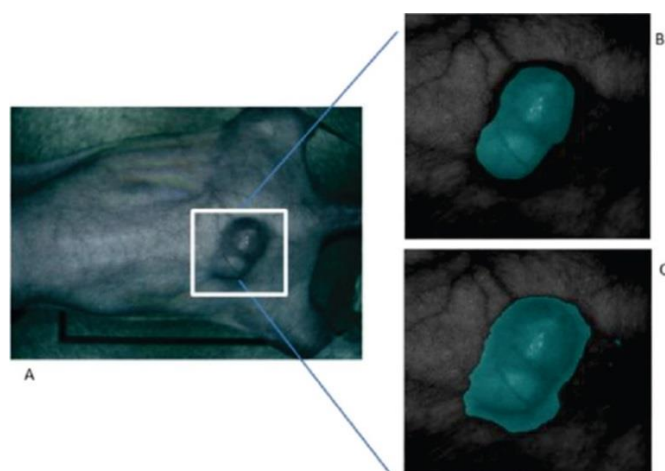
Prostate cancer has been also studied by the group of Dr. Fei using *in-vivo* HS images of mice affected by human prostate cancer. In 2012, Fei *et al.* [124] and Akbari *et al.* [125] employed an HSI system based on LCTFs and xenon illumination to capture *in-vivo* images in the range between 450 and 950 nm of mice affected by human prostate tumors. Their results showed a maximum sensitivity of 92.8% and a specificity of 96.9% in the classification of malignant and non-malignant regions using a least squares support vector machine (LS-SVM) classifier.

#### 2.4.2.3 Head and neck animal cancer

Other types of tumors have been also studied and analyzed using HSI, such as those of the head and neck cancer. As in the previous section, the same group of Dr. Fei performed several works in the analysis of head and neck cancer using *in-vivo* HS images from mice affected by head and neck cancer. All the studies were performed in the VNIR range comprised between 450 and 950 nm using the CRI Maestro HS acquisition system. In 2014, Lu *et al.* published several works in this field, where the tensor decomposition, PCA and KNN methods were employed to perform a feature extraction and automatic classification, achieving a sensitivity of 93.7% and a specificity of 91.3% in the discrimination of tumor and normal tissue [126], [127]. Furthermore, they accomplished an exhaustive margin delineation of the tumor during the surgical procedures performing an *in-vivo/in-vitro* registration between the *in-vivo* HS images and the histological images to validate the results [128].

On the other hand, their research has exhaustively analyzed which pre-processing techniques are more suitable to compensate the variations of the environmental conditions during the acquisition inside an operating theatre [129], [130]. In the work published in 2015, a method based on the mRMR (maximal Relevance and Minimal Redundancy) algorithm was proposed to address the problem of glare that usually appears in the HS images, improving the sensitivity and specificity results to 94.4% and 98.3%, respectively. In addition, other more sophisticated techniques were studied by this group such as the use of a minimum-spanning forest (MSF) algorithm for an automatic classification and segmentation of the *in-vivo* HS images [131] (**Figure 2-14**).





**Figure 2-14: Result of the tumor identification using the Minimum-Spanning Forest method developed in [131].** (a) RGB image of the original mouse; (b) Corresponding gold standard image; (c) Classification result obtained.

#### 2.4.2.4 Oral human cancer

A reduced number of studies can be found in the literature using HSI to analyze *in-vivo* samples of human subjects. Mainly, the studies are related with the use of endoscopic systems attached to HS camera.

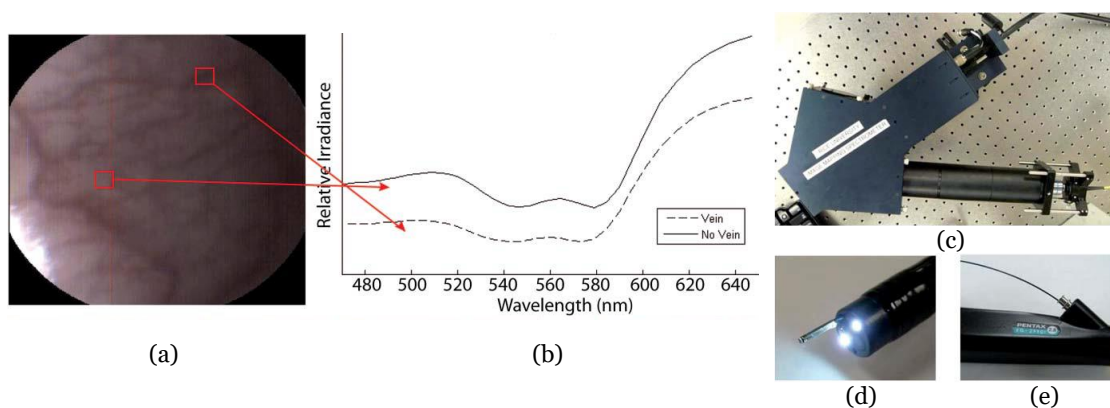
In 2011, Kester *et al.* developed a real-time snapshot HSI endoscope system based on an image mapping technique that is capable of operating at frames rates of 5.2 fps (frames per second), obtaining HS cubes of 48 bands in the visual range between 450 and 650 nm, with a spatial resolution of 100  $\mu\text{m}$  [132]. Using this system, they were able to capture *in-vivo* tissue, resolving a vasculature pattern of the lower lip while simultaneously detecting oxy-hemoglobin. **Figure 2-15** shows an example of the spectral signatures obtained by the system and the developed acquisition system.

Moreover, in 2011, another study was published by Jayanthi *et al.* related with the use of diffuse reflectance spectroscopy for early detection of malignant changes in the oral cavity [133]. The system was able to capture HS information within the visible spectral range (from 400 to 700 nm), obtaining 40 different bands. They used PCA to dimensionality reduce the images and LDA for the automatic classification of the data. They achieved sensitivity and specificity results higher than 95% in the discrimination between different lesions, such as normal/healthy, hyperplastic, dysplastic and squamous cell carcinoma (SCC) tissues.

In 2016, laryngeal cancer was investigated by Regeling *et al.* using a flexible endoscopy coupled to an HSI system that was able to obtain HS images composed by 30 bands in the visual spectral region between 390 and 680 nm [88]. This system was employed to obtain *in-vivo* HS images that had to be registered due to patient's heartbeat and removed the noise and the specular reflections. Finally, an image pre-processor method was proposed to solve these issues [134]. The images were registered using a rigid image-to-image registration based on normalized cross-correlation (NCC), the noise was reduced using the minimum noise fraction (MNF) transformation and the glare was detected using a customized method. In addition, the random forest (RF) algorithm was applied to distinguish between healthy and cancerous tissue, achieving an overall accuracy of 88%.



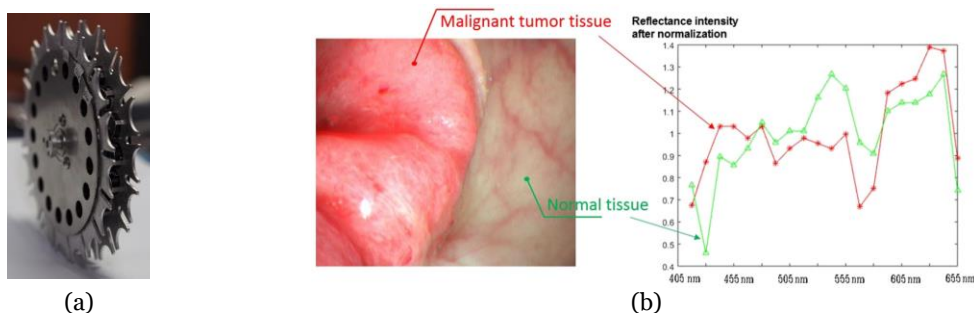
In addition, in the same year, Laffers *et al.* employed a rigid HS endoscopic system to capture HS images (in the spectral range comprised between 390 and 680 nm) of the oral cavity or oropharynx from 85 patients [135]. However, in this study they only took into consideration 3 patients, one of them used for training the algorithm and the other two for validation purposes. The classification results obtained using the RF algorithm presented sensitivities of 61% and 43%, and specificity of 100% in the two validation patients. These reduced sensitivity values could be mainly produced due to the low number of patients involved in the training of the classification algorithm. The inter-patient variability for the training phase was not correctly addressed in this study.



**Figure 2-15: HS image example of the lower lip of a normal human acquired with the image mapping spectroscopy (IMS) endoscope developed in [132].** (a) RGB representation; (b) Spectral signature of the normal tissue pixel and a vein pixel; (c) Clinical setup of the IMS endoscope; (d) Miniature imaging end of the IMS endoscope; (e) Fiber optics of the IMS endoscope inserted into the instrument channel.

#### 2.4.2.5 Colon human cancer

Following with the HS endoscopic systems, *in-vivo* colorectal tumors have been also studied in the literature. One of the main studies in this field was performed in 2016, when Han *et al.* used a flexible hyperspectral colonoscopy system based on a motorized filter wheel, capable of obtaining 27 different bands in the range comprised between 405 and 665 nm, to discriminate between malignant colorectal tumors and normal mucosa in human patients [136] (**Figure 2-16**). They used a wavelength selection algorithm based on the recursive divergence method to identify the most relevant wavelengths in the spectral range employed, demonstrating that HSI can be used *in-vivo* for outlining the disease region and enhancing the microvascular network on the mucosa surface.



**Figure 2-16: System and preliminary results obtained in [136].** (a) The optical filter wheel used in the HSI system; (b) Color image of a malignant colorectal tumor and a graph showing the spectral signature of the tumor and normal mucosa in the wavelength range of 405 to 655 nm.

### 2.4.2.6 Tongue human cancer

Finally, tongue cancer of *in-vivo* human samples was studied in 2012 by Liu *et al.* using HSI [137]. The HS system employed was based on an acousto-optic tunable filter (AOTF), capturing 81 bands in the VNIR spectral range comprised between 600 and 1000 nm. They developed a classifier based on the sparse representation (SR) method and compared the results obtained using traditional machine learning algorithms such as SVM or RVM (Relevance Vector Machine) classifiers. Sensitivity and specificity results of 91.3% and 93.7%, respectively, were obtained, increasing the accuracy in more than 4% with respect to the other two methods.



**Figure 2-17: Delineation of the tongue tumor region in [137].** Expert labeling (left) and classifier prediction of tumor regions (right).

### 2.4.3 Summary

**Table 2-1** presents a brief summary of the main characteristics of the related works previously presented that studied the use of HSI for cancer detection sorted by the year of publication.

## 2.5 Conclusions

In this chapter, a brief description of the current intraoperative brain surgical guidance tools employed to assist neurosurgeons in the crucial task of tumor resection has been presented. The advantages and disadvantages of each guidance method have been highlighted, concluding that there is an urgent necessity to find a suitable technique that could solve the problems faced by neurosurgeons inside the operating theatre. After this discussion, an introduction to the hyperspectral imaging concept detailing the current methods available to acquire this type of data has been provided as well as a brief description of the main algorithms employed to process HS data. Since the target of this thesis is to apply HSI to the detection of brain cancer during surgical procedures, an analysis of the current state-of-the-art related with the use of HSI in the medical field applied to cancer analysis of *in-vivo* and *ex-vivo* tissues has been presented. As stated before, only a few works can be found in the literature that study *in-vivo* cancer during surgical procedures in human beings. The main works performed in humans are related with *ex-vivo* tissue samples and the few *in-vivo* works are mainly related with HSI endoscopic systems. As far as we know, *in-vivo* brain tumors have not been studied before using HSI a part from the works performed by the HELICoiD team.

**Table 2-1: Summary of the state-of-the-art in the use of HSI for cancer analysis**

Ref.	Year	Type of Cancer <sup>Y</sup>	Type of Sample	Spectral Range (nm)	Image Size (pixels)	#Bands	Light source	Acq. Mode	Algorithms	Goal	Subject <sup>*</sup>
[122]	2007	Breast	<i>in-vivo</i>	450-700	1024×1528	34	InGaN LEDs	LCTF	Custom Algorithm	Classification	A
[132]	2011	Oral	<i>in-vivo</i>	450-650	350×350	48	Halogen	Snapshot	-	-	H
[133]	2011	Oral	<i>in-vivo</i>	400-700	-	40	Halogen	-	PCA, LDA	Dimensional reduction, Classification	H
[114]	2011	Gastric	<i>ex-vivo</i>	1000-2500	-	239	Halogen	Pushbroom	Std, SVM, Integral Method, NDCI	Classification, Margin delineation	H
[125]	2012	Prostate	<i>in-vivo</i>	450-950	1392×1040	251	Xenon	LCTF	LS-SVM	Classification	A
[137]	2012	Tongue	<i>in-vivo</i>	600-1000	1392×1040	81	Halogen	AOTF	SR, SVM, RVM	Classification	H
[124]	2012	Prostate	<i>in-vivo</i>	40-950	1392×1040	251	Xenon	LCTF	LS-SVM	Classification	A
[115]	2013	Gastric	<i>ex-vivo</i>	400-800	640×480	72	Halogen	-	Cutoff point	Optimal wavelength selection, Classification	H
[117]	2013	Breast	<i>ex-vivo</i>	380-720	-	101	Xenon	-	Polynomial SVM	Automatic ROI detection based on contrast and texture information	H
[118]	2013	Breast	<i>ex-vivo</i>	380-720	-	101	Xenon	-	Fourier coefficient selection features, mRMR, RBF SVM	Feature extraction, Dimensional reduction, Classification	H
[123]	2014	Breast	<i>in-vivo</i>	500-600	1392×1040	26	Halogen	LCTF	Gabor Filter, Expectation Maximization	Microvessel sO <sub>2</sub> segmentation and classification	A
[126], [127]	2014	H&N	<i>in-vivo</i>	450-950	1392×1040	251	Xenon	LCTF	Tensor Decomposition, PCA, KNN	Feature extraction, Classification	A
[128]	2014	H&N	<i>in-vivo</i>	450-950	1392×1040	251	Xenon	LCTF	PCA, FFD	Surgical margin delineation and <i>in-vivo/in-vitro</i> registration	A
[130]	2015	H&N	<i>in-vivo</i>	450-950	1392×1040	226	Xenon	LCTF	mRMR, KNN	Glare removal, Feature extraction, Automatic classification	A
[129]	2015	H&N	<i>in-vivo</i>	450-950	1392×1040	226	Xenon	LCTF	mRMR, RBF SVM, Chan-Vase active contour method	Glare removal, Feature extraction, Automatic classification, Active contour refinement	A
[116]	2015	Gastric	<i>ex-vivo</i>	400-800	480×640	81	Halogen	-	Mahalanobis distance, Cutoff point	Optimal wavelength selection, Classification	H
[135]	2016	Oral	<i>in-vivo</i>	390-680	-	30	-	-	RF	Classification	H
[88]	2016	Oral	<i>in-vivo</i>	390-680	1388×1040	30	Xenon	-	Customized	Image filtering (honeycomb pattern removal)	H
[136]	2016	Colon	<i>in-vivo</i>	405-665	585×752	27	Xenon	Filter Wheel	Recursive divergence, SVM	Wavelength selection, Classification	H
[131]	2016	H&N	<i>in-vivo</i>	450-950	1392×1040	251	Xenon	LCTF	SVM, MSF	Classification and segmentation	A
[134]	2016	Oral	<i>in-vivo</i>	390-680	1388×1040	30	Xenon	-	NCC, MNF, RF	Image registration and denoising, Glare detection, Classification	H
[121]	2017	H&N	<i>ex-vivo</i>	450-950	1392×1040	91	Xenon	LCTF	CNN, SVM, KNN, LR, DTC, LDA	Classification	H
[119]	2017	H&N	<i>ex-vivo</i>	450-950	1392×1040	91	Xenon	LCTF	Ensemble LDA	Classification	H
[120]	2017	H&N	<i>ex-vivo</i>	450-950	1392×1040	91	Xenon	LCTF	LDA, QDA, Ensemble LDA, Linear SVM, RBF SVM, RF	Classification	H

\* H: Human; A: Animal

<sup>Y</sup> H&N: Head and Neck



# Chapter 3: Intraoperative hyperspectral acquisition and processing system

## 3.1 Introduction

This chapter provides an overview of the hyperspectral imaging instrumentation used in order to develop the intraoperative demonstrator for brain cancer detection. Furthermore, a detailed description of the complete system is presented. **Figure 3-1** shows the block diagram of the demonstrator where all the parts of the system and their interconnections are shown. The acquisition platform is formed by two pushbroom HS cameras, covering the spectral range from 400 to 1700 nm, and the illumination system, mounted on a scanning platform guided by a high-precision stepper motor. The control unit is in charge of managing all the components of the system, while the hardware accelerator has the goal of speeding up the developed HS brain cancer detection algorithm in order to perform the image processing intraoperatively. The electromechanical elements allow the demonstrator's operator to focus and obtain the image in optimal conditions. Finally, the user interface was developed in a user-friendly way, facilitating the use of the system by non-expert users. Each of these parts will be described in detail in the following sections.

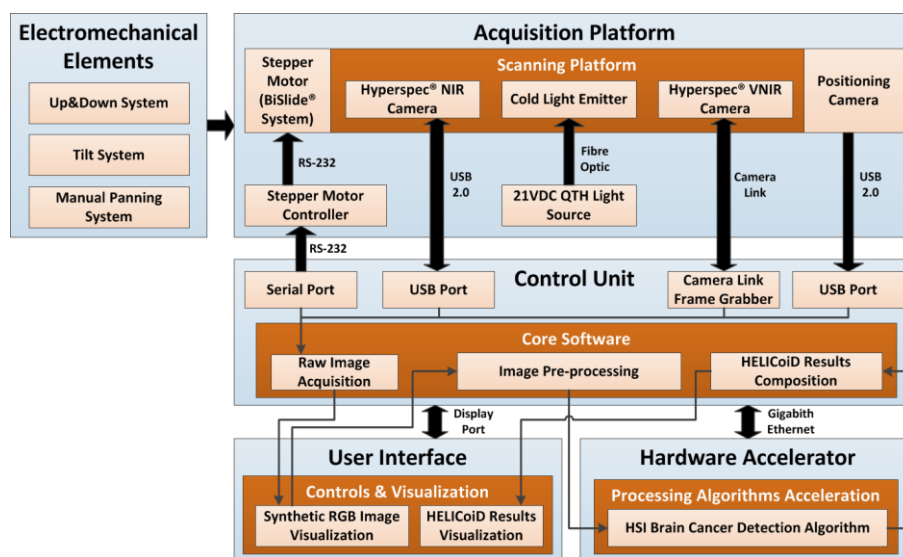


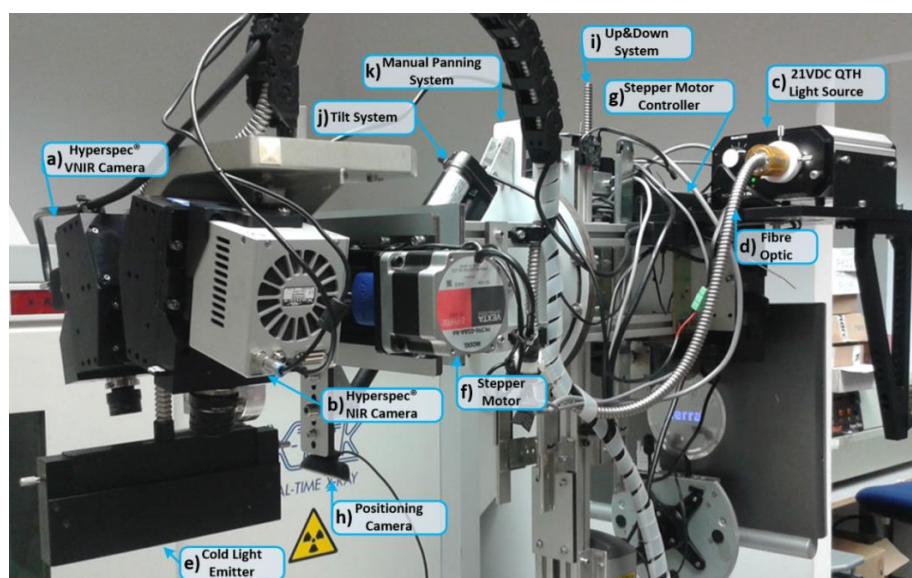
Figure 3-1: Block diagram of the intraoperative demonstrator.

The work related with the integration of the hardware accelerator with the intraoperative demonstrator was performed in collaboration with the research group of Prof. Eduardo Juárez at the Centre of Software Technologies and Multimedia Systems (CITSEM) of the *Universidad Politécnica de Madrid (UPM)*.

## 3.2 Development of the intraoperative demonstrator

### 3.2.1 Acquisition platform

The acquisition platform locates all the elements required to capture the HS images. Two HS cameras that cover the spectral range from 400 to 1700 nm are employed. Using these two cameras, two different HS cubes are generated: one in the VNIR spectral range (from 400 to 1000 nm) and another one in the NIR spectral range (from 900 to 1700 nm). Four different elements compose the acquisition platform: the HS cameras, the scanning platform, the illumination system, and the positioning camera. **Figure 3-2** summarizes all the elements that are placed in the acquisition platform of the demonstrator.



**Figure 3-2: The intraoperative demonstrator acquisition platform.** (a) and (b) VNIR and NIR HS cameras mounted on the scanning platform; (c), (d), and (e) QTH light source connected to the fiber optic system for the light transmission to obtain cold light emission in the scanning platform; (f) and (g) Stepper motor coupled to the spindle and connected to the stepper-motor controller to perform the linear movement of the cameras; (h) Positioning of the RGB camera used to identify the position of the cameras' FOV; (i) The Up&Down system used to focus the HS cameras; (j) and (k) Tilt and manual panning systems employed to correctly orientate the scanning platform.

#### 3.2.1.1 Hyperspectral cameras

The HS cameras selected for the acquisition platform of the system are the Hyperspec® VNIR A-Series (**Figure 3-2.a**) and the Hyperspec® NIR 100/U (**Figure 3-2.b**) cameras, manufactured by Headwall Photonics Inc. (Fitchburg, MA, USA). These HS cameras are based on a line-scanning technique. The camera sensor is a two-dimensional detector array in which one of the spatial dimensions and the complete spectral dimension of the scene are captured in one single shot (called a frame). The

second spatial dimension is obtained by shifting the camera's field of view relative to the scene by means of a linear motion system. These cameras offer the best compromise between spectral and spatial resolution and acquisition time. The spectral range covered by both cameras is between 400 and 1700 nm (VNIR and NIR). This range has been selected with the aim of finding the most relevant spectral regions where the tumor and normal brain tissues can be distinguished using machine learning algorithms. The main characteristics of the selected cameras are as follows:

- The Hyperspec® VNIR A-Series model covers spectral range from 400 to 1000 nm. It has a dispersion per pixel of 0.74 nm and a spectral resolution of 2–3 nm (with a 25- $\mu$ m slit), and is able to capture 826 spectral bands and 1004 spatial pixels. This device integrates a silicon CCD detector array (Adimec 1000-m, Adimec Electronic Imaging, Inc., Woburn, MA, USA) with a minimum frame rate of 90 fps. This sensor is a monochromatic camera connected to the control unit using a PIXCI® Camera Link Interface (EPIX, Inc., Buffalo Grove, IL), which provides a data transmission rate up to 255 MB/s. The lens used in this camera is a Xenoplan 1.4 (Schneider Optics, Hauppauge, NY, USA) with a focal length of 22.5 mm and a broadband coating for the spectral range of 400 to 1000 nm.
- The Hyperspec® NIR 100/U model covers the spectral range from 900 to 1700 nm. It has a dispersion per pixel of 4.8 nm and a spectral resolution of 5 nm (with a 25- $\mu$ m slit), being able to capture 172 spectral channels and 320 spatial pixels. This system incorporates an indium gallium arsenide (InGaAs) detector array (Xeneth XEVA 5052, Xenics nv, Leuven, Belgium), which provides a fast response, high quantum efficiency, and low dark current for the sensor area. This system has a frame rate of up to 100 fps. This camera is connected to the control unit by a USB 2.0 interface with a transfer rate up to 60 MB/s. The lens used with this camera is a Kowa LM25HC-SW 1.4 (Kowa Optimed Deutschland GmbH, Düsseldorf, Germany) with 25 mm of focal length and a broadband coating for the spectral range of 800–2000 nm.

### 3.2.1.2 Illumination system

HS cameras require strong and precise illumination of the scene to be captured in order to avoid external interferences produced by the environmental illumination where the capture is being performed. The illumination system used in this demonstrator is based on a quartz tungsten halogen (QTH) lamp of 150 W with a broadband emission between 400 and 2200 nm. This type of lamp is suitable for HS applications due to the high homogeneity of its spectrum across the entire spectral range [138]. The light source where the lamp is installed is a TechniQuip's Model 21 DC source light (TechniQuip, Pleasanton, CA, USA) connected to an optical fiber that transmits the light to a cold light emitter, ending in double glass isolation with an air chamber in the middle. Using this cold light system, the high temperature produced by the QTH lamp is isolated from the brain surface, since a high temperature irradiating over the brain surface can cause damage and even premature cell death [139]. **Figure 3-2.c** shows the light source placed in the back of the system connected to the optical fiber (**Figure 3-2.d**) that transmits the light to the cold light emitter located in the scanning platform (**Figure 3-2.e**).

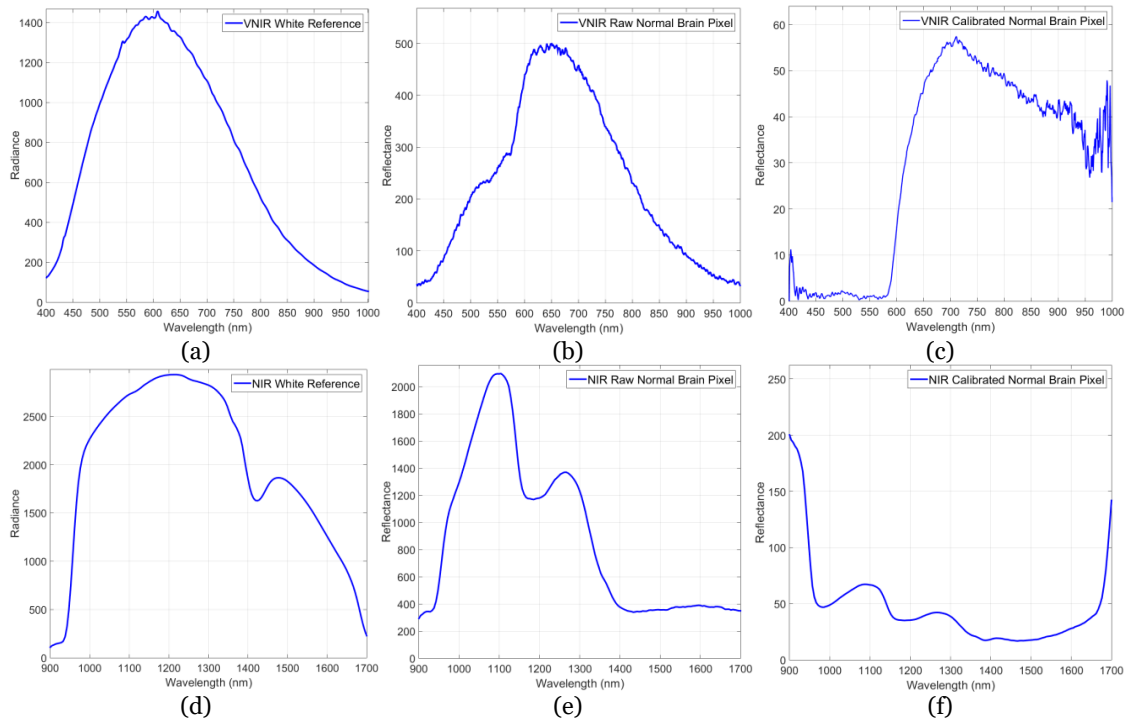
Although the illumination system employed in this demonstrator is able to avoid the interference of environmental illumination, HSI requires calibration of the raw images



to be performed for correct processing of the data. In the calibration process, the significant signal variations caused by the non-uniform illumination over the surface of the captured scene are corrected. The acquired raw image is calibrated using white and dark reference images. These reference images are acquired by the system with the VNIR and NIR cameras separately, but in the same illumination conditions inside the operating theatre before the start of the operation. A white reference image is acquired from a Spectralon® tile (SphereOptics GmbH, Herrsching, Germany), a type of material that reflects the 99% of the incoming radiation in the full spectral range considered in this work. This white reference is placed at the same location where the patient's head will be placed during the surgery, thus taking into account all the real light contributions. The dark reference image is obtained by keeping the camera shutter closed and is used to avoid the dark currents produced by the camera sensor. The HS-calibrated image is calculated by Equation (1), where  $\beta$  is the calibrated image,  $\alpha$  is the raw image, and  $\gamma$  and  $\delta$  are the white and dark reference images, respectively:

$$\beta = 100 \cdot \frac{\alpha - \delta}{\gamma - \delta} \quad (1)$$

**Figure 3-3.a** shows the white reference tile spectrum obtained with the VNIR camera, while **Figure 3-3.b** and **c** respectively present raw and calibrated spectrum examples of normal brain tissue pixels. In **Figure 3-3.d** the representation of the white reference tile spectrum obtained with the NIR camera can be seen, and in **Figure 3-3.e** and **Figure 3-3.f**, the raw and calibrated spectra of a normal brain tissue pixel are shown. Based on the repeatability experiments performed with the system and taking into account that the white reference tile is used only a few minutes for the calibration, through measurements, it is confirmed that the spectrum of the certified white reference tile does not show perceptible changes over time.



**Figure 3-3: Calibration process of a certain pixel of the VNIR and NIR cameras.**

(a) The VNIR white reference spectrum; (b) and (c) The VNIR raw and calibrated spectra of a pixel of normal brain tissue; (d) The NIR white reference spectrum; (e) and (f) The NIR raw and calibrated spectra of a pixel of normal brain tissue.



### 3.2.1.3 Scanning platform

Commonly, in the HS found in laboratories based on pushbroom cameras, the camera is usually fixed and the sample to be captured is moved, although some few examples can be found of moving cameras [140]. In brain tumor applications, it is not possible to move the brain of the patient to perform the capture; instead, the HS cameras (**Figure 3-2.a** and **Figure 3-2.b**) are installed in a scanning platform together with a cold light emitter (**Figure 3-2.e**). The scanning platform provides the necessary movement for the pushbroom scanning. This scanning platform is composed of a spindle and a stepper motor, called the BiSlide® motor-driven assembly (Velmex, Inc. Bloomfield, NY, USA, **Figure 3-2.f**). The spindle has a size of 1 m and allows the cameras to capture a scene of a maximum size of 230 mm in the X-axis. The step resolution of the scanning platform is 6.17  $\mu\text{m}$ . The stepper motor is managed by a Velmex VXM® stepping motor controller (Velmex, Inc. Bloomfield, NY, USA, **Figure 3-2.g**). This motor controller is connected to the control unit via a serial protocol and its programming is accomplished through a Recommended Standard 232 (RS-232) protocol.

### 3.2.1.4 Positioning camera

The positioning camera is installed in the acquisition platform to visualize the area that will be captured by the HS cameras. Since every HS camera sensor captures only one spatial line of the scene, it is not possible to determine the exact position of the current pushbroom frame over the brain. For this reason, the inclusion of an additional standard RGB camera in the acquisition platform was required, correctly aligned with the FOV of the HS cameras, in order to identify the area of the brain surface to be captured. However, unlike the HS cameras, this positioning camera is placed in a fixed position. This camera permits the user to visualize the complete area that is going to be captured by the cameras, allowing the system to be easily positioned in the correct place. **Figure 3-2.h** shows the positioning camera placed in the acquisition platform below the scanning platform.

## 3.2.2 Electromechanical elements

Three different electromechanical elements were installed in the HS acquisition system. These elements provide several degrees of freedom to the system, which are required to focus and orientate the cameras in a convenient way for obtaining high quality images. The Up&Down system (**Figure 3-2.i**) allows the movement of the acquisition platform in the Y-axis to focus the camera. Keeping the HS images well focused is fundamental for obtaining good quality spectral signatures. Effectively, the spectral signature of each pixel is distorted in the case they are unfocused. The focus of the system is performed by looking an X-Lambda image (all the bands of the captured line in a spatial 2D image) captured by the sensor, where the lambda is the wavelength. The focusing distance between the exposed brain tissue and the lens of the cameras is 40 cm. This distance is determined by the distribution of the HS cameras in the scanning platform. The FOV of both cameras is oriented and aligned to the beam of the cold light emitter to obtain the highest reflectance value in the sensor. Furthermore, this distance is determined by the minimum security distance (30 cm) that must exist between the exposed brain and the nearest element of the demonstrator (in this case, the cold light emitter). The Up&Down system is composed of a 24-VDC motor coupled to a spindle,

allowing a displacement of  $\pm 7.75$  cm. On the other hand, the tilt system (**Figure 3-2.j**) is composed of a 12-VDC linear actuator that permits the rotation of the scanning platform  $40^\circ$  forward and backward. Finally, the manual panning system (**Figure 3-2.k**) is employed to manually rotate (up to  $45^\circ$  to the left and  $45^\circ$  to the right) the scanning platform, using an aluminum plate.

### 3.2.3 Control unit

The control unit (CU) is responsible for managing all the subsystems that comprise the demonstrator. This CU is a computer based on an Intel® Core™ i7-4770k 3.5 GHz quad-core processor, with 8 GB of random access memory (RAM) and a high-capacity 512 GB solid-state drive with write speeds exceeding 500 MB/s. Specific software was developed to manage and integrate the different elements that conform the acquisition platform, allowing the user to perform the HS image acquisition in an easy and effective way. Furthermore, the CU is in charge of executing the HS brain cancer detection algorithm together with the hardware accelerator in order to finally present the tumor boundary prediction.

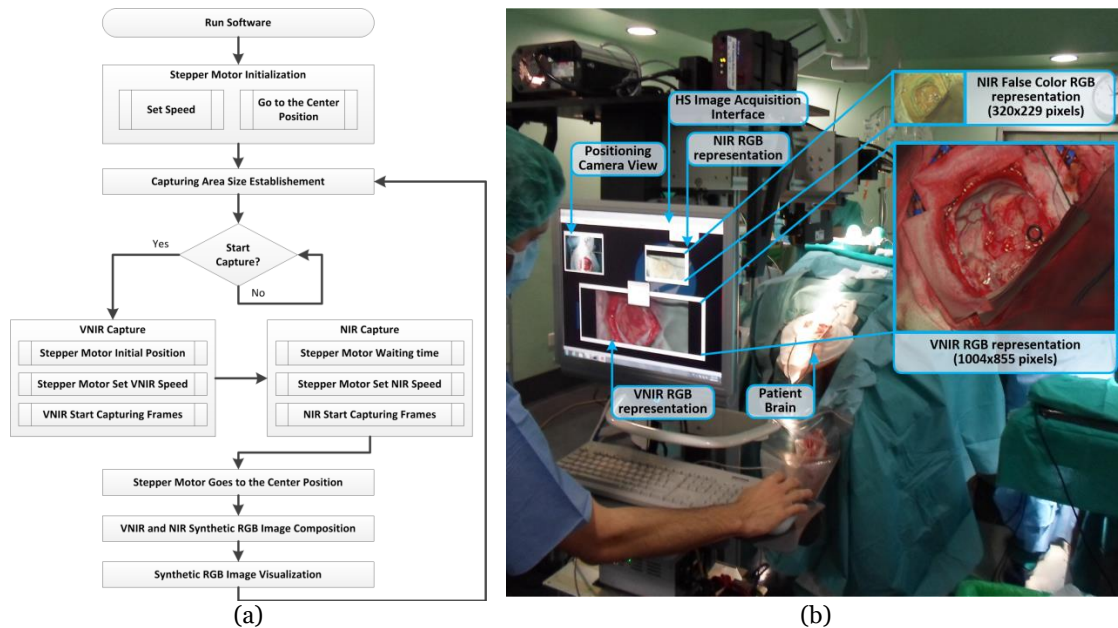
### 3.2.4 Hyperspectral image acquisition software

Customized software for image acquisition was developed due to the need to automate and accelerate the capture of both HS cameras of the system. The simplification of the acquisition procedure ensures easy interaction of the user with the system as well as reduced time needed to capture the HS images during neurosurgical procedures.

To develop this software, three different software development kits (SDKs) were integrated, belonging to the two HS cameras and the stepper motor controller. **Figure 3-4.a** shows the HS image acquisition software flow diagram for the capturing procedure. Firstly, after running the program, the scanning platform is initialized, detecting and establishing the absolute zero of the motor position. Then, the platform is positioned at the center of the scanning area. Taking into account the x-size value of the capturing area established by the user through the graphical user interface (GUI), the scanning platform is moved to the initial position. The VNIR capturing process is performed starting from the right to the left of the platform with the stepper motor speed fixed to 3 mm/s. This speed is calculated according to the pixel size (0.1287 mm and 0.48 mm for the VNIR and NIR cameras, respectively) and the frame rate of the camera (90 fps and 100 fps for the VNIR and NIR cameras, respectively). When the VNIR capture is done, the stepper motor stops at the final position, waits a few milliseconds to stabilize the system structure, and fixes the speed to 5 mm/s. Then, the NIR capturing process begins. This capture is performed starting from the left to the right of the platform. After that, the stepper motor moves the scanning platform to the central position. Then, the synthetic RGB images of both HS cubes are generated by selecting three bands that correspond with red (708.97 nm), green (539.44 nm), and blue (479.06 nm) colors for the VNIR image, and three bands of the NIR cube to generate a false color RGB image (red: 1094.89 nm, green: 1247.44 nm and blue: 1595.45 nm). These bands are selected to maintain the compatibility with the original software (Hyperspec® III software, Headwall Photonics Inc., Fitchburg, MA, USA) provided by the camera manufacturer. Using this technique for the acquisition process, a speedup of  $3\times$  with respect to the original software is achieved. The maximum image

size provided by the system is  $1004 \times 1787$  pixels ( $129 \times 230$  mm) for the VNIR image, and  $320 \times 479$  pixels ( $153 \times 230$  mm) for the NIR image, with spatial resolutions of  $128.7 \mu\text{m}$  and  $480 \mu\text{m}$ , respectively.

**Figure 3-4.b** shows the acquisition system being used during a neurosurgical operation and the RGB synthetic images of the captured HS cubes (VNIR and NIR) where their image sizes and relative spatial resolutions can be seen. The time employed by the system to obtain the maximum size image using the manufacturer's software is  $\sim 240$  s for the VNIR image and  $\sim 140$  s for the NIR image. However, employing the acquisition software developed in this work, the acquisition time for the maximum image size is reduced to  $\sim 80$  s and  $\sim 40$  s for the VNIR and NIR cameras, respectively.



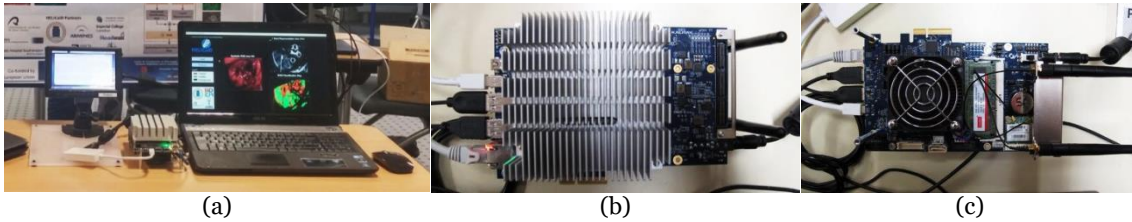
**Figure 3-4: HS image acquisition interface.** (a) HS image acquisition software flow diagram; (b) HS image acquisition user interface (and the RGB representations of each HS cube) being used during a neurosurgical intervention at the University Hospital Doctor Negrin of Las Palmas de Gran Canaria (Spain).

### 3.2.5 Hardware accelerator

Due to the high computational cost of the developed HS brain cancer detection algorithm and the large amount of data generated by the HS cameras, it is necessary to use a hardware accelerator (HA) where the most time-consuming parts of the algorithm are implemented. Therefore, the algorithm must be highly parallelized for processing to be completed during neurosurgical operations.

The HA selected for this purpose is the Kalray massively parallel processor array (MPPA<sup>®</sup>) EMBO1 board (Kalray S.A., Montbonnot Saint Martin, France) with a multiple instruction, multiple data (MIMD) many-core processor [141]. This accelerator is focused on computationally-intensive low-power embedded applications. The MPPA<sup>®</sup> EMBO1 processing performance reaches 230 GFlops, which, for the 5-W power consumption reported, turns into 46 GFlops/W, a much higher figure compared to other kinds of high-performance platforms. The MPPA<sup>®</sup> EMBO1 board contains a standard host  $\times 86$  ComExpress module working as an embedded computer, and a carrier board containing the MPPA-256 many-core chip. **Figure 3-5.a** shows the MPPA<sup>®</sup> board (in the center of the image) connected to a preliminary environment

developed to execute the hardware accelerated part of the algorithm. The host module side of the board (**Figure 3-5.b**) is composed of an AMD G-T40E Dual Core Processor with an integrated GPU (Graphics Processor Unit) running a CentOS 7 GNU/Linux operative system (OS) instance with 4 GB of RAM, 1 peripheral component interconnect express (PCIe) Gen2×2 for communication with the MPPA<sup>®</sup>-256 many-core chip, and a 16-GB solid-state drive (SSD) as a system disk. The carrier board can be seen in **Figure 3-5.c**. It features an MPPA<sup>®</sup>-256 many-core processor (under the fan). It also contains 4 GB of RAM and 64 MB of flash memory plus the host PCIe Gen2×2 port to communicate with the dual core processor.



**Figure 3-5: The Kalray MPPA<sup>®</sup> EMBo1 Platform.** (a) Developer environment; (b) EMBo1 top view where the host module is located; (c) EMBo1 bottom view where the carrier board is placed.

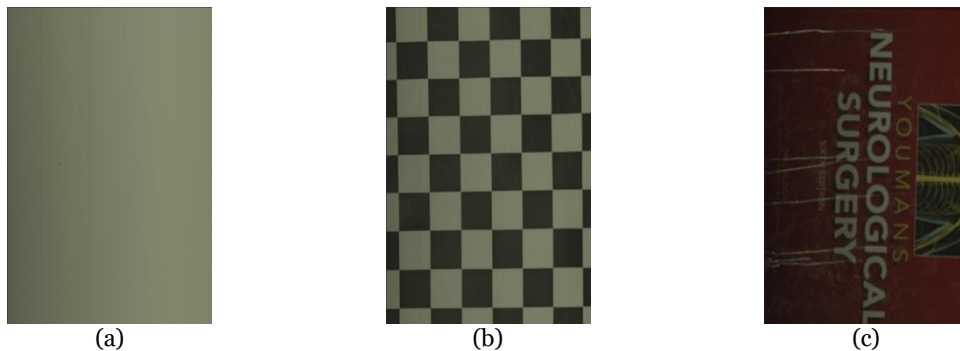
The Kalray MPPA-256 is a single-chip many-core processor that assembles 256 user cores distributed in 16 clusters running at 400 MHz. This chip comprises 256 user cores—32-bit very long instruction word (VLIW) processors with floating point units—distributed in several computing clusters. Additionally, this platform contains quad-core input/output (I/O) subsystems to manage the communications with the clusters. A network-on-a-chip (NoC) manages the synchronization and communications among the compute clusters and the I/O subsystem. Each cluster gathers 2 MB of memory—which is shared among the 16 cores—as well as a resource management (RM) core aimed at running the cluster operating system (NodeOS) and managing events and interrupts, and a direct memory access (DMA) module to transfer data from the shared memory to the NoC and vice versa. This architecture presents two main advantages: first, the system parallelization complexity is maintained within reasonable limits as the MPPA<sup>®</sup> includes mechanisms such as POSIX (Portable Operating System Interface), OpenMP, and OpenCL; and secondly, in comparison with other architectures like GPUs or FPGAs (Field Programmable Gate Arrays), the MPPA<sup>®</sup> platform leads in terms of energy efficiency [142].

### 3.3 Repeatability analysis of the HS acquisition system

The developed HS acquisition system was tested by performing two different types of repeatability experiments. The goal of this study was to evaluate the possible sources of systematic errors in the acquisition system and to verify the repeatability of the spectra when images of the same scene were obtained. This section summarizes the procedure and the results acquired in the spatial and spectral repeatability tests performed using three different pairs of HS cubes obtained with the previously introduced system.

### 3.3.1 Repeatability dataset

Three different scenes were captured twice and consecutively in the same environmental conditions to perform the repeatability experiments. In total, three pairs of HS cubes were obtained: a white reference tile employed to calibrate the system, a chessboard pattern and a book cover fragment with high spatial and spectral entropy (image with high amount of information). **Figure 3-6** shows the reconstructed RGB representations of these HS cubes. The white reference tile (**Figure 3-6.a**) and the chessboard pattern (**Figure 3-6.b**) are simple and geometrically uniform. These images were suitable to identify any relevant difference or geometric distortion between each pair of images. The book cover fragment (**Figure 3-6.c**) was selected due to the multiple internal reflections and changes in the reflected light path because of intermediate refractions.

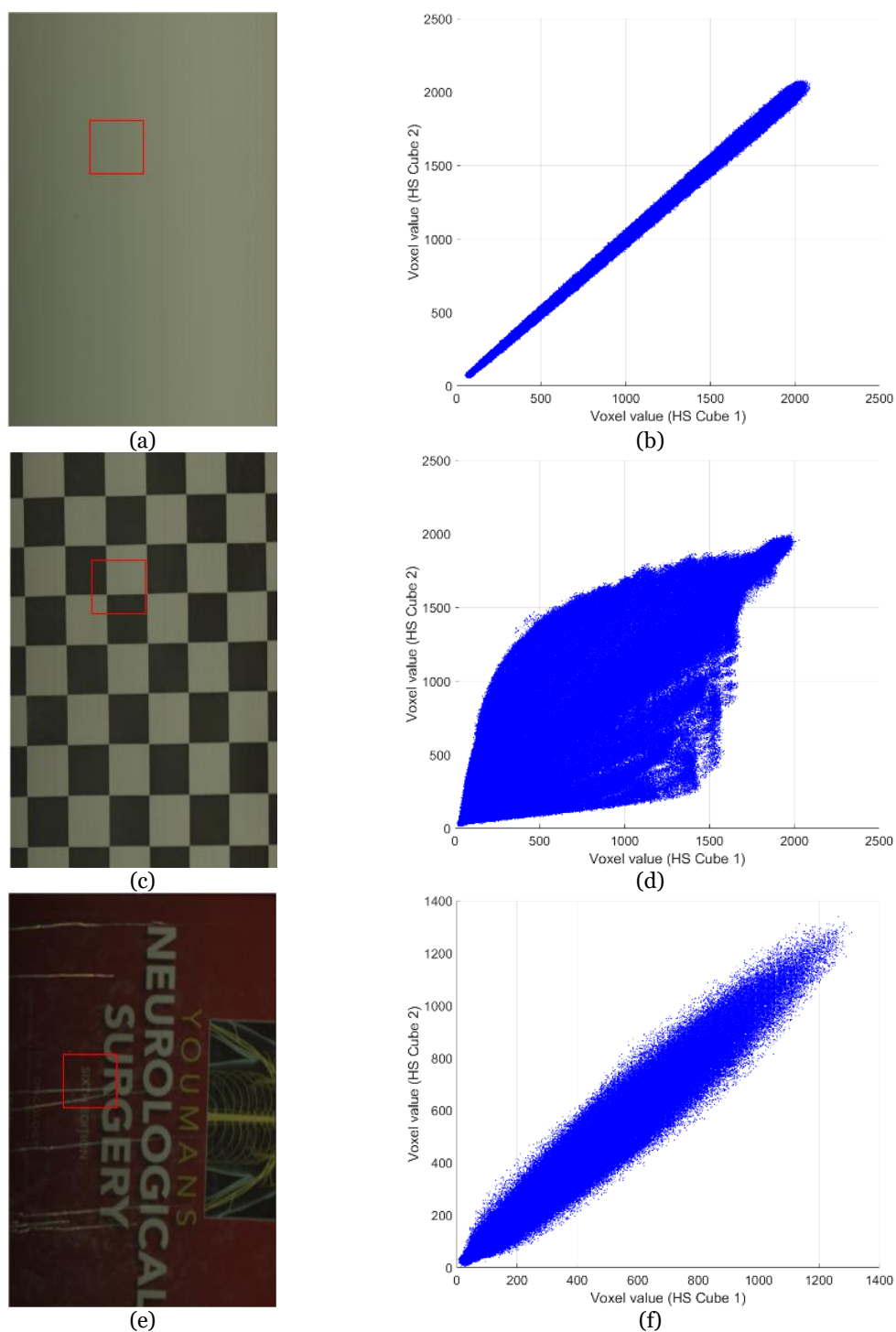


**Figure 3-6: HS images of the repeatability dataset.** (a) White reference tile; (b) Chessboard pattern; (c) Book cover fragment.

### 3.3.2 Repeatability metrics

The motivation for performing these experiments was to quantify the repeatability of the acquisition system, which enables the analyst to assess the a priori feasibility of performing “correct” regression or classification model for a given target. If the repeatability error is high across all the spectral bands, any statistical modeling will be prone to spurious results [143].

In **Figure 3-7**, the scatterplots of an example section of  $200 \times 200$  pixels obtained from the two HS cubes of the same target are shown. The selected areas have been surrounded using a red box. In the scatterplot, the voxel values of each HS cube section pair are represented (more than 33 million of voxel pairs). Ideally, this scatterplot should be a straight line, indicating that all the correspondent voxel value pairs contain the same exact information. In this case, the repeatability of the system will be optimal. However, in the real world, the scatterplot will be expanded depending on both the repeatability qualities of the system and the complexity and contrast of the captured scene. In this sense, **Figure 3-7.b** show the scatterplot of the white reference tile (a homogeneous scene), where it is possible to observe that the system offers a low variability in the voxel values from both HS cubes. Nevertheless, when the scene contrast increases (**Figure 3-7.c**), the scatterplot is highly scattered (**Figure 3-7.d**). A small variation in the scene position can produce a high variation in the voxel values due to the high contrast of the chessboard pattern borders. In the scatterplot of the book cover fragment (**Figure 3-7.f**), the expansion is lower than the chessboard pattern due to the scene contrast is lower. This last one is a more realistic example.



**Figure 3-7: HS images of the repeatability dataset and their correspondent scatterplot of the voxel values of an example section of 200x200 pixels obtained from two HS cubes of the same scene. (a) and (b) White reference tile; (c) and (d) Chessboard pattern; (e) and (f) Book cover fragment.**

The measures and protocols proposed in [143] were employed for this experiments. In [143], the *spatial repeatability* is defined as the differences between the pixel values of the respective spectral layers in two HS cubes from the same scene, while the *spectral repeatability* is defined as the differences between the spectral curves of their respective voxels (value of a pixel in a certain wavelength). The repeatability error (RE) is computed as the root mean square (*rms*) of the differences between two vectors  $(x, y)$ . The ideal value of RE is zero, but in practice RE is always higher than zero. In



this sense, this metric can be modified to represent the noise-to-signal ratio (N/S) or its inverse, signal-to-noise ratio (S/N), being zero and infinite their ideal values. These metrics are defined in the Equations (2) and (3), respectively. Furthermore, another metric employed to measure the repeatability of the system is the absolute relative difference percentage (RD) that is defined in Equation (4). In this metric, the relation between the absolute difference and the mean values of the two vectors is computed. In this case, the lower RD, the better the repeatability of the system will be. S/N and RD metrics were employed to measure the spectral and spatial repeatability of the system by using plot charts, while N/S and RD were employed to represent graphically the spectral repeatability in a certain band.

$$N/S = \frac{rms(x - y)}{rms(x \cup y)} \quad (2)$$

$$S/N = \frac{rms(x \cup y)}{rms(x - y)} \quad (3)$$

$$RD(\%) = \frac{abs(x - y) * 100}{[mean(x) + mean(y)]/2} \quad (4)$$

### 3.3.3 Spectral repeatability

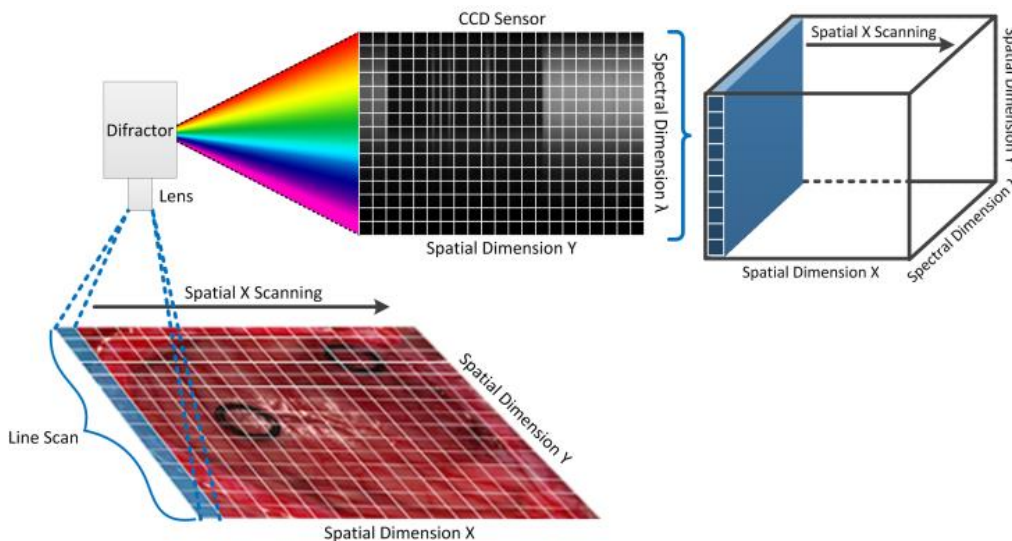
Spectral repeatability considers a spatial-slice as a vector by fixing the wavelengths ( $\lambda$ ) and calculating the previously defined metrics. Several HS cubes were created using a pushbroom technique, whereby the complete HS image of the target was generated by joining multiple contiguous non-overlapped image strips (line scans). During each line scan, the CCD sensor acquired a multi-layer slice of the HS cube, where each layer belonged to a predetermined spectral band. Each column of the CCD sensor acquired the spectrum of one pixel and each row (CCD bins rows) contained one spectral band of the HS cube slice. In this sense, it is possible to distinguish between spectral repeatability along the line scans and along the CCD bins rows of the HS cube. **Figure 3-8** shows an example of how the HS cube is generated using a pushbroom technique.

The spectral repeatability experiments allow measuring possible errors produced due to the vibrations of the acquisition system, the interline scanning errors or errors produced due to differential responses of the CCD bins. These are the most common sources of errors in pushbroom HS systems. **Figure 3-9** shows the spectral repeatability results of S/N and RD along the line scans for the three different pairs of HS images. These curves assess the stability of the repeatability indexes from line scan to line scan, as well as detecting the location of possible outlier voxels. As it can be seen in the results, the average of the S/N index decreases when the complexity of the captured scene increases. In the case of the RD<sub>mean</sub> metric, the mean value of each line scan was calculated and it increases when the complexity of the image increases. **Figure 3-9.a** shows the results obtained for the white reference image, where it is possible to observe that when the system captures a spatially homogeneous image, the spectral repeatability along the line scans is stable and minimal. However, in the case of the results obtained for the chessboard pattern image, the peaks obtained in the plot reveal that the repeatability errors are mainly produced in the borders of the image pattern (**Figure 3-9.b**). In the case of the book cover image (**Figure 3-9.c**) the error is spread in all the line scans and it is mainly produced due to the reflections of the light on the surface and the movement of the system. The worst S/N value is obtained for the chessboard pattern image, which can be caused by the abrupt changes in the pattern

due to the motion of the pushbroom sensor across the different scanlines. However, the average  $RD_{\text{mean}}$  metric is lower than the value obtained for the book cover image.

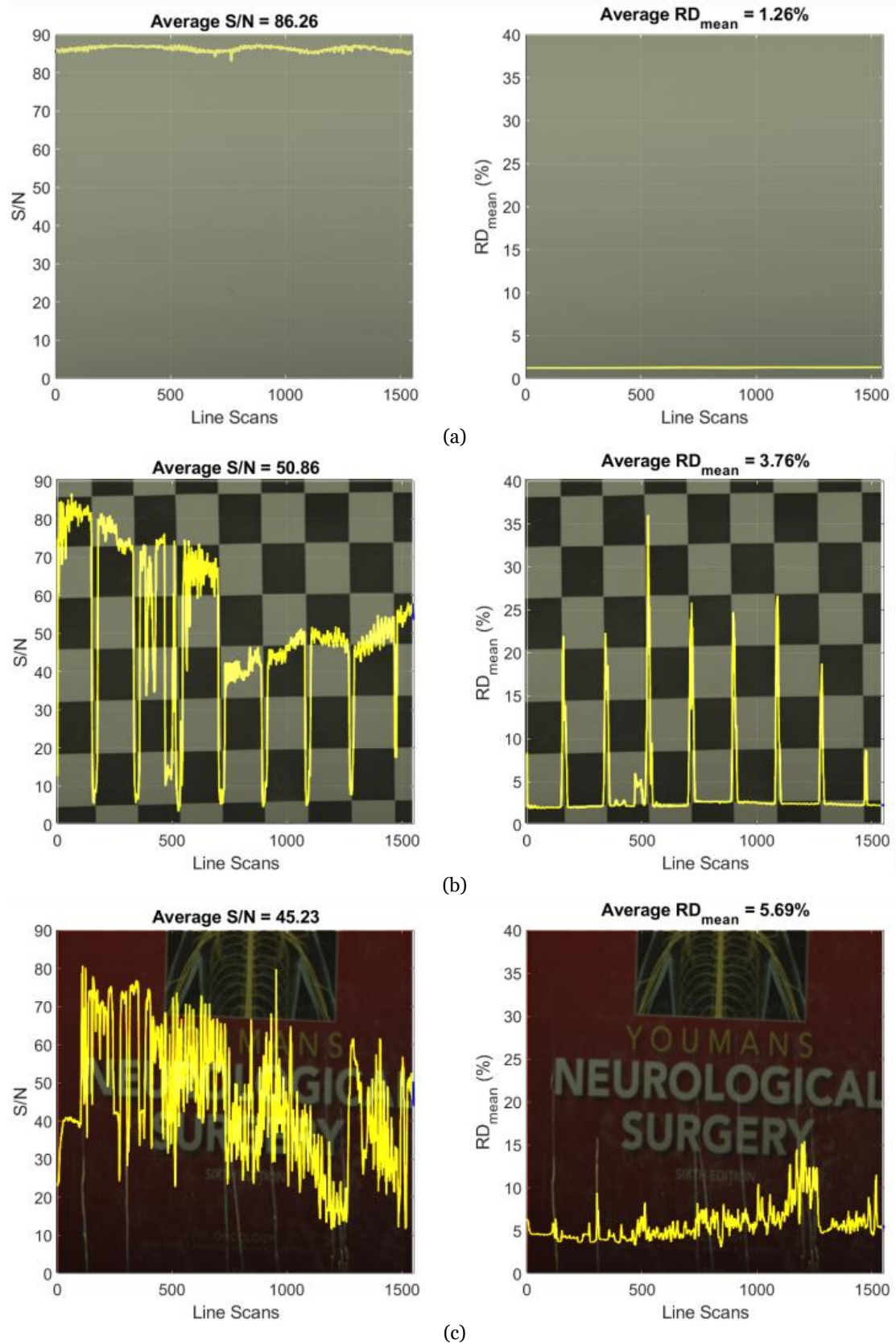
**Figure 3-10** presents the spectral repeatability results along the CCD bins for the three pairs of HS images. The dome-shaped curves obtained in the S/N and  $RD_{\text{mean}}$  metrics of the white reference image (**Figure 3-10.a**) show that the spectral repeatability was better in the center of the CCD array than in the borders. This is mainly caused due to optical aberrations produced at the ends of the sensor and to inhomogeneous illumination across the X pushbroom scan direction. **Figure 3-10.b** and **Figure 3-10.c** show the results obtained for the chessboard pattern and the book cover, respectively. In this case, the worst S/N value is obtained for the chessboard pattern image. However, the average  $RD_{\text{mean}}$  metric is lower than the one obtained for the book cover image.

Finally, **Figure 3-11** shows the spatial representation of the spectral repeatability indexes of N/S and  $RD_{\text{mean}}$  of the white reference tile (**Figure 3-11.a**), the chessboard pattern (**Figure 3-11.b**) and the book cover fragment (**Figure 3-11.c**) HS cube pairs at a certain wavelength ( $\lambda = 690.78$  nm). This  $\lambda$  value was selected as an example to represent the error in a centered wavelength of the spectrum. The repeatability indexes are depicted in false color images. The scales of the false colors on the right side of each image determine the values and ranges of the corresponding repeatability index. In these false color images, it is possible to identify directly by visual inspection the regions of the images where the repeatability of the system is extremely high or low. In this sense, the repeatability is quite low in the areas of the images with higher spatial entropy. These high-entropy areas cannot be accurately reproduced due to the fine resolution of the spatial scanning required to obtain the HS cube. For example, in the chessboard pattern image (**Figure 3-11.b**) the boundaries of the pattern have a low repeatability while in the book cover image (**Figure 3-11.c**) low repeatability areas are also in the borders of the letters and the drawing as well as in the relief produced by plasticizing the book cover. The spectral repeatability is a function of the ambient light and the nature of the materials presented in the scene [143].

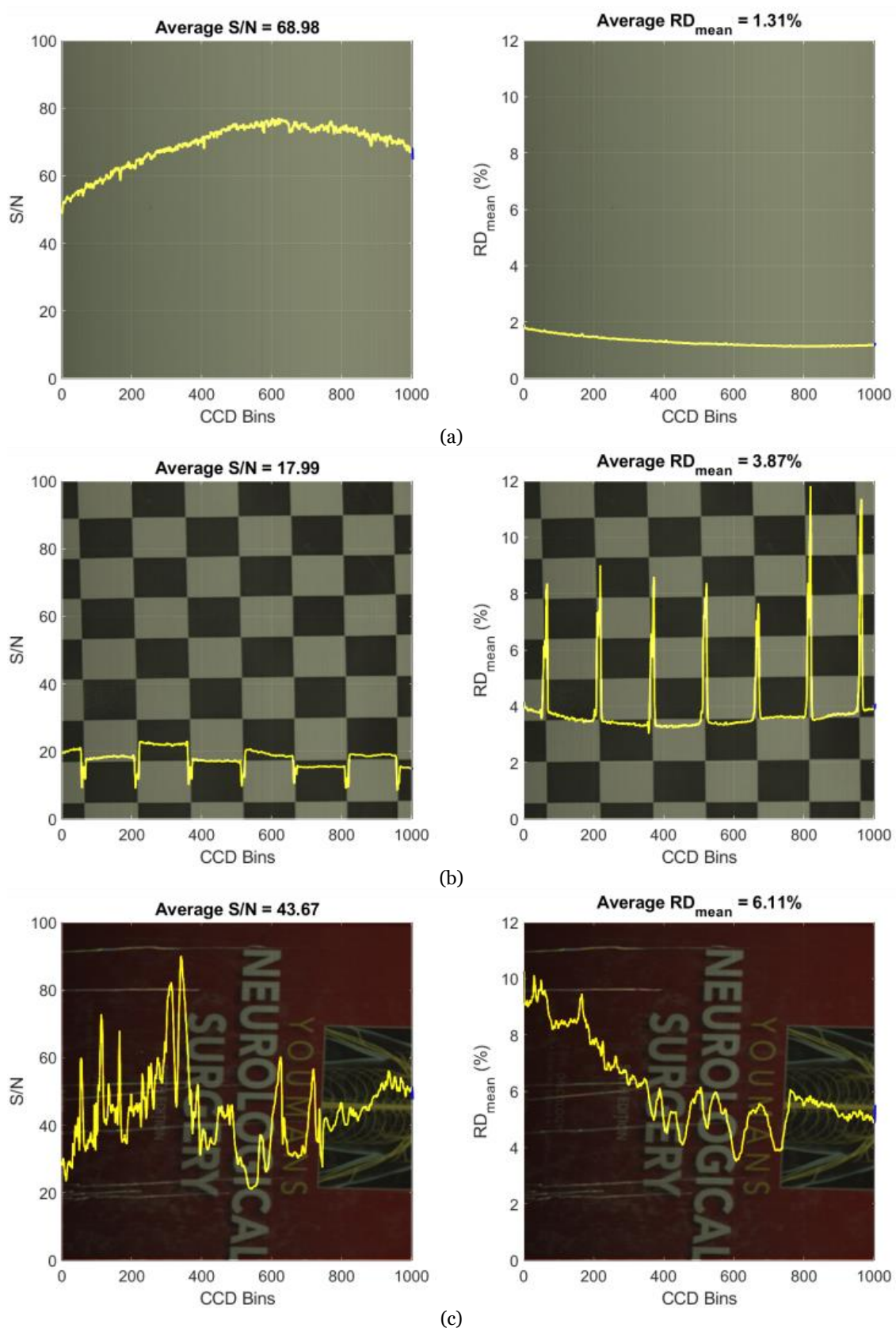


**Figure 3-8: Pushbroom technique block diagram example.**

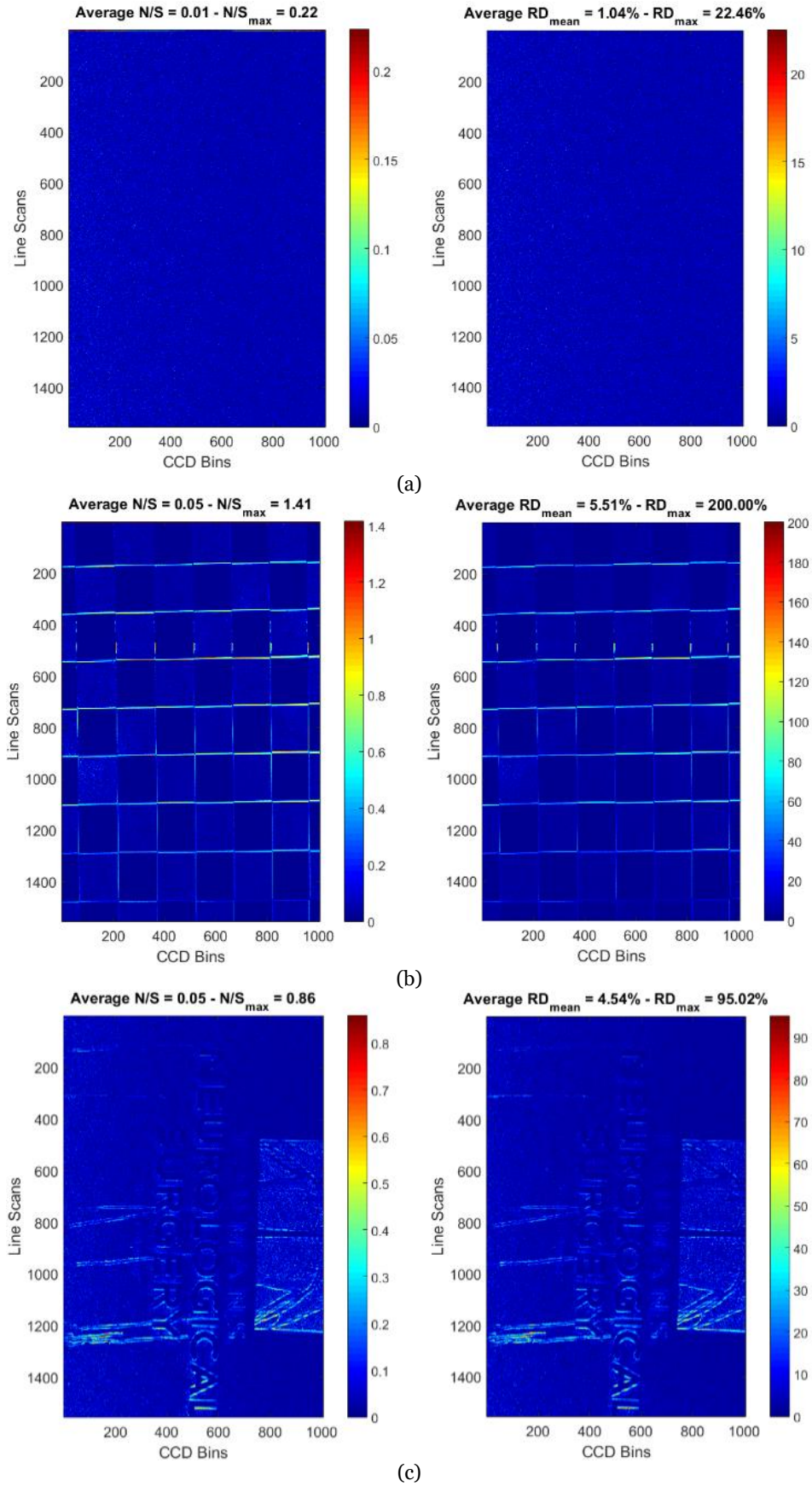




**Figure 3-9: Spectral repeatability indexes in line scans of the three different HS cube pairs.** (a) White reference tile; (b) Chessboard pattern; (c) Book cover fragment.



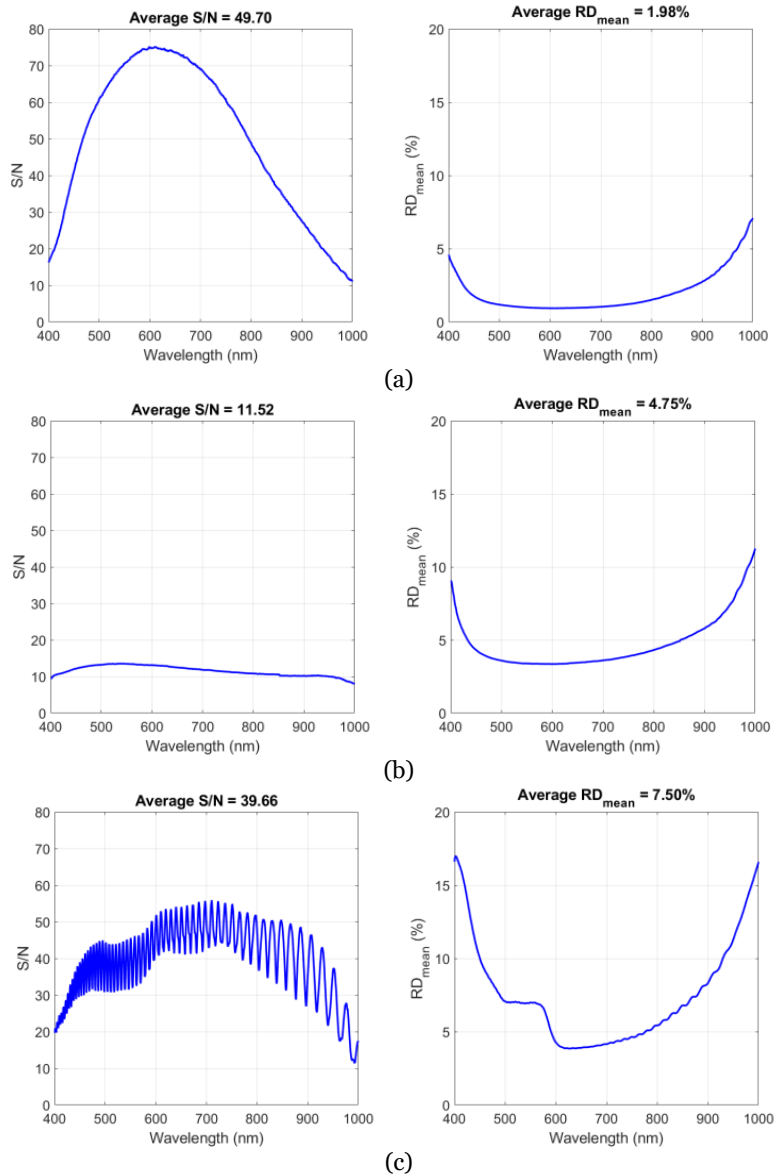
**Figure 3-10: Spectral repeatability indexes in CCD bins of the three different HS cube pairs.** (a) White reference tile; (b) Chessboard pattern; (c) Book cover fragment.



**Figure 3-11: Spatial representation of the spectral repeatability indexes of  $N/S$  and  $RD_{\text{mean}}$  of the three different HS cube pairs at a certain wavelength ( $\lambda = 690.78 \text{ nm}$ ). (a) White reference tile; (b) Chessboard pattern; (c) Book cover fragment.**

### 3.3.4 Spatial repeatability

The spatial repeatability measures the differences between pixel values at a certain wavelength in HS cubes of the same scene. **Figure 3-12** shows the S/N and  $RD_{\text{mean}}$  metrics for each one of the HS cube pairs to measure the spatial repeatability of the HS acquisition system. As it can be seen in the results, the spatial repeatability of the system was better in the center wavelengths and worse towards the first and the last spectral bands. This is produced because in the shorter wavelengths the photons have higher energy than in the longer ones. Consequently, they are absorbed closely to the CCD sensor surface and not by the active part of the detector [143]. The oscillations presented in the S/N plot of the book cover fragment (**Figure 3-12.c**) are produced due to the presence of multiple materials that have low and high reflectance values in different wavelengths. Taking into account the results of these experiments, the optimal spectral range where the system can operate efficiently is comprised between 450 and 900 nm approximately. For this reason, during the pre-processing of the HS cubes, the reflectance values outside of this range were avoided.



**Figure 3-12: Spatial repeatability indexes of the three different HS cube pairs.** (a) White reference tile; (b) Chessboard pattern; (c) Book cover fragment.

## 3.4 Conclusions

In this chapter, the detailed description of the work carried out to develop the intraoperative HS demonstrator has been presented. This intraoperative system is capable of acquiring HS images during neurosurgical procedures, allowing capturing HS images in the spectral range between 400 and 1700 nm. Two HS cubes can be obtained, one in the VNIR range (400 to 1000 nm) formed by 826 spectral bands and high spatial resolution ( $1004 \times 1787$  pixels) and one in the NIR range (900 to 1700 nm) formed by 172 spectral bands and low spatial resolution ( $320 \times 479$  pixels). These two spectral ranges were selected in order to study the most relevant spectral zones where the tumor and normal brain tissues can be distinguished by using HS classification algorithms.

In the following chapters, the work performed is based on the information obtained from the VNIR camera. Only the VNIR HS images were employed to generate the gold standard for the training of the HS classification algorithms and validate their results. Due to the low spatial resolution of the NIR camera, it has not been possible to perform a reliable labeling of the NIR HS cubes. Although some preliminary analysis of the NIR images performed by the research team [144] during the project execution reveal that the use of the NIR spectral range could help in the identification of blood vessels and extravasated blood, NIR images alone have not proven to be relevant for the goal of this thesis. Further experiments must be carried out performing a fusion of both types of HS images (VNIR and NIR) in order to further investigate if the NIR information could help to a more accurate classification of the boundaries between the tumor tissue and the surrounding hypervascularized normal tissue.

In addition, repeatability experiments where the spectral and spatial characteristics of the obtained HS cubes using the intraoperative HS acquisition system were performed. This study assessed the quality of the obtained data and the performance of the acquisition system. In addition, this repeatability analysis revealed that the suitable spectral range where the system can operate more efficiently is comprised between 450 and 900 nm.





# Chapter 4: In-vivo hyperspectral human brain image database

## 4.1 Introduction

Using the intraoperative HS acquisition system, an *in-vivo* HS human brain image database was created. The HS cubes were obtained in three different data campaigns that were performed during the course of the HELICoiD project. The first data campaign was carried out at the University Hospital Doctor Negrin of Las Palmas de Gran Canaria (Spain) from March 22<sup>th</sup> of 2015 until November 18<sup>th</sup> of 2015. In this data campaign, a total of 22 operations were attended, obtaining more than 50 HS images of *in-vivo* human brain tissue. The second data campaign was performed at the University Hospital of Southampton (United Kingdom) from March 7<sup>th</sup> of 2016 until June 6<sup>th</sup> of 2016. In this second data campaign, a total of 9 operations were attended, capturing 20 HS images of *in-vivo* human brain. Finally, the third data campaign was accomplished again at the University Hospital Doctor Negrin from October 11<sup>th</sup> of 2016 until December 28<sup>th</sup> of 2016. In this final data campaign, a total of 5 operations were attended, obtaining 11 HS images. In summary, during the course of the project, a total of 36 patients have been included in the research, with a dataset consisting in 80 HS cubes. This dataset involves several types of *in-vivo* tumors, *i.e.*: primary tumors diagnosed with different grades and secondary tumors belonging to different organ metastasis.

This section provides an overview of the procedure carried out to obtain the HS images of the human brain surface that were stored in the *in-vivo* HS human brain image database. Furthermore, the process to label the samples as tumor or normal tissue for the supervised algorithm development is described. Finally, a detailed description of the entire database employed in this thesis is presented.

The work presented in this chapter has been carried out in a very close collaboration with the research group of Dr. Adam Szolna and Mr. Jesús Morera at the Department of Neurosurgery of the University Hospital Doctor Negrin of Las Palmas de Gran Canaria and also with the research group of Dr. Diederik Bulters at the Wessex Neurological Centre of the University Hospital Southampton.

## 4.2 Participants

In this study, all adult patients (18 years old and above) undergoing craniotomy for resection of intra-axial brain tumors at both participating sites were approached for inclusion in the study. The University Hospital of Southampton (UHS), UK, and the University Hospital Doctor Negrin (UHDRN) of Las Palmas de Gran Canaria, Spain, were the participant sites. Patients with both primary and secondary tumors were included in the database. Patients that underwent resection of meningioma, where the dura was resected, were also included whenever it was possible to properly capture the exposed normal brain. The study protocol and consent procedures were approved by the *Comité Ético de Investigación Clínica-Comité de Ética en la Investigación* (CEIC/CEI) for the University Hospital Doctor Negrin and the National Research Ethics Service (NRES) Committee South Central - Oxford C for the University Hospital of Southampton. Written informed consent was obtained from all the subjects.

## 4.3 Intraoperative HS image acquisition procedure

This section provides an overview of the procedure carried out to obtain the HS *in-vivo* images from the human brain surface that were stored in the database (**Figure 4-1**). Furthermore, the process of labeling the samples as tumor tissue or normal brain tissue is described. The procedure followed to acquire and label the spectral signatures of the *in-vivo* brain surface is based on five steps: patient preparation, HS image acquisition, tissue resection, neuropathology evaluation and sample labeling.

### 4.3.1 Patient preparation

Before the operation, a computed tomography and a magnetic resonance imaging of the patient's head compatible with IGS are performed. These images are uploaded onto the IGS system before the operation started. Then, the patient is placed in a supine position, under general anesthesia and is registered to the IGS system. A scalp incision is made and a burr hole/s drill using a high-speed drill. A craniotome is then inserted into the burr hole/s and a bone flap cut out (craniotomy). The dura is then cut with a knife (durotomy) to expose the brain surface.

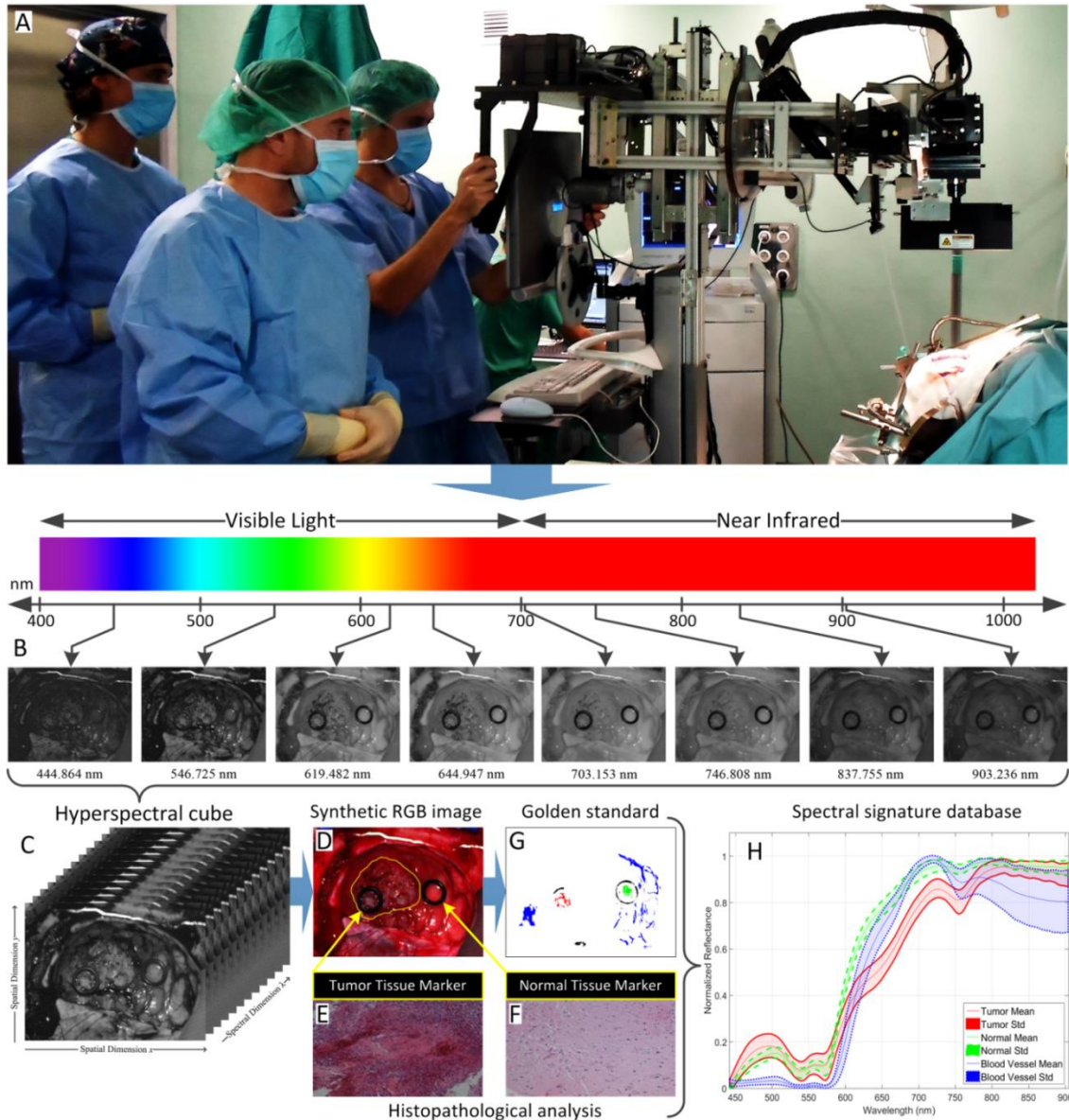
### 4.3.2 HS image acquisition

HS images are captured after durotomy, before the arachnoid and pia are breached in cases where the tumor extended to the brain surface. Sterilized rubber ring markers were placed to identify the position of the tumor and the normal brain (**Figure 4-1.d**), employing the IGS system pointer to establish the exact location of the markers over the brain. This pointer provides information about the position of the markers with respect to an MRI or CT, which are performed prior to the surgical procedure.

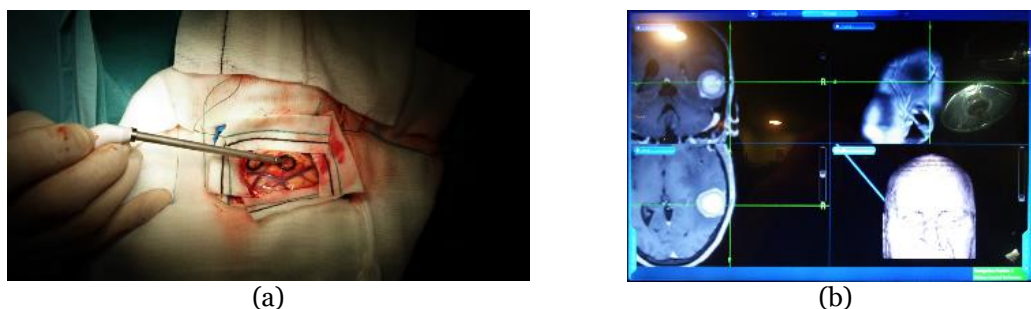
**Figure 4-2.a** and **b** show the use of the IGS system pointer to identify the position of the markers over the brain on MRI. Normal brain markers are also placed by the operating surgeon based on visual appearance and anatomical relationship to sulci and gyri, apart from the IGS feedback. Normal markers are placed where the operating surgeon is quite confident that the brain tissue is normal. The operator of the HS acquisition system then captures the HS image of the exposed brain surface. The image



size established by the operator for the image acquisition should be oversized to avoid the inherent movement of the system when the scanning platform is starting the capturing process. This will ensure the spatial coherence of the center of the image where the region of interest (the exposed brain surface) is located. In addition, the operator must avoid unintentional movements of the acquisition system during the image acquisition for the same reason. In case of an unexpected movement, the capturing process must be repeated.



**Figure 4-1: In-vivo HS brain surface acquisition procedure.** (a) Hyperspectral acquisition system being used during the acquisition process in a neurosurgical operation; (b) Hyperspectral images acquired with the acquisition system at different wavelengths from a patient affected by a glioblastoma tumor; (c) HSI data cube; (d) RGB image generated from the HS cube with the tumor tissue marker (left) and the normal tissue marker (right) placed on the brain surface; (e) and (f) Histopathological images of the tumor tissue sample (glioblastoma) and normal tissue sample respectively; (g) Gold standard map where certain pixels have been labeled in four different classes: normal brain tissue (green), tumor tissue (red), blood vessel (blue) and background (black); (h) Average and standard deviation (Std) of the pre-processed spectral signatures of tumor tissue, normal tissue and blood vessel labeled pixels, represented in red, green and blue color respectively.



**Figure 4-2: MRI markers registration.** (a) IGS system pointer over the tumor marker located on the exposed brain surface; (b) IGS system screen snapshot with the coordinates of the tumor marker in the MRI.

### 4.3.3 Tissue resection

After the first HS image capture, the HS acquisition system is moved out from the surgical area and the operating surgeons undertake the tumor resection. Surgeons take samples of the tissue located inside the tumor marker and place it in a sterile container. An identification (ID) number is assigned to the container with the corresponding marker number. These samples are sent to the neuropathology laboratory and the results are used for the gold standard dataset generation. The IDs assigned to the markers serve as guidance in the labeling process. When possible, a second set of images is captured while the tumor is being resected. When there is macroscopically normal brain and tumor exposed and when the operating surgeon feels that it is safe to temporarily hold surgery, the surgeon ensures perfect hemostasis and washes the field thoroughly with warm saline to wash away any residual blood while ensuring no significant temperature change (and resultant blood flow change). Next, the field is sucked dry by the application of a cottonoid to the parenchyma and applying suction to this. Then, the operating surgeon identifies the most suitable location to capture the images. Markers are again placed on the tumor (if it was possible) and also onto another area distant from the tumor where the operating surgeon is confident that it represents normal brain. HS images are then captured again and tissue samples, resected from the position of the tumor markers, are sent to the neuropathology laboratory for tissue diagnosis. The number of markers used in each surgery is variable and depends on the nature and characteristics of the tumor.

### 4.3.4 Neuropathology evaluation

The resected tissue is sent to the neuropathology laboratory where it is formalin fixed and undergoes standard H&E (Hematoxylin and Eosin) staining and any further required staining to establish a definitive histopathological diagnosis. Neuropathologists perform the histopathological diagnosis, employing techniques used in the routine clinical practice. Samples are classified as tumor or normal brain. Furthermore, tumor samples are subdivided into tumor type and grade. **Figure 4-1.e** and **Figure 4-1.f** show an example of a histopathological image of a glioblastoma and normal brain tissues, respectively.

### 4.3.5 Sample labeling

In the last step, by using the information provided by the neuropathologists and the knowledge of the operating surgeons, several pixels are labeled taking as a reference the

spectral signatures of certain pixels inside the markers and outside the markers for the non-tumor classes. After the labeling process (explained in Section 4.4), a gold standard map of each image is obtained (**Figure 4-1.g**). Pixels that present specular reflections produced by the non-uniformity of the brain surface are avoided.

The gold standard maps are composed of four classes: tumor tissue (red color), normal brain tissue (green color), blood vessels (blue color) and background (black color). Based on the indications given by the pathologist, the eventually possible normal inflamed labeled tissue has been included in the normal class. The background class comprises any other tissues, materials or substances that can be present in the surgical scene and are not relevant for the tumor resection. Blood vessels and background pixels are labeled by the surgeon with the naked eye. White pixels in the gold standard map are the pixels that are not labelled.

## 4.4 HS gold standard generation

In this application where human living patients are involved, it is not possible to achieve a complete gold reference map of the captured image with 100% of certainty that the pixel represents the established class. To achieve that, a pathologist should analyze the entire brain tissue exposed in the image and this is obviously not possible due to ethical reasons, since in this case the neurosurgeon should resect all the tissue exposed in the brain surface (including tumor and normal), causing serious problems to the patient health. In other fields such as remote sensing or even in the medical field but using *ex-vivo* or *in-vitro* tissue the complete gold reference generation is a relatively easy task, but using *in-vivo* human samples (and especially in the brain) this task is highly complex and practically impossible nowadays.

In this section, we propose a methodology to achieve a partial gold standard map of the HS image of the *in-vivo* brain surface based on four key factors: 1) The pathological analysis of a tumor sample to confirm the tumor tissue location and diagnosis; 2) The association of the HS captured image with the intraoperative neuronavigation system to locate the approximated area of the tumor; 3) The experience and knowledge of the neurosurgeon to identify the normal, hypervascularized and background classes and also the approximated area of the tumor tissue following the indications of the neuronavigation system and the pathological diagnosis; 4) The spectral properties of each tissue class to find the most similar pixels respect to a reference pixel selected by the operating surgeon by using a labelling tool specifically developed to this end.

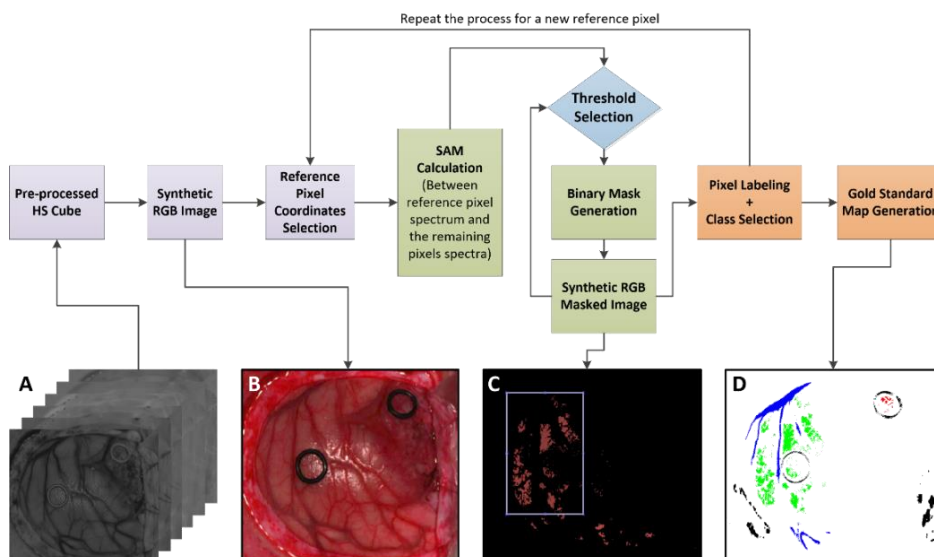
Commonly, manual gold standard dataset definition is usually done by visual inspection of the scene and the successive labeling of each sample. This labeling methodology can produce errors in the final gold standard map, since it is possible to label by mistake pixels with different spectral information in the same class due to the manual procedure. Therefore, in order to build a gold standard as reliable as possible, a methodology based on the Spectral Angle Mapper (SAM) algorithm [145] was proposed to generate a robust and efficient gold standard dataset.

An interactive graphical user interface was designed using the Matlab® GUIDE application (The MathWorks Inc., Natick, MA, USA). In the first step of the labeling process, the specialist (the operating surgeon) selects the coordinates of a reference pixel in a synthetic RGB image generated from the HS cube. The synthetic RGB image

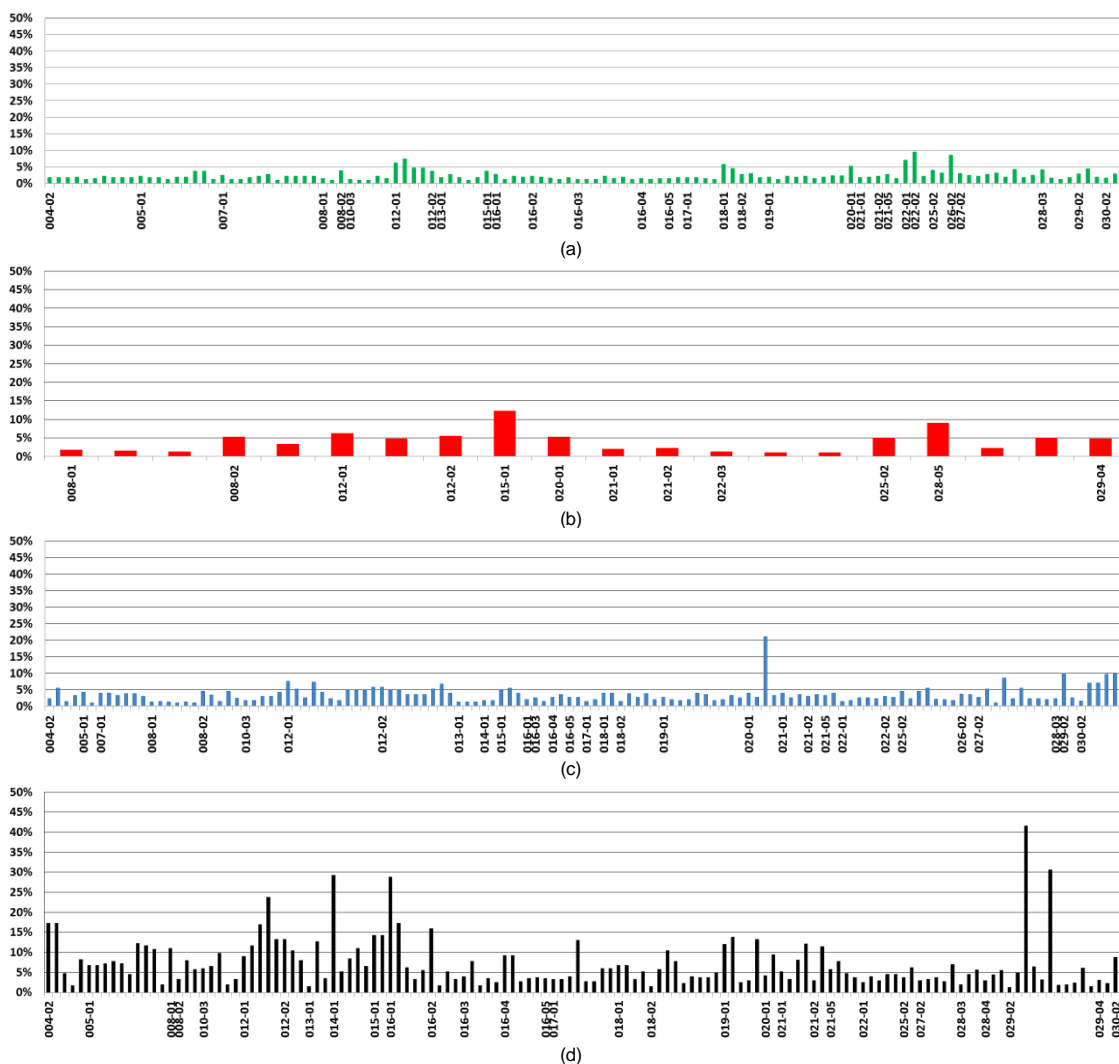
is generated by extracting three specific spectral bands from the HS cube that correspond with red (708.97 nm), green (539.44 nm), and blue (479.06 nm) colors. The reference pixel can be selected at the site where the biopsy was performed (where the marker is located) or at a site far enough from the tumor margins where the surgeon can be quite confident that the tissue is abnormal (in the case of tumor labeling). The tissue presented inside the tumor markers was sent to pathology for a precise diagnosis of the tumor. In the case of normal tissue, hypervascularized tissue, and background classes, the labeling is performed by selecting a reference pixel by the naked eye based on the surgeon's knowledge and experience. Then, the spectral angle between the selected pixel and the other pixels of the HS cube is calculated. In this moment, the operating surgeon manually establishes a threshold to match the physiological features of the selected tissue. This means that the most spectrally similar pixels to the selected reference pixel are highlighted using a binary mask. This masked image contains only pixels with a spectral angle lower than the established threshold with respect to the reference pixel. Once the user concludes that only the pixels belonging to one class have been highlighted, the selected pixels are assigned to that class. Neurosurgeons were instructed to select only a few sets of very reliable pixels instead of a wider set of uncertain pixels.

This labeling framework provides two main advantages to generate the gold maps. On the one hand, when the specialist selects a reference pixel, it is possible to ensure that the selected pixel indeed belongs to a certain class by looking at the synthetic RGB masked image, where the pixels with lower spectral angle with respect to the reference pixel are shown. On the other hand, the process of manually selecting pixels from a HS cube for each class is a time-consuming task, so this semi-automatic method allows generating the gold standard in an efficient way.

**Figure 4-3** presents the block diagram of this procedure and the information available at each stage of the labeling process. **Figure 4-3.a** represents the pre-processed HS cube that is the input to the labeling chain while **Figure 4-3.b** shows the synthetic RGB representation of the HS cube, where the reference pixels are selected. **Figure 4-3.c** illustrates the synthetic RGB masked image after applying the SAM algorithm between the reference pixel and the other pixels of the HS cube with a certain fixed threshold. In addition, in this image is possible to see the area selected by the specialist, which will be labeled in a certain class. Finally, **Figure 4-3.d** shows the final gold standard map generated after the labeling procedure, where the labeled pixels that belong to tumor tissue, normal brain tissue, blood vessels and background are identified with red, green, blue and black colors respectively. Each HS image of the generated database has its respective gold standard map. In addition, **Figure 4-4** represents the total number of reference pixels selected for each HS image and the threshold values established for each reference pixel for each class. As it can be seen, in average, the threshold values for the normal, tumor and hypervascularized classes are lower than 10%. However, in the background class there is a higher variability due to the different materials and tissues that can be included in this class.



**Figure 4-3: Semi-automatic labeling process flowchart.** (a) Pre-Processed HS cube; (b) Synthetic RGB image extracted from the HS cube; (c) SAM mask over the synthetic RGB image; (d) Final gold standard map.

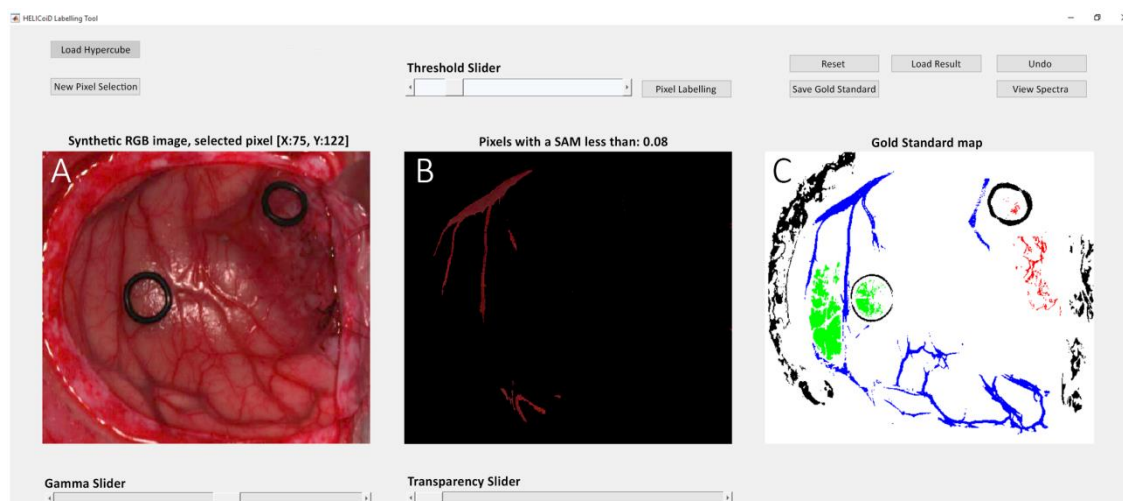


**Figure 4-4: Threshold values selected for each reference pixel in each image for each class.** (a) Normal class. (b) Tumor class. (c) Hypervascularized class. (d) Background class.



**Figure 4-5** shows a screenshot of the semi-automatic labeling tool where the labeling procedure of the blood vessel class has been done. On the left side of the image (**Figure 4-5.a**), the synthetic RGB representation of the HS cube is shown. In the center (**Figure 4-5.b**), the SAM representation is presented, where only the pixels that have a spectral angle less than  $0.08^\circ$  respect to the selected reference pixel are highlighted. In this case, the reference pixel and its correspondent SAM representation belongs to the blood vessel class. Finally, on the right side of the image (**Figure 4-5.c**), the gold standard map generated for patient 2 is shown, where tumor tissue, normal tissue, blood vessels and background are represented in red, green, blue and black colors respectively. Some sliders controls are presented in the labeling tool so as to adjust the gamma of the synthetic RGB image, the overlapping transparency of the SAM image over the synthetic RGB image and the threshold value.

Summarizing, the reliability of the gold standard is guaranteed by the use of the intraoperative MRI neuronavigation for placing the rubber ring markers; the operating surgeon knowledge and experience for the labeling of the normal tissues, blood vessels and background samples; and finally, the pathological analysis of the resected tissue for the tumor labeling.



**Figure 4-5: Screenshot of the semi-automatic labeling tool interactive interface.**  
(a) Synthetic RGB image; (b) SAM masked image; (c) Final gold standard map.

#### 4.4.1 Definition of the of the labeling classes

According to the WHO (World Organization Health) tumor classification list, a class definition for the labeling of the tissue samples was established (**Table 4-1**). This class list was done taking into account the different possible elements that can be observed in a HS image of a neurosurgical scene, allowing the inclusion of more classes if necessary, without altering the rest of the classes. **Table 4-2** shows the reduced final class definition list that was employed in the performed experiments taking into account the final sample types that were acquired during the data acquisition campaigns.

#### 4.4.2 Gold standard dataset

The labeled dataset generated using the semi-automatic labeling tool is composed by 37 *in-vivo* brain surface images from 22 different patients, where tumor and normal

tissue were labeled as well as blood vessels and other tissue, materials or substances that can be presented in the surgical scene (called background). These images were selected due to the captures were suitable for the labeling process, allowing the specialists performing the labeling with a high confidence. This dataset includes primary grade IV glioblastoma (GBM) tumors, primary grade III anaplastic oligodendroglioma tumors and some secondary tumors (lung, renal and breast). **Table 4-3** summarizes the operations and images that were labeled to generate the gold standard maps and the total number of labeled pixels per each HS image. **Table 4-4** details the total number of pixels labeled per each class. **Figure 4-6** shows the average and standard deviation of each type of tissue presented in the labeled dataset across all the patients, differentiating between the tumor types. Furthermore, **Figure 4-7** illustrates the synthetic RGB images and the gold standard maps, generated by the specialists using the semi-automatic labeling tool, of each HS image.

**Table 4-1: Labeling class list**

Class Id	Class Name				Color Map		
100	Normal (Healthy)	Non-defined				Green	[0 255 0]
101		Grey Matter (GM)					
102		White Matter (WM)					
200	Tumor	Primary	High Grade (HG)	Grade IV (GIV)	Pure Glioblastoma (PGBM)	Red	[255 0 0]
201					Mixed (MixedGIV) [With lower grade component, G III, G II]		
202					mMGMT		
203					1p19q Mutation (1p19q)		
220			Oligodendroglial				
221			Astroglial				
222			Mixed (MixedGIII)				
230		Low Grade (LG)	Grade II (GII)	Ependymoma			
240				Ganglioglioma			
241				Meningioma			
250		Secondary			Lung		
251					Breast		
252					Skin		
253					Renal		
254					GI		
255					Prostate		
256					Ovarian		
257	Colon						
270	Other			Necrosis			
300	Blood Vessel			Generic Blood	Blue	[0 0 255]	
301				Venous Blood Vessel			
302				Arterial Blood Vessel			
303				Non-Defined Blood Vessel			
310				Clot			
320	Background	Meninges		Dura Mater	Black	[0 0 0]	
321				Arachnoid			
322				Pia Mater			
330		External		Skin			
331				Skull Bone			
400				Surgical Elements			

**Table 4-2: Final labeling class list**

Class Id	Class Name				Color Map	
100	Normal (Healthy)				Green	[0 255 0]
200	Tumor	Primary	High Grade (HG)	Grade IV (GIV)	Glioblastoma (GBM)	
220				Grade III (GIII)	Anaplastic Oligodendroglioma	
250		Secondary			Lung	
251					Breast	
253					Renal	
300	Blood Vessel				Blue	[0 0 255]
400	Background				Black	[0 0 0]

**Table 4-3: Summary of the in-vivo HS human brain image database**

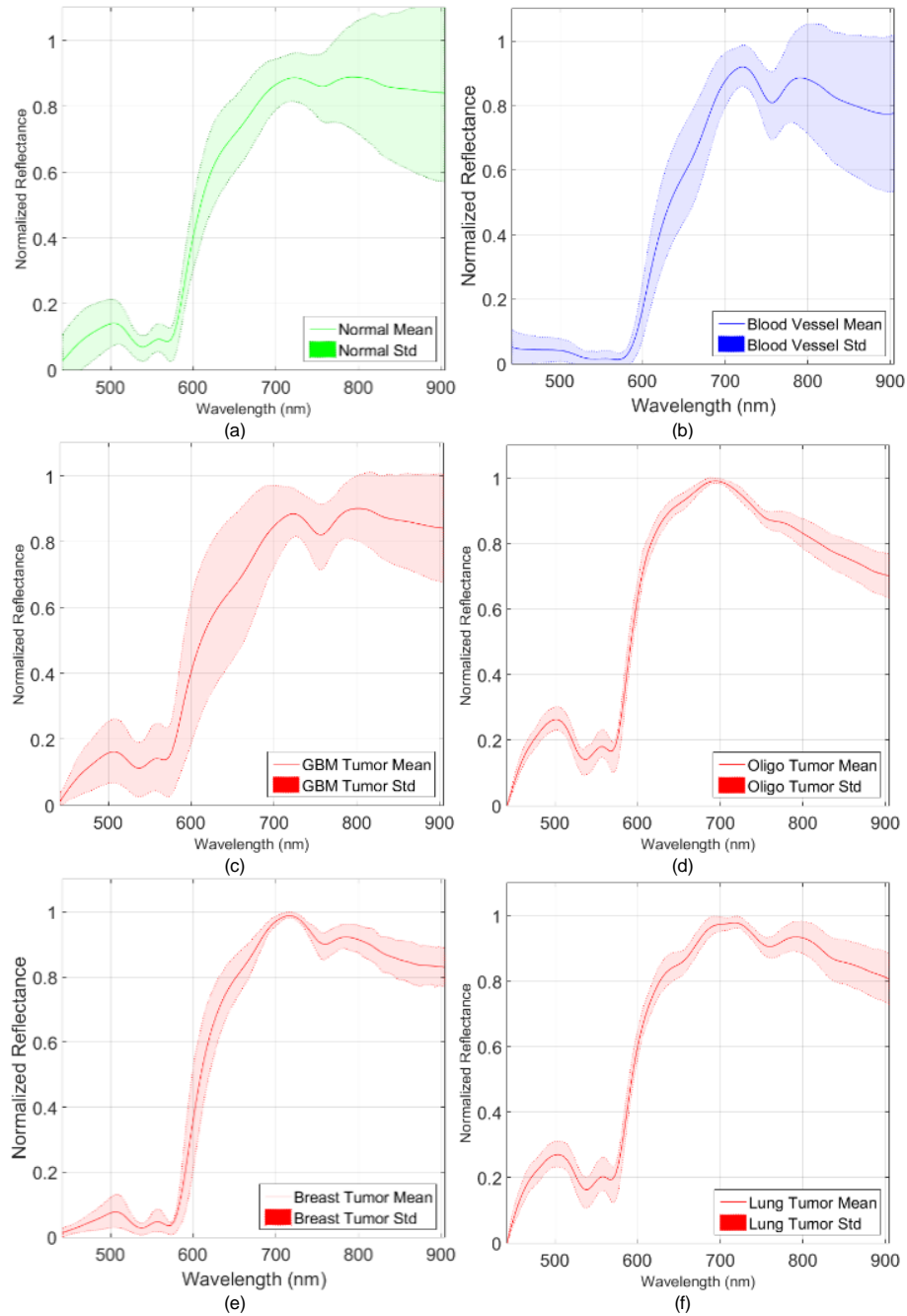
Hospital	Patient ID	Image ID	Size (width x height x bands)	#Labeled Pixels				Diagnosis
				N	T	BV	B	
UHDRN	004	02	389 x 345 x 826	5,007	0	965	1,992	Normal Brain
		03	271 x 234 x 826	0	28	0	0	Lung Adenocarcinoma (S)
	005	01	483 x 488 x 826	6,061	21	1,727	20,483	Renal Carcinoma (S)
	007	01	582 x 400 x 826	7,714	0	1,089	0	Normal Brain
	008	01	460 x 549 x 826	2,295	1,221	1,331	630	GIV Glioblastoma (P)
		02	480 x 553 x 826	2,187	138	1,000	7,444	GIV Glioblastoma (P)
	010	03	371 x 461 x 826	10,626	0	2,332	3,972	GIV Glioblastoma (P)
	012	01	443 x 497 x 826	4,516	855	8,697	1,685	GIV Glioblastoma (P)
		02	445 x 498 x 826	6,553	3,139	6,041	8,731	GIV Glioblastoma (P)
	013	01	298 x 253 x 826	1,827	16	129	589	Lung Carcinoma (S)
	014	01	317 x 244 x 826	0	30	64	1,866	GIV Glioblastoma (P)
	015	01	376 x 494 x 826	1,251	2,046	4,089	696	GIV Glioblastoma (P)
	016	01	335 x 323 x 826	3,970	0	246	12,002	Normal Brain
		02	335 x 326 x 826	349	0	0	2,767	Normal Brain
		03	315 x 321 x 826	603	0	234	1,696	Normal Brain
		04	383 x 297 x 826	1,178	96	1,064	956	GIV Glioblastoma (P)
		05	414 x 292 x 826	2,643	0	452	5,125	GIV Glioblastoma (P)
	017	01	441 x 399 x 826	1,328	179	68	3,069	GIV Glioblastoma (P)
	018	01	479 x 462 x 826	13,450	0	488	9,773	GI Ganglioglioma (P)
		02	510 x 434 x 826	4,813	0	958	5,895	GI Ganglioglioma (P)
	019	01	601 x 535 x 826	6,499	0	1,350	1,933	Meningioma
	020	01	378 x 330 x 826	1,842	3,655	1,513	2,625	GIV Glioblastoma (P)
	021	01	452 x 334 x 826	3,405	167	793	5,330	Breast Carcinoma (S)
02		448 x 324 x 826	2,353	31	555	2,137	Breast Carcinoma (S)	
05		433 x 340 x 826	969	127	1,637	1,393	Breast Carcinoma (S)	
022	01	597 x 527 x 826	2,806	0	1,064	3,677	GIII Anaplastic Oligodendroglioma (P)	
	02	611 x 527 x 826	8,174	0	680	0	GIII Anaplastic Oligodendroglioma (P)	
	03	592 x 471 x 826	0	96	0	0	GIII Anaplastic Oligodendroglioma (P)	
UHS	025	02	473 x 403 x 826	977	1,282	907	3,687	GIV Glioblastoma (P)
	026	02	340 x 324 x 826	507	0	128	0	Normal Brain
	027	02	493 x 476 x 826	6,352	0	5,606	21,785	Normal Brain
	028	03	422 x 398 x 826	2,839	0	73	13,341	Normal Brain
		04	482 x 408 x 826	0	0	0	10,025	Lung Adenocarcinoma (S)
		05	482 x 390 x 826	0	1,920	0	0	Lung Adenocarcinoma (S)
	029	02	365 x 371 x 826	2,098	0	3,341	11,258	Normal Brain
		04	399 x 342 x 826	0	1,748	0	3,785	GII Anaplastic Oligodendroglioma (P)
	030	02	382 x 285 x 826	2,050	0	9,242	15,337	Normal Brain
	Total	22 Operations - 37 Captures			117,242	16,795	57,863	185,684

\*(N) Normal tissue; (T) Tumor tissue; (BV) Blood vessel; (B) Background; (S) Secondary; (P) Primary.

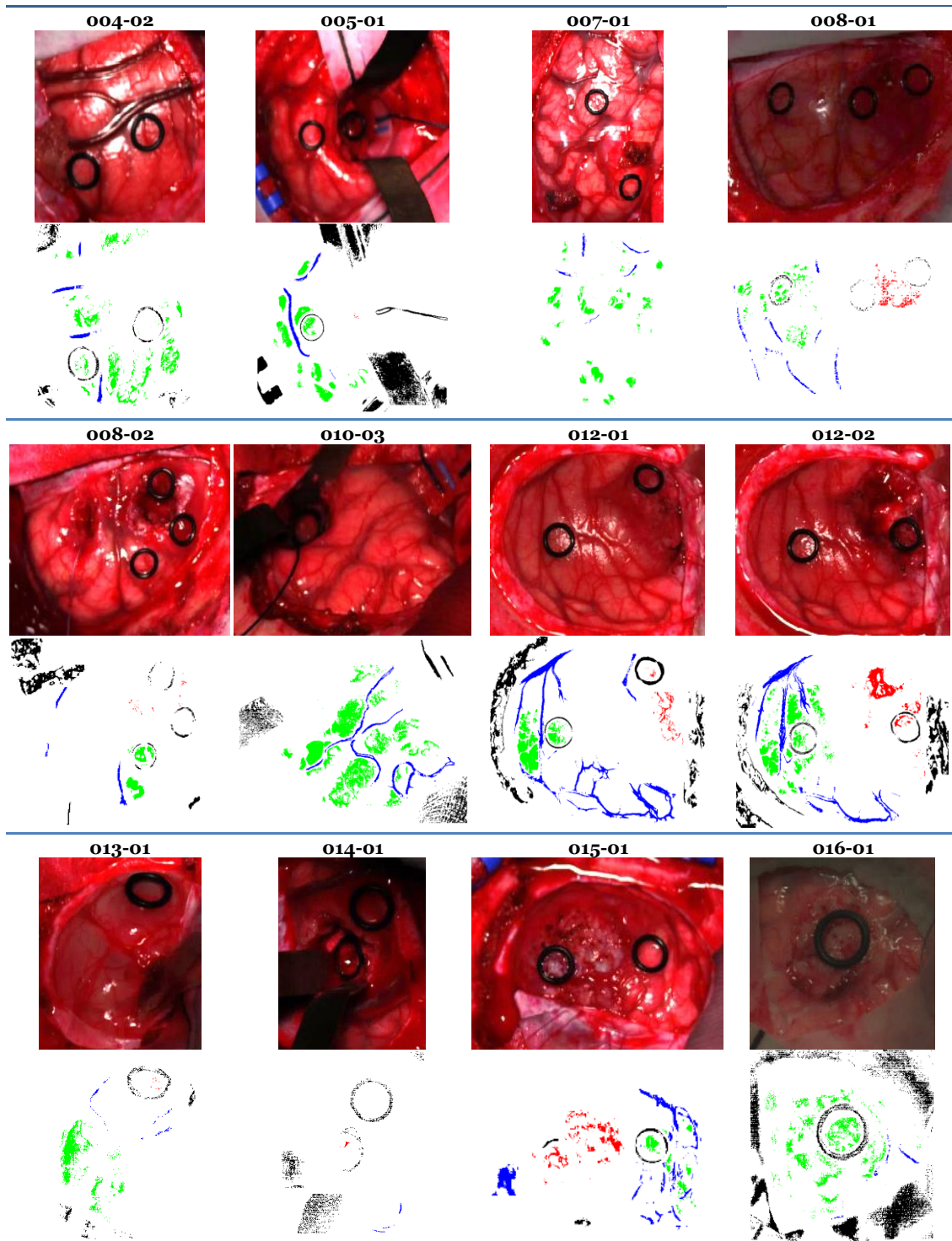


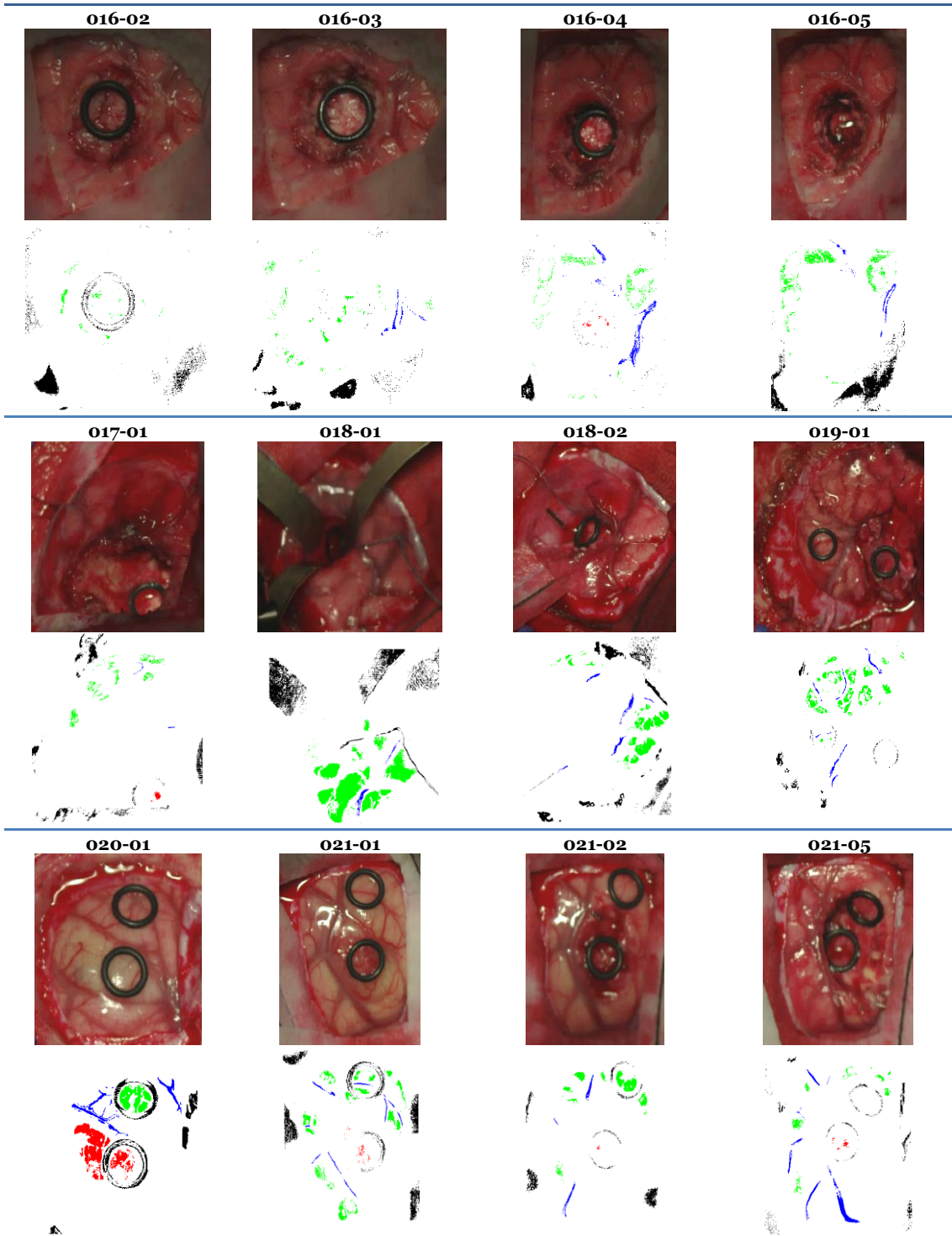
**Table 4-4: Summary of the labeled dataset**

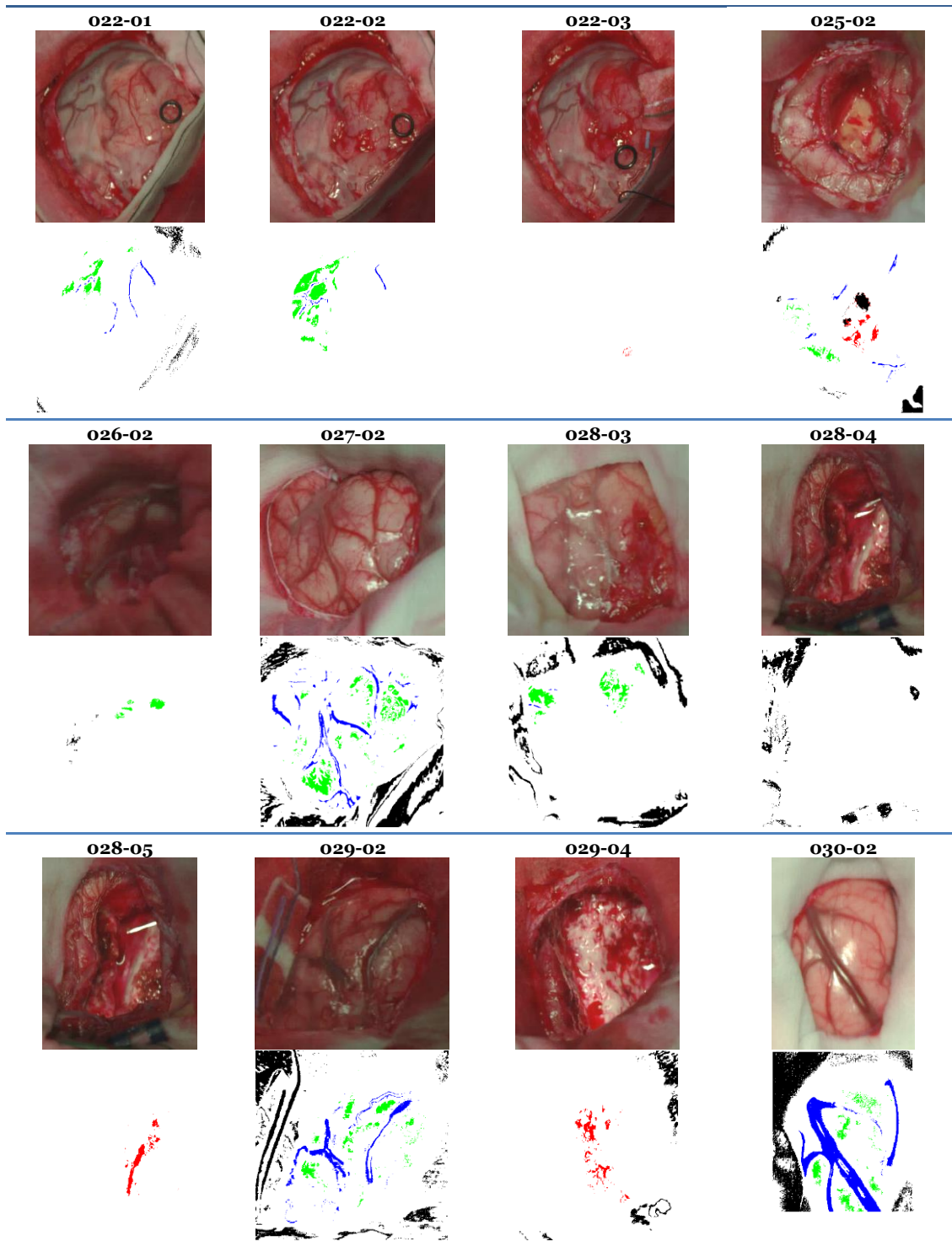
Class			#Labeled pixels
Normal			117,242
Tumor	Primary (GIV)	GBM	12,641
	Primary (GIII)	Anaplastic Oligodendroglioma	1,844
	Secondary	Lung	1,964
		Renal	21
		Breast	325
Blood Vessel			57,863
Background			185,684
<b>Total:</b>			<b>377,584</b>



**Figure 4-6: Average and standard deviation (Std) across all the patients of the different types of spectral signatures in the labeled database. (a) Normal tissue. (b) Blood vessels. (c) GBM tumor. (d) Anaplastic oligodendroglioma tumor. (e) Secondary breast tumor. (f) Secondary lung tumor.**







**Figure 4-7: RGB representations and gold standard maps of the HS images that compose the *in-vivo* HS human brain image database.** The numeric code shown above each image represents the Patient ID and Image ID (PatientID-ImageID) that are detailed in **Table 4-3**.

## 4.5 Conclusions

In this chapter, the procedure and methodology followed to generate the *in-vivo* HS human brain image database, employing the intraoperative HS acquisition system described in Chapter 3, were presented. This procedure involves a multidisciplinary team of engineers, neurosurgeons and pathologists in order to ensure the generation of a reliable image database. The HS acquisition system was assessed during surgical procedures in two different hospitals in UK and Spain, obtaining 80 HS images from 36 different patients in the VNIR and NIR spectral ranges. However, in the work performed in this thesis only the VNIR information was employed, involving 44 HS cubes from 35 different patients.

A specific methodology to obtain a golden standard database to be employed in the development of the HS brain cancer detection algorithms was established. This gold standard dataset was generated using a semi-automatic labeling tool based on the SAM algorithm. The labeling tool was employed by the specialists (neurosurgeons) in order to label 37 HS images from 22 different patients, generating a gold standard map of each image. In these images, tumor and normal tissue were labeled (when possible) as well as the blood vessels and other tissues, materials or substances that can be found in the surgical scene and are not relevant for the surgical resection procedure (called background). This dataset includes both primary (grade IV glioblastoma and grade III and II anaplastic oligodendrogliomas) and secondary (lung, renal and breast) tumors. A total of 377,584 spectral signatures were included in the gold standard dataset. The higher quality images obtained in this database have been uploaded in an open access repository to provide the scientific community with the first HS human brain database for research purposes [146].



# Chapter 5: Hyperspectral brain cancer detection algorithm

## 5.1 Introduction

This chapter presents the development of a novel classification method for brain cancer detection that employs the especial characteristics of HS images to help neurosurgeons to accurately determine the tumor boundaries in surgical-time during the resection, avoiding excessive excision of normal tissue or unintentionally leaving residual tumor. The algorithm proposed in this work consists of a hybrid framework that combines both supervised and unsupervised machine learning methods. Firstly, a supervised pixel-wise classification using a SVM classifier is performed. The generated classification map is spatially homogenized using a one-band representation of the HS cube, employing the FR-tSNE dimensional reduction algorithm, and performing a KNN filtering. The information generated by the supervised stage is combined with a segmentation map obtained via unsupervised clustering employing a HKM algorithm. The fusion is performed using a majority voting approach that associates each cluster with a certain class. To evaluate the proposed approach, five HS images of the brain surface affected by GBM tumor from five different patients have been used in this chapter. The final classification maps obtained were analyzed and validated by specialists.

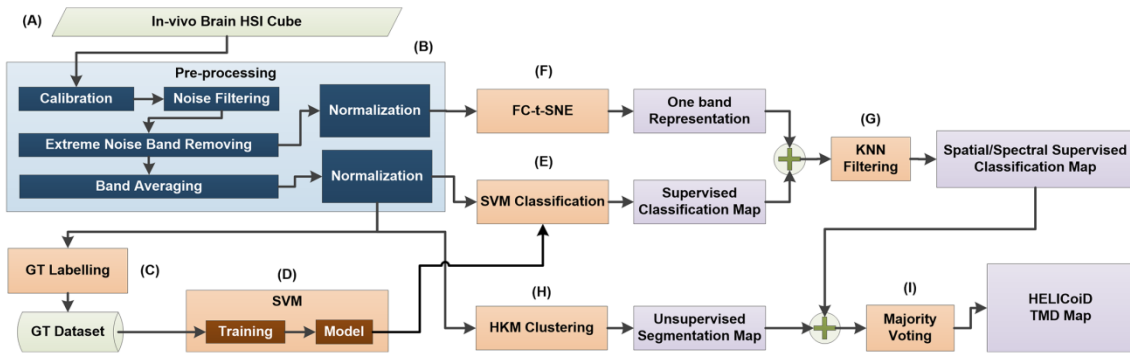
This work has been carried out in collaboration with the research group of Prof. Guang-Zhong Yang at the Hamlyn Centre of the Imperial College London and also with the research group of Prof. Bogdan Stanciulescu at the *Ecole Nationale Supérieure des Mines de Paris* (ENSMP). The main contributions of this work have been reported in several publications [144], [146]–[151].

## 5.2 Brain cancer detection algorithm

The classification framework developed in this study aims to exploit both the spatial and spectral features of the HS images. **Figure 5-1** illustrates the scheme of this classification framework based on five main steps: data pre-processing, dimensional reduction, spatial-spectral supervised classification, unsupervised clustering segmentation and hybrid classification. After capturing the *in-vivo* brain surface HS cube (**Figure 5-1.a**), the raw image is pre-processed in order to homogenize the



spectral signatures of each pixel (**Figure 5-1.b**). Then, the gold standard employed for building the supervised classifier model is extracted by the specialists (**Figure 5-1.c**) using the previously described labeling tool and the SVM classifier is trained (**Figure 5-1.d**). Once the SVM model is generated, it is used to perform the supervised pixel-wise classification over the pre-processed HS cube (**Figure 5-1.e**). Next, a spatial-spectral homogenization is accomplished [152] using a KNN filtering (**Figure 5-1.g**), where a one-band representation of the HS cube is employed. The dimensionality reduction algorithm used to obtain the one-band representation of the HS cube is the FR-t-SNE algorithm (**Figure 5-1.f**). This algorithm has been selected because it provides the best score along different HS images compared to other dimensionality reduction algorithms [153]. Once the spatial-spectral homogenization has been performed, a filtered classification map is available. In order to obtain the final classification map, the spatial-spectral supervised classification map is combined with a segmentation map obtained via unsupervised hierarchical clustering (**Figure 5-1.h**) using a majority voting approach [154] (**Figure 5-1.i**).



**Figure 5-1: Brain cancer detection and delimitation algorithm framework overview diagram.** (a) HS cube of *in-vivo* brain surface; (b) Pre-processing stage of the algorithm; (c) Database of labeling samples generation; (d) SVM model training process employing the labeled samples dataset; (e), (f) and (g) Algorithms that conform the spatial-spectral supervised classification stage; (h) and (i) Algorithms that generate the unsupervised segmentation map and the final HELICoiD TMD map, respectively.

### 5.2.1 Data pre-processing

After the acquisition of the *in-vivo* brain surface HS cube (**Figure 5-1.a**), a pre-processing chain, already explained in [147], is applied to the HS cube to homogenize the spectral signatures of each pixel (**Figure 5-1.b**) and to reduce the dimensionality of the HS image without losing the main spectral information contained on it. This pre-processing chain consists of five steps.

The first step performs a radiometric calibration of the raw spectral signature of each pixel using the black and white reference images captured by the acquisition system inside the operating theatre, with the same illumination conditions where the image will be captured. The white reference image is obtained using a standard white reference tile and the dark reference image is acquired by keeping the camera shutter closed. **Figure 5-2.a** and **b** show an example of a single raw spectral signature and the calibrated spectral signature of a grade IV GBM tumor respectively.

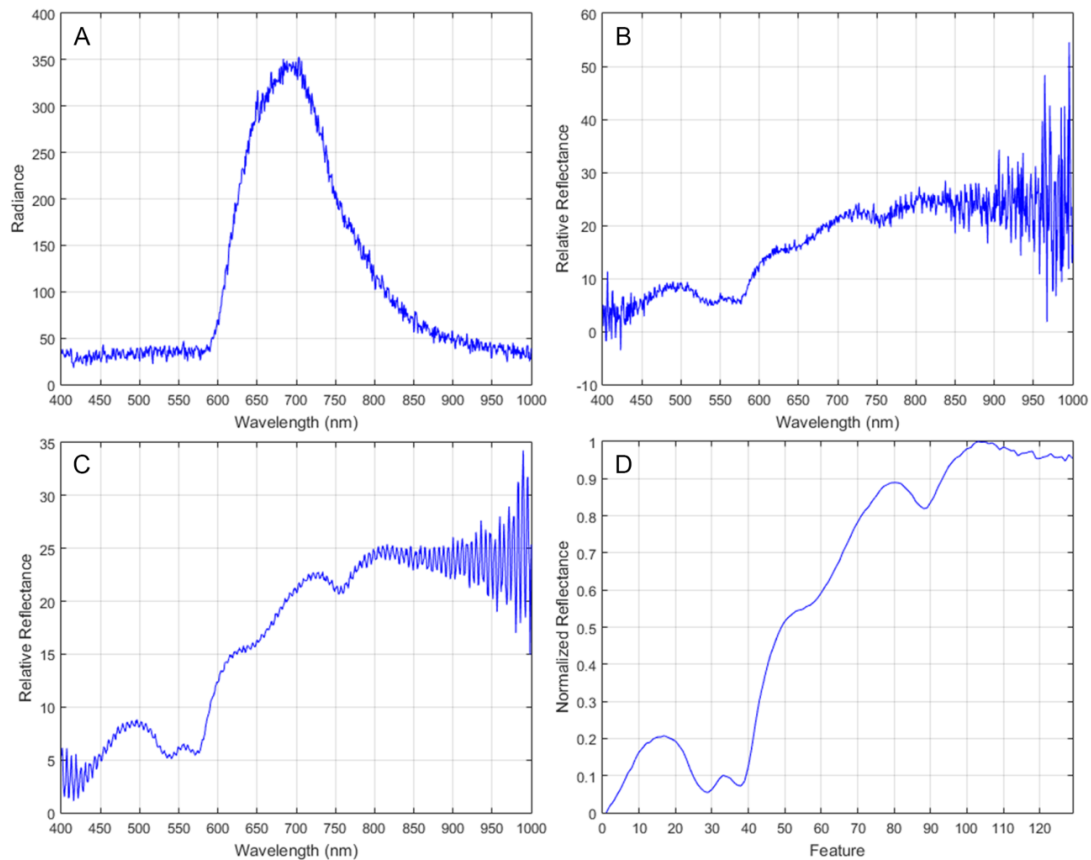
The second step applies noise filtering using the first stage of the HySIME algorithm where a function called Hyperspectral Noise Estimation infers the noise in the HS data, by assuming that the reflectance at a given band is well modeled by a linear regression



on the remaining bands. **Figure 5-2.c** plots the spectral signature after the HySIME noise filtering application.

In the third step, the spectral bands from the lowest and highest bands are removed due to their low SNR because of the limited performance of the CCD sensor in these ranges. Bands from 0 to 50 and from 750 to 826 are removed. After the extreme noise band removing step, the spectral signatures are reduced in bands through spectral averaging due to the information redundancy between contiguous bands. The reduced HS cube is formed of 129 spectral bands.

Finally, the last step of the pre-processing chain applies normalization over the samples to avoid the different radiation intensities of each pixel produced by the non-uniform surface of the brain. **Figure 5-2.d** illustrates the final pre-processed spectral signature.

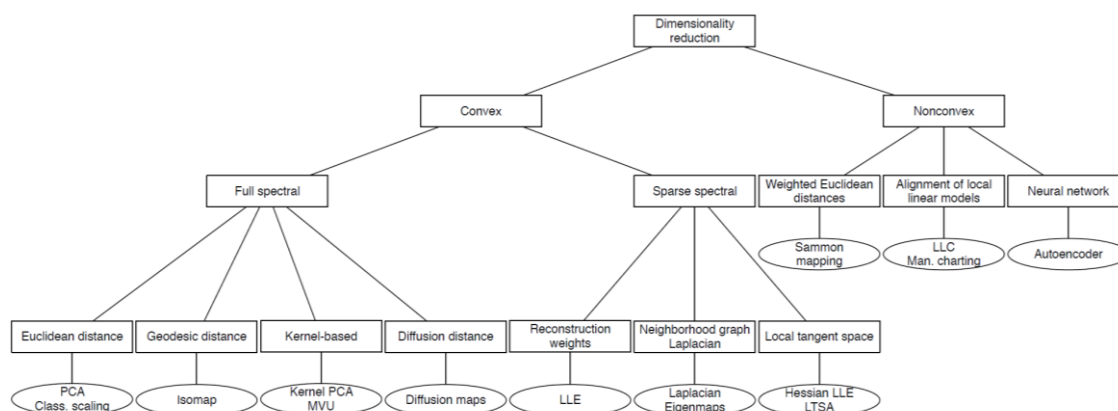


**Figure 5-2: Spectral signature of a grade IV GBM tumor tissue.** (a) Raw spectral signature; (b) Calibrated spectral signature; (c) HySIME filtered spectral signature; (d) Final pre-processed spectral signature.

## 5.2.2 Dimensional reduction algorithms

From an information-processing point of view, the intrinsic dimensionality of HS images can be significantly reduced before subsequent image characterization steps are applied. Dimensionality reduction algorithms map high-dimensional data into a meaningful representation of reduced dimensional space so that the observed properties of the initial data are still preserved in the low dimensional space. Since the intrinsic dimension, as well as the geometry of the initial data, is unknown, dimensionality reduction, in general, is an ill-posed problem that can only be solved by

assuming certain data properties. Thus far, many algorithms for dimensionality reduction have been developed in literature [155]. **Figure 5-3** shows the taxonomy of the different dimensionality reduction techniques established by Van Der Maaten *et al.* in [155].



**Figure 5-3: Taxonomy of dimensionality reduction techniques [155].**

These techniques can be subdivided into two main types: 1) techniques that attempt to preserve global properties of the original data in the low-dimensional representation (Convex); 2) techniques that attempt to preserve local properties of the original data in the low-dimensional representation (Nonconvex). Within these two categories, there is a relevant differentiation between linear and non-linear techniques.

Principal Component Analysis (PCA) [156] is one of the most popular linear techniques for dimensionality reduction. It maps the data preserving as much as possible their variance. However, PCA has two important limitations: it is based on a global property (the variance of the data) and it is a linear technique.

Non-linear methods have the advantage that can deal better with complex real world data. Their workflow is usually as follows: they decompose the nonlinear structures into linear subspaces, in the same way that some curves can be approximated by linear subspaces and use a solution similar to the PCA on each subspace. Techniques such as Isomap [157], Locally Linear Embedding (LLE) [158], Hessian [159] and Laplacian [160] are examples of non-linear methods.

As a cross-cutting work performed during the development of this thesis, several dimensional techniques were analyzed and reported by Ravi *et al.* in [153]. In this work, a new quality score to compare dimensional reduction techniques was proposed, where the criterion based on local and global properties proposed in [161] was combined with a global contrast factor (GCF) [162] and a measure that depends on the shape of the histogram of the embedded image. These two criteria take into account also the visual quality of the embedded image. The medical HS images of human brain surface generated during development of the work described in this thesis were employed to perform the comparison study. In addition, in this work, authors propose the Fixed Reference t-Distributed Stochastic Neighbors Embedding (FR-t-SNE) algorithm that is an extension of the t-Distributed Stochastic Neighbors Embedding (t-SNE) [163]. t-SNE is a non-linear technique well suited for embedding high-dimensional data into a lower dimensional space. It models each high-dimensional object by a low-dimensional point in such a way that similar objects are modeled by nearby points and dissimilar objects are modeled by distant points. The main advantage of t-SNE is that it captures

the local structure of the high-dimensional data and reveals global structures similar to clusters at the same time.

As stated in [153], embedding a HS image using t-SNE may not guarantee consistent results since, at each dimensional reduction process of a new image, the random nature of the t-SNE can create embedded representations that are not persistent. Therefore, it can happen that similar tissues will be represented with different low dimensional representations across different images. This makes subsequent tissue characterization more difficult. This problem is mainly generated by the lack of a fixed coordinate system, which does not allow the comparison of the embedded results across different tissue samples [164].

FR-t-SNE tries to overcome these limitations by using a learning process aimed at finding a fixed reference coordinate system. FR-t-SNE is divided in three main steps: in Step 1, an optimal reference system is fixed to maintain a consistent manifold embedding along with all the images and circumvent the lack of a fixed coordinate system. In Step 2, the manifold is gradually tested on the training set using the predefined fixed reference. Finally, in the last step, a HS image is embedded efficiently. A KNN classification algorithm is used to obtain the low vector representation of each high dimensional vector after all the training images are processed and the manifold discovered. This KNN classifier will use a lookup table, containing the values of the learned reference coordinates to predict the embedded value of each sample in each new HS image.

**Table 5-1** shows the comparative study performed in [153], where 23 different dimensional reduction approaches were compared using the proposed quality score employing three different brain images to evaluate the performance.





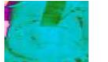
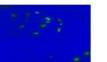
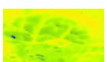





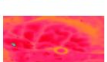





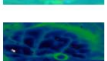




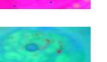





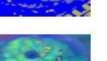















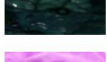





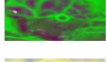








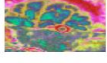

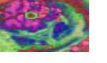


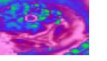
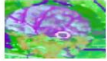

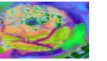
### 5.2.3 Spatial-spectral supervised classification

The spatial-spectral supervised stage of the brain cancer detection algorithm is based on three steps: pixel-wise supervised classification, dimensional reduction and spatial homogenization filtering.

The pixel-wise classifier employed in the supervised classification is the SVM algorithm. This algorithm requires a confident labeled dataset in order to train the model that will be used to classify the input data. In this work, the labeled dataset of *in-vivo* brain samples that is used to train the SVMs was created by combining the efforts of neurosurgeons and pathologist, as it has been previously described in section 4.4. In this work, the LIBSVM [165] has been used for support vector classification MATLAB® implementation.

Before explaining the methodology employed for performing a supervised classification over the available HS data, some considerations have to be taken into account. Due to the impossibility of having a way to extract the labeled information from all the pixels in a HS cube of brain tissue, there are two ways of measuring the performance of the generated supervised models. For the available labeled dataset, it is possible to use standard metrics in order to measure the accuracy provided by the model when classifying unseen data. Nevertheless, for evaluating a supervised model applied to a whole HS cube (where not all pixels have been labeled) only the visual evaluation of an expert is possible.

**Table 5-1: Comparison of the dimensional reduction algorithms sorted according to the proposed quality score [83]**

Approach	Image 1	Image 2	Image 3	Score
LCC [166]				1.18
Diffusion Maps [167]				1.47
Landmark MVU [168]				1.50
LLE [158]				1.53
Hessian LLE [159]				1.53
NPE [169]				1.57
LTSA [170]				1.58
PCA [156]				1.63
Autoencoder [171]				1.66
Isomap [172]				1.71
LLTSA [173]				1.73
Landmark Isomap [174]				1.76
CCA [175]				1.78
SPE [176]				1.85
Prob. PCA [177]				1.90
Sammon [178]				1.98
Factor Analysis [179]				2.06
LPP [180]				2.08
MVU [181]				2.25
Fast MVU [182]				2.33
Laplacian [160]				2.38
FR-t-SNE [153]				2.61
t-SNE [163]				2.66

The methodology for evaluating the supervised classifiers in a quantitative way is as follows: first, we use the labeled information corresponding to the dataset, and then we apply a 10-fold cross validation in order to measure the performance of the model. The quantitative evaluation metrics used for this purpose are sensitivity, specificity and overall accuracy metrics, and will be defined in section 5.3. Once the quantitative metrics have been obtained, the previously trained SVM classifier is used to classify a whole HS cube, and then it is evaluated by neurosurgeons in order to analyze the quality of the algorithm in distinguishing different types of tissues, materials or substances.

In order to include the spatial features of the HS images, a spatial homogenization is applied to improve the supervised classification results by incorporating the neighborhood information of each pixel into the classification chain. The algorithm proposed in [152], which refines the pixel-wise classification probability map using a KNN filtering on non-local neighborhoods of a pixel, were used. The algorithm has shown competitive classification accuracy results compared with other state-of-art spatial-spectral classification approaches [152].

This algorithm requires two inputs: the probability maps or confidence scores obtained from the supervised classifier ( $P$ ) and the guidance image ( $I$ ) (which is usually a one-band representation of the input HS image). The spatial-spectral feature vector is defined in Equation (5), where  $I$  is the normalized pixel value (spectrum) at location  $i$  and  $l(i)$ ,  $h(i)$  are the normalized longitude and latitude of the pixel  $i$ . The output of the KNN-filtering is given by Equation (6), where  $N_i$  refers to the  $K$ -nearest neighbors of the pixel  $i$  found in the feature space  $F(i)$ . It can be seen that at  $\lambda = 0$  there is no spatial information, while when non-zero it captures the spatial information of pixel  $i$  given by  $l(i)$  and  $h(i)$ .

$$F(i) = (I(i), \lambda l(i), \lambda h(i)) \quad (5)$$

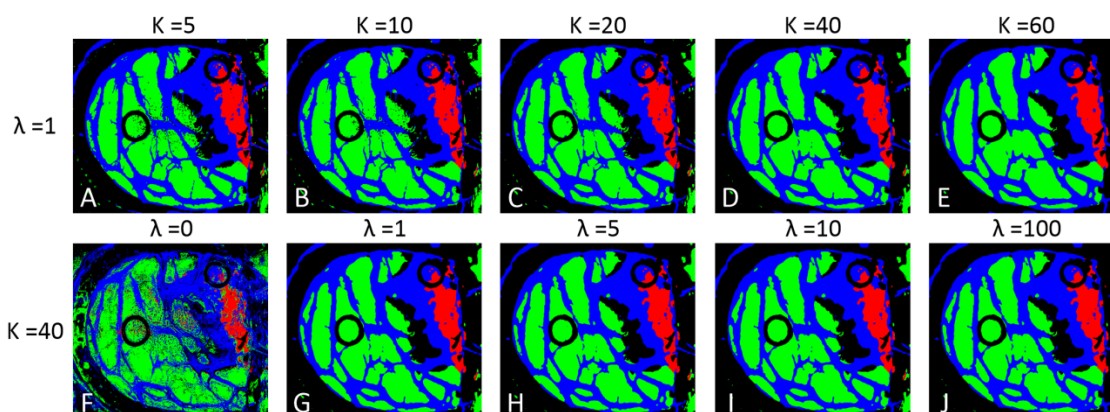
$$O(i) = \frac{\sum P(j)}{K}, j \in N_i \quad (6)$$

When  $\lambda$  is set to zero, the spatial coordinates are not considered in the KNN filtering process, and when the value of  $\lambda$  increases, the classification results tend to be oversmoothed, decreasing the accuracy of the classification results. The parameter  $K$  has a similar influence in the classification results: when the  $K$  value is high, the filtering method oversmooths the classification results, worsening the accuracy of the classification results. In this approach, it is not possible to provide a quantitative measure of the influence of  $K$  and  $\lambda$  parameters, due to the absence of a complete gold standard map. Nevertheless, the influence of these parameters in the generation of the classification maps was studied.

As mentioned before, large values of  $K$  or  $\lambda$  tends to oversmooth the obtained classification maps. Several executions of the KNN filtering were performed employing different values of  $K$  (5, 10, 20, 40 and 60) and  $\lambda$  (0, 1, 5, 10 and 100). **Figure 5-4** shows the filtered classification maps of the patient 12 capture 1 (Op12C1) using different values of  $K$  and  $\lambda$ . In both cases, small values of  $K$  and  $\lambda$  result in a mix of small classes that do not represent the real distribution of the tissues. On the other hand, large values of  $K$  and  $\lambda$  tend to oversmooth the classes. After a visual inspection

of the results by the specialists (neurosurgeons), the final values of  $K$  and  $\lambda$  chosen for this study were  $K = 40$  and  $\lambda = 1$ . These values generate a filtered map where the different classes are homogenized enough without oversmoothing the classification result (**Figure 5-4.d** and **Figure 5-4.g**).

In this spatial-spectral supervised classification algorithm, the probability maps are obtained from the confidence scores of the SVM classification result, while the guidance image is obtained by calculating the one band representation of the HS cube by performing a dimensionality reduction using the FR-t-SNE algorithm [153]. The one-band representation was obtained from the pre-processed HS cube with 750 bands (without applying the band averaging step in the pre-processing chain).



**Figure 5-4: KNN filtered maps obtained with different  $K$  and  $\lambda$  values.** (a), (b), (c), (d) and (e) filtered maps obtained with  $K$  equal to 5, 10, 20, 40, and 60, while keeping  $\lambda$  value fixed to 1; (f), (g), (h), (i) and (j) filtered maps obtained with  $\lambda$  equal to 0, 1, 5, 10, and 100, while keeping  $K$  value fixed to 40.

#### 5.2.4 Unsupervised clustering segmentation

The unsupervised stage of the algorithm is based on a clustering method [183]. This method provides a segmentation map where all the different tissues, materials or substances found in the HS image are grouped forming clusters that have similar spectral characteristics. Three different clustering algorithms were applied to the available HS images differentiating between 24 clusters: H2NMF [183], HKM and HSKM [86].

After a visual evaluation of the resulting maps by the specialists, it was found that all clustering methods provided useful information about the different tissues, materials and substances that were presented in the scene. Due to the fact that all three clustering methods provided similar information, HKM was selected in this study since it had the lower computational cost providing similar results. In the context of this work, the clustering process provides a good delimitation of the different areas presented in the image that should be identified by a specialist or by an automatic process, *i.e.*, supervised classification. For this reason, a method to merge the results from the supervised and unsupervised stages of the brain cancer algorithm is required to obtain the final classification map.

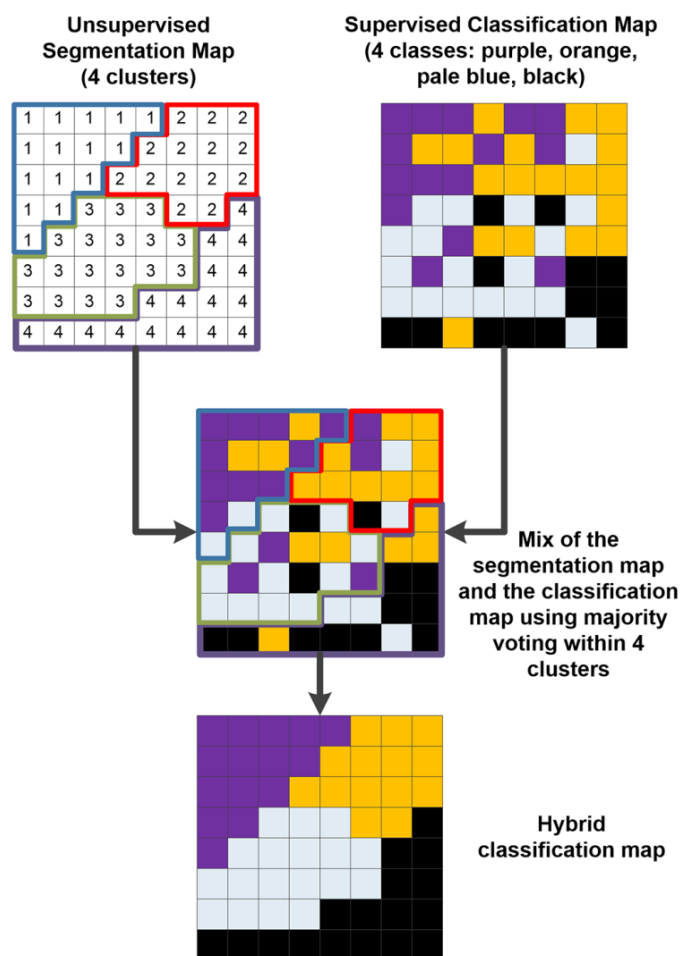
### 5.2.5 Hybrid classification

In the previous sections, the advantages of supervised and unsupervised learning methods have been introduced. On the one hand, supervised learning can infer the knowledge previously provided by neurosurgeons and pathologists, but it can poorly provide a good delimitation of the tumor area. On the other hand, the unsupervised clustering results provide a good association of similar pixels, but each cluster is semantically meaningless. In order to solve this problem, an algorithm for merging these two sources of information was employed. This hybrid algorithm was previously used in hyperspectral imaging [154], and consists of a technique that merges the information from a supervised classification map and an unsupervised segmentation map (**Figure 5-5**).

In the first step of this algorithm, the segmentation map and the supervised classification map are calculated independently from the same pre-processed HS cube. Once both maps have been obtained, the information is merged using the majority voting algorithm. For each cluster found by the clustering algorithm, all pixels are assigned to the most frequent class in each region in the supervised classification map. The combination of the supervised classification with the segmentation map provides some advantages. On the one hand, the unsupervised segmentation maps obtained with the clustering process have shown good capability in finding homogeneous spatial data structures from the HS cube. However, it does not provide any identification of the tissue, material or substance that the cluster belongs to. On the other hand, the supervised classification approach employs the diagnosis information provided by medical doctors (neurosurgeons and pathologists) to generate a classification map where each pixel of the image has been assigned to a certain class. However, the amount of labeled information is limited. Using the previously described MV algorithm, the strengths of each method are exploited.

As stated in [154], oversegmentation (different clusters correspond to the same class) is not a crucial problem, but undersegmentation is not desired. **Figure 5-5** graphically represents the method of the hybrid algorithm where an unsupervised map, composed by four different clusters that have no semantic meaning, is merged with a supervised classification map, composed by four different classes that have histological meaning. The final hybrid classification map represents each pixel within a certain class (identified by the supervised classification algorithm) grouped taking into account the clusters obtained by the unsupervised segmentation map (that delimitates the borders of each cluster region).





**Figure 5-5: Hybrid classification example based on a majority voting technique.** The unsupervised segmentation map and the supervised classification maps are merged using the majority voting method.

### 5.3 Evaluation metrics

The methodology for evaluating the supervised classifiers in a quantitative way is as follows: firstly, the labeled information corresponding to a simulation was used, and then, a 10-fold cross validation was applied in order to measure the performance of the model. The quantitative evaluation metrics used for this purpose are sensitivity, specificity and overall accuracy metrics. These are calculated from the following conditions:

- **True Positive (TP):** Correctly detected conditions. The result of the test is positive and the actual value of the classification is positive.
- **False Positive (FP):** Incorrectly detected conditions. The result of the test is negative and the actual value of the classification is positive.
- **True Negative (TN):** Correctly rejected conditions. The result of the test is negative and the actual value of the classification is negative.
- **False Negative (FN):** Incorrectly rejected conditions. The result of the test is positive and the actual value of the classification is negative.



*Sensitivity* is the proportion of the actual positives that are correctly identified as positives by the classifier (Equation (7)). *Specificity* is the proportion of the actual negatives that the classifier successfully evaluates as negative (Equation (8)). *Overall Accuracy* refers to the ability of the model to correctly predict the class label of new or previously unseen data (Equation (9)).

$$Sensitivity = \frac{TP}{TP + FN} \quad (7)$$

$$Specificity = \frac{TN}{TN + FP} \quad (8)$$

$$Accuracy = \frac{TP + TN}{TP + FP + TN + FN} \quad (9)$$

Once the quantitative metrics were obtained, the previously trained SVM classifier is used to classify a whole HS cube, and the result was evaluated by neurosurgeons in order to analyze the quality of the algorithm in distinguishing different types of tissues, materials or substances.

## 5.4 HS brain cancer detection algorithm results

To evaluate the efficiency of the brain cancer detection algorithm described in this chapter, a set of five HS images, selected from the database belonging to five different patients affected by GBM tumor, were employed. A total of 44,555 labeled spectral signatures were used for the training of the supervised classification algorithm. **Table 5-2** summarizes the total number of labeled spectral signatures generated for each class, the number of tumor biopsies performed and the number of images captured for each patient.

**Table 5-2: Gold standard dataset for the preliminary evaluation of the developed brain cancer detection algorithm**

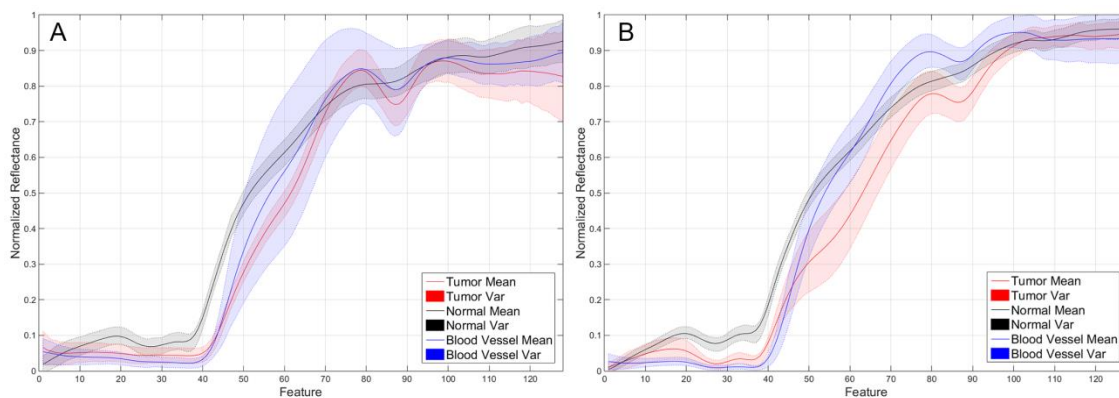
Patient ID	#Image ID	#Tumor Biopsies	Tissue Type (#pixels)				Total (#pixels)
			Normal Tissue	Tumor Tissue	Blood Vessel	Background	
008	01	2	2,295	1,221	1,331	630	5,477
012	01	1	4,516	855	8,697	1,685	15,753
015	01	1	1,251	2,046	4,089	696	8,082
020	01	1	1,842	3,655	1,513	2,625	9,635
025	01	1	977	1,221	907	2,503	5,608
<b>Total (#pixels)</b>			<b>10,881</b>	<b>8,998</b>	<b>16,537</b>	<b>8,139</b>	<b>44,555</b>

### 5.4.1 Hyperspectral imaging can distinguish tissues by their spectra

**Figure 5-6.a** and **Figure 5-6.b** show the mean and variances of the pre-processed spectral signatures of the tumor tissue, normal tissue and blood vessel labeled pixels obtained from the gold standard database of patient 8 and 12, respectively. As it can be seen in this figure, the shape of the signature depends on the tissue heterogeneity, especially in the tumor class. There are some similarities between the spectral signature of the blood vessel class and the tumor class that could produce some misclassifications, as it will be explained later. However, it is possible to see that the differences between the normal class and the tumor class are remarkable. These

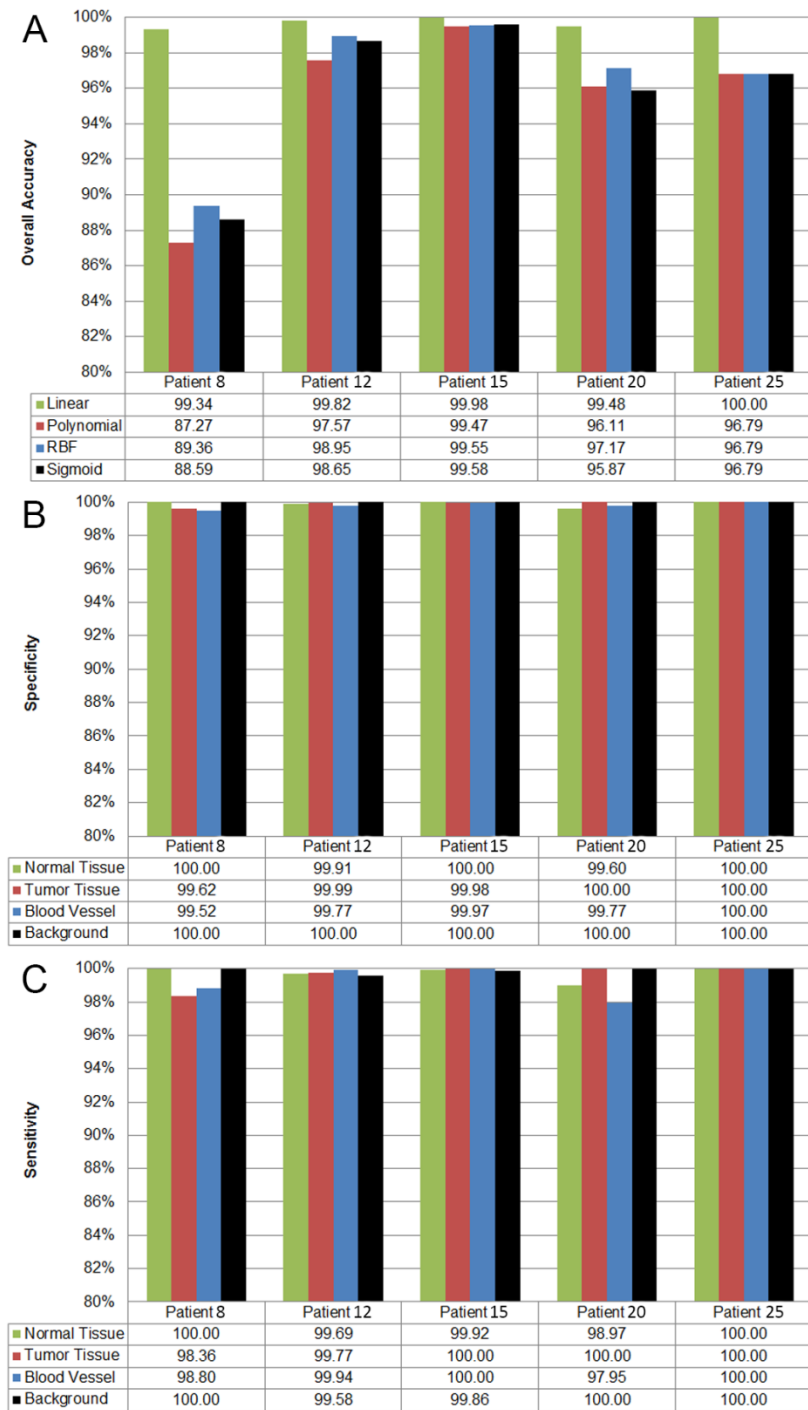
differences will ensure a successful classification of the normal and tumor pixels by the supervised classifier.

In order to demonstrate that the use of a supervised classifier will achieve a reliable differentiation between the labeled pixels that conforms the gold standard database, these pixels have been spectrally analyzed employing an SVM classifier. Afterwards, the SVM model generated using the gold standard database for each patient was employed to classify the entire HS cube of this patient (intra-patient evaluation). As it was previously mentioned, the gold standard information was extracted from the HS data using a specific tool developed to this end.



**Figure 5-6: Mean and variances of the pre-processed spectral signatures.** Tumor, normal and blood vessel classes of the labeled pixels from patient 8 (a) and patient 12 (b) are represented in red, black and blue color respectively.

In order to measure the supervised classifier performance and to select the optimal configuration of the SVM model, a three-way cross validation was employed. Linear, Radial Basis Function (RBF), polynomial and Sigmoid kernels were tested and compared. **Figure 5-7.a** shows the overall accuracy classification results obtained in the experiments comparing the four SVM kernels with the default parameters, using the labeled dataset for each patient individually and performing the three-way cross validation. Linear kernel provides the best accuracy results for this type of sample having a lower computational cost than the other kernels exceeding 99% of overall accuracy. This indicates that there is a strong reliability on classifying the spectral samples of the brain surface using a supervised classifier. **Figure 5-7.b** and **Figure 5-7.c** illustrate the results of specificity and sensitivity metrics respectively with the linear kernel for each patient and class using the one-vs.-all method. As it can be seen in these figures, the SVM classifier offers specificity and sensitivity results higher than 96%, reaching in most cases 100% specificity and sensitivity.



**Figure 5-7: Quantitative results of the supervised classification performed with the SVM classifier applied to the labeled data of each patient.** (a) Overall accuracy results of supervised classification per SVM kernel type and patient; (b) and (c) Specificity and sensitivity results obtained using the SVM classifier with linear kernel for each patient and class employing the one-vs.-all evaluation method.

**Figure 5-8.a-e** show the synthetic RGB images generated from each HS cube where the tumor area has been surrounded with a yellow line in each RGB image. **Figure 5-8.f-j** show the gold standard maps generated using the labeling tool, where red, green, blue and black colors represent the *tumor tissue*, *normal tissue*, *blood vessels* and *background*, respectively. The qualitative results generated by the supervised classifier are shown in **Figure 5-8.k-o**. These supervised classification maps were

obtained using the SVM model generated from the gold standard. The color representation is the same as the gold standard representation previously introduced, except for the blue color representing the hypervascularized tissue presenting on the brain surface apart from the blood vessels. In each supervised map, it is possible to identify the tumor area. Some false positives can be found in the images. This result is produced due to the spectral similarities between the tumor tissue and the main blood vessels or areas with extravasated blood in the surgical field as a result of the resection.

In **Figure 5-8.k**, the supervised classification map of patient 8 is shown. In this result, it can be seen that there are some false positives (delineated by an orange line) where a main blood vessel is presented (red area in the center of the image) and near other blood vessels far from the tumor area. Furthermore, there is another false positive in a small region in the right bottom of the image where the bone of the skull is visible (outside of the region where the parenchyma is exposed) due to the extravasated blood from the craniotomy. The same effect is observed with patient 15 (**Figure 5-8.m**) where there are some false positives outside of the parenchymal area. Despite these false positives, the tumor area is clearly identifiable in each image, and in any case blood vessels and extra-parenchymal tissue are very evident to the surgeon during resection, so that no diagnostic confusion is likely to happen.

This first step of the cancer detection algorithm results in the approximate identification of the tumor and normal tissue areas using the SVM supervised classifier. The next step is to improve the classification maps employing spatial information provided by the HS image.

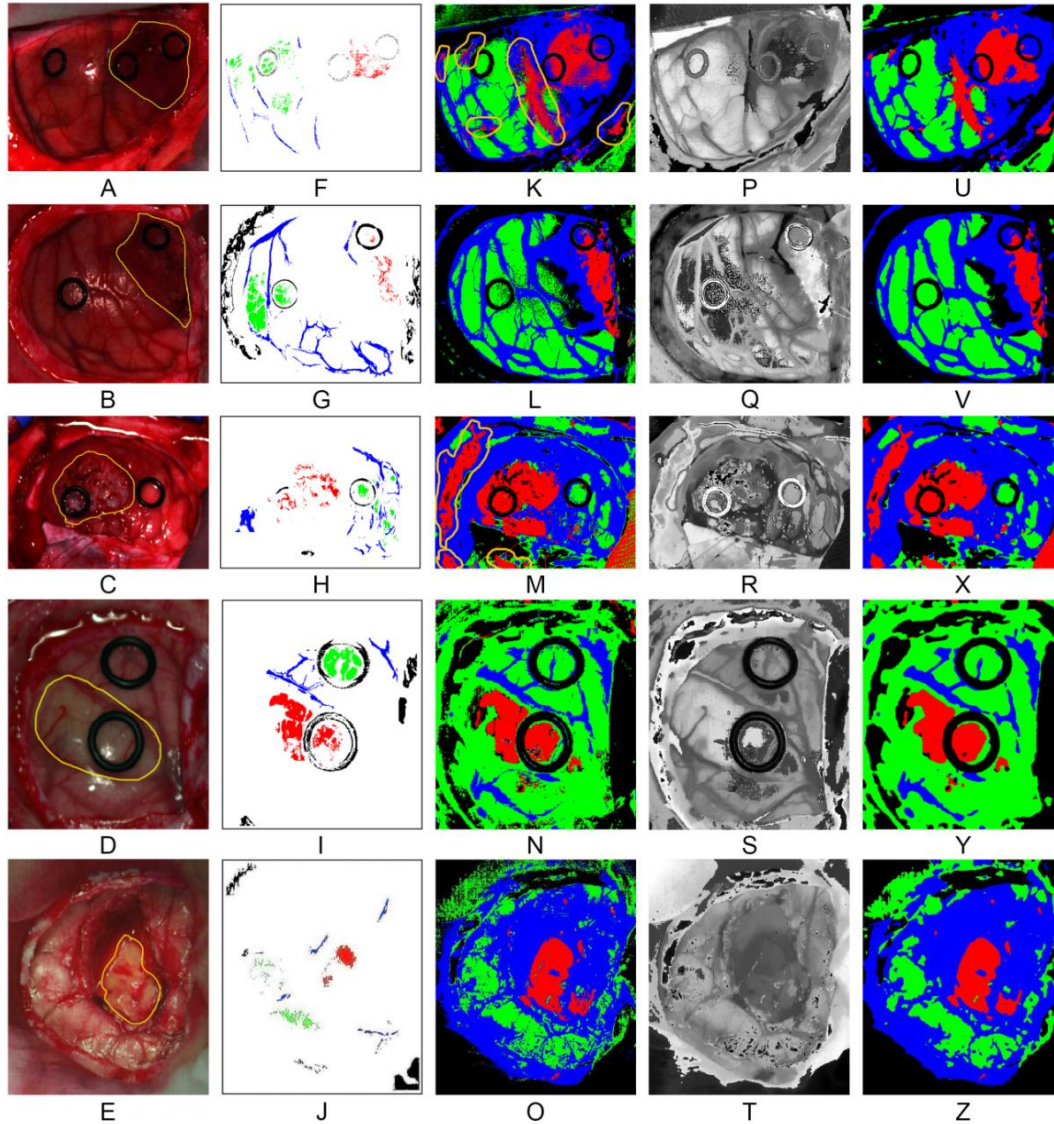
#### 5.4.2 Improving the spatial coherence of the classification maps

The supervised classification maps generated in the first step of the cancer detection algorithm were improved by combining these results with a one-band representation of the HS cube using a KNN filtering method. The one-band representation of the HS image, where the most significant information of the image is revealed, were generated using the FR-t-SNE algorithm, which offers a high contrast value compared to alternative dimensional reduction algorithms.

**Figure 5-8.p-t** present the FR-t-SNE one-band representation of each HS cube. In these images, it is possible to identify the different areas presenting on the brain surface as their borders are highlighted. In these one-band representations, it is possible to identify the tumor area in each image. FR-t-SNE results together with the probability scores obtained from the supervised classification maps are the inputs for the KNN filtering. This filtering process is used to increase the spatial coherence of the supervised classification maps, providing the contextual information of each pixel in the classification scheme. **Figure 5-8.u-z** illustrate the spatially optimized classification maps obtained after the KNN filtering process. It is apparent that the region of each class in the images has been homogenized giving coherence to the classification maps.

Although the differences between the supervised classification maps and the spatially optimized classification maps are not very noticeable when looking at the resulting images by the naked eye (**Figure 5-8.k-o** and **Figure 5-8.u-z**), this is a high important task since this homogenization will improve the final stage of the cancer detection algorithm, which will assign the classes to the otherwise meaningless clusters

provided by the unsupervised clustering algorithm. If the number of pixels that belongs to a certain class (tumor, normal, hypervascularized or background) increases or decreases in the spatially optimized classification map, the final brain cancer classification map could be affected, showing different densities of a certain class in a certain region delimited by the unsupervised clustering algorithm.



**Figure 5-8: Results of each step of the optimized spatial-spectral supervised classification of the five different patients.** (a), (b), (c), (d) and (e) Synthetic RGB images generated from the HS cubes; (f), (g), (h), (i) and (j) Gold standard maps used for the supervised classification training; (k), (l), (m), (n) and (o) Supervised classification maps generated using the SVM algorithm; (p), (q), (r), (s) and (t) FR-t-SNE one band representation of the HS cubes; (u), (v), (x), (y) and (z) Spatially optimized classification maps obtained after the KNN filtering.

### 5.4.3 Unsupervised clustering for accurate boundaries delineation

**Figure 5-9.a-e** show the segmentation maps generated for each patient employing the HKM clustering algorithm. As it can be seen, structures such as blood vessels, materials like the ring markers and different tissue regions are delineated by the clustering algorithm. Furthermore, the region of interest that is formed by the parenchymal area of the brain can be clearly differentiated. Inside this area, some

different structures of tissue are highlighted, delimiting with high accuracy the boundaries of each region. However, the information provided by the segmentation maps is meaningless: the colors that represent each cluster are randomly selected and there is no class associated for each cluster. For this reason, it is necessary to combine the supervised identified classes with the unsupervised accurate clusters.

#### 5.4.4 Delimiting and identifying the brain area affected by cancer

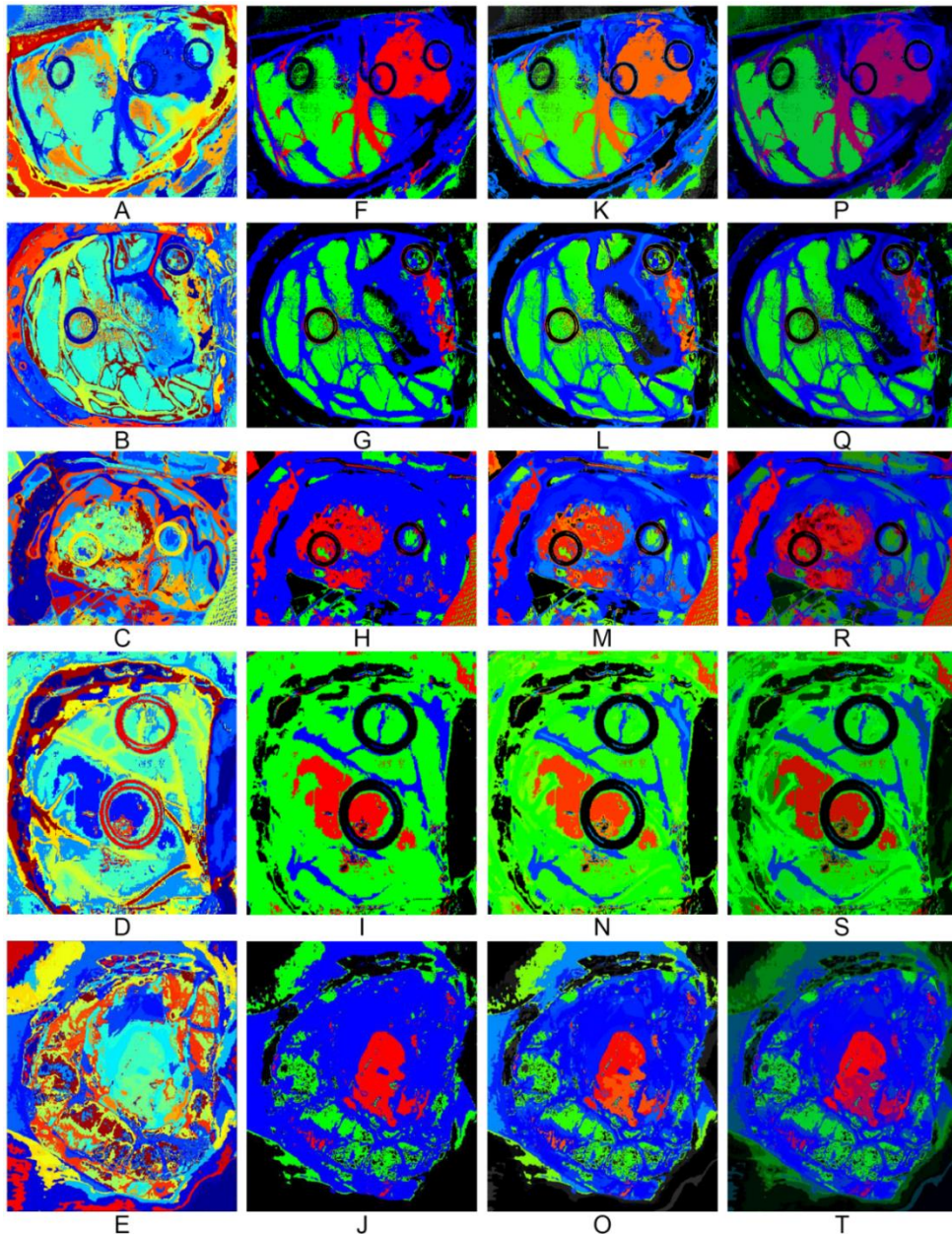
The final stage of the cancer detection algorithm has the goal of combining the segmentation map, obtained by the clustering algorithm, and the spatially homogenized classification maps, generated after the KNN filtering process, to build the final classification map employing the MV algorithm. **Figure 5-9.f-j** show the MV classification map results. These results have been generated applying the maximum majority class of the supervised classification map to each cluster of the segmentation map. These MV maps provide more accurate results than the spatially optimized supervised classification maps. The boundaries of each class region are better delineated. In some cases, the tumor area is reduced, having mixed tissue (normal and tumor) in the area where only tumor class was presented in the supervised classification map (see patient 12, **Figure 5-9.g**). The same effect is observed in patient 15, where small islands of normal tissue are found to be mixed in the tumor region (see patient 15, **Figure 5-9.h**).

Although this MV classification map provides better delineation of the areas affected by cancer on the brain surface, it is possible to have additional hidden information in these maps. For example, if a cluster that represents a certain class includes a zone with a high percentage (but not the maximum) of another class, this information is not revealed in the resulting image. For this reason, another visualization of the MV classification map was developed, the One Maximum Density (OMD) map. In this case, only the maximum probability results obtained by the MV algorithm for each cluster are used to determine the color map, and the color of each class is then degraded using the percentage of the probability. For example, if the probability of the tumor class for a certain cluster is 80%, the cluster color is degraded 20% (the cluster RGB color will be  $R = 0.8$ ,  $G = 0$ ,  $B = 0$ ). The color gradient is performed only for the tumor tissue, normal tissue and blood vessel/hypervascularized tissue classes. The background class is not degraded. **Figure 5-9.k-o** show the OMD maps for each capture, with areas of degraded color. This observation indicates that the MV result probability was somewhat lower than for undegraded areas, and may point to the presence of different tissue classes merged in this cluster.

In order to represent the classes that are mixed in a certain cluster, a third map is based on the three maximum probability values of the MV results in each cluster. This representation, the Three Maximum Density (TMD) map, offers more information from the MV results, mixing the color of each class using the percentage of the three maximum MV probability values. For instance, if the probability of tumor class for a certain cluster is 60%, the probability of normal tissue is 10% and the probability of blood vessel/hypervascularized tissue is 30%, the RGB color of the cluster will be  $R = 0.6$ ,  $G = 0.1$  and  $B = 0.3$ . By employing this technique, it is possible to visualize the clusters where their respective mixed classes are hidden. **Figure 5-9.p-t** show the TMD maps of each capture, where clusters that are partially mixed between the classes present darker colors. Patient 15 is a good example that contains hidden information in



the MV map (**Figure 5-9.h**). After the generation of the TMD map (**Figure 5-9.r**), it is possible to visualize a new area surrounding the main tumor region represented in purple color, which corresponds with hypervascularized tissue with tumor infiltration. In this case, the system can estimate the proportion of malignant tissue that is mixed with the normal hypervascularized tissue. When the tissue is classified as normal (green color), there is no mixture between malignant and normal tissue. When there is some minimum amount of malignant tissue, the proportion of malignant tissue is showed in the TMD map with a gradient of red color and thus is marked for being resected in order to avoid tumor recurrence.



**Figure 5-9: Results of each step of the proposed cancer detection algorithm applied to the five different patients.** (a), (b), (c), (d) and (e) Segmentation maps generated using the HKM algorithm; (f), (g), (h), (i) and (j) MV classification maps; (k), (l), (m), (n) and (o) OMD maps that take into account only the major probability per class obtained from the MV algorithm; (p), (q), (r), (s) and (t) TMD maps that take into account the first three major probabilities per class obtained from the MV algorithm.

## 5.5 Conclusions

In this chapter, a novel approach to classify hyperspectral images for brain cancer detection and delineation based on the spatio-spectral properties of HSI has been presented. The preliminary results obtained in the supervised classification of the tissues that were previously labeled by the specialists, demonstrate that it is possible to accurately discriminate between normal tissue, tumor tissue, blood vessels and background with an overall accuracy higher than 99% in an intra-patient validation. Using the supervised models generated with the labeled data, the entire HS images were classified and qualitatively evaluated. Five SVM classification maps obtained from five different patients affected by a grade IV GBM tumor were generated. These maps can identify the regions where the tumor is located. Employing a spatial-spectral optimization method based on a KNN filtering and a FR-t-SNE dimensional reduction, the SVM classification maps were spatially homogenized. A clear identification of the tumor regions using this spatial-spectral supervised classification maps was provided. However, these maps did not offer an accurate delineation of the boundaries. The unsupervised stage of the algorithm based on a HKM clustering method provided a segmentation map where the boundaries of 24 different regions with similar spectral characteristics were delineated. The fusion of the spatial-spectral supervised classification map and the unsupervised segmentation map through the MV algorithm generated the final classification map, where the boundaries of the different tissues materials or substances presented in the image were identified within a certain class. In summary, the spatial-spectral classification maps allowed assigning each cluster in the segmentation map to an identifiable tissue class.

Employing the information provided by the MV algorithm, three different ways to represent the final results were analyzed. The first one was the MV map to assign the maximum probability of each class to each cluster, representing the cluster with the correspondent color: red for tumor tissue, green for normal tissue, blue for blood vessel/hypervascularized tissue and black for background. On the other hand, the OMD map displayed the color of each class degraded according to the value of the first major probability. By using this technique, it was possible to identify the clusters that conformed only slightly to their assigned class. Finally, the TMD map represented each color as a combination between the different classes mixed in a certain cluster. This map was the most valuable to the operating neurosurgeon, since it offered the possibility to assess the degree of tumor infiltration into the surrounded normal brain. This assessment is key for judging the desired extent of resection.

Although some false positives were encountered in the results, these could be solved with further investigations. For instance, there were some misclassifications between blood or blood vessels and tumor tissue due to the high intra-class variability between the vascularized tissues, although these false positives do not affect the area of identified tumor so that the margins of the tumor remained clearly evident. The use of an increased database to generate the supervised classification model, where the inter-patient variability is taken into account, is expected to produce better classification results. It is expected that the inclusion of more labeled samples of normal tissue will reduce the occurrence of false positives in the results. Furthermore, an extensive clinical validation is required to validate if the boundaries of the tumor area represented in the TMD map are accurately identified. Several biopsies of the



boundaries of tumor area must be obtained and analyzed by the pathologists to certify the brain cancer algorithm results.

On the other hand, there were some misclassifications between different tissues with high vascularization. In some cases, extravasated blood and normal tissue affected by edema were classified as blood vessel/hypervascularized tissue (blue color). This misclassification was produced due to the similar spectral characteristics of the blood vessels and the tissue affected by edema. Further investigations, where these spectral differences are included in the training of the brain cancer algorithm, could alleviate this problem, or perhaps a new class could be created to identify the normal brain with high vascularization.



# Chapter 6: HS brain cancer detection algorithm fine-tuning and acceleration

## 6.1 Introduction

In this chapter, the optimizations performed to the HS brain cancer detection algorithm, developed in Chapter 5, in order to reduce the execution time and to achieve more accurate results during surgical procedures are described. Furthermore, a brief explanation of the algorithm implementation and acceleration onto the intraoperative demonstrator is presented. This implementation was performed in collaboration with the research group of Prof. Eduardo Juárez at the CITSEM of the UPM. Finally, in order to validate the final intraoperative demonstrator, a set of 4 operations were attended with the fully working system to analyze its performance. Part of the work performed in this chapter has been reported in [184]–[192].

## 6.2 Evaluation methodology

This section briefly describes the case studies (CSs) established to evaluate the results of the different optimizations performed to the HS brain cancer detection algorithm. Three CSs were proposed where each one differs on which patients were included as subject of study for the training and testing stages of the algorithm. These CSs are defined below.

**Case Study 1 (CS1):** The goal of this CS is to check if the discrimination between healthy and tumor tissue can be performed using the available labeled data, and avoiding the inter-patient variability of data. It means that the datasets explored in this CS include HS cubes from surgical operations where both type of tissues, healthy and tumor, are present. In order to avoid the inter-patient variability of data, each surgical procedure is used independently for training and testing the supervised classifier.

**Case Study 2 (CS2):** In CS2, all the available labeled data are merged in a unified dataset. It means that a unique database is created by joining all single patient data, so the inter-patient variability is taken into account. In this CS it is possible to build a

model that aims to discriminate between different types of tumor using a complex label scheme based on several patients.

**Case Study 3 (CS3):** This case study is the most realistic one. In this approach, each surgical procedure data are used as test set of a classification algorithm, and that classifier model is built using the information from the rest of HS labeled data (belonging to different patients). This case study represents the real case of a new operation, where the classification must be performed with a classifier trained with previous operations HS data (leave-one-out cross validation).

## 6.3 Fine-tuning for surgical-time processing

The fine tuning performed to the proposed algorithm seeks two main goals: a) obtaining more accurate density maps and b) reducing the computational time consumed in the algorithm execution. In this chapter, the fine-tuning of the brain cancer detection algorithm to achieve surgical real-time processing is presented.

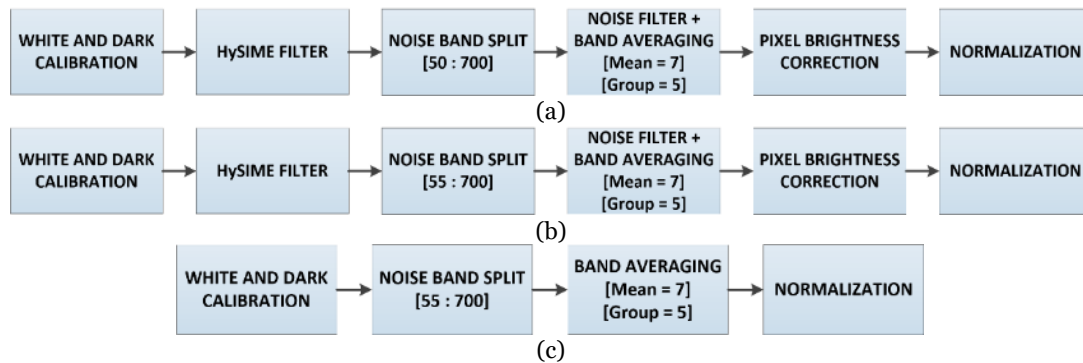
The results presented in Chapter 5 were obtained using five reference images of five different patients affected by GBM tumor and employing the CS1 evaluation method, where each HS cube is classified using only its own training samples. In this section, the comparison of the results is done using a quantitative and qualitative comparison of the results obtained for the same patients and employing also the CS1. The SVM classification map (SVM Map), the KNN filtered classification map (KNN Map) and the Majority Voting Map (MV Map) were used for the comparison depending on the stages that were affected by the algorithm modifications.

### 6.3.1 Data pre-processing fine-tuning

This section provides a comparison study between three different pre-processing chains developed to optimize the performance of the algorithm. In this study, the main goal is to reduce the computational time required by the algorithm, obtaining as accurate results as possible. This optimization will facilitate the real-time processing of the HS images during the neurosurgical procedures. Below, each proposed pre-processing chain is described ranked by complexity level:

- 1) **CP129:** Complete pre-processing chain where all the steps are performed (**Figure 6-1.a**) obtaining as a result a HS cube of 129 bands. This pre-processing chain is the one that was presented in Chapter 5.
- 2) **CP128:** Complete pre-processing chain applied to the HS cube where the noise band split range was modified to obtain a final HS cube formed by 128 bands (**Figure 6-1.b**). This modification was performed to optimize the performance of the hardware implementation. Having a pre-processed HS cube where the number of bands is integer multiple of 16 allows to more effectively taking advantage of the resources of the hardware accelerator employed in the algorithm implementation (MPPA Kalray platform).
- 3) **SP128:** Reduced pre-processing chain where the steps of noise filtering (HySIME filter and smooth filter) and pixel brightness correction were removed (**Figure 6-1.c**). This low complex pre-processing chain allows reducing drastically the computational time consumed in the pre-processing

implementation, facilitating the achievement of the goal of obtaining real-time processing during neurosurgical procedures. It has been observed that in such controlled surgery environment, the noise amount is really low, thus proven the noise filtering stage to be unnecessary.



**Figure 6-1: Different data pre-processing chains.** a) CP129 pre-processing chain; b) CP128 pre-processing chain; c) SP128 pre-processing chain.

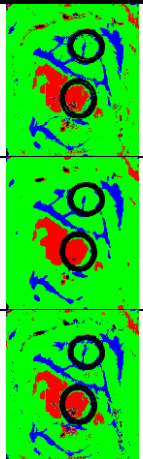
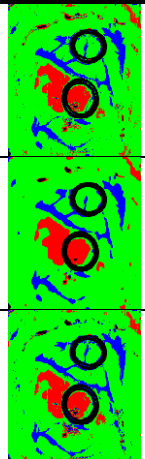

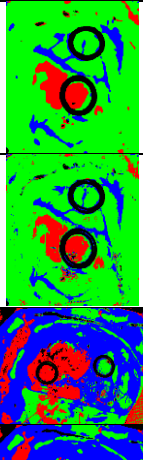
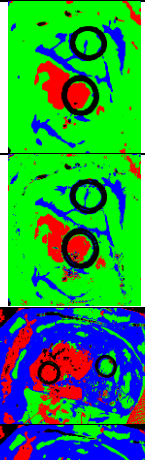

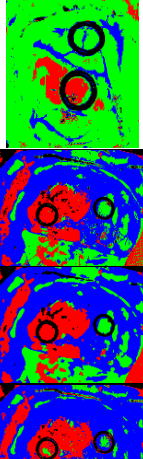
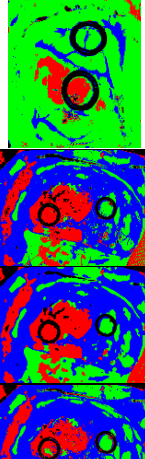

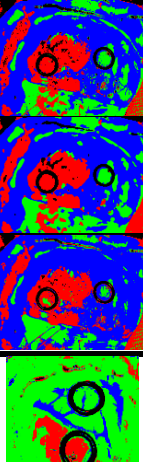
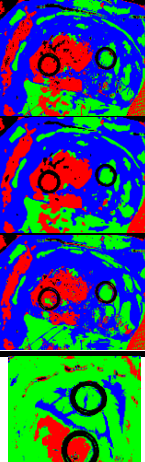

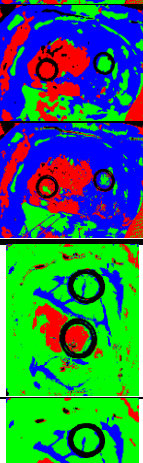
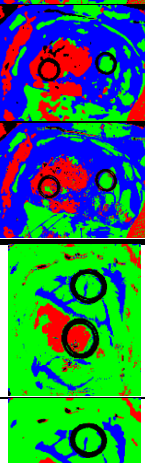
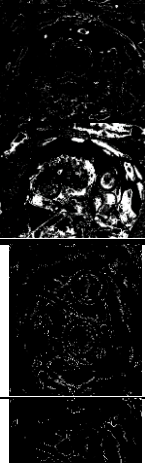
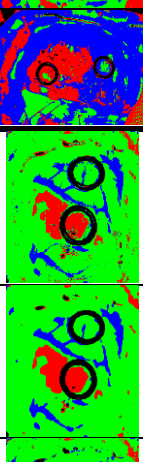
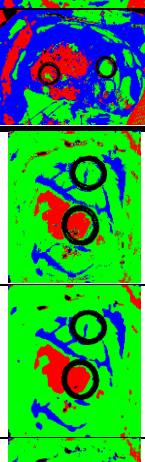

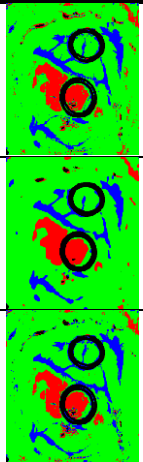
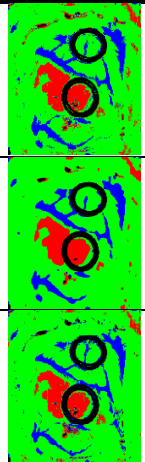

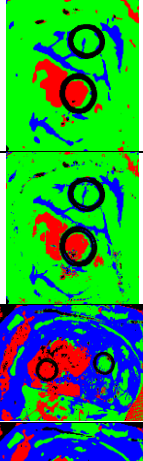
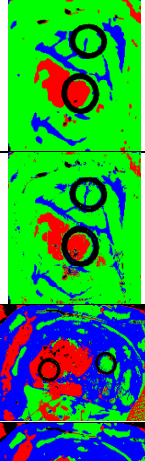

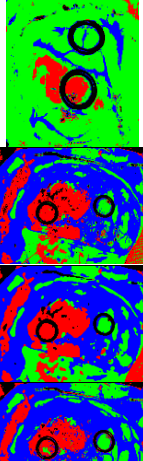
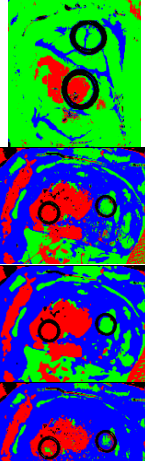
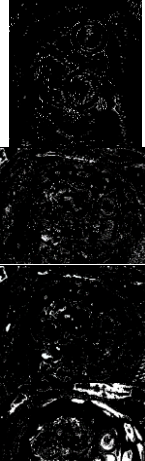
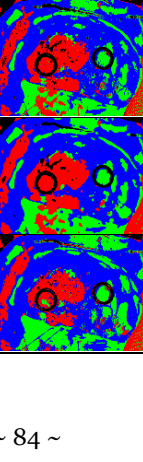
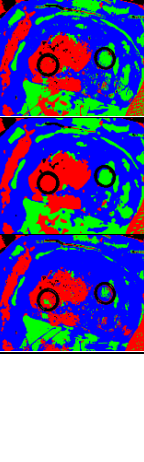

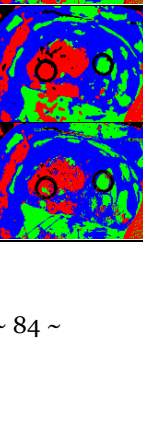
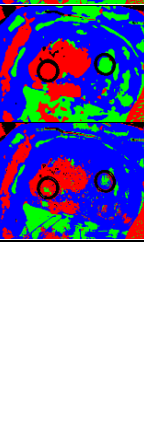

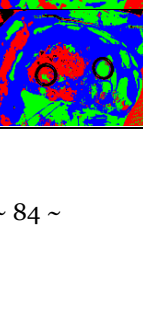
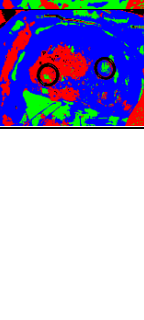

The results obtained at each step of the algorithm employing the CP128 and SP128 were qualitatively evaluated comparing the classification maps obtained in each step against a reference classification map (the results of CP129 in case of CP128 and the results of CP128 in case of SP128). For the purpose of finding the best data pre-processing chain, four HS images were employed (Op8C1, Op12C1, Op15C1 and Op20C1). As an example, **Table 6-1** presents the results obtained in the comparison between CP128 and SP128 against the reference pre-processing, CP129 and CP128, respectively for two images (Op20C1 and Op15C1). The results are presented in two different ways. On the one hand, the absolute difference between the results achieved with the reduced pre-processing chain is shown. This percentage of difference between the reference map and the optimized pre-processing map was calculated by subtracting the results of both classification maps. On the other hand, the difference results are presented as a binary map, where the pixels whose classification varies when the pre-processing chain is reduced appear in white. Pixels without any variation appear in black.

As it can be seen in the results, changing the pre-processing chain from CP129 to CP128 does not imply a relevant variation of the final results. Only Op15C1 presents a noticeable difference of ~17% between the reference and the optimized map. However, this difference is produced due to the pixel assignation between the tumor class and the hypervascularized class and between the normal class and the hypervascularized class. Although there are differences in this capture, the final result obtained by the TMD map identifies the tumor area correctly, highlighting the different boundaries in the tumor areas.

The final optimized pre-processing chain (SP128), where the HySIME filter and the brightness correction were removed, was compared with the CP128. The comparison between CP129 and CP128 was performed before determining that no relevant changes are presented in the results. Assuming this, the SP128 is only compared with the CP128. The main changes obtained in this optimization are shown also in the Op15C1, where especially the normal tissue area is mixed with the hypervascularized class. This fact could be produced due to the Op15C1 capture has a highly hypervascularization and the tumor was extremely advanced in the brain surface. The employment of this

optimized pre-processing chain drastically reduces the computational time required for the pre-processing, which is crucial to achieve real-time processing during a neurosurgical operation.

**Table 6-1: Pre-processing chains comparison**

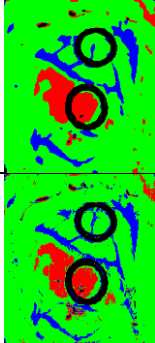
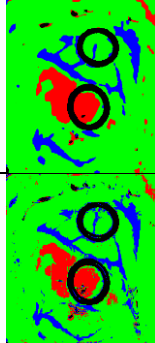

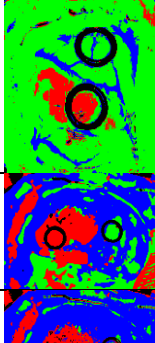
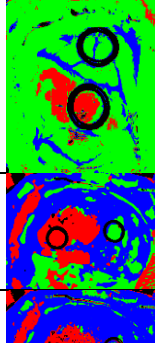
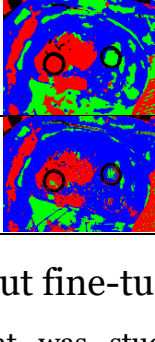
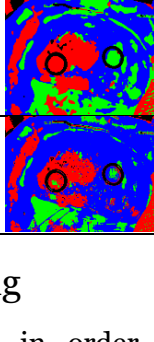
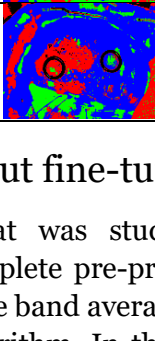
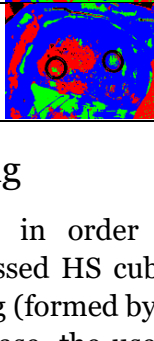
Pre- proc.	Reference Map	Capture ID	Map Type	Difference (%)	Reference Map	Optimized Map	Difference Binary Map
CP128	CP129	Op20C1	SVM	0.87			
			KNN	0.60			
			MV	1.09			
		Op15C1	SVM	2.56			
			KNN	2.33			
			MV	17.06			
SP128	CP128	Op20C1	SVM	2.33			
			KNN	1.53			
			MV	1.98			
		Op15C1	SVM	4.61			
			KNN	3.48			
			MV	14.19			

### 6.3.2 Dimensional reduction fine-tuning

The role of the dimensionality reduction approach in the proposed brain cancer detection algorithm is to generate a one-band representation of the HS cube to be used as input of the KNN filtering for the spatial homogenization of the SVM classification map. In order to reduce the computational time of the spatio-spectral stage of the algorithm, the use of PCA algorithm instead of FR-t-SNE was evaluated. Since PCA implies lower computational cost than t-SNE, the use of PCA could offer faster processing time results in the implementation of the final algorithm achieving thus real-time results during the neurosurgical procedure. In this section, the substitution of the FR-t-SNE algorithm by the PCA method is analyzed using the evaluation metrics employed in the previous section. Only KNN and MV maps were evaluated, as the change of the dimensional algorithm does not affect the SVM map.

In this case, the reference maps were generated by the algorithm using the FR-t-SNE dimensional reduction. As it can be seen in **Table 6-2**, the use of PCA barely affects the outputs of the algorithm and only Op20C1 is minimally affected in the majority-voting map. This fine-tuning in the brain cancer detection algorithm supposes a speedup in the processing time of the algorithm, which helps in the achievement of the real-time goal of the application without losing useful information for the neurosurgeon.

**Table 6-2: Dimensional reduction fine-tuning comparison**

Capture ID	Map Type	Difference (%)	Reference Map (using FR-t-SNE)	Optimized Map (using PCA)	Difference Binary Map
Op20C1	KNN	0.91			
	MV	0.21			
Op15C1	KNN	1.05			
	MV	0.00			

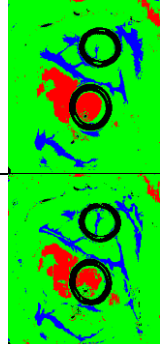
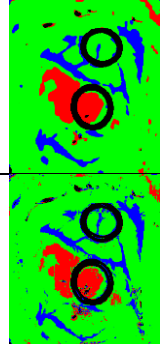

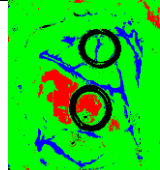
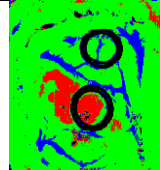
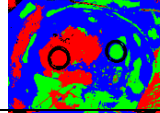
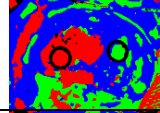
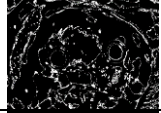
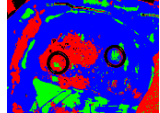
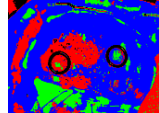
### 6.3.3 Dimensional reduction input fine-tuning

Another part of the algorithm that was studied in order to accelerate its implementation was the use of the complete pre-processed HS cube (formed by 128 bands) instead of the HS cube without the band averaging (formed by 750 bands) as the input of the dimensional reduction algorithm. In this case, the use of the same pre-processed HS cube for each step of the algorithm (PCA, SVM and HKM) allows simplifying the algorithm implementation to obtain better computational time results, providing also a partial noise reduction. As it will be explained later in Section 6.5, the implementation of the algorithm was partitioned into two platforms. The pre-

processing, the HKM and the MV algorithms were implemented onto the CU of the demonstrator, while the PCA, SVM and the KNN filtering were implemented onto the HA. The communication between the two platforms was carried out by using an Ethernet protocol. The optimization presented in this section was performed so as to avoid sending two different HS cubes from the CU to the HA, since this fact drastically increases the computational time required by the algorithm for processing the entire HS image. Using this optimization, the time total time execution is reduced approximately in a 20%.

**Table 6-3** shows the example of the comparison results of this optimization using the same metrics previously employed. The reference map was obtained using the HS cube without the band averaging applied for the input of the PCA algorithm and the complete pre-processed cube, using the SP128 pre-processing chain, for the input of the SVM and HKM algorithm. This map is compared with the optimized map, where the complete pre-processed HS cube was used as the input for the PCA, SVM and HKM algorithms. As it can be seen in the results, in the KNN maps there are some differences regarding to the borders of the different classes of the images. However, in the MV maps, where the KNN maps are merged with the segmentation maps, there are no relevant changes. By assuming these changes, the implementation of the algorithm will experiment a high acceleration, allowing the achievement of surgical real-time processing.

**Table 6-3: Dimensional reduction input fine-tuning comparison**

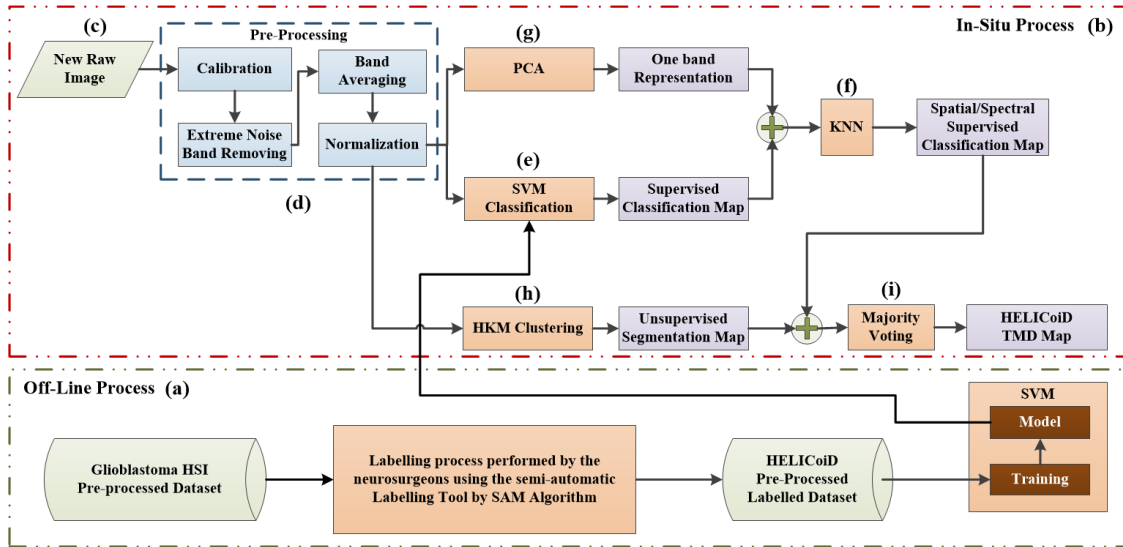
Capture ID	Map Type	Difference (%)	Reference Map (750 bands)	Optimized Map (128 bands)	Difference Binary Map
Op20C1	KNN Map	6.23			
	MV Map	3.65			
Op15C1	KNN Map	10.81			
	MV Map	0.00			



### 6.3.4 Fine-tuning for real-time processing summary

After performing the previously described modifications and fine-tuned optimizations for the real-time processing of the algorithms, the final brain cancer detection algorithm was simplified. **Figure 6-2** shows the block diagram of the final fine-tuned algorithm for real-time processing. The modifications performed were:

- 1) the simplification of the pre-processing chain;
- 2) the use of PCA instead of FR-t-SNE;
- 3) the use of the complete pre-processed HS cube as the PCA input.



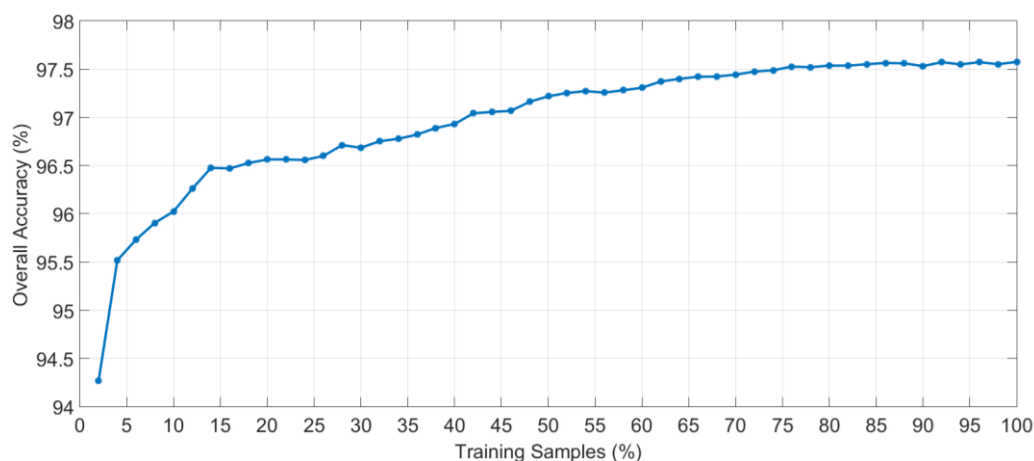
**Figure 6-2: Fine-tuned brain cancer detection algorithm for real-time processing.**

## 6.4 Fine-tuning for accurate classification results

After performing the fine-tuning of the brain cancer detection algorithm to optimize the computational time of the implementation, different SVM classifiers were trained employing different types and quantities of samples to evaluate the results in CS3. In addition, a study of the suitable number of samples that should be used to train the SVM algorithm was performed based on CS2.

### 6.4.1 SVM training samples percentage evaluation

In order to determine the suitable percentage of samples of the training database that should be used to train the supervised algorithm, several experiments to generate and evaluate the supervised model were carried out employing different number of training samples. Each experiment was performed following a 10-fold cross-validation method to calculate the average overall accuracy result in CS2. **Figure 6-3** shows the overall accuracy results varying the percentage of training samples with increments of 2%, starting at 2% and finishing at 100%. The evolution of the overall accuracy shows that when more than 75% of the training samples are used, the results stabilize, with overall accuracy of around 97.5%. With this experiment, it can be seen that there is no overfitting effect and the use of all the training samples will provide the best classification map.



**Figure 6-3: Overall accuracy evolution depending on the percentage of training samples employed to generate the supervised classification model of the HS brain cancer detection algorithm.**

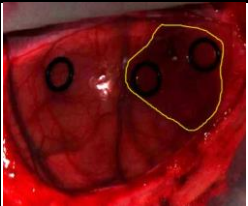
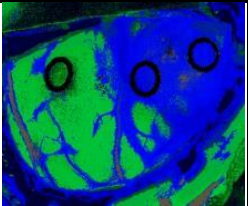
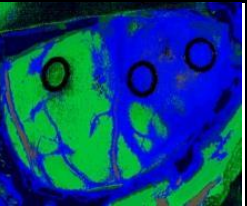
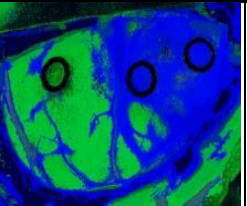
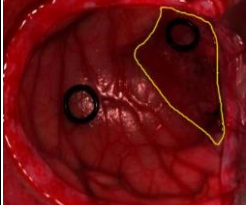
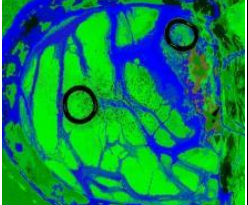
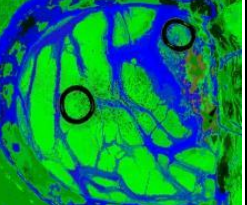
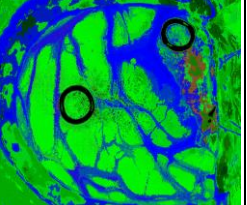

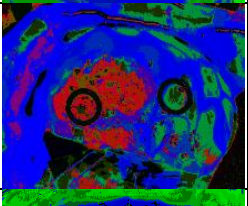
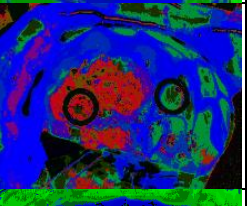
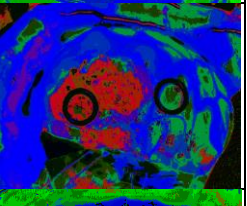
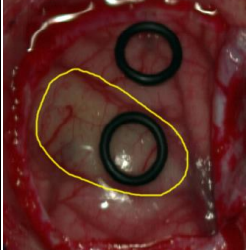
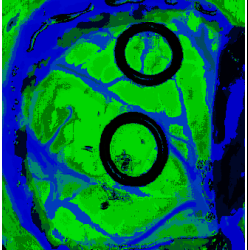
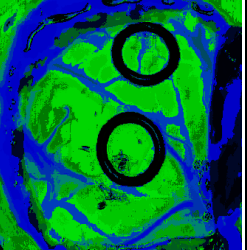
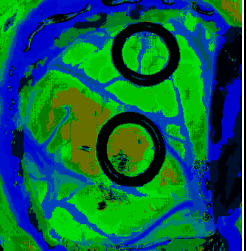
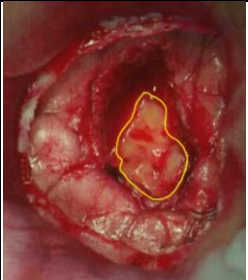
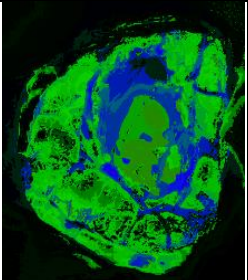
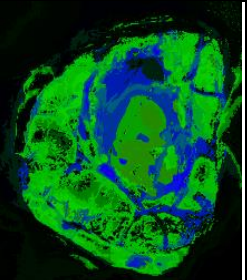
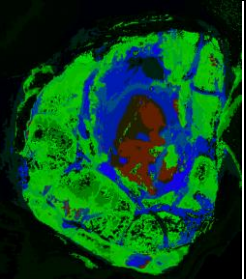
### 6.4.2 SVM model generation study

This section presents the results of the analysis performed to obtain a definitive model for the supervised classifier of the final brain cancer detection algorithm. Three different SVM models were generated based on the available number of labeled tumor samples in the HS database. In these SVM models, the entire labeled samples of normal tissue, blood vessels and background elements were employed for the training. Only the tumor samples vary in the learning process depending on the SVM model that is going to be generated. The proposed SVM models employed to determine their capabilities in identifying the tumor margins were the following:

- 1) The **SVM GBM model** was trained using exclusively the labeled samples belonging to grade IV GBM.
- 2) The **SVM Primary model** was created using only the labeled samples from Primary tumors.
- 3) The **SVM Brain Tumor model** was created using all the available captured images where both primary and secondary tumors were labeled.

These models were generated for each patient following the CS3 approach, where there are no samples from the patient who is going to be classified in the training dataset. **Table 6-4** shows the TMD maps obtained for the test images using each SVM model. In the synthetic RGB images, the areas where the tumor is located are delineated in yellow. As it can be seen in the results, Op8C1 does not offer good results employing any of the SVM models. This fact is mainly caused due to the bad quality of the captured image. The focus and illumination of the scene was not optimal during the acquisition process. On the other hand, the rest of the images offer promising results when the SVM brain tumor model (that employed all the tumor samples available in the database) is used. It is worth noting that Op15C1 always presents accurate results. This fact indicates that with a high number of tumor samples and more types of tumors, the system would be able to identify accurately the tumor boundaries of any kind of image. Furthermore, in the RGB representation of the Op20C1 is not possible to identify the tumor with the naked eye; however, the brain cancer detection algorithm can reveal the tumor area with high precision.

**Table 6-4: Comparison of the TMD maps obtained with each SVM model generated with a leave-one-patient-out cross-validation method.**

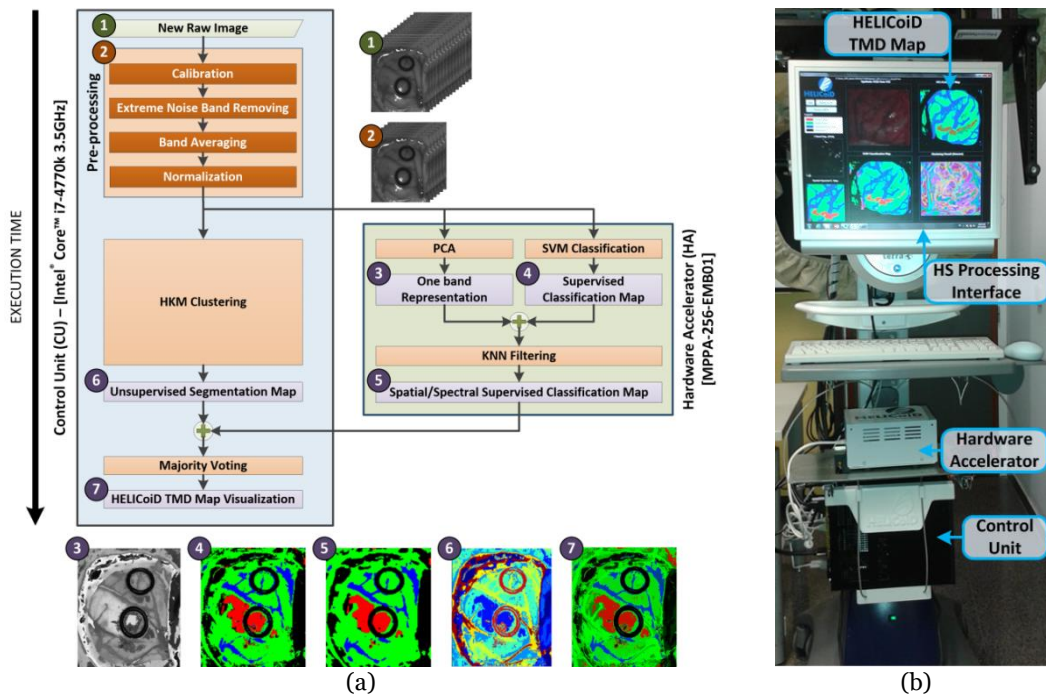
Cap. ID	sRGB Image	SVM GBM	SVM Primary	SVM Brain Tumor
Op8C1				
Op12C1				
Op15C1				
Op20C1				
Op25C2				

## 6.5 HS brain cancer algorithm implementation

This section briefly presents the overall description of the brain cancer algorithm implementation onto the intraoperative demonstrator. This algorithm can be divided into two main steps: the off-line process and the in situ process. The off-line process is the part of the algorithm in which the information previously provided by the experts in labeled samples is employed to train the supervised stage (SVM classifier) of the algorithm. On the other hand, the in situ process is carried out during surgery inside the operating theatre when a new HS image is acquired from the undergoing patient. This part of the algorithm is implemented and accelerated using the intraoperative HS demonstrator.

**Figure 6-4.a** depicts the different blocks of the HS brain cancer detection algorithm, as well as their distribution in the implementation onto both platforms and the execution scheduling. Furthermore, the RGB representation of the outputs obtained at each step of the algorithm is also shown. The blue block represents the steps of the algorithm that were mapped to the CU, while the green block represents the steps mapped to the HA. As can be observed, the pre-processing stage, the HKM clustering and the MV algorithm are executed on the CU. In contrast, the spatial–spectral supervised classification stage, where the PCA, the SVM classification, and the KNN filtering are performed, is executed on the HA due to its high computational load. The implementation of this algorithms have been reported in several publications [185]–[192].

The data flow sequence of the implementation follows the next steps. Firstly, the raw image is pre-processed on the CU and the resulting HS cube is sent to the HA through the Gigabit Ethernet interface, to be employed as the input of the PCA and SVM classification algorithms. The same HS cube is used in the CU as the input of the HKM clustering algorithm. Secondly, HKM clustering is executed on the CU, while the spatial–spectral supervised classification—PCA, SVM classification and KNN filtering—is executed on the HA. Both the unsupervised and the supervised stages are executed simultaneously. In addition, the PCA algorithm and the SVM classification are executed in parallel in the HA. Finally, once the previous stages are finalized, the MV algorithm is executed on the CU to compute the final TMD map. This TMD map is a RGB representation of the first three major probabilities per cluster obtained from the HKM clustering algorithm, where the brain tumor is marked in red. This image is shown to the user (the neurosurgeon) through the HS processing interface. **Figure 6-4.b** shows the different parts that comprise the intraoperative HS demonstrator in relation to HS data processing.



**Figure 6-4: Implementation of the HS brain cancer detection algorithm onto the intraoperative demonstrator.** (a) HS brain cancer detection algorithm implementation flow diagram and the RGB representation of the output of each step; (b) Different parts related to the HS data processing of the intraoperative demonstrator.



## 6.6 Intraoperative demonstrator validation

The validation of the final intraoperative demonstrator was performed during neurosurgical operations at the University Hospital Doctor Negrin of Las Palmas de Gran Canaria, employing the data of four different patients affected by different types of tumors. **Table 6-5** details the characteristics of the validation database used to test the developed HS brain cancer detection system and their corresponding pathological diagnosis. Seven images were included. These images involved normal brain tissue acquired during the first stage of the surgical operation, used to test if the system included false positives when no tumor as present in the image, and three different types of primary tumors.

**Table 6-5: Validation HS image dataset characteristics.**

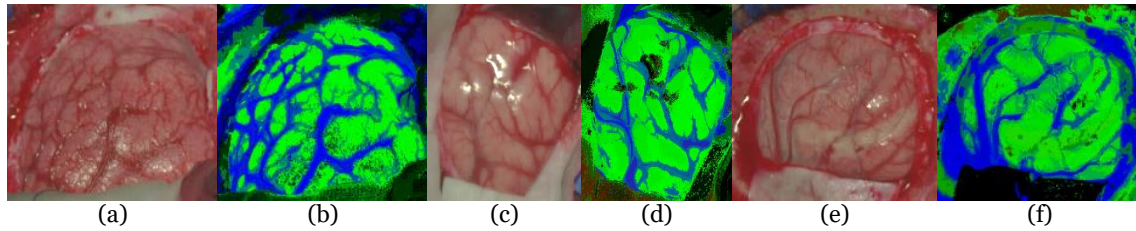
Image ID	Size (MB)	#Pixels	Dimension (Width × Height × Bands)	Pathological Diagnosis
Op35C1	362.62	224,770	495 × 456 × 826	Normal Brain
Op35C2	197.90	122,670	471 × 262 × 826	Primary Grade II Oligodendroglioma
Op36C1	225.35	139,682	332 × 423 × 826	Normal Brain
Op36C2	276.99	171,699	364 × 474 × 826	Primary GBM
Op37C1	402.26	249,344	513 × 488 × 826	Normal Brain
Op37C2	230.34	143,560	485 × 296 × 826	Primary GBM
Op38C1	372.47	230,878	480 × 483 × 826	Primary Grade I Meningioma

The TMD maps of the validation database obtained by the intraoperative demonstrator during the surgical operations and their respective synthetic RGB images are shown in **Figure 6-5** and **Figure 6-6**. The TMD maps are represented in four colors that can be mixed depending on the density of each class presented in the image.

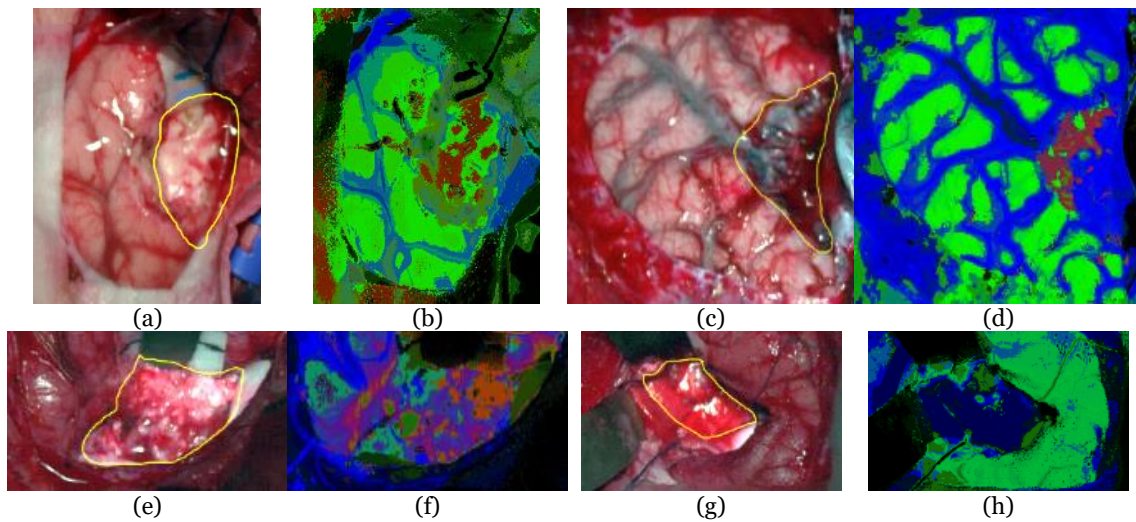
**Figure 6-5** shows the results obtained from the normal brain images. In these results, it can be seen that the system does not present any false positives in the parenchymal area, and normal tissue and blood vessels are clearly identified. Furthermore, bright pixels, which can be found in the images due to the light reflections over the arachnoid of the brain or due to the presence of surgical serum in the surface, are identified as background pixels. On the other hand, **Figure 6-6** shows the results obtained from the HS images of the brain surface affected by a tumor, where the tumor areas are surrounded with a yellow line in the synthetic RGB representations. These results offer a clear indication that the intraoperative demonstrator is able to identify the tumor tissue presented in the images. In **Figure 6-6.b**, there are some false positives in the bottom corner of the TMD map, however, this false information is located outside the area of exposed brain parenchyma and thus, it does not affect the neurosurgeon decisions during the tumor resection.

It is worth noting that two of the cases (**Figure 6-6.b** and **Figure 6-6.d**) identify two tumor types (grade II oligodendroglioma and grade I meningioma) for which there are no spectral signatures within the training database. These results highlight the robustness and the generalization capabilities of the intraoperative demonstrator to identify other types of tumor rather than only the ones available in the HS training database. Finally, it should be mentioned that the tumor identification becomes more difficult when the tumor is located deeper in the brain. **Figure 6-6.f** and **Figure 6-6.h** show the TMD maps of GBM tumors at an advanced stage of the surgical procedure. It

can be seen that, in case of **Figure 6-6.f**, the tumor tissue is clearly identified although it is located in a deep layer. However, in **Figure 6-6.h**, there is no correct identification of the tumor tissue due to problems with shadows and the presence of extravasated blood in the tumor area. Since HSI is not able to penetrate into the surface, extravasated blood present in the image is identified as a hypervascularized tissue class (blue color) in the TMD map.



**Figure 6-5: Normal brain image results obtained from the validation database employing the HELICoiD demonstrator.** (a) and (b) Synthetic RGB image and TMD map of the Op35C1 HS image; (c) and (d) Synthetic RGB image and TMD map of the Op36C1 HS image; (e) and (f) synthetic RGB image and TMD map of the Op37C1 HS image.



**Figure 6-6: Tumor tissue identification results obtained from the validation database employing the HELICoiD demonstrator.** (a) and (b) synthetic RGB image and TMD map of the Op36C2 HS image; (c) and (d) synthetic RGB image and TMD map of the Op38C1 HS image; (e) and (f) synthetic RGB image and TMD map of the Op35C2 HS image; (g) and (h) synthetic RGB image and TMD map of the Op37C2 HS image.

Finally, **Table 6-6** shows the execution times obtained using the intraoperative demonstrator to acquire and process the validation database during surgery. To assess the processing times obtained using the hardware acceleration in the spatial-spectral supervised classification stage, **Table 6-6** also shows the processing times obtained when the whole algorithm is implemented in the CPU, i.e., sequential time results. The total processing time required in the accelerated version is computed taking into account the maximum time obtained between the spatial-spectral supervised classification (PCA + SVM + KNN) and the unsupervised clustering (HKM). In summary, when the hardware accelerator is not employed, the spatial-spectral supervised classification is the most time-consuming stage. In contrast, an average speedup factor of  $24\times$  is achieved in the spatial-spectral supervised classification stage when the hardware accelerator is employed, becoming the unsupervised clustering the limiting factor in this case. These results show that the proposed system provides a

TMD map of the captured scene during the surgery in approximately 1 min, depending on the size of the captured image.

**Table 6-6: Execution time comparison between the sequential (Seq.) and accelerated (Acc.) implementations.**

Image ID	Processing Type	Acquisition Time (s)	Pre-Processing (s)	Transmission (s)	PCA + SVM (s)	KNN (s)	HKM (s)	MV (s)	Total Processing Time (s)
Op35C1	Seq.	19.98	15.07	0.00	11.32	378.87	39.68	0.009	444.95
	Acc.			14.00	6.02	8.16			68.76 *
	Speedup	N/A †	N/A †	0.00	1.88	46.45	N/A †	N/A †	6.47
Op35C2	Seq.	19.02	6.50	0.00	5.90	196.64	21.87	0.004	230.92
	Acc.			7.15	4.35	4.23			35.53 *
	Speedup	N/A †	N/A †	0.00	1.36	46.44	N/A †	N/A †	6.50
Op36C1	Seq.	13.40	9.35	0.00	6.72	158.66	24.96	0.005	199.70
	Acc.			8.07	4.48	3.48			42.38 *
	Speedup	N/A †	N/A †	0.00	1.50	45.62	N/A †	N/A †	4.71
Op36C2	Seq.	14.70	12.59	0.00	8.96	212.96	30.45	0.006	264.97
	Acc.			9.56	5.02	4.66			52.61 *
	Speedup	N/A †	N/A †	0.00	1.78	45.74	N/A †	N/A †	5.04
Op37C1	Seq.	20.71	19.72	0.00	13.68	434.96	44.57	0.008	512.93
	Acc.			13.34	6.72	9.44			77.63 *
	Speedup	N/A †	N/A †	0.00	2.03	46.10	N/A †	N/A †	6.61
Op37C2	Seq.	19.58	8.94	0.00	7.73	234.90	25.75	0.005	277.33
	Acc.			9.45	4.66	5.08			44.15 *
	Speedup	N/A †	N/A †	0.00	1.66	46.27	N/A †	N/A †	6.28
Op38C1	Seq.	19.38	13.84	0.00	11.49	377.60	41.59	0.007	444.52
	Acc.			12.36	6.29	8.15			67.79 *
	Speedup	N/A †	N/A †	0.00	1.83	46.34	N/A †	N/A †	6.56

\* The total time obtained in the accelerated version is computed taking into account the maximum time obtained between the spatial-spectral supervised classification and the unsupervised clustering.

† Measurement not available.

## 6.7 Conclusions

There is a clear trade-off between the complexity of the algorithm and its execution time. Some bottlenecks have been identified and evaluated in this chapter. For example, the type of pre-processing chain that is applied, or the dimensionality reduction technique that is used to guide the spatial homogenization of the final classification maps. Although there are some differences between the results obtained using the original algorithm compared to the results provided by the simplified version, the use of the fine-tuned algorithm provides accurate results in a reduced execution time. The tumor regions identified using both versions of the algorithm (original and fine-tuned) do not vary significantly.

In addition, different types of SVM models have been proposed, depending on which samples were employed to train the model. It should be taken into account that all the experiments carried out in the model study aims to evaluate the detection of tumor tissue in a CS3 scenario, what is a realistic situation where the models were trained using the samples acquired from previous patients. The capabilities of the algorithm to detect the tumor areas using samples from the undergoing patient have been proven in Chapter 5.

As a proof-of-concept, the intraoperative demonstrator developed in this work was able to generate thematic maps of the exposed brain surface during surgical operations using the fine-tuned HS brain cancer detection algorithm. The implementation of the

algorithm was partitioned between the control unit and a hardware accelerator, where the higher computational tasks were implemented in a many-core platform to achieve intraoperative processing time (~1 min). The demonstrator was validated using seven HS images obtained in four neurosurgical operations. The TMD maps obtained demonstrate that the system did not introduce false positives in the parenchymal area when no tumor was present and it was able to identify different types of tumor that were not present in the training database. Further investigations have to be carried out in order to enlarge the training database and the validation database with more patients and types of tumors. Moreover, an extensive clinical validation of the system must be carried out. In this clinical validation, a comprehensive pathological analysis of the entire tumor area outlined by the TMD map (especially in the boundaries between tumor and the surrounding normal tissue) must be performed as well as to correlate the results with the MRI information in order to know if the tumor infiltration into normal brain tissue can be properly identified by the system. Additionally, through clinical validation, the relation between the improvement of the patient outcomes and the use of the system during the surgery should be studied.



# Chapter 7: Improvement of the classification results using Deep Learning techniques

## 7.1 Introduction

In the previous chapters, the classification and delineation of the tumor boundaries using HSI and a customized brain cancer detection algorithm based on traditional machine learning algorithms were investigated. In Chapter 5, quantitative and qualitative HSI analysis were accomplished with the goal of delineating tumor boundaries and performing an intra-patient validation by employing both the spatial and spectral features of HSI. On the other hand, in Chapter 6, qualitative results were obtained intraoperatively by performing an inter-patient validation.

In the study presented in this chapter, the objective is to use deep learning algorithms to improve the classification results previously obtained and perform an exhaustive quantitative comparison between the different approaches. Furthermore, a novel deep learning framework is proposed and mixed with the current HS brain cancer detection algorithm to create a surgical aid visualization system capable of identifying and detecting the boundaries of brain tumors during surgical procedures using a manual tuning of the classification parameters. This tool could assist neurosurgeons in the task of identifying the cancer tissue during brain surgery using their criteria to select the optimal classification threshold.

This work has been carried out in a close collaboration with the research group of Prof. Baowei Fei at the Department of Bioengineering of the University of Texas at Dallas and it has been reported in [193].

## 7.2 Deep learning techniques

Two deep learning methods were employed in this experiment. On the one hand, a 2D convolutional neural network (2D-CNN) classifier, selected because of its ability to incorporate both spectral and spatial components for machine learning, was implemented in a batch-based training approach using TensorFlow on a Titan-XP NVIDIA GPU [194]. From each pixel of interest, an 11x11 pixel mini-patch was

constructed centered on the pixel of interest. The 2D-CNN was trained with a batch size of 12 patches, which were augmented to 96 patches during training by applying rotations and vertical mirroring to produce 8 times augmentation. The 2D-CNN architecture was based approximately on the AlexNet architecture [195]. This is a basic 2D-CNN architecture that was intentionally selected to test the ability of a standard CNN to solve the problem studied in this work. The details of the architecture are presented in **Table 7-1**. It consisted of three convolutional layers, one average pooling layer, and one fully-connected layer. Gradient optimization was applied to the AdaDelta optimizer with a learning rate of 1.0 and with 200 and 50 epochs for the training data in the binary and multiclass classification, respectively.

On the other hand, a deep neural network was implemented in TensorFlow on a NVIDIA Quadro K2200 GPU and was trained using only the spectral characteristics of the HS samples. This 1D-DNN was composed of two hidden layers with 28 and 40 nodes, respectively, using the rectified linear unit as activation function. The learning rate was established as 0.1 and the network was trained for 40 epochs of training data.

Cross-validation was performed in both algorithms using the leave-one-patient-out method and the stop criteria for each training epoch number was based on the stabilization of the accuracy to a maximum in the validation group. All parameters were maintained for each patient iteration. Furthermore, the training dataset was randomly balanced to the class with the minimum number of samples (the tumor class in this case).

**Table 7-1: Schematic of the proposed 2D-CNN architecture.** The input size is given in each row. The output size is the input size of the next row. All convolutions were performed with sigmoid activation and 40% dropout.

Layer	Kernel size / Remarks	Input Size
Conv.	3x3 / 'same'	11x11x128
Conv.	3x3 / 'same'	11x11x64
Conv.	3x3 / 'same'	11x11x92
Avg. Pool	3x3 / 'valid'	11x11x128
Linear	Flatten	9x9x128
Fully-Conn.	-	1x10368
Linear	Logits	1x1000
Softmax	Classifier	1x4

### 7.2.1 Proposed deep learning pipeline

The previously described deep learning methods were combined following the framework shown in **Figure 7-1**. This framework was developed with the goal of achieving high accuracy results with a reduced execution time. The proposed framework is formed by four main steps: blood vessel detection, parenchymal detection, image classification and morphological post-processing.

Firstly, three spectral channels are selected from the HS cube ( $\lambda_{42} = 591.10 \text{ nm}$ ,  $\lambda_{50} = 620.21 \text{ nm}$  and  $\lambda_{80} = 729.34 \text{ nm}$ ), where the subscript of each wavelength indicates the number of the spectral channel in the spectral signature. These spectral channels are linearly combined following Equation (10) to obtain a gray-scale representation ( $I$ ) of the HS cube where the blood vessels are highlighted (**Figure 7-2**). The selection of the most appropriate spectral channels and weights was performed empirically, evaluating the contrast of the image by visual inspection. The spectral channel  $\lambda_{42}$  was selected because it presents one of the absorption peaks of hemoglobin in the HS image dataset employed in the experiments. Previous works have shown that

the hemoglobin concentration absorption peak is normally found between 500 and 590 nm [196]–[198]. As it can be seen in **Figure 7-2**,  $\lambda_{42}$  shows a high contrast between the brain tissue and the blood vessels, but background (especially rubber ring markers) and the specular glare are indistinguishable with the blood vessels. In order to solve this, the spectral channel  $\lambda_{50}$  is included in the equation, since it provides a higher contrast between blood vessels and background. In addition, a reflectance peak of the hypervascularized tissue was found in the spectral channel  $\lambda_{80}$ , where differences between the brain tissue, background and the blood vessels are highlighted. As previously mentioned, these spectral channels were linearly combined, obtaining the gray-scale representation image used for the blood vessel and parenchymal area detection (**Figure 7-1.a**).

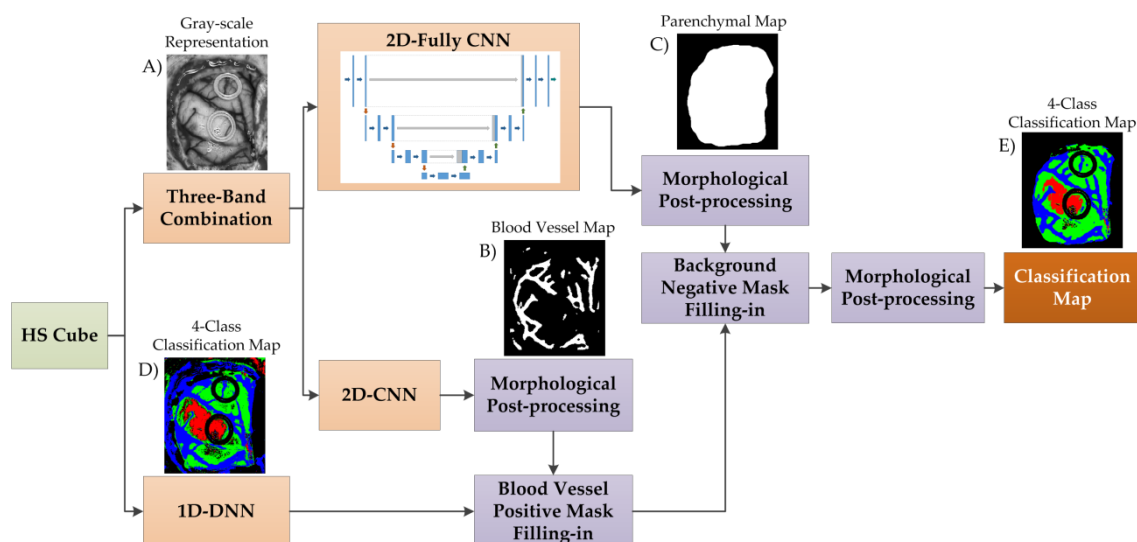
$$I = 0.7 * \lambda_{42} + 0.3 * \lambda_{50} + 0.8 * (1 - \lambda_{80}) \quad (10)$$

From this image, image patches of  $41 \times 41$  pixels were generated to be centered on the pixel of interest and were classified using the 2D-CNN structure previously presented to distinguish between two classes: blood vessels and background. A classification map (**Figure 7-1.b**) is obtained and optimized using a morphological close operation followed by a morphological open operation with disk structural element of 1 pixel in radius [199]. Similar results were obtained when using multi-band representations for this classification problem. However, the gray-scale representation was employed in this framework with the goal of achieving real-time processing.

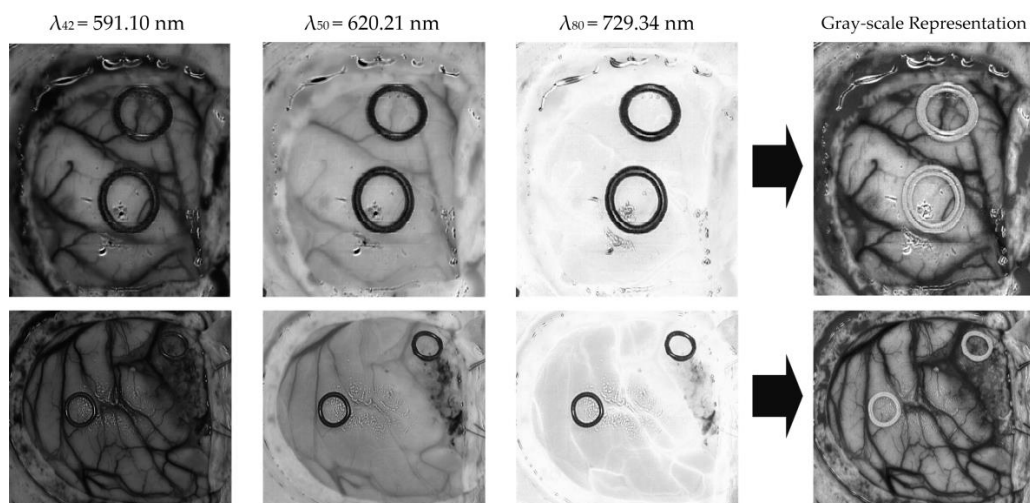
For identification of the parenchymal area, which corresponds to the primary surgical area of exposed brain, the gray-scale representation was used as input of a 2D fully-convolutional CNN. The fully-convolutional algorithm implemented was based on the U-Net architecture [200], which was trained for 34 epochs of training data on a manual segmentation of 20 images, which were augmented by a factor of 8 with rotations and reflections. The parenchymal map is obtained after applying a morphological close operation followed by a morphological open operation, with a disk structural element of 35 pixels in radius, and a hole filling operation (**Figure 7-1.c**). The final model was used to generate the parenchymal maps of 8 testing images, achieving a Dice similarity coefficient of 86.5% compared to a manual segmentation generated by the operating surgeon.

In the third step, the HS cube is classified by the 1D-DNN obtaining a 4-class classification map (**Figure 7-1.d**) where the preliminary classification of the normal tissue, tumor tissue, blood vessels/hypervascularized tissue and background is performed. Then, the blood vessel map is merged to the 1D-DNN classification map through a positive mask filling-in and this result is merged with the parenchymal map using a negative mask filling-in.

Finally, in the last step, a morphological open operation, with disk structural element of 1 pixel in radius, is performed to generate the final classification map (**Figure 7-1.e**).



**Figure 7-1: Block diagram of the proposed DL framework.**



**Figure 7-2: Gray-scale representation image examples and the correspondent three selected spectral channels employed in the three-band combination for the parenchymal and blood vessel detection.**

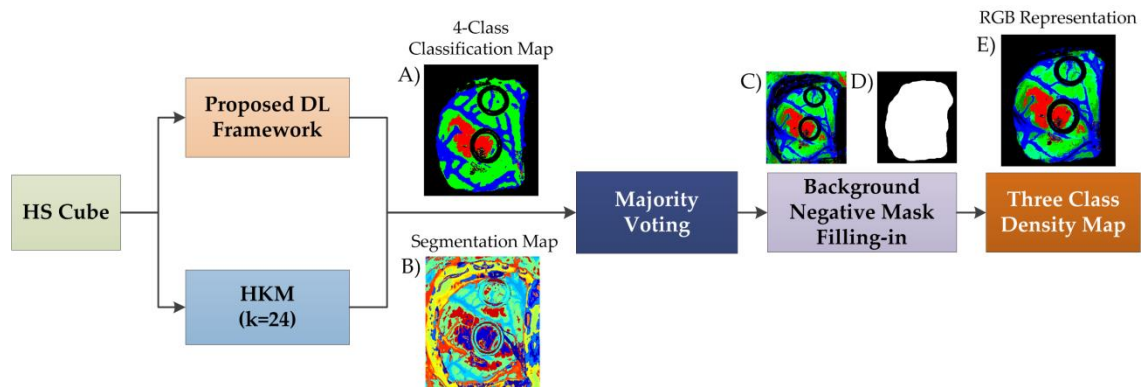
### 7.2.2 DL surgical aid visualization system

To evaluate the results obtained by the previously presented supervised classification framework, a surgical aid visualization system was developed using the MATLAB® GUIDE program. In this software, the classification map obtained by the 1D-DNN can be optimized by adjusting the threshold (operating point) where each pixel is assigned to a certain class depending on the probability values obtained for each class. Three threshold sliders were used in the visualization system, which offer the possibility to adjust and overlap the DNN classification results for the tumor, normal and hypervascularized classes, following the same priority order to overlap the layers.

In this surgical aid visualization system, a processing pipeline based on the proposed DL framework was implemented (**Figure 7-3**). This pipeline is able to generate a density map where the three classes (normal, tumor, and hypervascularized tissue) are represented in gradient colors using the classification map of the DL pipeline and an unsupervised segmentation map generated by a clustering algorithm. Concretely, the

HS cube is processed by the DL pipeline and a hierarchical K-Means (HKM) algorithm, which generate a 4-class classification map (**Figure 7-3.a**) and an unsupervised segmentation map of 24 clusters (**Figure 7-3.b**), respectively. Both maps are merged using a majority voting (MV) algorithm, *i.e.*, all pixels of each cluster on the segmentation map are assigned to the most frequent class in the same region of the classification map [146]. At this point, a new classification map is obtained where the classes are determined by the DL pipeline, and the boundaries of the class regions are determined by the HKM map. In addition, a 3-class probability cube is formed by using the probability values of each class in each cluster, where the first, second and third layers represent the probabilities for the tumor, normal, and hypervascularized classes, respectively. The background class is disregarded when performing the gradient representation of the colors since it will be always represented in black color.

Finally, the 3-class probability cube is used to generate the RGB density map where each pixel color value (red, green, and blue) is proportionally degraded using the probability values of each layer (**Figure 7-3.c**). The parenchymal map (**Figure 7-3.d**) obtained in the DL pipeline is also used at this point to identify exclusively the classification results obtained in the parenchymal area through a negative mask filling-in method, obtaining the final three class density map (**Figure 7-3.e**). The algorithm for generating the three-class density map was previously reported [146]. However, this paper uses the DL architecture instead of the supervised spatial-spectral classifier (PCA, SVM and KNN filtering pipeline) as well as the addition of the parenchymal detection.



**Figure 7-3: Block diagram of the proposed surgical aid visualization algorithm to generate the three class density map.** A hierarchical K-Means (HKM) algorithm and the proposed DL framework were used to generate the maps for majority voting algorithm.

### 7.3 Quantitative evaluation

The validation of the proposed algorithm was performed using inter-patient classification (CS3), *i.e.*, training on a group of patient samples that includes all the patients except the samples of the patient to be tested (leave-one-out cross-validation). Overall accuracy, sensitivity and specificity metrics were calculated to measure the performance of the different approaches. These metrics were already defined in Section 5.3 of Chapter 5. In addition, the receiver operating characteristic (ROC) curve was used to obtain the optimal operating point, where the classification offers the best

performance for each patient image, and provide the area under the curve (AUC) metric in the results.

To compute all performance metrics, a bootstrapping method was employed to produce the evaluation metrics with class-balancing and a confidence range. In this method, the class with the lowest number of samples in the test HS image is identified. Next, this number of samples is randomly selected with replacement from all remaining classes, and the performance metrics are computed. This procedure is repeated 1000 times, reporting the average value and the 2.5 and 97.5 percentiles to produce the 95% confidence interval. This method was used for each iteration of the leave-one-patient-out cross-validation for the binary mode (tumor and normal samples) and multiclass mode (four classes available in the HSI dataset). The class balancing was necessary to be performed so that all classes contribute equally to the final metric (AUC, accuracy, sensitivity, or specificity), in order to remove bias from the experiment since the classes were not originally balanced. **Table 7-2** shows the summary of the labeled testing data employed for the quantitative and qualitative evaluation of the algorithms. In addition, using the classification models generated for each test patient, the classification of the entire HS image was performed to evaluate the results qualitatively. In this study, the classification and visualization systems were evaluated in eight HS images obtained from six GBM patients. The gold standard map of each image was composed by labeled pixels of the four classes (normal, tumor, hypervascularized and background), allowing the correct computation of the evaluation metrics for each test image performing a leave-one-out cross-validation.

**Table 7-2: Summary of the test dataset employed for the quantitative evaluation.**

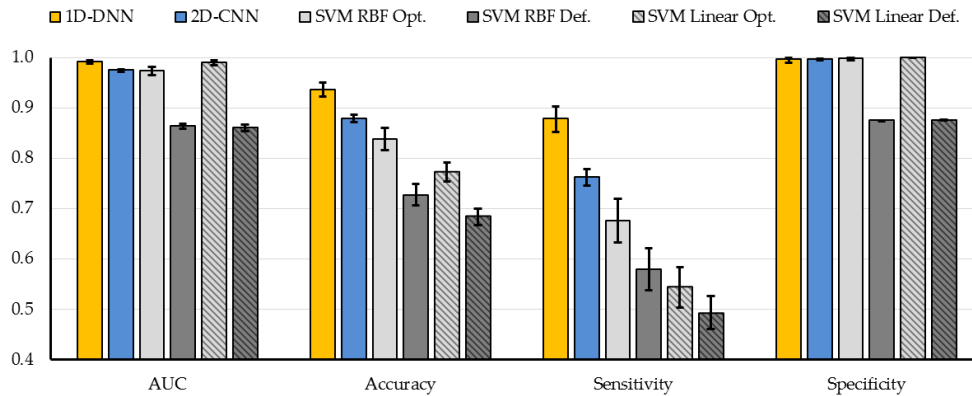
Patient ID	Image ID	#Labeled Pixels			
		NT	TT	HT	BG
8	1	2,295	1,221	1,331	630
	2	2,187	138	1,000	7,444
12	1	4,516	855	8,697	1,685
	2	6,553	3,139	6,041	8,731
15	1	1,2 <sup>o</sup> 51	2,046	4,089	696
16	4	1,178	96	1,064	956
17	1	1,328	179	68	3,069
20	1	1,842	3,655	1,513	2,625
<b>Total</b>	<b>8</b>	<b>21,150</b>	<b>11,329</b>	<b>23,803</b>	<b>25,836</b>

‡ (NT) Normal tissue; (TT) Tumor tissue; (HT) Hypervascularized tissue; (BG) Background.

In order to evaluate the deep learning methods against traditional SVM-based machine learning algorithms, a binary classification, where only the tumor and normal samples of the database were employed, was performed. Different configurations of the SVM classifier were tested using a binary dataset (tumor vs. normal tissue) to compare the performance of the algorithms. Linear and radial basis function (RBF) kernels, with the default and optimized hyperparameters, were studied in the binary classification. An exhaustive analysis to find the optimal hyperparameters for both kernels was accomplished, performing a parameter sweep selecting the value that achieved maximum accuracy. Both kernels have a common parameter called *cost* ( $C$ ). This parameter is the constant of constraint violation that observes if a data sample is classified on the wrong side of the decision limit. The optimal cost value for the both kernels was  $C = 2^6$ . In addition, RBF kernel has another specific hyperparameter that is the width of the Gaussian radial basis function, which can be adjusted by the parameter gamma ( $\gamma$ ). The optimal pair of values (cost and gamma) for RBF was obtained using a

grid search method [201], achieving the maximum accuracy with  $C = 2^6$  and  $\gamma = 2^1$ . The LIBSVM package was employed for the SVM implementation [165].

**Figure 7-4** shows the average classification results obtained with the six different classification approaches. AUC, overall accuracy, sensitivity and specificity metrics and their respective 95% confidence interval were computed using the bootstrapping method (see **Table 7-3**). The deep learning methods improve the accuracy and the sensitivity compared to the traditional SVM-based machine learning techniques. Particularly, the 1D-DNN achieved the best results, obtaining 94% accuracy, 88% sensitivity, and an AUC of 0.99. Compared to the best SVM-based method, an improvement of 6% in the accuracy is achieved.



**Figure 7-4: Average results of the leave-one-out cross-validation of the binary dataset obtained for each classification approach using the class-balancing and bootstrapping method with the 95% confidence interval.**

**Table 7-3: Average results of the leave-one-out cross-validation of the binary dataset obtained for each classification approach using the bootstrapping method with the 95% confidence interval.**

Method	Average [95% Confidence Interval]			
	AUC	Accuracy	Sensitivity	Specificity
<b>1D-DNN</b>	0.99 [0.99, 0.99]	0.94 [0.94, 0.94]	0.88 [0.88, 0.88]	1.00 [1.00, 1.00]
<b>2D-CNN</b>	0.97 [0.97, 0.97]	0.88 [0.88, 0.88]	0.76 [0.76, 0.76]	1.00 [1.00, 1.00]
<b>SVM RBF Opt.</b>	0.97 [0.97, 0.97]	0.84 [0.84, 0.84]	0.68 [0.68, 0.68]	1.00 [1.00, 1.00]
<b>SVM RBF Def.</b>	0.86 [0.86, 0.86]	0.73 [0.73, 0.73]	0.58 [0.58, 0.58]	0.88 [0.88, 0.88]
<b>SVM Linear Opt.</b>	0.99 [0.99, 0.99]	0.77 [0.77, 0.77]	0.54 [0.54, 0.54]	1.00 [1.00, 1.00]
<b>SVM Linear Def.</b>	0.86 [0.86, 0.86]	0.68 [0.68, 0.68]	0.49 [0.49, 0.49]	0.88 [0.88, 0.88]

However, when the four-class dataset is used, the results obtained by both DL techniques are quite similar. **Figure 7-5** and **Table 7-4** and **Table 7-5** show the average classification results of the multiclass classification with the 95% confidence interval. In this case, the overall accuracy obtained with the 2D-CNN and the 1D-DNN are similar to the traditional SVM-based approaches; however, the sensitivity of the tumor class has been improved by ~16% when using the DL approaches. In this particular case of in-vivo tissue, it is a challenging task to achieve a high sensitivity in the tumor class.

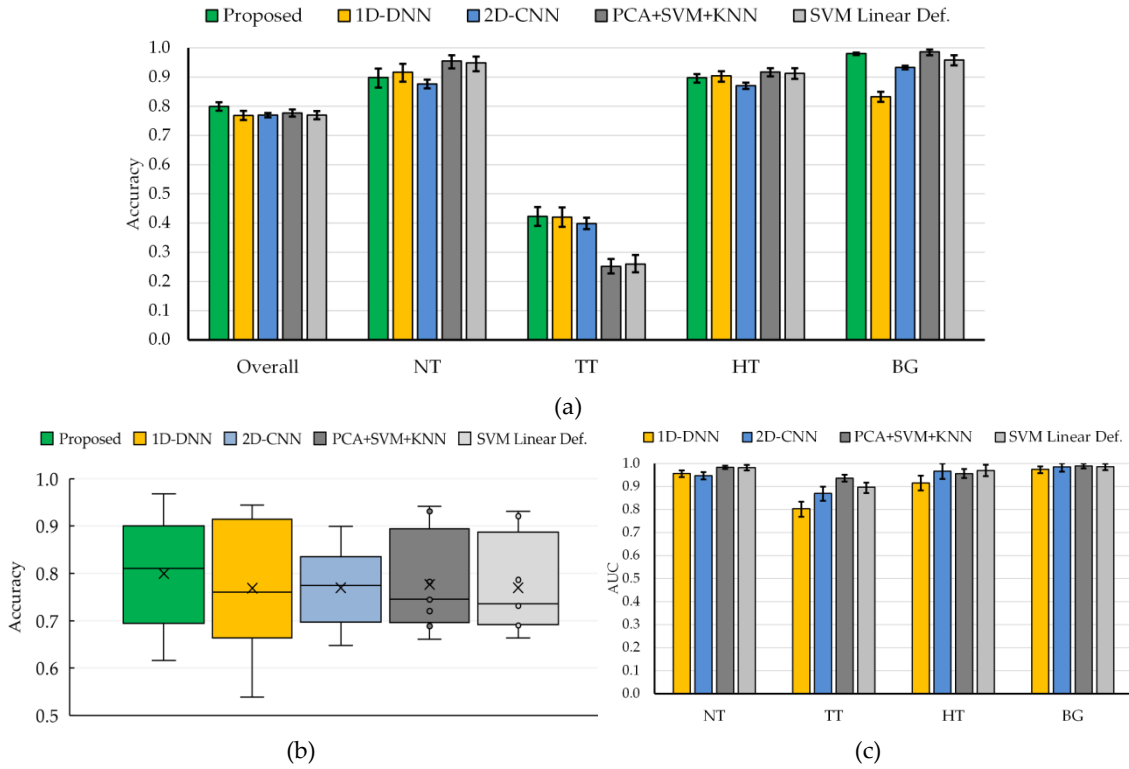
In order to combine the strengths of both DL techniques, the proposed deep learning framework presented in Section 2.4 was evaluated. Since the main goal of this



study is to provide real-time classification during neurosurgical procedures, the development of a fast execution algorithm is critical. As seen in Table S2, the 2D-CNN offers similar results than the 1D-DNN (77% of overall accuracy). However, the required time to transfer and process the HS data by the 2D-CNN (image patches from each pixel with a dimension of  $11 \times 11 \times 128$ ) is significantly greater than the time required by the 1D-DNN, since the 1D-DNN only exploits the spectral information of the HS cube (pixel-based approach where each pixel has a dimension of  $1 \times 128$ ). Therefore, in the proposed framework we use the 1D-DNN as the main classifier, including the 2D-CNN to detect the blood vessels in a gray-scale representation of the HS cube, using image patches from each pixel with a dimension of  $41 \times 41$ . Furthermore, another 2D-Fully-CNN is used to detect the parenchymal area of the exposed brain employing the full gray-scale representation image. These intermediate CNN classification maps take into account the spatial information required to homogenized and reduce the false positives in the multiclass classification result obtained by the 1D-DNN (**Figure 7-1**).

In this sense, the proposed framework achieves an overall accuracy of 80%. AUC metrics cannot be obtained for this algorithm since the optimization process (mixing the blood vessel and parenchymal maps with the 1D-DNN classification map) is performed over the classification map, and the probability map cannot be obtained to compute the AUC. **Figure 7-5.a** shows the average overall accuracy and accuracy per class results obtained by each algorithm, and **Figure 7-5.b** presents the boxplot of the overall accuracy results. Although the results obtained are quite similar, it is possible to observe that the proposed framework offers a better generalization in the results, increasing the overall accuracy of the system. Although the tumor sensitivity results obtained in this work need to be further improved, this study shows that DL techniques perform better than the traditional SVM-based algorithms.

For the binary classification scheme, the advantage in performance from the DNN compared to all SVM-based algorithms was found to be strongly statistically significant ( $0.01 < p < 0.03$ ), using a paired, one-tailed Student's T-test. This relationship was not found for the CNN compared to all SVM-based algorithms, despite the increase in average performance. Therefore, the method proposed in the paper used the DNN approach. Moreover, the difference in performance between the DNN and CNN was not found to be statistically significant. Additionally, for the multiclass classification scheme, the performance advantage from the proposed algorithm was found to be marginally statistically significant compared to the DNN alone, PCA+SVM+KNN, and SVM approaches ( $0.08 < p < 0.09$ ), using a paired, one-tailed Student's T-test.



**Figure 7-5: Average results of the leave-one-out cross-validation of the four-class dataset obtained for each classification approach using the class-balancing and bootstrapping method with the 95% confidence interval. (a) Overall accuracy and accuracy per class results. (b) Boxplot of the overall accuracy results. (c) AUC results per class. [NT] Normal tissue; [TT] Tumor tissue; [HT] Hypervascularized tissue; [BG] Background.**

**Table 7-4: Average accuracy results of the leave-one-out cross-validation of the four-class dataset obtained for each classification approach using the bootstrapping method with the 95% confidence interval.**

Method	Average Accuracy [95% Confidence Interval]				
	Overall	Normal	Tumor	Hypervascularized	Background
<b>Proposed</b>	0.80 [0.78, 0.81]	0.90 [0.86, 0.93]	0.42 [0.39, 0.45]	0.90 [0.92, 0.89]	0.98 [0.98, 0.98]
<b>1D-DNN</b>	0.77 [0.75, 0.78]	0.92 [0.88, 0.95]	0.42 [0.39, 0.45]	0.90 [0.92, 0.89]	0.83 [0.82, 0.85]
<b>2D-CNN</b>	0.77 [0.76, 0.78]	0.88 [0.86, 0.89]	0.40 [0.38, 0.42]	0.87 [0.88, 0.86]	0.93 [0.93, 0.94]
<b>PCA+SVM+KNN</b>	0.78 [0.76, 0.79]	0.96 [0.93, 0.97]	0.25 [0.23, 0.28]	0.92 [0.93, 0.90]	0.99 [0.97, 0.99]
<b>SVM Linear Def.</b>	0.77 [0.76, 0.78]	0.95 [0.92, 0.97]	0.26 [0.23, 0.29]	0.91 [0.93, 0.90]	0.96 [0.94, 0.97]

**Table 7-5: Average AUC results of the leave-one-out cross-validation of the four-class dataset obtained for each classification approach using the bootstrapping method with the 95% confidence interval.**

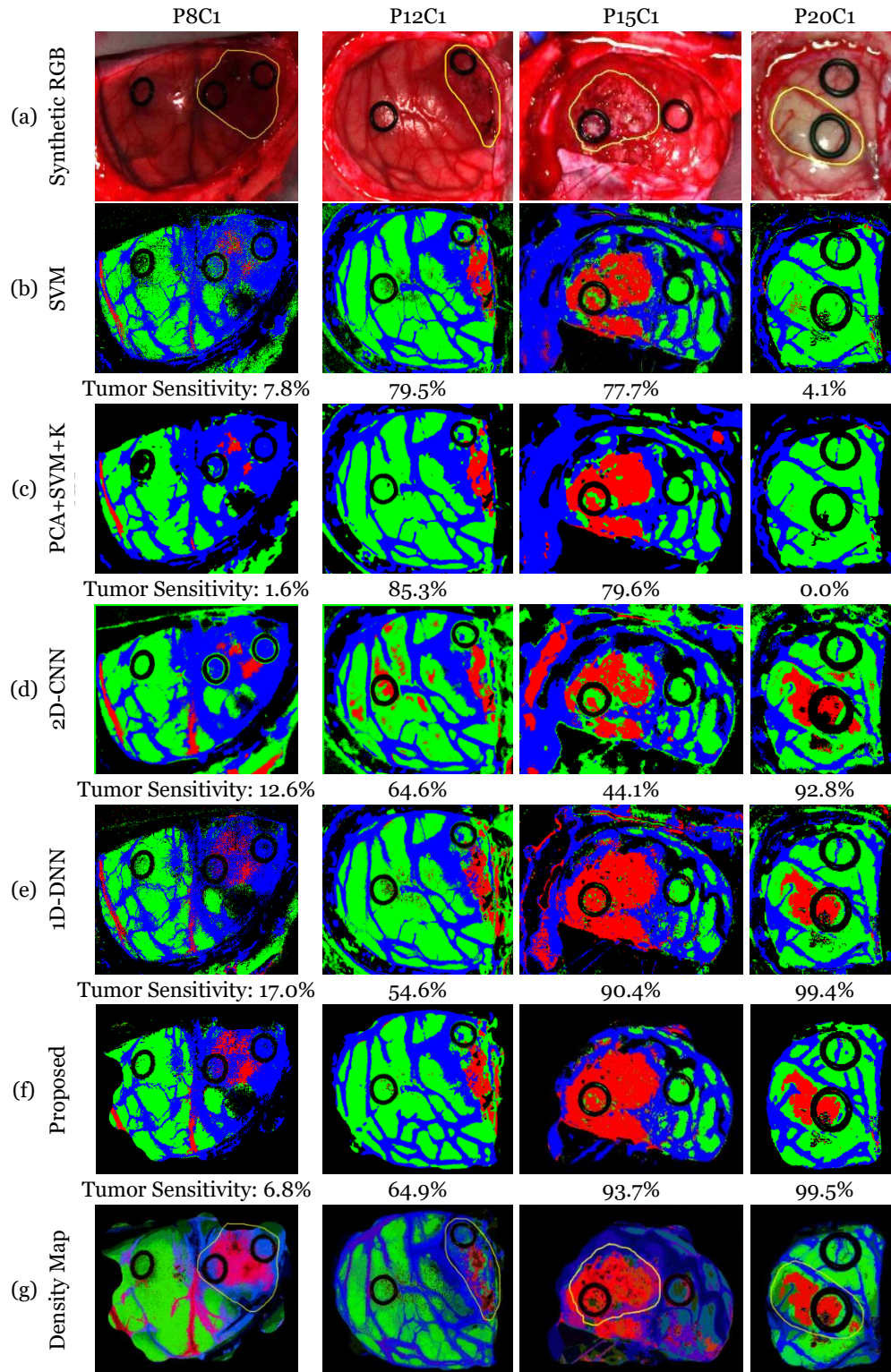
Method	Average AUC [95% Confidence Interval]			
	Normal	Tumor	Hypervascularized	Background
<b>1D-DNN</b>	0.96 [0.95, 0.96]	0.80 [0.78, 0.83]	0.92 [0.91, 0.92]	0.97 [0.97, 0.98]
<b>2D-CNN</b>	0.95 [0.94, 0.95]	0.87 [0.86, 0.88]	0.97 [0.96, 0.97]	0.98 [0.98, 0.99]
<b>PCA+SVM+KNN</b>	0.98 [0.98, 0.99]	0.94 [0.92, 0.95]	0.96 [0.95, 0.96]	0.99 [0.98, 0.99]
<b>SVM Linear Def.</b>	0.98 [0.98, 0.99]	0.90 [0.88, 0.92]	0.97 [0.96, 0.97]	0.99 [0.98, 0.99]

## 7.4 Qualitative evaluation

Although the tumor sensitivity results obtained in this work need to be further improved, this study shows that DL techniques perform better than the traditional SVM-based algorithms. **Figure 7-6** shows the classification maps and their respective tumor sensitivity results (below each map) obtained for four test images, which demonstrate that the DL methods significantly improve the results of Patient 20 (P20C1). Furthermore, the results of Patient 8 (P8C1) demonstrate that the proposed DL pipeline (**Figure 7-6.f**) offers the best results in the detection of the tumor tissue. It is worth noticing that this image was captured under non-optimal illumination conditions, introducing substantial noise in the HS cube. For this reason, the detection of the parenchymal area in this image was not successfully achieved, and the classification results include some false positives (mainly misclassifying blood vessels with the tumor class). These results were qualitatively evaluated by the operating surgeons, who outlined in yellow the approximate tumor area (over the synthetic RGB representation, **Figure 7-6.a**) taking into account the information provided by the intraoperative MRI and their knowledge and experience in the field. The results obtained with the proposed framework are quite promising, especially in Patient 20, where the location of the tumor was extremely difficult to identify using only the naked eye.

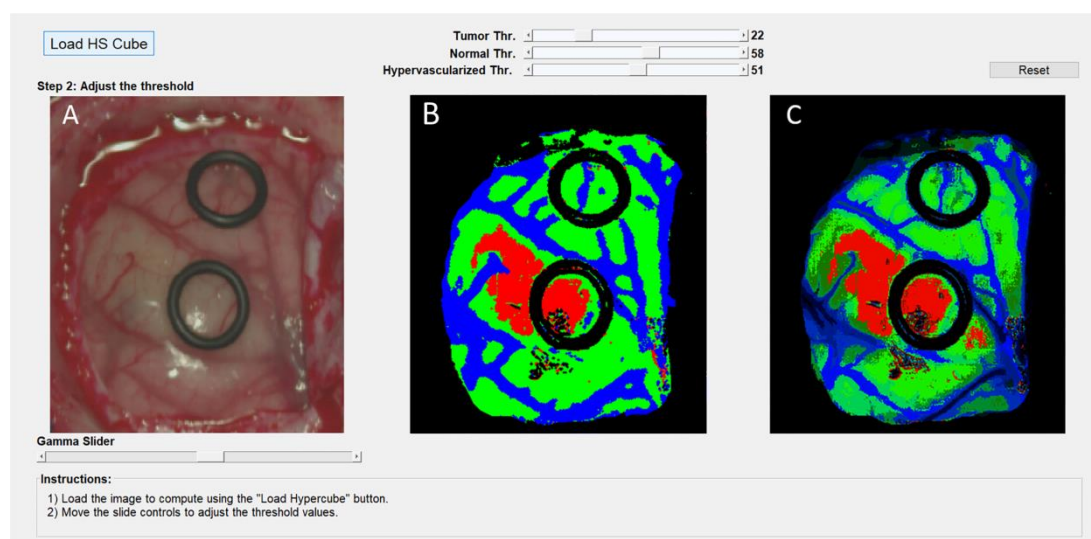
Finally, the ROC curves obtained in the basic approaches (**Figure 7-5.c** and **Table 7-5**) show that each class has an optimal operating point where the algorithm is able to classify the samples with high accuracy. In this sense, the development of a surgical aid visualization system is based on the use of the optimal operating point to generate the density maps. **Figure 7-6.g** shows the density maps of each test image obtained with the proposed surgical aid visualization algorithm (**Figure 7-3**), where the optimal operating point was employed to classify each pixel. In these maps, the colors of each class were degraded depending on the probability values obtained for each class in each cluster. Hence, it is possible to reveal, in some cases, tumor areas that cannot be seen directly in the classification map, as well as remove some false positives produced in the supervised classification.

As it can be seen in these results, the predicted tumor area overlaps well with the gold standard cancer area (yellow contour in **Figure 7-6.a**). The ability to accurately localize the cancer area can also be seen in the high average AUC values for the tumor class ranging from 0.80 to 0.94 for the algorithms tested in this work. The reason for the low sensitivities is the large optimal threshold differences between the test patients, partially due to the lower number of tumor samples in the training set. Additionally, the gold standard used for obtaining the quantitative results did not comprise the entire tumor area. Only pixels with high certainty of class membership were selected, which could have also contributed to the low sensitivity results that do not accurately reflect the efficacy of the proposed method. However, to solve this problem in the proposed surgical aid visualization interface, the operating surgeon can visualize multiple thresholds to determine the sufficient operating point for the cancer detection.



**Figure 7-6: Classification maps of four of the test HS images and their respective tumor accuracy below each map.** (a) Synthetic RGB image with the tumor area surrounded by the yellow lines; (b), (c), (d), (e) and (f) Multiclass classification maps obtained with the SVM, PCA+SVM+KNN, 2D-CNN, 1D-DNN and the proposed pipeline, respectively. Normal, tumor, and hypervascularized tissue are represented in green, red and blue colors, respectively, while the background is represented in black color; (g) Density maps generated using the surgical aid visualization algorithm with the optimal threshold established for the tumor class. In these maps the colors have been adjusted depending on the probability values obtained after the majority voting algorithm.

Since the automatic computation of the optimal operating point cannot be performed during the surgical procedures due to the absence of a gold standard of the undergoing patient, the surgical aid visualization system was developed based on manual selection of this operating point. Using the developed user interface (**Figure 7-7**), the operating surgeon is able to easily determine the optimal result on the density map (**Figure 7-7.c**) by manually adjusting the threshold values of the tumor, normal, and hypervascularized classes. These threshold values establish the minimum probability where the pixel must correspond to a certain class in the classification map generated by the 1D-DNN (**Figure 7-7.b**). After that, the overlapping and the majority-voting algorithms are computed to generate the updated density map. This user interface combines the information provided by the HSI processing and the expertise and knowledge of the operating surgeon.



**Figure 7-7: Surgical aid visualization with manual adjustable threshold values.** (a) Synthetic RGB image generated from the HSI cube; (b) 1D-DNN classification map generated with the established threshold; (c) Density map generated with the new classification map.

## 7.5 Conclusions

The work presented in this chapter employs deep learning techniques for the detection of in-vivo brain tumors using intraoperative hyperspectral imaging. Classification methods using 1D-CNN have been demonstrated to have a high accuracy for binary cancer detection in HS images. However, our investigations reveal that both spectral-spatial classification with 2D-CNN and pixel-wise classification with 1D-DNN perform well within no significant difference in accuracy using a multiclass dataset. We believe that the high spectral resolution of the HS cameras used in this study allows the 1D-DNN to perform with comparable accuracy to CNN methods. Additionally, the limited spatial resolution of the push-broom cameras (compared with other spectral-scanning HS cameras that provide higher spatial resolution) may also reduce the performance of CNN methods.

In addition, a novel classification framework based on a supervised DL pipeline combined with an unsupervised classification stage has been proposed. This framework was integrated in a user interface with the goal of intraoperatively assisting

neurosurgeons during tumor resection, allowing the fine-tuning of the outcome of the algorithm. With the goal of achieving surgical-time results in the operating room and taking into account that both DL methods obtain similar results, the proposed framework uses a DNN for classification because the CNN requires more execution time (~1 minute per HS cube) compared to the DNN (~10 seconds per HS cube).

Moreover, an overall average accuracy of 80% for the proposed method was achieved. Since the training dataset had approximately half of the number of samples in the tumor class compared to other classes, the number of samples for each class was balanced. This reduced the total number of training samples. Additionally, several images were out of focus, not fully illuminated, or presented artifacts due to brain movement during scanning, so the number of high-quality tumor training samples was also limited. In this sense, more data collection with more emphasis on collecting high-quality tumor samples could help to balance the dataset and produce better training paradigms for the proposed algorithm, which could potentially lead to better results.

In addition, this data increment in the *in-vivo* HS human brain database could allow further experiments, where the possibility of employing a reduced pre-processing chain, which only involves the image calibration and normalization, could be evaluated. In this way, it may be possible that more advanced deep learning approaches could learn how to filter out the noise in the spectral signatures, which could lead to an improvement of the sensitivity of the classification results.

The results of this preliminary study show that deep learning outperforms traditional machine learning techniques in the classification of hyperspectral tumor samples, although further experiments need to be conducted to optimize the deep learning algorithms. It is worth noticing that our proposed approach achieves very high specificity for both binary and multiclass classification schemes, obtaining 100% and ~90%, respectively. These results demonstrate the ability of the proposed approach to achieve high confidence in the correct detection of non-tumor areas, which is ideal in the design of a surgical aid visualization system. In any case, further experiment should be performed to evaluate the ability of the proposed framework to reduce surgical resection margins, employing much more patient data and a multi-centered trial. However, the outcomes achieved in this preliminary work demonstrate the feasibility of using hyperspectral imaging as a promising tool for brain surgical guidance.





# Chapter 8: Conclusions & Future Lines

## 8.1 Conclusions

Since brain tumors are extremely infiltrative, the task of identifying the boundary between the tumor tissue and the normal tissue that surrounds it during a neurosurgical operation is extremely difficult for neurosurgeons by only using the naked eye. The identification of tumor boundaries and tumor infiltration into normal brain tissue is extremely important in order to avoid excessive resection of normal brain tissue and to avoid unintentionally leaving behind residual tumor. The current tools employed to this end have presented many limitations to assist in the delineation of the tumor boundaries. MRI-based neuronavigation accuracy is affected by the brain shift during resection and depends on a questionable correlation between the extent of enhancement on MRI and cellular infiltration. Other techniques, like 5-ALA fluorescence, do not work in low-grade lesions in addition to be highly invasive and not recommended for use in children. For these reasons, there is a real need to develop new techniques for tumor margin delineation in real-time, maximizing the resection of the tumor and minimizing the resection of the adjacent normal brain. In this sense, HSI offers a new possibility to address these issues, being a non-contact, non-ionizing and non-invasive technique.

As a proof-of-concept, the work presented in this thesis develops a demonstrator capable of generating thematic maps of the exposed brain surface using HS information in the VNIR range (between 400 and 1000 nm). The HS images captured by the acquisition system were processed by an HS brain cancer detection algorithm based on unsupervised and supervised machine learning approaches, providing the classification results in surgical time. In these maps, the tumor boundaries can be easily identifiable by the neurosurgeon's naked eye, differentiating between four different classes: normal tissue, tumor tissue, blood vessels/hypervascularized tissue, and background.

The supervised algorithm was trained by employing a labeled dataset composed of more than 300,000 spectral signatures, extracted by medical doctors from 36 different HS cubes captured with the acquisition system from 22 different patients from Spain and UK. In this work, only the information obtained from the VNIR camera was employed to generate the gold standard for the training of the classification algorithm and validate its results. Due to the low spatial resolution of the NIR camera, currently it is not possible to perform reliable labeling of the NIR HS cubes. Although some preliminary analysis of the NIR images performed by this research team [144] reveal that the use of the NIR spectral range could help in the identification of blood vessels

and extravasated blood, NIR images alone are not relevant for the goal of this study. The methodology followed to generate the labeled dataset mainly exploits the spectral characteristics of HSI to differentiate between the different types of tissues. Intraoperative MRI and the knowledge and experience of the surgeons that participated in the project were employed as a guidance tool to identify the suitable areas to be labeled in the images. In addition, the pathological analysis results of the tumor tissue resected during the surgical procedures were employed to accurately identify the tumor areas and type.

Moreover, due to the difficulties to acquire in-vivo HS images during human neurosurgical procedures, during 2 years we were only able to capture the most common tumor types that were available during the surgical procedures in both participant hospitals. It is an extremely hard task to achieve a comprehensive database that covers the entire heterogeneity that could be found across the different patients and the different types of brain tumors. For this reason, in this thesis we worked with a preliminary database mainly focused to GBM tumors that are the most common type. On the other hand, since the customized HS acquisition system is a preliminary demonstrator, the system has several limitations. One of them is that the system was only able to capture tumor images where the tumor was either on the surface or in a deeper layer, but easy enough to be focused and captured. Furthermore, the HS pushbroom camera employed for the demonstrator development requires to perform a spatial scanning, considerably increasing the acquisition time of the HS image. The inherit movement of the undergoing patient's brain and also the possible artifacts, which can appear in the image (such as extravasated blood or surgical serum) during the acquisition, can affect the spatial coherence of the image. In this sense, snapshot cameras (HS cameras that are able to acquire both the spatial and spectral features of a scene in a single shot) are the most suitable option for this application, achieving real-time image acquisition. However, the number of spectral bands in these cameras is extremely lower compared to pushbroom cameras (~10 times less).

The development of the HS brain cancer detection algorithm was based in one multiclass classifier, generated for the supervised part of the algorithm, employing all the tumor types available in the training database to distinguish mainly between tumor and normal tissue, without identifying the different types of tumors. The classification of secondary tumors and their differentiation with primary tumors were not addressed in this thesis due to the reduced number of secondary tumor labeled samples available in the HS database. It is not possible to generate a robust and reliable classifier for discriminating between secondary and primary tumors because there is little availability of metastatic tissue samples, and even the few available ones belong to different organs. For this reason, all the experiments presented in this work were centered in the detection of primary tumors (mainly GBM).

Several HS images were employed to evaluate the results obtained with the developed algorithms. These images were acquired before and after the beginning of the resection. In this last case, the images were captured when part of the tumor had been resected from the superficial tumor, or when the normal brain of the surface was resected to reveal a deep layer tumor. Due to the procedure carried out to perform the resection of the tumor, several effects can be produced in the exposed brain surface. These effects could produce misclassifications of the tumor pixels, presenting false positives in the classification maps. The effects produced by the resection tools in the

normal tissue that surrounds the tumor area, usually produced false positives in these areas. Moreover, extravasated blood present in the tumor area also generated problems in the classification results. Although the surface of the brain was cleaned before the HS image acquisition, the time involved in the acquisition process (~one minute) creates the opportunity for extravasated blood in the image if the tumor area is highly vascularized. This produces misclassifications, especially between the hypervascularized class and the tumor class. Finally, it was more difficult to get high-quality images when deep-layer tumors were captured due to the limitations of the HS acquisition system. Particularly, when the tumor area was captured with a non-optimal focus, the spectral signatures of the tumor area were misclassified. In summary, the accuracy of the tumor detection was statistically significant when high-quality HS images of the tumor exposed in the brain surface were employed. On the other hand, the accuracy of the remaining classes (normal tissue, hypervascularized tissue and background) was optimal in the majority of the cases. The main problem found here was the classification of images that were captured under non-optimal conditions or captured after the beginning of the resection, which produces several effects in the tissue that surrounds the resected area. Nevertheless, false negatives were also found in the classification map results where normal tissue or hypervascularized tissue was identified within the tumor area. In this case, due to the multiform nature of the GBM tumor, these results should be validated through histopathological analysis in further experiments, since it could be possible that in fact were correct classification results. Although the algorithm is not capable to accurately identify the tumor area in all situations, the work presented in this thesis demonstrates that there are important evidences that reveal that the proposed HS brain cancer detection algorithm is a valuable resource to this end. Additionally, the final demonstrator was validated using seven HS images obtained in four neurosurgical operations that not were included in the training database. The thematic maps obtained in this case (see Section 6.6) demonstrate that the system did not introduce false positives in the parenchymal area when no tumor was present and it was able to identify the location of different types of tumor that were not present in the training database.

Regarding to the implementation of the algorithm onto the intraoperative demonstrator, in this thesis it has been presented a preliminary work that demonstrates the ability of HSI classification to achieve surgical time execution by using a hardware accelerator based on a manycore platform. The algorithm was partitioned between the control unit of the demonstrator and the hardware accelerator, where the highest computational tasks were implemented, to achieve intraoperative processing time (~1 min). Later, these processing time results were improved by implementing the entire HS brain cancer detection algorithm onto a high performance GPU-based platform (see Annex A). Due to the non-power limitation in the operating room, high-power consumption computing platforms are the suitable option to achieve real-time execution. In this GPU-based implementation of the HS brain cancer algorithm, an average processing time of ~15 seconds was achieved. In addition, a preliminary study to compare the performance of the use of deep learning techniques instead of traditional machine approaches based on SVM classifiers was performed. As it can be seen in the quantitative and qualitative results presented in Chapter 7, deep learning techniques outperforms the traditional SVM-based approaches, achieving more accurate results in the identification of the tumor samples. It is remarkable that the proposed DL pipeline approach achieves a very high specificity for both binary and

multiclass classification schemes (100% and ~90%, respectively), demonstrating the capability of the algorithm in achieving high confidence in the accurate detection of non-tumor areas. In this application, although the binary classification provides better results than the multiclass classification, the use of a four-class classification scheme is required to provide surgeons with an easily interpretable classification map. In this map, the different structures are shown, providing more information about the tissue condition thanks to the hypervascularized class. Furthermore, the usage of additional classes has been demonstrated to reduce the misclassifications between hypervascularized and tumor classes, which can be produced when classifying the entire HS cube. On the contrary, the low accuracy obtained for the tumor class (~42%) indicates that there was an overall error rate of ~58% in the correct identification of the tumor pixels. This result was obtained in multiclass classification, where each class accuracy is defined as the sensitivity obtained for that class. This means that, on average, the proposed method classifies 58% of the tumor pixels as “non-tumor”, i.e. the conjunction of the normal, hypervascularized, and background classes. Taking into account the results obtained in the binary classification, where only normal brain and tumor tissues were classified, the sensitivity and specificity results were 88% and 100%, respectively. Therefore, in the multiclass classification, the majority of the misclassifications produced in the tumor class were related to the hypervascularized and background classes. Mainly, the false negatives obtained in the results were tumor pixels assigned to the hypervascularized or background classes. Furthermore, this error was higher or lower, depending on the HS image that was classified. In summary, both the binary and multiclass classification schemes had very high specificity (100% for binary and 90% for multiclass), averaging the accuracy of all the non-tumor classes. Therefore, we can conclude that the proposed technique performs well on correctly classifying cases of being disease-free. In other words, the method has a high confidence for “ruling in” cases of disease [55]. In brain cancer resection, an intraoperative guidance system should have a very high specificity to have confidence that the areas resected are not normal brain tissue, which is very valuable for better patient outcomes. In summary, the work described in this thesis demonstrates that HSI can be employed as a new non-invasive and non-ionizing surgical-time aid visualization tool that can improve the outcomes of the undergoing patient, assisting neurosurgeons in the resection of brain tumors. To the best of our knowledge, there are no other HS systems capable of intraoperatively capturing and classify brain cancer HS images.

## 8.2 Future lines

The work presented in this thesis was pioneer in the use of HSI to be employed as an aid imaging modality to assist neurosurgeons during brain tumor resections, providing a non-contact, non-ionizing and non-invasive intraoperative tool. After the execution of this project, several research lines are open to be investigated in the future to improve the results achieved.

Further data acquisition campaigns must be carried out in order to enlarge the training database and the validation database with more patients and types of tumors with a more detailed pathological description including molecular profiling. An increased HS brain database could be employed to perform further investigations in the use of HSI to: 1) identify the different tissue and tumor types; 2) delineate the

boundaries of the tumors, parenchyma, blood vessels or other regions of interest for the neurosurgeons; 3) provide other kind of information to the surgeons that can be useful to improve the outcomes of the surgery.

Additionally, the fusion of both types of HS images (VNIR and NIR) must be investigated in order to demonstrate if the NIR information could help to more accurately distinguish the boundaries between the tumor tissue and the surrounding hypervascularized normal tissue. On the other hand, an improvement of the acquisition system, where the HS camera is able to acquire images in real time, is also required to obtain high-quality HS images and perform a study that could demonstrate the ability of HSI to provide ongoing feedback during the entire tumor resection process. However, for this improvement it is required to reduce the size of the HS cameras and also to employ snapshot cameras. Therefore, further investigations must be performed by using HS images captured with pushbroom cameras (with high spectral resolution) in order to identify the most relevant bands that allow the identification and delineation of brain tumors. These results will provide valuable feedback to snapshot camera manufacturers that will be able to develop specific HS sensors for this particular application, reducing the size, the acquisition time and probably the cost of the cameras.

In addition to this, further investigations must be carried out to implement the new proposed deep learning framework onto the demonstrator and evaluate its performance for real-time processing during the surgical operations. Furthermore, the inclusion of the proposed surgical aid visualization tool in the intraoperative demonstrator, which can be used both with the SVM-based and the DL approaches, will allow the operating surgeon to visualize different results, manually modified following his/her knowledge and experience, to select the more accurate result. This surgical aid visualization system combines the information provided by the HSI processing and the expertise of the operating surgeon.

On the other hand, an extensive clinical validation of the intraoperative HS system must be carried out, employing much more patient data and a multi-centered trial. In this clinical validation, a comprehensive pathological analysis of the entire tumor area outlined by the thematic map (especially in the boundaries between tumor and the surrounding normal tissue) must be performed as well as to correlate the results with the MRI information in order to know if the tumor infiltration into normal brain tissue can be properly identified by the system. By using new HS data, the classifiers generated with the previously obtained database could be tested without having to perform the leave-one-patient-out cross-validation. Additionally, through clinical validation, the relation between the improvement of the patient outcomes and the use of the system during the surgery could be studied.

Moreover, further investigations should be done in order to properly correlate the biological properties of the different brain tissue types (especially of the different types of tumors and normal tissues) with the spectral responses obtained by the HS cameras at each wavelength. It has been demonstrated that the differences in the water content found in the tumor tissue with respect to the normal tissue can achieve a more accurate identification of brain tumors [56]. Raman spectroscopy was employed to study this correlation, demonstrating that in the spectral region comprised between 2817–2985 nm (wavenumber region 3350–3550  $\text{cm}^{-1}$ ), the water content can be quantified and used to discriminate between tumor and normal tissue in oral cancer [57]. Following

this approach, the use of HSI should be investigated to demonstrate whether the water content of the tumor tissue could be identified and used to improve the accuracy of tumor identification at lower wavelengths. On the other hand, same investigations should be performed to spectrally analyze the physiological characteristics of hemoglobin in the brain surface. The outcomes of this research could lead into a better identification of the wavelengths that could be used to improve the discrimination of the blood vessels in the brain. Furthermore, this hemoglobin characterization could help in the differentiation between the tumor tissue and the surrounded hypervascularized normal tissue, improving the delineation of the tumor margins.

These studies could help in the better discrimination of the different types of tissues, providing better outcomes in the delineation and identification of the tumors, especially in the surrounding normal tissue infiltrated by the tumor. Specific studies should be done to determine these differences and provide a more detailed labeled dataset. Although the labeled dataset presented in this work was obtained conservatively (only the pixels where the experts were highly confident that belonged to a certain class were labeled) using the methodology based on the combination between the SAM algorithm and the pathological analysis, a new detailed labeled dataset could be used to validate it. In addition, other types of neurosurgical procedures not involving brain tumor should be included in further data campaigns in order to obtain a higher number of normal tissue samples, ensuring that they are not affected by the infiltrated tumor.

Finally, in this thesis, the classification frameworks were evaluated following a pixel-by-pixel approach due to the limitations of the *in vivo* HS brain database. In a pixel-by-pixel approach, two classifiers could be considered statistically indistinguishable if there are two different locations of tumor areas (two tumor sites) in the same image, and both classifiers achieve the same accuracy, but identify pixels in different areas. In this sense, to find the best classification framework, a site-by-site approach should be used to evaluate the results. An aid visualization tool is particularly useful when two or more tumor sites need to be classified, and when the accuracy is different at different tumor sites. Further experiments should be carried out in this direction using a much larger dataset in order to improve the comparison of the classifiers by using a site-by-site approach.

Taking into account the previously mentioned limitations, currently, other investigations are being carried out by the research team in order to improve the outcomes of the work presented in this thesis. Some of the investigations have been performed in collaboration with other research groups from several institutions.

In collaboration with the research group of Prof. Francesco Leporati of the Department of Electrical, Computer and Biomedical Engineering at the University of Pavia, some works have been carried out to implement the entire HS brain cancer detection algorithm based on machine learning techniques onto GPUs (see Annex A). Part of this work has been already reported in [202]–[204]. On the other hand, within the research group where this thesis has been developed, some other works related with the implementation of classification algorithms of HS images have been carried out. The use of random forest algorithm is currently studied to be implemented and accelerated onto GPUs [205]. In addition, several works are currently on-going related with the implementation of the HS brain cancer detection algorithm onto FPGAs. In the field of low-power consumption implementations, there are on-going several

collaborations with the research group of Dr. Eduardo Juárez from the CITSEM (*Centro de Investigación en Tecnologías Software y Sistemas Multimedia para la Sostenibilidad*) at the UPM (*Universidad Politécnica de Madrid*).

Currently, some modifications of the HS acquisition system described in this thesis are being addressed as part of the new research project ITHaCA (*IdenTificación Hiperespectral de tumores CerebrAles* - ProID2017010164) achieved by this research group. The main modification to be performed over the acquisition system is the correct alignment of the two HS cameras (VNIR and NIR) employing two different light sources. Having both FOVs of the cameras parallel between them and perpendicular to the scene that is going to be captured (the exposed brain in this case), it will be possible to obtain both HS images with the same perspective. This will allow using HS image fusion algorithms to obtain one HS data cube containing the information provided by both cameras (between 400 and 1700 nm). As stated before, the inclusion of the NIR information could help in the discrimination of the tumor and hypervascularized tissue, which produces the main misclassifications in the current demonstrator.

In the same direction, a strong collaboration is being carried out with the research group of Prof. Baowei Fei from the Quantitative BioImaging Laboratory (QBIL) of the University of Texas (UT) at Dallas and UT Southwestern Medical Center. Investigations regarding to the use of deep learning algorithms to improve the classification results of the traditional machine learning algorithms have been carried out (already presented in Chapter 7) [193]. Furthermore, there is a current collaboration where the HS acquisition system is going to be replicated at the UT Dallas in order to start an acquisition data campaign to acquire new HS brain cancer images at the UT Southwestern Medical Center, one of the major medical research institutions of the United States.

In addition, as part of the PhD thesis of Samuel Ortega, one of the researchers of the group that was very close involved in the investigations described in this thesis, some investigations are being carried out with the goal of applying HSI techniques to improve and accelerate the histopathological analysis of tumor samples using a customized HS microscope developed to this end. Some preliminary studies performed in this area have been already reported [206]–[208].





# Annex A: Brain cancer detection algorithm implementation and acceleration using GPUs

The brain cancer detection algorithm developed in this thesis was implemented in two different hardware accelerators: a manycore-based platform and a GPU-based platform. The implementation and acceleration of the algorithm using the manycore-based platform was performed by Raquel Lazcano and Daniel Madroñal, supervised by Dr. Rubén Salvador and Dr. Eduardo Juárez from the UPM in collaboration with the ULPGC team. The results of this implementation were already presented in Section 6.5 of Chapter 6. On the other hand, the GPU-based implementation was performed by Giordana Florimbi, Giovanni Rausa and Emanuele Torti, supervised by Prof. Francesco Leporati from the *Università Degli Studi Di Pavia* in collaboration with the ULPGC team. Next, a brief summary of this implementation and the achieved results in this collaboration will be presented.

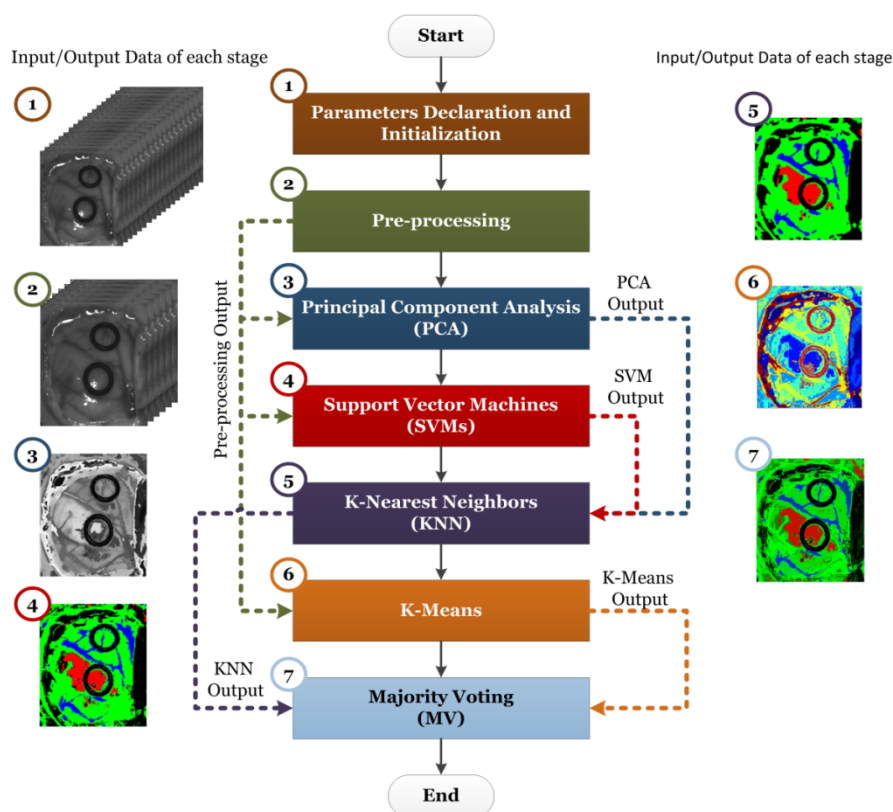
Due to the non-power limitations or restrictions during surgical procedures in an operating theatre, it is possible to employ high energy consumption computing platforms to achieve real-time execution of the HS brain cancer detection algorithms. In this sense, GPUs with high power usage are suitable to achieve real-time performance. For this reason, the HS brain cancer detection algorithm described in Chapter 5 and fine-tuned in Chapter 6 was implemented onto a CPU-GPU computing platform. The dataset employed for the experiments are detailed in **Table A-1**.

**Table A-1: Details of the HS brain image dataset employed for the implementation validation.**

Image ID	#Pixel	Dimensions (Width × Height × Bands)
<b>P8C1</b>	251,532	548×459×826
<b>P8C2</b>	264,408	552×479×826
<b>P12C1</b>	219,232	496×442×826
<b>P15C1</b>	185,368	493×376×826
<b>P20C1</b>	124,691	329×379×826

**Figure A-1** shows the serial CPU implementation of the entire algorithm and the data dependencies between the different stages of the algorithm. Solid arrows indicate

the sequential execution of each stage, while dashed arrows indicate the data transferring between the different stages. As it can be seen, the serial CPU implementation starts with the declaration and initialization of the parameters employed in each stage and it is followed by the pre-processing stage where the calibration and the noise and dimensionality reduction of the HS cube (input data) captured by the HS camera are performed. The pre-processed HS cube generated in this stage will be employed in three of the next stages of the algorithm (PCA, SVM and K-means). The PCA algorithm is the first stage to be executed after finishing the pre-processing of the input data, in order to obtain a one-band representation of the HS cube. This stage is followed by the SVM classification, where a four-class probability classification map is obtained. The outputs of the PCA and SVM stages (the one-band representation and the four-class probability classification map) are employed as inputs in the KNN filter stage, where a spatial homogenization of the SVM probabilities is performed, generating a filtered four-class probability classification map. The next stage is the unsupervised segmentation performed by executing the K-means algorithm. The input of this stage is the pre-processed HS cube and the output is an unsupervised segmentation map where 24 spectral regions are grouped and differentiated. Finally, the majority voting stage is in charge of merging the results of the KNN and the K-means stages (the filtered four-class probability classification map and the unsupervised segmentation map) in order to obtain the final density map (output data).



**Figure A-1: Serial CPU implementation of the HS brain cancer detection algorithm.** The flow of the serial execution is represented by the black solid arrows and the input/output flow is indicated by the colored dashed lines.

Several tests were performed to achieve the best execution time results with different parallel configurations of each independent stage. Each algorithm was

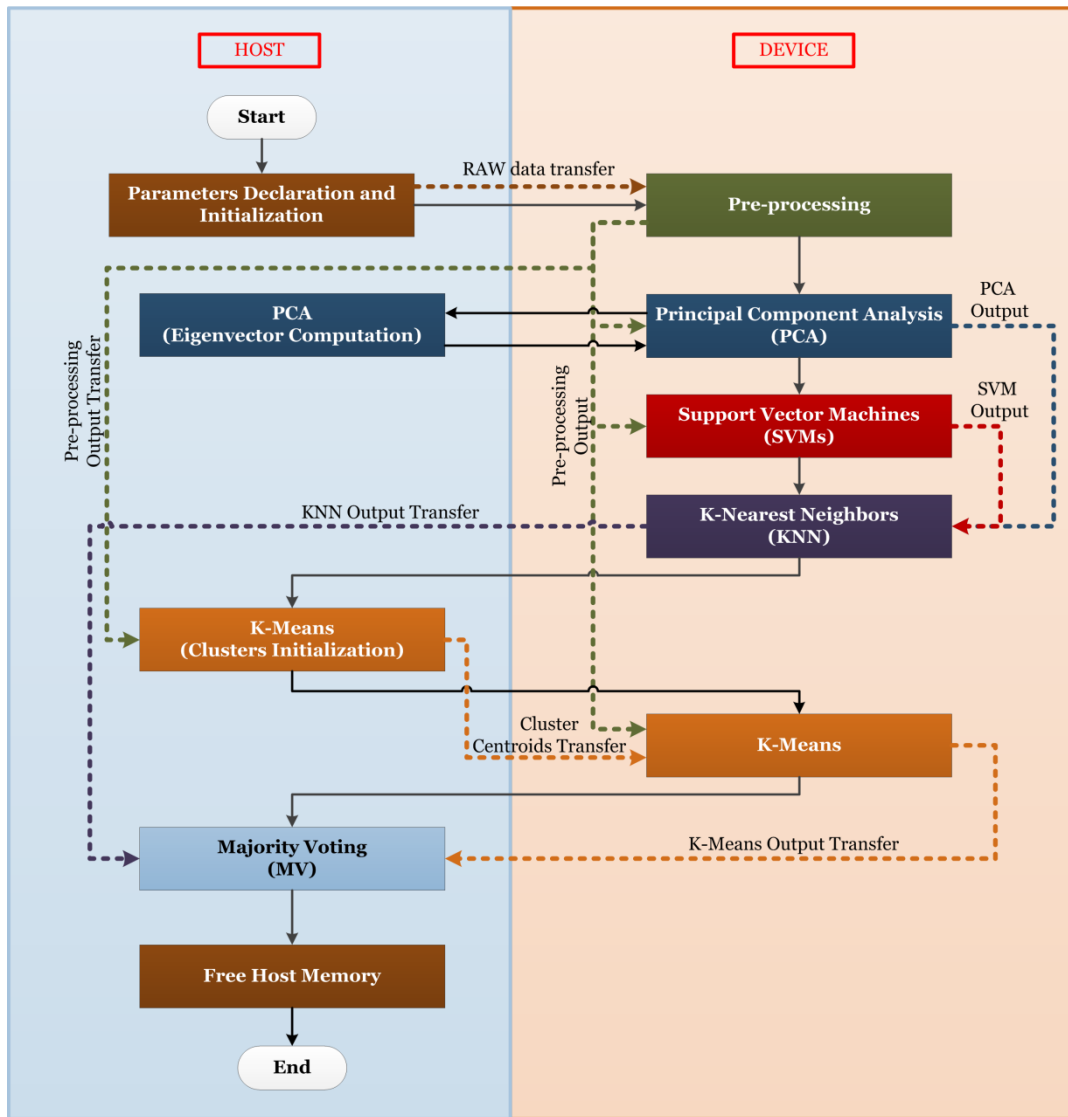
analyzed and studied in detail providing the suitable CPU-GPU configuration in each case. At the end, the complete system was implemented in two parallel versions, for a *single-GPU* architecture and for a *multi-GPU* architecture. In both architectures, several configurations were tested and in the following paragraphs the best configurations for each case are presented. C language was employed for the serial implementation, while CUDA programming was used to develop the parallel versions [209]. The NVIDIA Tesla K40 GPU was used for the experiments [210].

**Figure A-2** shows the parallel implementation of the HS brain cancer detection algorithm for the *single-GPU* architecture. As it can be seen, all the stages, except the majority voting, are mainly executed onto the GPU (also called *device*). The pre-processing, SVM and KNN stages are entirely implemented onto the GPU due to the speedup achieved is considerably high respect to the CPU implementation. On the contrary, the eigenvector computation step of the PCA is executed onto the CPU (also called *host*), since this step offers better results when it is executed out of the GPU. Furthermore, for the same reason, the cluster initialization step of the K-means algorithm is executed onto the CPU and the results are transferred to the GPU in order to complete the K-means stage. At the end, the K-means and the KNN results are transferred to the CPU in order to compute the Majority Voting in the host, due to the computation of this algorithm is more effective when is performed onto the CPU.

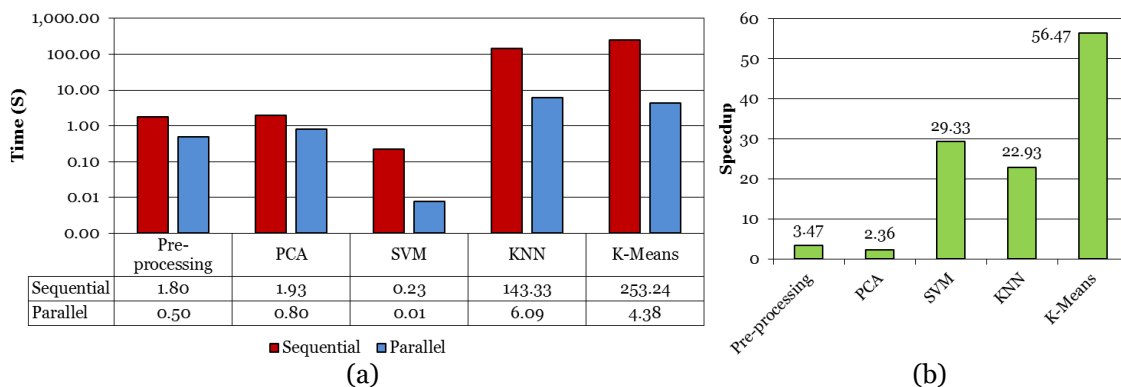
The total time and speedup results achieved for each independent implementation can be seen in **Table A-2**, where it is possible to observe that the algorithm with the highest speedup is the K-Means (average  $\sim 100x$ ), followed by the SVM (average  $\sim 39x$ ), KNN (average  $\sim 22x$ ), Pre-processing (average  $\sim 3.4x$ ) and PCA (average  $\sim 2.3x$ ). **Figure A-3** graphically shows the results obtained for each parallel implementation of the HS brain cancer algorithm compared to the serial implementation. In addition, **Table A-3** details the total time results and speedup achieved with the single-GPU implementation in comparison with the serial CPU implementation. In this parallel implementation an average speedup of 34.8x is achieved in the execution of the entire algorithm (performing the classification in  $\sim 15$  seconds).

**Table A-2: Execution time comparison between the sequential (Seq.) and accelerated (Acc.) implementations of each stage of the algorithm.**

Image ID	Processing Type	Pre-processing	PCA	SVM	KNN	K-Means
P8C1	Seq. (s)	2.27	2.27	0.27	190.02	214.52
	Acc. (s)	0.59	0.95	0.01	7.63	3.99
	Speedup	3.85x	2.39x	30.00x	24.90x	53.76x
P8C2	Seq. (s)	2.31	2.63	0.30	202.41	465.61
	Acc. (s)	0.61	0.97	0.01	8.01	7.45
	Speedup	3.79x	2.71x	33.33x	25.27x	62.50x
P12C1	Seq. (s)	1.98	1.98	0.23	146.92	151.50
	Acc. (s)	0.52	0.78	0.01	6.44	2.96
	Speedup	3.81x	2.54x	28.75x	22.81x	51.18x
P15C1	Seq. (s)	1.66	1.66	0.20	121.37	162.37
	Acc. (s)	0.47	0.71	0.01	5.57	2.97
	Speedup	3.53x	2.34x	28.57x	21.79x	54.67x
P20C1	Seq. (s)	0.78	1.10	0.13	55.91	272.20
	Acc. (s)	0.33	0.61	0.01	2.81	4.52
	Speedup	2.36x	1.80x	26.00x	19.90x	60.22x



**Figure A-2: Single-GPU parallel implementation of the HS brain cancer detection algorithm.** The flow of the parallel execution is represented by the black solid arrows and the data transfer flow between the host and the device and also between the different stages are indicated by the colored dashed lines.



**Figure A-3: Average parallel implementation results of each stage of the HS brain cancer detection algorithm.** (a) Average execution time results. (b) Average speedup achieved respect to the serial implementation.

**Table A-3: Execution time comparison between the sequential (Seq.) and accelerated (Acc.) implementations of both GPU-based parallel implementations.**

Image ID	Serial (s)	Single-GPU		Multi-GPU	
		Time (s)	Speedup	Time (s)	Speedup
P8C1	600.22	17.95	33.43x	13.45	44.63x
P8C2	719.31	19.49	36.91x	14.22	50.58x
P12C1	459.74	14.01	32.81x	11.34	40.55x
P15C1	387.43	12.02	32.23x	8.99	43.19x
P20C1	301.17	7.79	38.66x	6.41	46.98x

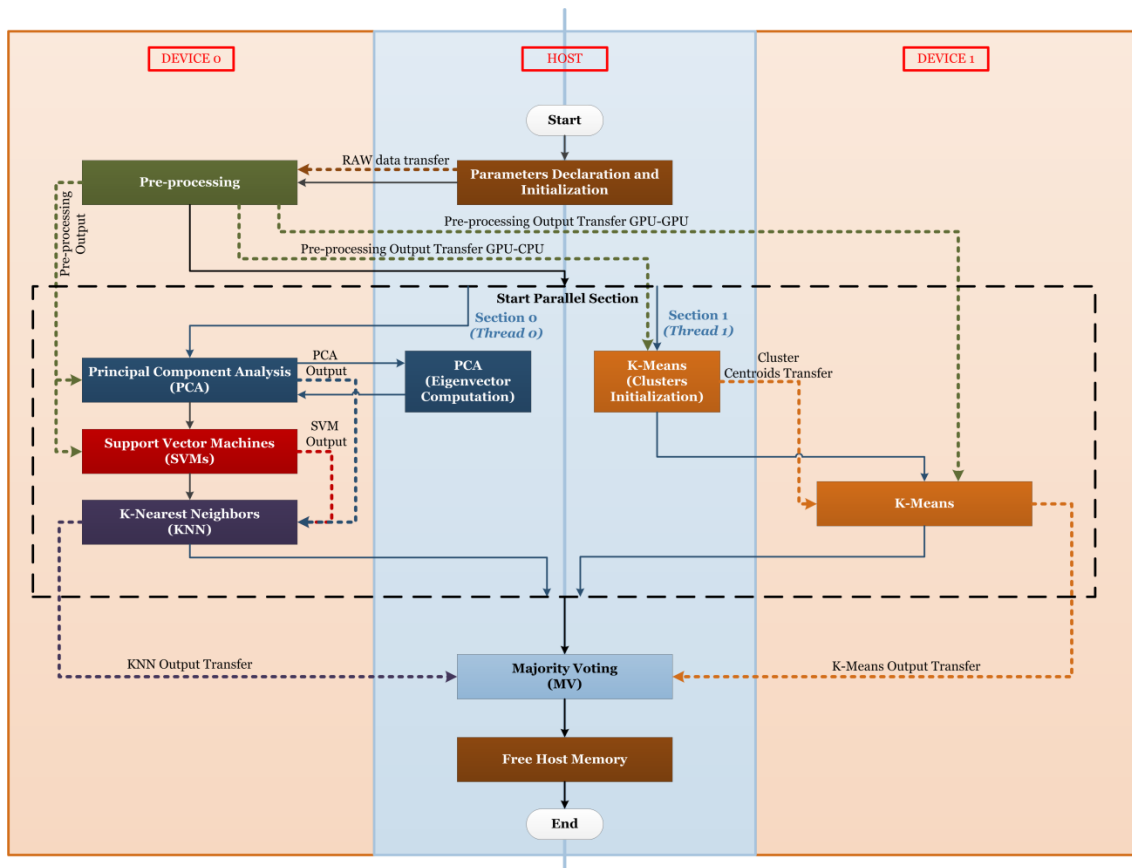
Regarding to the *multi-GPU* parallel implementation, **Figure A-4** shows the CPU-GPUs partition between the different stages of the algorithm. In this implementation, two NVIDIA Tesla K40 GPUs (*device 0* and *device 1*) were employed to partition the algorithms performing a parallel execution between the two devices.

As it can be seen, the reading of the data is performed in the host and then the input data is transferred to the device 0, where the pre-processing stage is executed. The output of this stage (the pre-processed HS cube) is then, transferred to the host (GPU-CPU transferring) and to the device 1 (GPU-GPU transferring). Furthermore, the pre-processed HS cube is employed in the device 0 for the next stages executed in this device.

After the pre-processing stage, a parallel section is opened. On one hand, in section 0 (thread 0) of the parallel section, the PCA, SVM and KNN are executed sequentially in the device 0 (including the eigenvector computation of the PCA that is executed in the host). On the other hand, the K-means algorithm is executed in section 1 (thread 1) onto the host and device 1. After the ending of PCA, SVM, KNN and K-means executions, the parallel section is closed and the outputs of the KNN and the K-means are transferred to the host from device 0 and device 1, respectively. At the end, the Majority Voting algorithm is executed in the host and generates the final density map.

**Table A-3** presents the execution time results achieved by the serial, *single-GPU* and *multi-GPU* implementations, as well as the speedup obtained by the GPU-based implementation regarding to the serial implementation. In average, the *multi-GPU* implementation achieve an speedup of 45.1x respect to the serial implementation, classifying the captured HS in ~10 seconds. The average speedup obtained with the *multi-GPU* implementation respect to the single-GPU architecture is ~1.3x.

In summary, the use of high performance GPU-based implementations for the execution of the HS brain cancer detection algorithms outperforms the results obtained with the manycore platform, achieving an average speedup of ~4.3x and ~5.7x for the *single-GPU* and *multi-GPU* architectures, respectively, respect to the manycore implementation results obtained in Chapter 6. However, the power consumption required by the GPUs is extremely higher than the manycore platform employed in the experiments. In any case, in this application, where the system will be employed within the operating theater of a Hospital, the power consumption it is not a restriction.



**Figure A-4: Multi-GPU parallel implementation of the HS brain cancer detection algorithm.** The flow of the parallel execution is represented by the black and blue solid arrows and the data transfer flow between the host and the devices and also between the different stages are indicated by the colored dashed lines.

# Annex B: Publications

In this annex, all the scientific communications published during the development of the work described in this thesis are detailed. The scientific communications have been divided into conference presentations and journal publications and they have been organized in chronological order. Furthermore, as part of the outcomes achieved during the development of this research project, a patent has been obtained. Specifically, 17 journal citation reports (JCR) papers (one of them submitted and the rest already published), 18 peer-reviewed conference papers and 1 patent have been achieved during the course of this thesis. In total, 36 scientific contributions have been accomplished.

## Journal publications

- [J1] **Fabelo, H.;** Ortega, S.; Szolna, A.; Bulters, D.; Pineiro, J. F.; Kabwama, S.; J-O'Shanahan, A.; Bulstrode, H.; Bisshopp, S.; Kiran, B. R.; Ravi, D.; Lazcano, R.; Madronal, D.; Sosa, C.; Espino, C.; Marquez, M.; Plaza, M. de L. L.; Camacho, R.; Carrera, D.; Hernandez, M.; Callico, G. M.; Morera, J.; Stanciulescu, B.; Yang, G.-Z.; Salvador, R.; Juarez, E.; Sanz, C.; Sarmiento, R. *In-Vivo* Hyperspectral Human Brain Image Database for Brain Cancer Detection. *IEEE Access*. **2019**, 1–1, doi:10.1109/ACCESS.2019.2904788. [IF: **3.557 (2017)** – **Q1**] [Related with **Chapter 4**]
- [J2] **Fabelo, H.;** Halicek, M.; Ortega, S.; Shahedi, M.; Szolna, A.; Piñeiro, J.; Sosa, C.; O'Shanahan, A.; Bisshopp, S.; Espino, C.; Márquez, M.; Hernández, M.; Carrera, D.; Morera, J.; Callico, G.; Sarmiento, R.; Fei, B.; Fabelo, H.; Halicek, M.; Ortega, S.; Shahedi, M.; Szolna, A.; Piñeiro, J. F.; Sosa, C.; O'Shanahan, A. J.; Bisshopp, S.; Espino, C.; Márquez, M.; Hernández, M.; Carrera, D.; Morera, J.; Callico, G. M.; Sarmiento, R.; Fei, B. Deep Learning-Based Framework for In Vivo Identification of Glioblastoma Tumor using Hyperspectral Images of Human Brain. *Sensors* **2019**, *19*, 920, doi:10.3390/s19040920. [IF: **2.475 (2017)** – **Q2**] [Related with **Chapter 7**]
- [J3] Ortega, S.; **Fabelo, H.;** Iakovidis, D.; Koulaouzidis, A.; Callico, G.; Ortega, S.; Fabelo, H.; Iakovidis, D. K.; Koulaouzidis, A.; Callico, G. M. Use of Hyperspectral/Multispectral Imaging in Gastroenterology. Shedding Some–Different–Light into the Dark. *J. Clin. Med.* **2019**, *8*, 36, doi:10.3390/jcm8010036. [IF: **5.583 (2017)** – **Q1**] [Related with **Chapter 2**]
- [J4] **Fabelo, H.;** Ortega, S.; Casselden, E.; Loh, J.; Bulstrode, H.; Zolnourian, A.; Grundy, P.; Callico, G. M.; Bulters, D.; Sarmiento, R. SVM Optimization for Brain Tumor



- Identification Using Infrared Spectroscopic Samples. *Sensors* **2018**, *18*, 4487, doi:10.3390/s18124487. [IF: 2.475 (2017) – Q2] [Related with Chapter 5]
- [J5] **Fabelo, H.**; Ortega, S.; Ravi, D.; Kiran, B. R.; Sosa, C.; Bulters, D.; Callicó, G. M.; Bulstrode, H.; Szolna, A.; Piñeiro, J. F.; Kabwama, S.; Madroñal, D.; Lazcano, R.; J-O'Shanahan, A.; Bisshopp, S.; Hernández, M.; Báez, A.; Yang, G.-Z.; Stanciulescu, B.; Salvador, R.; Juárez, E.; Sarmiento, R. Spatio-spectral classification of hyperspectral images for brain cancer detection during surgical operations. *PLoS One* **2018**, *13*, 1–27, doi:10.1371/journal.pone.0193721. [IF: 2.766 (2017) – Q1] [Related with Chapter 5]
- [J6] **Fabelo, H.**; Ortega, S.; Lazcano, R.; Madroñal, D.; M. Callicó, G.; Juárez, E.; Salvador, R.; Bulters, D.; Bulstrode, H.; Szolna, A.; Piñeiro, J. F.; Sosa, C.; J. O'Shanahan, A.; Bisshopp, S.; Hernández, M.; Morera, J.; Ravi, D.; Kiran, B. R.; Vega, A.; Báez-Quevedo, A.; Yang, G.-Z.; Stanciulescu, B.; Sarmiento, R. An intraoperative visualization system using hyperspectral imaging to aid in brain tumor delineation. *Sensors* **2018**, *18*, doi:10.3390/s18020430. [IF: 2.475 (2017) – Q2] [Related with Chapters 3 and 6]
- [J7] Ortega, S.; **Fabelo, H.**; Camacho, R.; Plaza, M. L.; Callicó, G. M.; Sarmiento, R. Detecting brain tumor in pathological slides using hyperspectral imaging. *Biomed. Opt. Express* **2018**, *9*, doi:10.1364/BOE.9.000818. [IF: 3.482 (2017) – Q1] [Related with Chapter 5]
- [J8] Florimbi, G.; **Fabelo, H.**; Torti, E.; Lazcano, R.; Madroñal, D.; Ortega, S.; Salvador, R.; Loporati, F.; Danese, G.; Báez-Quevedo, A.; Callicó, G. M.; Juárez, E.; Sanz, C.; Sarmiento, R. Accelerating the K-Nearest Neighbors Filtering Algorithm to Optimize the Real-Time Classification of Human Brain Tumor in Hyperspectral Images. *Sensors (Basel)*. **2018**, *18*, doi:10.3390/s18072314. [IF: 2.475 (2017) – Q2] [Related with Annex A]
- [J9] Torti, E.; Florimbi, G.; Castelli, F.; Ortega, S.; **Fabelo, H.**; Callicó, G.; Marrero-Martin, M.; Loporati, F.; Torti, E.; Florimbi, G.; Castelli, F.; Ortega, S.; Fabelo, H.; Callicó, G. M.; Marrero-Martin, M.; Loporati, F. Parallel K-Means Clustering for Brain Cancer Detection Using Hyperspectral Images. *Electronics* **2018**, *7*, 283, doi:10.3390/electronics7110283. [IF: 2.110 (2017) – Q2] [Related with Annex A]
- [J10] Torti, E.; Fontanella, A.; Florimbi, G.; Loporati, F.; **Fabelo, H.**; Ortega, S.; Callico, G. M. Acceleration of brain cancer detection algorithms during surgery procedures using GPUs. *Microprocess. Microsyst.* **2018**, *61*, 171–178, doi:10.1016/j.micpro.2018.06.005. [IF: 1.049 (2017) – Q3] [Related with Annex A]
- [J11] Ravi, D.; **Fabelo, H.**; Callico, G. M.; Yang, G.-Z. Manifold Embedding and Semantic Segmentation for Intraoperative Guidance with Hyperspectral Brain Imaging. *IEEE Trans. Med. Imaging* **2017**, *36*, doi:10.1109/TMI.2017.2695523. [IF: 6.130 – Q1] [Related with Chapter 5]
- [J12] Lazcano, R.; Madroñal, D.; Salvador, R.; Desnos, K.; Pelcat, M.; Guerra, R.; **Fabelo, H.**; Ortega, S.; Lopez, S.; Callico, G. M.; Juarez, E.; Sanz, C. Porting a PCA-based hyperspectral image dimensionality reduction algorithm for brain cancer detection on a manycore architecture. *J. Syst. Archit.* **2017**, *77*, 101–111, doi:10.1016/j.sysarc.2017.05.001. [IF: 0.913 – Q3] [Related with Chapter 6]
- [J13] Madroñal, D.; Lazcano, R.; Salvador, R.; **Fabelo, H.**; Ortega, S.; Callico, G. M.; Juarez, E.; Sanz, C. SVM-based real-time hyperspectral image classifier on a manycore architecture. *J. Syst. Archit.* **2017**, *80*, doi:10.1016/j.sysarc.2017.08.002. [IF: 0.913 – Q3] [Related with Chapter 6]

- [J14] Ortega, S.; **Fabelo, H.**; Camacho, R.; Plaza, M. L.; Callico, G. M.; Lazcano, R.; Madroñal, D.; Salvador, R.; Juárez, E.; Sarmiento, R. PO3.18 Detection of human brain cancer in pathological slides using hyperspectral images. *Neuro. Oncol.* **2017**, 19, iii37, doi:10.1093/neuonc/nox036.133. [IF: 9.384 – Q1] [Related with Chapter 5]
- [J15] Pineiro, J. F.; Bulters, D.; Ortega, S.; **Fabelo, H.**; Kabwama, S.; Sosa, C.; Bishop, S.; Martinez-Gonzalez, A.; Szolna, A.; M. Callico, G. Hyperspectral imaging for brain tumour identification and boundaries delineation in real-time during neurosurgical operations. *Neuro. Oncol.* **2017**, doi:https://doi.org/10.1093/neuonc/nox036.160. [IF: 9.384 – Q1] [Related with Chapter 5]
- [J16] Szolna, A.; Morera, J.; Piñeiro, J. F.; Callicó, G. M.; **Fabelo, H.**; Ortega, S. Hyperspectral Imaging as A Novel Instrument for Intraoperative Brain Tumor Detection. *Neurocirugia* **2016**, 27, 166. [IF: 0.310 – Q4] [Related with Chapters 3, 4 and 5]
- [J17] Kabwama, S.; Bulters, D.; Bulstrode, H.; **Fabelo, H.**; Ortega, S.; Callico, G. M.; Stanculescu, B.; Kiran, R.; Ravi, D.; Szolna, A.; others Intra-operative hyperspectral imaging for brain tumour detection and delineation: Current progress on the HELICoiD project. *Int. J. Surg.* **2016**, 36, S140. [IF: 2.693 – Q2] [Related with Chapters 3, 4 and 5]

## Patents

- [P1] Gustavo Marrero Callico; **Himar Fabelo Gomez**; Samuel Ortega Sarmiento; Bogdan Stanculescu; Ravi Kiran Bangalore, “Method of Non-Invasive Detection of Tumour and/or Healthy Tissue and Hyperspectral Imaging Apparatus”, Universidad de las Palmas de Gran Canaria, PCT/EP2016/078477, Spain, Canary Islands.

## Conferences

- [C1] **Fabelo, H.**; Halicek, M.; Ortega, S.; Szolna, A.; Morera, J.; Sarmiento, R.; Callicó, G. M.; Fei, B. Surgical aid visualization system for glioblastoma tumor identification based on deep learning and in-vivo hyperspectral images of human patients. In *Medical Imaging 2019: Image-Guided Procedures, Robotic Interventions, and Modeling*; Fei, B., Linte, C. A., Eds.; SPIE, 2019; Vol. 10951, p. 35. [RFW Best Student Paper Award]
- [C2] Halicek, M.; **Fabelo, H.**; Ortega, S.; Little, J. V.; Wang, X.; Chen, A. Y.; Callicó, G. M.; Myers, L.; Sumer, B.; Fei, B. Cancer detection using hyperspectral imaging and evaluation of the superficial tumor margin variance with depth. In *Medical Imaging 2019: Image-Guided Procedures, Robotic Interventions, and Modeling*; Fei, B., Linte, C. A., Eds.; SPIE, 2019; Vol. 10951, p. 45.
- [C3] Madroñal, D.; Lazcano, R.; Ortega, S.; **Fabelo, H.**; Salvador, R.; M. Callico, G.; Juarez, E.; Sanz, C. Implementation of a spatial-spectral classification algorithm using medical hyperspectral images. In *2017 32nd Conference on Design of Circuits and Integrated Systems (DCIS)*; Barcelona, 2017.
- [C4] Madronal, D.; Lazcano, R.; **Fabelo, H.**; Ortega, S.; Salvador, R.; Callico, G. M.; Juarez, E.; Sanz, C. Energy consumption characterization of a Massively Parallel Processor Array (MPPA) platform running a hyperspectral SVM classifier. In *Conference on Design and Architectures for Signal and Image Processing, DASIP*; 2017; Vol. 2017–Septe.

- [C5] Lazcano, R.; Madronal, D.; **Fabelo, H.**; Ortega, S.; Salvador, R.; Callico, G. M.; Juarez, E.; Sanz, C. Parallel implementation of an iterative PCA algorithm for hyperspectral images on a manycore platform. In *Conference on Design and Architectures for Signal and Image Processing, DASIP*; 2017; Vol. 2017–Septe.
- [C6] Madroñal, D.; Lazcano, R.; **Fabelo, H.**; Ortega, S.; Callicó, G. M.; Juarez, E.; Sanz, C. Hyperspectral image classification using a parallel implementation of the linear SVM on a Massively Parallel Processor Array (MPPA) platform. In *Conference on Design and Architectures for Signal and Image Processing, DASIP*; 2017.
- [C7] Lazcano, R.; Madroñal, D.; **Fabelo, H.**; Ortega, S.; Salvador, R.; Callicó, G. M.; Juárez, E.; Sanz, C. Parallel exploitation of a spatial-spectral classification approach for hyperspectral images on RVC-CAL. In *Proceedings of SPIE - The International Society for Optical Engineering*; 2017; Vol. 10430.
- [C8] Salvador, R.; **Fabelo, H.**; Lazcano, R.; Ortega, S.; Madroñal, D.; Callicó, G. M.; Juárez, E.; Sanz, C. Demo: HELICoiD tool demonstrator for real-time brain cancer detection. In *Conference on Design and Architectures for Signal and Image Processing, DASIP*; 2017. **[Best Demo Award]**
- [C9] Salvador, R.; Ortega, S.; Madroñal, D.; **Fabelo, H.**; Lazcano, R.; Marrero, G.; Juárez, E.; Sarmiento, R.; Sanz, C. HELICoiD: Interdisciplinary and collaborative project for real-time brain cancer detection. In *ACM International Conference on Computing Frontiers 2017, CF 2017*; 2017.
- [C10] Hernandez, A.; **Fabelo, H.**; Ortega, S.; Baez, A.; Callico, G. M.; Sarmiento, R. Random forest training stage acceleration using graphics processing units. In *2017 32nd Conference on Design of Circuits and Integrated Systems (DCIS)*; 2017; pp. 1–6.
- [C11] Domingo, R.; Salvador, R.; **Fabelo, H.**; Madronal, D.; Ortega, S.; Lazcano, R.; Juarez, E.; Callico, G. M.; Sanz, C. High-level design using Intel FPGA OpenCL: A hyperspectral imaging spatial-spectral classifier. In *12th International Symposium on Reconfigurable Communication-Centric Systems-on-Chip, ReCoSoC 2017 - Proceedings*; 2017.
- [C12] Torti, E.; Cividini, C.; Gatti, A.; Danese, G.; Leporati, F.; **Fabelo, H.**; Ortega, S.; Callicò, G. M. The HELICoiD Project: Parallel SVM for Brain Cancer Classification. In *Proceedings - 20th Euromicro Conference on Digital System Design, DSD 2017*; 2017.
- [C13] **Fabelo, H.**; Ortega, S.; Kabwama, S.; Callico, G. M.; Bulters, D.; Szolna, A.; Pineiro, J. F.; Sarmiento, R. HELICoiD project: A new use of hyperspectral imaging for brain cancer detection in real-time during neurosurgical operations. In *Proceedings of SPIE - The International Society for Optical Engineering*; 2016; Vol. 9860.
- [C14] **Fabelo, H.**; Ortega, S.; Guerra, R.; Callicó, G.; Szolna, A.; Piñeiro, J. F.; Tejedor, M.; López, S.; Sarmiento, R. A novel use of hyperspectral images for human brain cancer detection using *in-vivo* samples. In *BIOSIGNALS 2016 - 9th International Conference on Bio-Inspired Systems and Signal Processing, Proceedings; Part of 9th International Joint Conference on Biomedical Engineering Systems and Technologies, BIOSTEC 2016*; 2016.
- [C15] Madroñal, D.; **Fabelo, H.**; Lazcano, R.; Callicó, G. M.; Juárez, E.; Sanz, C. Parallel implementation of a hyperspectral image linear SVM classifier using RVC-CAL. In *Proceedings of SPIE - The International Society for Optical Engineering*; 2016; Vol. 10007.
- [C16] Ortega, S.; Callico, G. M.; Plaza, M. L.; Camacho, R.; **Fabelo, H.**; Sarmiento, R. Hyperspectral database of pathological *in-vitro* human brain samples to detect carcinogenic tissues. In *Proceedings - International Symposium on Biomedical Imaging*; 2016; Vol. 2016–June.

- [C17] Dopido, I.; Deniz, C.; **Fabelo, H.**; Callico, G. M.; Lopez, S.; Sarmiento, R.; Bulters, D.; Casselden, E.; Bulstrode, H. Decision Tree Classification System for Brain Cancer Detection using Spectrographic Samples. In *2015 Conference on Design of Circuits and Integrated Systems, DCIS 2015*; 2016.
- [C18] **Fabelo, H.**; M. Callico, G.; Vega, A.; Aleman, M.; de Pablo, A.; Sanjuan, L.; Sarmiento, R. HELICoiD Demonstrator for Intraoperative Brain Cancer Detection using Hyperspectral Images. In *Jornadas de Computación Empotrada (JCE 15)*; Cordoba, 2015. **[Best Paper Award]**



## Annex C: Sinopsis en español

La imagen hiperespectral es una tecnología que combina dos técnicas que han coexistido independientemente durante décadas: la espectroscopia y la fotografía digital. Por una parte, la espectroscopia estudia la interacción entre la radiación electromagnética y la materia. Dicha interacción es única para cada material. La curva que relaciona la radiación electromagnética con un determinado material se denomina firma espectral, y a través de su análisis es posible discriminar entre distintos materiales. Se trata pues, de una especie de huella digital que identifica cada material. Por otro lado, la fotografía digital permite capturar imágenes de una determinada escena, haciendo posible el análisis de características espaciales de determinados objetos tales como su morfología o su textura.

La imagen hiperespectral ha sido empleada tradicionalmente para labores de teledetección (*Remote Sensing*), incluyendo diversas aplicaciones como podrían ser la agricultura de precisión, la mineralogía o los estudios medioambientales. La potencialidad de esta tecnología para diferenciar entre distintos tipos de materiales, ha hecho que se empleen en otros campos muy diversos. Por ejemplo, los restauradores de obras de arte emplean esta tecnología para identificar qué pigmentos son los que han sido empleados en una determinada obra con el fin de mejorar su restauración. Por otro lado, en ciertas plantas de reciclaje esta tecnología se emplea para ordenar automáticamente los distintos tipos de materiales. En la industria alimentaria, esta técnica se emplea para la inspección de la calidad de diferentes alimentos, evitando los análisis biológicos invasivos requeridos en las metodologías tradicionales. También en la industria farmacéutica se aprovecha de las capacidades de las imágenes hiperespectrales para realizar un análisis químico no invasivo, por ejemplo, con el fin de diferenciar entre medicamentos originales y de contrabando que, a simple vista, parecen idénticos.

En el campo de la medicina, las imágenes hiperespectrales también han despertado el interés de la comunidad científica en los últimos años. Esto se debe a que se ha demostrado que la interacción entre la radiación electromagnética y los tejidos proporciona información útil para el diagnóstico. En los últimos años el uso de esta tecnología ha tenido un gran auge en el campo de la biomedicina, dada su eficacia para detectar enfermedades y su carácter no invasivo. Por ejemplo, esta técnica se ha utilizado para detectar niveles altos de colesterol del rostro humano o para la detección de artritis a través de la inspección de la luz reflejada en la piel. Esta tecnología también ha sido empleada para la mejora en la visualización de los vasos sanguíneos o para diferenciar automáticamente entre venas y arterias en procedimientos quirúrgicos. Su

carácter no invasivo, ha permitido además que esta tecnología se use para medir los niveles de oxigenación de la retina, del cerebro o del riñón.

En lo que respecta a la detección de cáncer, Las imágenes hiperespectrales se plantean con el fin de proporcionar a los cirujanos una herramienta de ayuda al diagnóstico que permita la resección total del tejido tumoral, así como evitar la resección errónea de tejido sano. Se ha descrito su potencial utilidad en la detección de diferentes tipos de tumores en animales (cáncer de próstata, cáncer de cabeza y cuello o cáncer de mama) y en humanos (cáncer de lengua, tumores de piel o de estómago).

Uno de los principales beneficios de esta tecnología es que puede utilizarse como una herramienta de asistencia visual durante las resecciones de tumores cerebrales. Este tipo de tumor se clasifica según su histología y parámetros moleculares, siendo los gliomas malignos la forma predominante de tumores cerebrales primarios en adultos, que causan entre el 2 y el 3% de las muertes por cáncer en todo el mundo. La cirugía es una de las principales opciones de tratamiento para los tumores cerebrales, además de la radioterapia y la quimioterapia. Sin embargo, el cirujano a menudo es incapaz de distinguir con precisión entre el tumor y el tejido cerebral normal a simple vista debido a que los tumores cerebrales se infiltran y difunden en el tejido normal circundante. Durante las operaciones neuroquirúrgicas es frecuente que se extraiga demasiado tejido cerebral normal (llamado margen de seguridad) o que no se retire del todo el tejido tumoral (llamado tumor residual). Varios estudios han demostrado que el tumor residual es la causa más común de recurrencia del tumor y es una causa importante de morbilidad y mortalidad. En contraste, se ha demostrado que la sobre-resección del tejido del tumor cerebral causa daños neurológicos permanentes que afectan la calidad de vida de los pacientes.

Varias herramientas de ayuda al diagnóstico por imagen, como la neuronavegación intraoperatoria, la resonancia magnética intraoperatoria (iMRI), el ultrasonido intraoperatorio (iUS) y los marcadores tumorales fluorescentes (por ejemplo, ácido 5-aminolevulínico, 5-ALA), se utilizan comúnmente para ayudar a los cirujanos a delinear los tumores cerebrales. No obstante, estas tecnologías tienen varias limitaciones. La neuronavegación intraoperatoria se ve afectada por el fenómeno llamado *brain shift* (desplazamiento de la masa cerebral), donde el vínculo de la imagen preoperatoria con la posición real del cerebro del paciente se ve afectado por la deformación cerebral producida después de la craneotomía y la durtomía. La iMRI extiende significativamente la duración de la cirugía (entre 20 y 75 minutos por imagen), generando un número limitado de imágenes y requiriendo salas de operaciones especiales. Por otro lado, el iUS es barato, obtiene los resultados en tiempo real y no se ve afectado por el *brain shift*. Sin embargo, el uso de iUS puede causar la resección del parénquima histológicamente normal. Finalmente, aunque el 5-ALA puede identificar los límites del tumor, éste produce efectos secundarios relevantes en el paciente y solo se puede utilizar para tumores de alto grado. Por lo tanto, la imagen hiperespectral puede ser una prometedora solución para la delimitación intraoperatoria del margen de los tumores cerebrales, al ser una modalidad de imagen que no ionizante, no invasiva y que no requiere contacto.

En esta tesis se describen los trabajos desarrollados con el objetivo de resolver los problemas expuestos anteriormente relacionados con la detección y delimitación intraoperatoria de tumores cerebrales. En estos estudios, se ha investigado el desarrollo de algoritmos de aprendizaje de máquina y de aprendizaje profundo que utilizan

imágenes hiperespectrales de cáncer cerebral obtenidas *in-vivo* para identificar los márgenes de tumores cerebrales.

Todos estos estudios fueron realizados dentro del proyecto europeo HELICoiD (*HypErspectraL Imaging Cancer Detection* - 618080) cuyo objetivo principal era utilizar imágenes hiperespectrales para generalizar una metodología que permitiera discriminar entre tejidos normales y malignos en tiempo real durante procedimientos neuroquirúrgicos. Para este propósito, se diseñó y construyó un demostrador intraoperatorio capaz de adquirir imágenes intraoperatorias hiperespectrales y procesarlas en tiempo real para ayudar a los neurocirujanos durante la resección. Este demostrador es capaz de capturar imágenes hiperespectrales en el rango espectral comprendido entre 400 y 1700 nm en aproximadamente 2 minutos usando dos cámaras tipo pushbroom. El sistema obtiene dos cubos hiperespectrales, uno en el rango VNIR (*Visual and Near Infrared* - 400 a 1000 nm) formado por 826 bandas espectrales y una alta resolución espacial de  $1004 \times 1787$  píxeles ( $129 \times 230$  mm) y otro en el rango NIR (*Near Infrared* - 900 a 1700 nm) formado por 172 bandas espectrales y una baja resolución espacial de  $320 \times 479$  píxeles ( $153 \times 230$  mm). Sin embargo, únicamente la información del rango VNIR fue empleada para el desarrollo de los algoritmos, debido a la baja resolución de la cámara NIR. Esta baja resolución no permite hacer un etiquetado fiable con el que realizar el entrenamiento de los algoritmos de aprendizaje automático supervisado.

El sistema de adquisición de HS se evaluó durante procedimientos quirúrgicos en dos hospitales diferentes en el Reino Unido y España, obteniendo 80 imágenes hiperespectrales de 36 pacientes diferentes en los rangos espectrales VNIR y NIR. Sin embargo, en el trabajo realizado en esta tesis solo se empleó la información VNIR, que incluyó 44 cubos de 35 pacientes diferentes, debido a la baja resolución de la cámara NIR. Esta baja resolución no permite hacer un etiquetado fiable con el que realizar el entrenamiento de los algoritmos de aprendizaje automático supervisado. Además, se estableció una metodología específica para obtener una base de datos de referencia para ser empleada en el desarrollo de los algoritmos hiperespectrales de detección de cáncer cerebral. Este conjunto de datos de referencia se generó utilizando una herramienta de etiquetado semiautomática basada en el algoritmo SAM (*Spectral Angle Mapper*). La herramienta de etiquetado fue empleada por los especialistas (neurocirujanos) para etiquetar 37 imágenes de 22 pacientes diferentes, generando un mapa de referencia de cada imagen. En estas imágenes, el tumor y el tejido normal se etiquetaron (cuando era posible), así como los vasos sanguíneos y otros tejidos, materiales o sustancias que se pueden encontrar en la escena quirúrgica y no son relevantes para el procedimiento de resección quirúrgica (llamado *background*). Este conjunto de datos incluye tumores primarios (glioblastoma grado IV y oligodendrogliomas anaplásicos de grado III y II) y tumores secundarios (cuyo origen era pulmón, riñón y mama). Un total de 377,584 firmas espectrales se incluyeron en el conjunto de datos de referencia.

Utilizando la base de datos obtenida, se desarrolló un algoritmo para clasificar imágenes hiperespectrales para la detección y delimitación de cáncer cerebral en función de las propiedades espaciales y espectrales de las imágenes hiperespectrales. Los resultados preliminares obtenidos en la clasificación supervisada de los tejidos que fueron previamente etiquetados por los especialistas, demuestran que es posible discriminar con precisión entre tejido normal, tejido tumoral, vasos sanguíneos y fondo

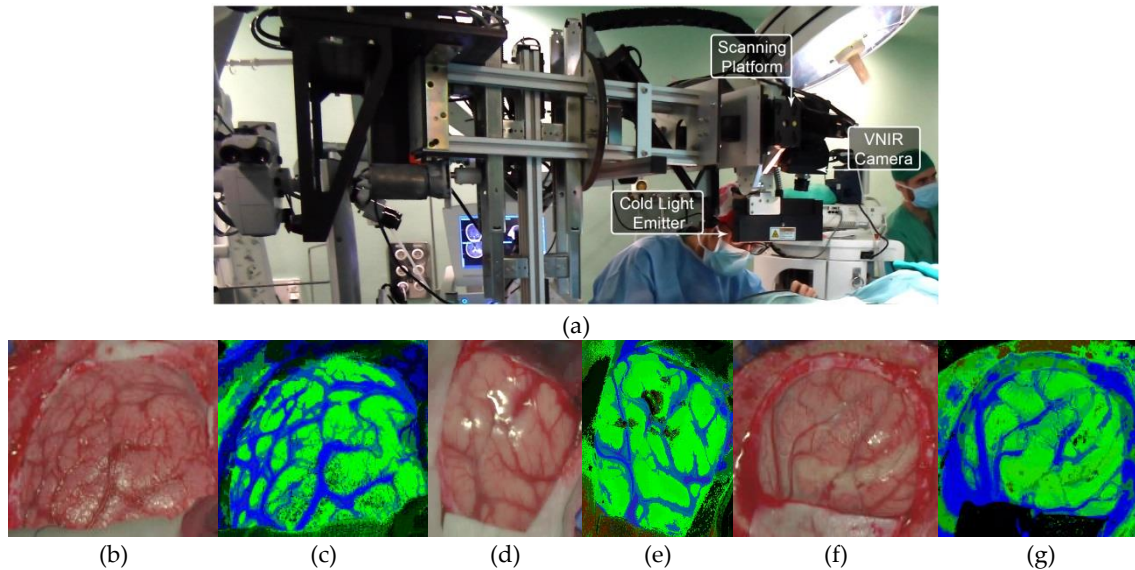


con una precisión superior al 99% mediante validación intra-paciente. Utilizando los modelos supervisados generados con los datos etiquetados, se clasificaron y evaluaron cualitativamente 5 cubo hiperespectrales al completo. Se generaron cinco mapas de clasificación con el algoritmo SVM (*Support Vector Machine*) obtenidos de cinco pacientes diferentes afectados por un tumor glioblastoma de grado IV. Estos mapas permiten identificar las regiones donde se localiza el tumor. Empleando un método de optimización espectral-espacial basado en un filtro KNN (*K-Nearest Neighbors*) y una reducción dimensional de FR-t-SNE (*Fixed Reference t-Distributed Stochastic Neighbor Embedding*), los mapas de clasificación de SVM se homogeneizaron espacialmente, obteniendo una identificación clara de las regiones tumorales utilizando estos mapas de clasificación supervisados espacial-espectrales. Sin embargo, estos mapas no ofrecían una descripción precisa de los límites, por lo que se incluyó una etapa no supervisada en el algoritmo basada en el método de agrupamiento HKM (*Hieararchical k-Means*). Éste método proporcionó un mapa de segmentación donde se delinearón los límites de 24 regiones diferentes con características espectrales similares. La fusión del mapa de clasificación supervisado espacial-espectral y el mapa de segmentación no supervisada a través de un algoritmo de votación mayoritaria (*Majority Voting - MV*) generó el mapa de clasificación final, donde los límites de los diferentes tejidos, materiales o sustancias presentados en la imagen se identificaron dentro de una clase determinada. En resumen, los mapas de clasificación espectral espacial permitieron asignar cada grupo en el mapa de segmentación a una clase de tejido identificable.

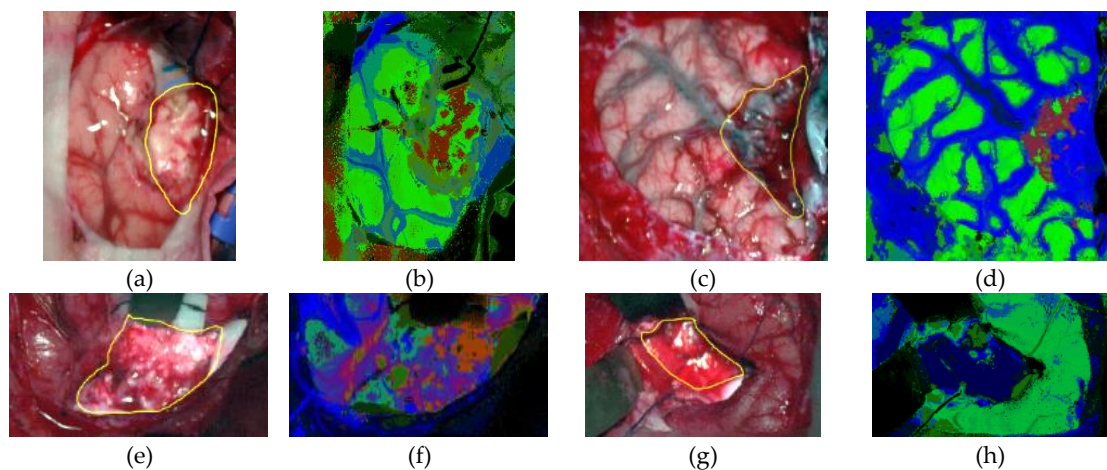
Empleando la información proporcionada por el mapa final, se analizaron tres formas diferentes de representar los resultados finales. El primero fue el mapa de MV, donde se asigna la probabilidad máxima de cada clase a cada grupo, representando el grupo con el color correspondiente: rojo para el tejido tumoral, verde para el tejido normal, azul para el tejido hipervasculizado y negro para el *background*. Por otro lado, el mapa de primera densidad máxima (OMD – *One Maximum Density*) muestra el color de cada clase degradado de acuerdo con el valor de la probabilidad máxima para cada clase. Mediante el uso de esta técnica, fue posible identificar los grupos que se ajustaban solo ligeramente a su clase asignada. Finalmente, el mapa tres máximas densidades (TMD – *Three Maximum Density*) representa cada color como una combinación entre las diferentes clases mezcladas en un cierto grupo. Este mapa es el más valioso para el neurocirujano, ya que ofrece la posibilidad de evaluar el grado de infiltración del tumor en el tejido cerebral normal circundante. Esta evaluación es clave para juzgar la extensión deseada de la resección.

Como prueba de concepto, el demostrador intraoperatorio desarrollado en este trabajo fue capaz de generar mapas temáticos de la superficie cerebral expuesta durante las operaciones quirúrgicas utilizando el algoritmo hiperespectral de detección de cáncer cerebral *in vivo* desarrollado y optimizado para su ejecución en tiempo de cirugía. La implementación del algoritmo se dividió entre la unidad de control y un acelerador de hardware, donde las tareas computacionales más altas se implementaron en una plataforma de varios núcleos para lograr un tiempo de procesamiento intraoperatorio (~ 1 min). El demostrador se validó utilizando siete imágenes obtenidas en cuatro operaciones neuroquirúrgicas. Los mapas de TMD obtenidos demuestran que el sistema no introdujo falsos positivos en el área de la parénquima cuando no había tumor presente y fue capaz de identificar diferentes tipos de tumores que no estaban presentes en la base de datos de entrenamiento. Figure C-1 y Figure C2 muestran el

demostrador de HELICoiD, las representaciones RGB sintéticas del cubo HS y los mapas temáticos correspondientes obtenidos con este algoritmo para el cerebro normal y el cerebro afectado por cáncer, respectivamente. En los mapas temáticos, el tejido tumoral se representa en color rojo, el tejido normal en verde, el tejido hipervascularizado en azul y el *background* en negro.



**Figure C-1: Demostrador de HELICoiD y resultados obtenidos en imágenes de cerebro normal de la base de datos de validación.** (a) Demostrador de HELICoiD; (b, d, f) Imágenes RGB sintéticas; (c, e, g) Mapas temáticos de la imagen hiperespectral, donde el tejido tumoral está representado en color rojo, el tejido normal en verde, el tejido hipervascularizado en azul y el *background* en negro.



**Figure C-2: Resultados de identificación del tejido tumoral obtenidos de la base de datos de validación empleando el demostrador HELICoiD.** (a,c,e,g) Imágenes RGB sintéticas; (b,d,f,h) Mapas temáticos de la imagen hiperespectral, donde el tejido tumoral está representado en color rojo, el tejido normal en verde, el tejido hipervascularizado en azul y el *background* en negro.

Finalmente, una de las últimas investigaciones realizadas en esta tesis presentó una comparación entre el uso de algoritmos basados en SVM y el uso de algoritmos de aprendizaje profundo. Estos experimentos se llevaron a cabo utilizando solo las muestras de tumor de glioblastoma disponibles en la base de datos (26 imágenes hiperespectrales de 16 pacientes) y teniendo en cuenta la variabilidad inter-paciente

mediante el método de validación cruzada. Los resultados obtenidos utilizando arquitecturas de aprendizaje profundo fueron altamente prometedores, mejorando la precisión de la identificación del tumor en aproximadamente un 16% con respecto a los resultados de los algoritmos basados en SVM. Sin embargo, se deben realizar investigaciones adicionales para ampliar la base de datos de entrenamiento y la base de datos de validación con más pacientes y tipos de tumores. Además, debe realizarse una extensa validación clínica del sistema. En esta validación clínica, se debe realizar un análisis patológico completo de toda el área del tumor delineada por el mapa de clasificación (especialmente en los límites entre el tumor y el tejido normal circundante), así como para correlacionar los resultados con la información de la MRI (*Magnetic Resonance Imaging*) para saber si la infiltración del tumor en el tejido cerebral normal puede ser identificada adecuadamente por el sistema. Además, a través de la validación clínica, se debe estudiar la relación entre la mejoría de los resultados del paciente y el uso del sistema durante la cirugía. Por último, deberá estudiarse el uso de la información NIR para evaluar si puede ser beneficioso para la mejora de los resultados de la clasificación.

# Bibliography

- [1] N. I. for H. and C. Excellence, “Improving Outcomes for People with Brain and Other CNS Tumours,” *Cancer service guideline [CSG10]*, 2016. .
- [2] D. N. Louis *et al.*, “The 2016 World Health Organization Classification of Tumors of the Central Nervous System: a summary,” *Acta Neuropathologica*, vol. 131, no. 6. pp. 803–820, 2016.
- [3] D. K. Robson, “Pathology & Genetics. Tumours of the Nervous System. World Health Organisation Classification of Tumours. P. Kleihues and k. Cavenee (eds). IARC Press, Lyon, 2000. No. of pages: 314. ISBN: 92 832 2409 4,” *J. Pathol.*, vol. 193, no. 2, p. 276, 2001.
- [4] W. Stummer *et al.*, “Counterbalancing risks and gains from extended resections in malignant glioma surgery: A supplemental analysis from the randomized 5-aminolevulinic acid glioma resection study: Clinical article,” *J. Neurosurg.*, vol. 114, no. 3, pp. 613–623, 2011.
- [5] N. Sanai and M. S. Berger, “Glioma extent of resection and its impact on patient outcome,” *Neurosurgery*, vol. 62, no. 4. pp. 753–764, 2008.
- [6] N. Sanai and M. S. Berger, “Operative Techniques for Gliomas and the Value of Extent of Resection,” *Neurotherapeutics*, vol. 6, no. 3, pp. 478–486, 2009.
- [7] K. Petrecca, M. Guiot, V. Panet-Raymond, and L. Souhami, “Failure pattern following complete resection plus radiotherapy and temozolomide is at the resection margin in patients with glioblastoma,” *J. Neurooncol.*, vol. 111, no. 1, pp. 19–23, 2013.
- [8] I. J. Gerard, M. Kersten-Oertel, K. Petrecca, D. Sirhan, J. A. Hall, and D. L. Collins, “Brain shift in neuronavigation of brain tumors: A review,” *Medical Image Analysis*, vol. 35. pp. 403–420, 2017.
- [9] R. E. Kast *et al.*, “Raman molecular imaging of brain frozen tissue sections,” *J. Neurooncol.*, vol. 120, no. 1, pp. 55–62, 2014.
- [10] M. H. T. Reinges *et al.*, “Course of brain shift during microsurgical resection of supratentorial cerebral lesions: Limits of conventional neuronavigation,” *Acta Neurochir. (Wien)*, vol. 146, no. 4, pp. 369–377, 2004.
- [11] C. Nimsky, O. Ganslandt, P. Hastreiter, and R. Fahlbusch, “Intraoperative compensation for brain shift,” *Surg. Neurol.*, vol. 56, no. 6, pp. 357–364, 2001.
- [12] K. A. Ganser *et al.*, “Quantification of brain shift effects in MRI images,” *Biomed. Tech. (Berl)*, vol. 42 Suppl, pp. 247–248, 1997.
- [13] W. Stummer, U. Pichlmeier, T. Meinel, O. D. Wiestler, F. Zanella, and H. J. Reulen, “Fluorescence-guided surgery with 5-aminolevulinic acid for resection of malignant glioma: a randomised controlled multicentre phase III trial,” *Lancet Oncol.*, vol. 7, no. 5, pp. 392–401, 2006.
- [14] F. W. Floeth *et al.*, “Comparison of 18F-FET PET and 5-ALA fluorescence in cerebral gliomas,” *Eur. J. Nucl. Med. Mol. Imaging*, vol. 38, no. 4, pp. 731–741, 2011.

- [15] M. Kamruzzaman and D.-W. Sun, "Introduction to Hyperspectral Imaging Technology," *Comput. Vis. Technol. Food Qual. Eval.*, pp. 111–139, Jan. 2016.
- [16] C. Starr, C. Evers, and L. Starr, *Biology: concepts and applications without physiology*. Cengage Learning, 2010.
- [17] D. Manolakis and G. Shaw, "Detection Algorithms for Hyperspectral Imaging Applications," *IEEE Signal Process. Mag.*, pp. 29–43, 2002.
- [18] M. Govender, K. Chetty, and H. Bulcock, "A review of hyperspectral remote sensing and its application in vegetation and water resource studies," *Water SA*, vol. 33, no. 2, pp. 145–152, 2009.
- [19] F. D. van der Meer *et al.*, "Multi- and hyperspectral geologic remote sensing: A review," *Int. J. Appl. Earth Obs. Geoinf.*, vol. 14, no. 1, pp. 112–128, Feb. 2012.
- [20] H. Liang, "Advances in multispectral and hyperspectral imaging for archaeology and art conservation," *Appl. Phys. A Mater. Sci. Process.*, vol. 106, no. 2, pp. 309–323, 2012.
- [21] V. Miljković and D. Gajski, "Adaptation of industrial hyperspectral line scanner for archaeological applications," in *International Archives of the Photogrammetry, Remote Sensing and Spatial Information Sciences - ISPRS Archives*, 2016, vol. 41, pp. 343–345.
- [22] W. Fortunato de Carvalho Rocha, G. P. Sabin, P. H. Março, and R. J. Poppi, "Quantitative analysis of piroxicam polymorphs pharmaceutical mixtures by hyperspectral imaging and chemometrics," *Chemom. Intell. Lab. Syst.*, vol. 106, no. 2, pp. 198–204, Apr. 2011.
- [23] L. de M. França, M. F. Pimentel, S. da S. Simões, S. Grangeiro, J. M. Prats-Montalbán, and A. Ferrer, "NIR hyperspectral imaging to evaluate degradation in captopril commercial tablets," *Eur. J. Pharm. Biopharm.*, vol. 104, pp. 180–188, Jul. 2016.
- [24] G. J. Edelman, E. Gaston, T. G. van Leeuwen, P. J. Cullen, and M. C. G. Aalders, "Hyperspectral imaging for non-contact analysis of forensic traces," *Forensic Science International*, vol. 223, no. 1–3, pp. 28–39, 2012.
- [25] C. S. Silva, M. F. Pimentel, R. S. Honorato, C. Pasquini, J. M. Prats-Montalbán, and A. Ferrer, "Near infrared hyperspectral imaging for forensic analysis of document forgery," *Analyst*, vol. 139, no. 20, pp. 5176–5184, Jul. 2014.
- [26] M. Á. Fernández de la Ossa, J. M. Amigo, and C. García-Ruiz, "Detection of residues from explosive manipulation by near infrared hyperspectral imaging: A promising forensic tool," *Forensic Sci. Int.*, vol. 242, pp. 228–235, Sep. 2014.
- [27] P. W. Yuen and M. Richardson, "An introduction to hyperspectral imaging and its application for security, surveillance and target acquisition," *Imaging Sci. J.*, vol. 58, no. 5, pp. 241–253, 2010.
- [28] V. C. Coffey, "Hyperspectral Imaging for Safety and Security," *Opt. Photonics News*, vol. 26, no. 10, p. 26, Oct. 2015.
- [29] M. Teke, H. S. Deveci, O. Haliloglu, S. Z. Gurbuz, and U. Sakarya, "A short survey of hyperspectral remote sensing applications in agriculture," *2013 6th Int. Conf. Recent Adv. Sp. Technol.*, pp. 171–176, 2013.
- [30] L. M. Dale *et al.*, "Hyperspectral imaging applications in agriculture and agro-food product quality and safety control: A review," *Appl. Spectrosc. Rev.*, vol. 48, no. 2, pp. 142–159, Mar. 2013.
- [31] D. Wu and D.-W. Sun, "Advanced applications of hyperspectral imaging technology for food quality and safety analysis and assessment: A review—Part I: Fundamentals," *Innov. Food Sci. Emerg. Technol.*, vol. 19, pp. 1–14, 2013.
- [32] Y.-Z. Feng and D.-W. Sun, "Application of Hyperspectral Imaging in Food Safety Inspection and Control: A Review," *Crit. Rev. Food Sci. Nutr.*, vol. 52, no. 11, pp. 1039–1058, Nov. 2012.
- [33] D. Lorente, N. Aleixos, J. Gómez-Sanchis, S. Cubero, O. L. García-Navarrete, and J. Blasco, "Recent Advances and Applications of Hyperspectral Imaging for Fruit and Vegetable Quality Assessment," *Food Bioprocess Technol.*, vol. 5, no. 4, pp. 1121–1142, Nov. 2011.

- [34] G. Lu and B. Fei, "Medical hyperspectral imaging: a review.," *J. Biomed. Opt.*, vol. 19, no. 1, p. 10901, 2014.
- [35] M. A. Calin, S. V. Parasca, D. Savastru, and D. Manea, "Hyperspectral imaging in the medical field: Present and future," *Appl. Spectrosc. Rev.*, vol. 49, no. 6, pp. 435–447, 2014.
- [36] A. Bjorgan, M. Denstedt, M. Milanič, L. A. Paluchowski, and L. L. Randeberg, "Vessel contrast enhancement in hyperspectral images," in *Optical Biopsy XIII: Toward Real-Time Spectroscopic Imaging and Diagnosis*, 2015.
- [37] H. Akbari, Y. Kosugi, K. Kojima, and N. Tanaka, "Blood vessel detection and artery-vein differentiation using hyperspectral imaging," in *Proceedings of the 31st Annual International Conference of the IEEE Engineering in Medicine and Biology Society: Engineering the Future of Biomedicine, EMBC 2009*, 2009, pp. 1461–1464.
- [38] H. Akbari, Y. Kosugi, K. Kojima, and N. Tanaka, "Detection and Analysis of the Intestinal Ischemia Using Visible and Invisible Hyperspectral Imaging," *IEEE Trans. Biomed. Eng.*, vol. 57, no. 8, pp. 2011–2017, 2010.
- [39] D. J. Mordant *et al.*, "Spectral imaging of the retina," *Eye*, vol. 25, no. 3, pp. 309–320, Mar. 2011.
- [40] W. R. Johnson, D. W. Wilson, W. Fink, M. Humayun, and G. Bearman, "Snapshot hyperspectral imaging in ophthalmology," *J. Biomed. Opt.*, 2007.
- [41] L. Gao, R. T. Smith, and T. S. Tkaczyk, "Snapshot hyperspectral retinal camera with the Image Mapping Spectrometer (IMS)," *Biomed. Opt. Express*, vol. 3, no. 1, p. 48, Jan. 2012.
- [42] M. Milanic, A. Bjorgan, M. Larsson, T. Strömberg, and L. L. Randeberg, "Detection of hypercholesterolemia using hyperspectral imaging of human skin," in *Clinical and Biomedical Spectroscopy and Imaging IV*, 2015.
- [43] L. Zhi, D. Zhang, J. qi Yan, Q. L. Li, and Q. lin Tang, "Classification of hyperspectral medical tongue images for tongue diagnosis," *Comput. Med. Imaging Graph.*, vol. 31, no. 8, pp. 672–678, 2007.
- [44] D. Yudovsky, A. Nouvong, and L. Pilon, "Hyperspectral Imaging in Diabetic Foot Wound Care," *J. Diabetes Sci. Technol.*, vol. 4, no. 5, pp. 1099–1113, Sep. 2010.
- [45] M. Knauth, C. R. Wirtz, V. M. Tronnier, N. Aras, S. Kunze, and K. Sartor, "Intraoperative MR imaging increases the extent of tumor resection in patients with high-grade gliomas," *Am. J. Neuroradiol.*, 1999.
- [46] T. Chowdhury *et al.*, "The Role of Intraoperative MRI in Awake Neurosurgical Procedures: A Systematic Review.," *Front. Oncol.*, vol. 8, p. 434, 2018.
- [47] R. M. Young, A. Jamshidi, G. Davis, and J. H. Sherman, "Current trends in the surgical management and treatment of adult glioblastoma.," *Ann. Transl. Med.*, 2015.
- [48] A. G. Chacko, N. K. S. Kumar, G. Chacko, R. Athyal, V. Rajshekhar, and G. Unsgaard, "Intraoperative ultrasound in determining the extent of resection of parenchymal brain tumours - A comparative study with computed tomography and histopathology," *Acta Neurochir. (Wien)*, 2003.
- [49] M. a Hammoud, B. L. Ligon, R. elSouki, W. M. Shi, D. F. Schomer, and R. Sawaya, "Use of intraoperative ultrasound for localizing tumors and determining the extent of resection: a comparative study with magnetic resonance imaging.," *J. Neurosurg.*, 1996.
- [50] F. Prada *et al.*, "Intraoperative contrast-enhanced ultrasound for brain tumor surgery," *Neurosurgery*, 2014.
- [51] A. V. Moiyadi and P. Shetty, "Direct navigated 3D ultrasound for resection of brain tumors: a useful tool for intraoperative image guidance," *Neurosurg. Focus*, 2016.
- [52] W. Stummer, U. Pichlmeier, T. Meinel, O. D. Wiestler, F. Zanella, and H. J. Reulen, "Fluorescence-guided surgery with 5-aminolevulinic acid for resection of malignant glioma: a randomised controlled multicentre phase III trial," *Lancet Oncol.*, vol. 7, no. 5, pp. 392–401, 2006.

- [53] W. Stummer *et al.*, “Intraoperative detection of malignant gliomas by 5-aminolevulinic acid- induced porphyrin fluorescence,” *Neurosurgery*, vol. 42, no. 3, pp. 518–526, 1998.
- [54] T. Adão *et al.*, “Hyperspectral imaging: A review on UAV-based sensors, data processing and applications for agriculture and forestry,” *Remote Sens.*, vol. 9, no. 11, 2017.
- [55] N. Hagen and M. W. Kudenov, “Review of snapshot spectral imaging technologies,” *Opt. Eng.*, 2013.
- [56] M. Li, S. Zang, B. Zhang, S. Li, and C. Wu, “A review of remote sensing image classification techniques: The role of Spatio-contextual information,” *Eur. J. Remote Sens.*, 2014.
- [57] M. Fauvel, Y. Tarabalka, J. A. Benediktsson, J. Chanussot, and J. C. Tilton, “Advances in spectral-spatial classification of hyperspectral images,” *Proc. IEEE*, vol. 101, no. 3, pp. 652–675, 2013.
- [58] G. Cano *et al.*, “Automatic selection of molecular descriptors using random forest: Application to drug discovery,” *Expert Syst. Appl.*, vol. 72, pp. 151–159, 2017.
- [59] T. Puchert, D. Lochmann, J. C. Menezes, and G. Reich, “Near-infrared chemical imaging (NIR-CI) for counterfeit drug identification: A four-stage concept with a novel approach of data processing (Linear Image Signature),” *J. Pharm. Biomed. Anal.*, vol. 51, no. 1, pp. 138–145, 2010.
- [60] A. Gowen, C. Odonnell, P. Cullen, G. Downey, and J. Frias, “Hyperspectral imaging-an emerging process analytical tool for food quality and safety control,” *Trends Food Sci. Technol.*, vol. 18, no. 12, pp. 590–598, 2007.
- [61] Y. Montembeault, P. Lagueux, V. Farley, A. Villemaire, and K. C. Gross, “Hyper-Cam: Hyperspectral IR imaging applications in defence innovative research,” in *2010 2nd Workshop on Hyperspectral Image and Signal Processing: Evolution in Remote Sensing*, 2010.
- [62] P. Fisher, “The pixel: A snare and a delusion,” *Int. J. Remote Sens.*, 1997.
- [63] C.-I. Chang, *Hyperspectral imaging: techniques for spectral detection and classification*, vol. 1. Springer Science & Business Media, 2003.
- [64] H. F. Grahn and P. Geladi, Eds., *Techniques and Applications of Hyperspectral Image Analysis*. Chichester, UK: John Wiley & Sons, Ltd, 2007.
- [65] L. Zhang, L. Zhang, and B. Du, “Deep learning for remote sensing data: A technical tutorial on the state of the art,” *IEEE Geosci. Remote Sens. Mag.*, 2016.
- [66] T. G. Dietterich, “Ensemble Methods in Machine Learning,” in *Multiple Classifier Systems*, Springer Nature, 2000, pp. 1–15.
- [67] J. C.-W. Chan and D. Paelinckx, “Evaluation of Random Forest and Adaboost tree-based ensemble classification and spectral band selection for ecotope mapping using airborne hyperspectral imagery,” *Remote Sens. Environ.*, vol. 112, no. 6, pp. 2999–3011, Jun. 2008.
- [68] J. A. Benediktsson, J. A. Palmason, and J. R. Sveinsson, “Classification of hyperspectral data from urban areas based on extended morphological profiles,” *IEEE Trans. Geosci. Remote Sens.*, vol. 43, no. 3, pp. 480–491, Mar. 2005.
- [69] H. Akbari, Y. Kosugi, K. Kojima, and N. Tanaka, “Wavelet-Based Compression and Segmentation of Hyperspectral Images in Surgery,” in *Lecture Notes in Computer Science*, Springer Nature, pp. 142–149.
- [70] F. Blanco, M. López-Mesas, S. Serranti, G. Bonifazi, J. Havel, and M. Valiente, “Hyperspectral imaging based method for fast characterization of kidney stone types,” *J. Biomed. Opt.*, vol. 17, no. 7, p. 760271, Jul. 2012.
- [71] G. Camps-Valls and L. Bruzzone, “Kernel-based methods for hyperspectral image classification,” *IEEE Trans. Geosci. Remote Sens.*, vol. 43, no. 6, pp. 1351–1362, Jun. 2005.
- [72] Y. D. Zhang *et al.*, “Facial emotion recognition based on biorthogonal wavelet entropy,

- fuzzy support vector machine, and stratified cross validation,” *IEEE Access*, vol. 4, pp. 8375–8385, 2016.
- [73] Y. Zhang *et al.*, “Comparison of machine learning methods for stationary wavelet entropy-based multiple sclerosis detection: decision tree, k-nearest neighbors, and support vector machine,” *Simulation*, vol. 92, no. 9, pp. 861–871, 2016.
- [74] S. Wang *et al.*, “Wavelet entropy and directed acyclic graph support vector machine for detection of patients with unilateral hearing loss in MRI scanning,” *Front. Comput. Neurosci.*, vol. 10, no. OCT, pp. 1–11, 2016.
- [75] V. Dey, Y. Zhang, and M. Zhong, “A review on image segmentation techniques with remote sensing perspective,” *ISPRS TC VII Symp. – 100 Years ISPRS*, 2010.
- [76] S. Theodoridis and K. Koutroumbas, “Clustering Algorithms I: Sequential Algorithms,” in *Pattern Recognition*, 2009.
- [77] J. A. Moore, “K-means and Hierarchical Clustering,” *Stat. Data Min. Tutorials*, 2001.
- [78] F. Zhang, B. Du, L. Zhang, and L. Zhang, “Hierarchical feature learning with dropout k-means for hyperspectral image classification,” *Neurocomputing*, 2016.
- [79] G. H. Ball and D. J. Hall, “ISODATA, a novel method of data analysis and pattern classification,” *Analysis*, 1965.
- [80] S. A. El-Rahman, “Hyperspectral imaging classification using ISODATA algorithm: Big data challenge,” in *Proceedings - 2015 5th International Conference on e-Learning, ECONF 2015*, 2016.
- [81] S. Narumalani, D. R. Mishra, J. Burkholder, P. B. T. Merani, and G. Willson, “A comparative evaluation of ISODATA and spectral angle mapping for the detection of saltcedar using airborne hyperspectral imagery,” *Geocarto Int.*, 2006.
- [82] Y. Zhao and G. Karypis, “Hierarchical clustering algorithms for document datasets,” *Data Min. Knowl. Discov.*, 2005.
- [83] S. C. Johnson, “Hierarchical clustering schemes,” *Psychometrika*, 1967.
- [84] N. Gillis, D. Kuang, and H. Park, “Hierarchical clustering of hyperspectral images using rank-two nonnegative matrix factorization,” *IEEE Trans. Geosci. Remote Sens.*, 2015.
- [85] K. Arai and A. R. Barakbah, “Hierarchical K-means: an algorithm for centroids initialization for K-means,” *Rep. Fac. Sci. Engrg. Reports Fac. Sci. Eng. Saga Univ. Saga Univ.*, 2007.
- [86] A. Banerjee, I. Dhillon, J. Ghosh, and S. Sra, “Generative model-based clustering of directional data,” in *Proceedings of the ninth ACM SIGKDD international conference on Knowledge discovery and data mining*, 2003, pp. 19–28.
- [87] K. Masood, N. Rajpoot, K. Rajpoot, and H. Qureshi, “Hyperspectral Colon Tissue Classification using Morphological Analysis,” in *International Conference on Emerging Technologies*, 2006, pp. 735–741.
- [88] B. Regeling *et al.*, “Hyperspectral Imaging Using Flexible Endoscopy for Laryngeal Cancer Detection,” *Sensors*, vol. 16, no. 8, p. 1288, 2016.
- [89] Y. A. LeCun, Y. Bengio, and G. E. Hinton, “Deep learning,” *Nature*, 2015.
- [90] G. Hinton, “Deep belief networks,” *Scholarpedia*, vol. 4, no. 5, p. 5947, 2009.
- [91] Y. LeCun, L. Bottou, Y. Bengio, and P. Haffner, “Gradient-based learning applied to document recognition,” *Proc. IEEE*, 1998.
- [92] Y. LeCun *et al.*, “Backpropagation Applied to Handwritten Zip Code Recognition,” *Neural Comput.*, 1989.
- [93] T. Li, J. Zhang, and Y. Zhang, “Classification of hyperspectral image based on deep belief networks,” in *2014 IEEE International Conference on Image Processing (ICIP)*, 2014, pp. 5132–5136.
- [94] K. Makantasis, K. Karantzalos, A. Doulamis, and N. Doulamis, “Deep Supervised Learning for Hyperspectral Data Classification through Convolutional Neural Networks,”



- IGARSS 2015. 2015 IEEE Int. Geosci. Remote Sens. Symp. Proc.* \, 2015.
- [95] W. Hu, Y. Huang, L. Wei, F. Zhang, and H. Li, "Deep convolutional neural networks for hyperspectral image classification," *J. Sensors*, 2015.
- [96] J. Yue, W. Zhao, S. Mao, and H. Liu, "Spectral-spatial classification of hyperspectral images using deep convolutional neural networks," *Remote Sens. Lett.*, 2015.
- [97] W. Zhao and S. Du, "Spectral-Spatial Feature Extraction for Hyperspectral Image Classification: A Dimension Reduction and Deep Learning Approach," *IEEE Trans. Geosci. Remote Sens.*, 2016.
- [98] D. Ravi *et al.*, "Deep Learning for Health Informatics," *IEEE J. Biomed. Heal. Informatics*, 2017.
- [99] M. M. A. Rahhal, Y. Bazi, H. Alhichri, N. Alajlan, F. Melgani, and R. R. Yager, "Deep learning approach for active classification of electrocardiogram signals," *Inf. Sci. (Ny)*, 2016.
- [100] Y. R. Tabar and U. Halici, "A novel deep learning approach for classification of EEG motor imagery signals," *J. Neural Eng.*, 2017.
- [101] S. Jirayucharoenasak, S. Pan-Ngum, and P. Israsena, "EEG-based emotion recognition using deep learning network with principal component based covariate shift adaptation," *ScientificWorldJournal*, 2014.
- [102] D. Maji, A. Santara, P. Mitra, and D. Sheet, "Ensemble of Deep Convolutional Neural Networks for Learning to Detect Retinal Vessels in Fundus Images," *CoRR*, 2016.
- [103] M. Melinscak, P. Prentasic, and S. Loncaric, "Retinal Vessel Segmentation Using Deep Neural Networks," in *International Conference on Computer Vision Theory and Applications (VISAPP 2015)*, 2015.
- [104] A. Lahiri, A. G. Roy, D. Sheet, and P. K. Biswas, "Deep neural ensemble for retinal vessel segmentation in fundus images towards achieving label-free angiography," in *Proceedings of the Annual International Conference of the IEEE Engineering in Medicine and Biology Society, EMBS*, 2016.
- [105] J. Y. Choi, T. K. Yoo, J. G. Seo, J. Kwak, T. T. Um, and T. H. Rim, "Multi-categorical deep learning neural network to classify retinal images: A pilot study employing small database," *PLoS One*, 2017.
- [106] B. Korbar *et al.*, "Deep Learning for Classification of Colorectal Polyps on Whole-slide Images," *J. Pathol. Inform.*, vol. 8, p. 30, 2017.
- [107] P. J. Chen, M. C. Lin, M. J. Lai, J. C. Lin, H. H. S. Lu, and V. S. Tseng, "Accurate Classification of Diminutive Colorectal Polyps Using Computer-Aided Analysis," *Gastroenterology*, 2018.
- [108] E. Ribeiro, A. Uhl, G. Wimmer, and M. Häfner, "Exploring Deep Learning and Transfer Learning for Colonic Polyp Classification," *Comput. Math. Methods Med.*, 2016.
- [109] D. Wang, A. Khosla, R. Gargeya, H. Irshad, and A. H. Beck, "Deep Learning for Identifying Metastatic Breast Cancer," *arXiv Prepr.*, 2016.
- [110] K. Sirinukunwattana, S. E. A. Raza, Y. W. Tsang, D. R. J. Snead, I. A. Cree, and N. M. Rajpoot, "Locality Sensitive Deep Learning for Detection and Classification of Nuclei in Routine Colon Cancer Histology Images," *IEEE Trans. Med. Imaging*, 2016.
- [111] H. Sharma, N. Zerbe, I. Klempert, O. Hellwich, and P. Hufnagl, "Deep convolutional neural networks for automatic classification of gastric carcinoma using whole slide images in digital histopathology," *Comput. Med. Imaging Graph.*, 2017.
- [112] D. Bychkov *et al.*, "Deep learning based tissue analysis predicts outcome in colorectal cancer," *Sci. Rep.*, 2018.
- [113] A. Cruz-Roa *et al.*, "Automatic detection of invasive ductal carcinoma in whole slide images with convolutional neural networks," in *Proc. of SPIE*, 2014.
- [114] H. Akbari, K. Uto, Y. Kosugi, K. Kojima, and N. Tanaka, "Cancer detection using infrared hyperspectral imaging," *Cancer Sci.*, vol. 102, no. 4, pp. 852–857, 2011.

- [115] S. Kiyotoki *et al.*, “New method for detection of gastric cancer by hyperspectral imaging: a pilot study,” *J. Biomed. Opt.*, vol. 18, no. 2, p. 026010, 2013.
- [116] A. Goto *et al.*, “Use of hyperspectral imaging technology to develop a diagnostic support system for gastric cancer,” *J. Biomed. Opt.*, vol. 20, no. 1, p. 016017, 2015.
- [117] B. Kim, N. Kehtarnavaz, P. LeBoulluec, H. Liu, Y. Peng, and D. Euhus, “Automation of ROI extraction in hyperspectral breast images,” *Conf. Proc. ... Annu. Int. Conf. IEEE Eng. Med. Biol. Soc. IEEE Eng. Med. Biol. Soc. Annu. Conf.*, vol. 2013, pp. 3658–3661, 2013.
- [118] R. Pourreza-Shahri, F. Saki, N. Kehtarnavaz, P. Leboulluec, and H. Liu, “Classification of ex-vivo breast cancer positive margins measured by hyperspectral imaging,” in *2013 IEEE International Conference on Image Processing, ICIP 2013 - Proceedings*, 2013, pp. 1408–1412.
- [119] B. Fei *et al.*, “Label-free reflectance hyperspectral imaging for tumor margin assessment: a pilot study on surgical specimens of cancer patients,” *J. Biomed. Opt.*, vol. 22, no. 08, p. 1, 2017.
- [120] G. Lu *et al.*, “Detection of head and neck cancer in surgical specimens using quantitative hyperspectral imaging,” *Clin. Cancer Res.*, vol. 23, no. 18, pp. 5426–5436, 2017.
- [121] M. Halicek *et al.*, “Deep convolutional neural networks for classifying head and neck cancer using hyperspectral imaging,” *J. Biomed. Opt.*, vol. 22, no. 6, p. 060503, Jun. 2017.
- [122] S. V. Panasyuk *et al.*, “Medical hyperspectral imaging to facilitate residual tumor identification during surgery,” *Cancer Biol. Ther.*, vol. 6, no. 3, pp. 439–446, Mar. 2007.
- [123] D. R. McCormack *et al.*, “In vivo hyperspectral imaging of microvessel response to trastuzumab treatment in breast cancer xenografts,” *Biomed. Opt. Express*, vol. 5, no. 7, p. 2247, 2014.
- [124] B. Fei, H. Akbari, and L. V. Halig, “Hyperspectral imaging and spectral-spatial classification for cancer detection,” in *2012 5th International Conference on Biomedical Engineering and Informatics, BMEI 2012*, 2012, pp. 62–64.
- [125] H. Akbari *et al.*, “Hyperspectral imaging and quantitative analysis for prostate cancer detection,” *J. Biomed. Opt.*, vol. 17, no. 7, p. 0760051, Jul. 2012.
- [126] G. Lu, L. Halig, D. Wang, Z. G. Chen, and B. Fei, “Spectral-Spatial Classification Using Tensor Modeling for Cancer Detection with Hyperspectral Imaging,” *Proc. SPIE-the Int. Soc. Opt. Eng.*, vol. 9034, p. 903413, 2014.
- [127] G. Lu, L. Halig, D. Wang, X. Qin, Z. G. Chen, and B. Fei, “Spectral-spatial classification for noninvasive cancer detection using hyperspectral imaging,” *J. Biomed. Opt.*, vol. 19, no. 10, p. 106004, 2014.
- [128] G. Lu, L. Halig, D. Wang, Z. G. Chen, and B. Fei, “Hyperspectral imaging for cancer surgical margin delineation: registration of hyperspectral and histological images,” 2014, vol. 9036, p. 90360S.
- [129] G. Lu, X. Qin, D. Wang, Z. G. Chen, and B. Fei, “Quantitative wavelength analysis and image classification for intraoperative cancer diagnosis with hyperspectral imaging,” in *Progress in Biomedical Optics and Imaging - Proceedings of SPIE*, 2015, vol. 9415.
- [130] G. Lu *et al.*, “Framework for hyperspectral image processing and quantification for cancer detection during animal tumor surgery,” *J. Biomed. Opt.*, vol. 20, no. 12, p. 126012, 2015.
- [131] R. Pike, G. Lu, D. Wang, Z. G. Chen, and B. Fei, “A Minimum Spanning Forest-Based Method for Noninvasive Cancer Detection With Hyperspectral Imaging,” *IEEE Trans. Biomed. Eng.*, vol. 63, no. 3, pp. 653–663, 2016.
- [132] R. T. Kester, N. Bedard, L. Gao, and T. S. Tkaczyk, “Real-time snapshot hyperspectral imaging endoscope,” *J. Biomed. Opt.*, vol. 16, no. 5, p. 56005, 2011.
- [133] J. L. Jayanthi *et al.*, “Diffuse reflectance spectroscopy: diagnostic accuracy of a non-invasive screening technique for early detection of malignant changes in the oral cavity,”

- BMJ Open*, vol. 1, no. 1, p. e000071, Jun. 2011.
- [134] B. Regeling *et al.*, “Development of an image pre-processor for operational hyperspectral laryngeal cancer detection,” *J. Biophotonics*, vol. 9, no. 3, pp. 235–245, Mar. 2016.
- [135] W. Laffers *et al.*, “Early recognition of cancerous lesions in the mouth and oropharynx: Automated evaluation of hyperspectral image stacks,” *HNO*, vol. 64, no. 1, pp. 27–33, Jan. 2016.
- [136] Z. Han, A. Zhang, X. Wang, Z. Sun, M. D. Wang, and T. Xie, “*In vivo* use of hyperspectral imaging to develop a noncontact endoscopic diagnosis support system for malignant colorectal tumors,” *J. Biomed. Opt.*, vol. 21, no. 1, p. 016001, 2016.
- [137] Z. Liu, H. Wang, and Q. Li, “Tongue tumor detection in medical hyperspectral images,” *Sensors*, vol. 12, no. 1, pp. 162–174, 2012.
- [138] C. D. Elvidge, D. M. Keith, B. T. Tuttle, and K. E. Baugh, “Spectral identification of lighting type and character,” *Sensors*, vol. 10, no. 4, pp. 3961–3988, 2010.
- [139] P. J. Quinn, “Effects of temperature on cell membranes.,” *Symp. Soc. Exp. Biol.*, vol. 42, pp. 237–58, 1988.
- [140] H. Akbari and Y. Kosugi, “Hyperspectral imaging: A new modality in surgery,” in *Recent advances in biomedical engineering*, InTech, 2009.
- [141] B. D. De Dinechin *et al.*, “A clustered manycore processor architecture for embedded and accelerated applications,” in *2013 IEEE High Performance Extreme Computing Conference, HPEC 2013*, 2013.
- [142] D. Madroñal *et al.*, “Energy consumption characterization of a Massively Parallel Processor Array (MPPA) platform running a hyperspectral SVM classifier,” in *Conference on Design and Architectures for Signal and Image Processing, DASIP*, 2017.
- [143] K. Peleg, G. L. Anderson, and C. Yang, “Repeatability of hyperspectral imaging systems - Quantification and improvement,” *Int. J. Remote Sens.*, vol. 26, no. 1, pp. 115–139, 2005.
- [144] H. Fabelo *et al.*, “HELICoiD project: A new use of hyperspectral imaging for brain cancer detection in real-time during neurosurgical operations,” in *Proceedings of SPIE - The International Society for Optical Engineering*, 2016, vol. 9860.
- [145] F. A. Kruse *et al.*, “The spectral image processing system (SIPS)-interactive visualization and analysis of imaging spectrometer data,” *Remote Sens. Environ.*, vol. 44, no. 2–3, pp. 145–163, 1993.
- [146] H. Fabelo *et al.*, “Spatio-spectral classification of hyperspectral images for brain cancer detection during surgical operations,” *PLoS One*, vol. 13, no. 3, pp. 1–27, 2018.
- [147] H. Fabelo *et al.*, “A novel use of hyperspectral images for human brain cancer detection using in-vivo samples,” in *BIOSIGNALS 2016 - 9th International Conference on Bio-Inspired Systems and Signal Processing, Proceedings; Part of 9th International Joint Conference on Biomedical Engineering Systems and Technologies, BIOSTEC 2016*, 2016.
- [148] D. Ravi, H. Fabelo, G. M. Callic, and G.-Z. Yang, “Manifold Embedding and Semantic Segmentation for Intraoperative Guidance with Hyperspectral Brain Imaging,” *IEEE Trans. Med. Imaging*, vol. 36, no. 9, 2017.
- [149] J. F. Pineiro *et al.*, “Hyperspectral imaging for brain tumour identification and boundaries delineation in real-time during neurosurgical operations,” *Neuro. Oncol.*, 2017.
- [150] A. Szolna, J. Morera, J. F. Piñeiro, G. M. Callicó, H. Fabelo, and S. Ortega, “Hyperspectral Imaging as A Novel Instrument for Intraoperative Brain Tumor Detection,” *Neurocirugia*, vol. 27, p. 166, 2016.
- [151] S. Kabwama *et al.*, “Intra-operative hyperspectral imaging for brain tumour detection and delineation: Current progress on the HELICoid project,” *Int. J. Surg.*, vol. 36, p. S140, 2016.
- [152] K. Huang, S. Li, X. Kang, and L. Fang, “Spectral–Spatial Hyperspectral Image

- Classification Based on KNN,” *Sens. Imaging*, vol. 17, no. 1, pp. 1–13, 2016.
- [153] D. Ravi, H. Fabelo, G. M. Callico, and G. Yang, “Manifold Embedding and Semantic Segmentation for Intraoperative Guidance with Hyperspectral Brain Imaging,” *IEEE Trans. Med. Imaging*, 2017.
- [154] Y. Tarabalka, J. Benediktsson, and J. Chanussot, “Spectral–Spatial Classification of Hyperspectral Imagery Based on Partitional Clustering Techniques,” *IEEE Trans. Geosci. Remote Sens.*, vol. 47, no. 8, pp. 2973–2987, 2009.
- [155] L. J. P. Van Der Maaten, E. O. Postma, and H. J. Van Den Herik, “Dimensionality Reduction: A Comparative Review,” *J. Mach. Learn. Res.*, vol. 10, pp. 1–41, 2009.
- [156] K. Pearson, “On lines and planes of closest fit to systems of point in space,” *Philos. Mag.*, vol. 2, no. 11, pp. 559–572, 1901.
- [157] J. B. Tenenbaum, V. de Silva, and J. C. Langford, “A global geometric framework for nonlinear dimensionality reduction.,” *Science*, vol. 290, no. 5500, pp. 2319–23, 2000.
- [158] S. T. Roweis and L. K. Saul, “Nonlinear dimensionality reduction by locally linear embedding.,” *Science*, vol. 290, no. 5500, pp. 2323–6, 2000.
- [159] D. L. Donoho and C. Grimes, “Hessian eigenmaps: locally linear embedding techniques for high-dimensional data.,” *Proc. Natl. Acad. Sci. U. S. A.*, vol. 100, no. 10, pp. 5591–5596, 2003.
- [160] M. Belkin and P. Niyogi, “Laplacian Eigenmaps and Spectral Techniques for Embedding and Clustering,” *Nips*, vol. 14, pp. 585–591, 2001.
- [161] D. Meng, Y. Leung, and Z. Xu, “A new quality assessment criterion for nonlinear dimensionality reduction,” *Neurocomputing*, vol. 74, no. 6, pp. 941–948, Feb. 2011.
- [162] K. Matkovic, L. Neumann, A. Neumann, T. Psik, and W. Purgathofer, “Global Contrast Factor - a New Approach to Image Contrast,” *Comput. Aesthet. Graph. Vis. Imaging*, 2005.
- [163] L. J. P. Van Der Maaten and G. E. Hinton, “Visualizing high-dimensional data using t-sne,” *J. Mach. Learn. Res.*, vol. 9, pp. 2579–2605, 2008.
- [164] K. Lekadir *et al.*, “Tissue characterization using dimensionality reduction and fluorescence imaging,” in *9th International Conference on Medical Image Computing and Computer Assisted Intervention (MICCAI’06)*, 2006, vol. 4191, pp. 586–593.
- [165] C. Chang and C. Lin, “LIBSVM: A Library for Support Vector Machines,” *ACM Trans. Intell. Syst. Technol.*, vol. 2, pp. 1–39, 2013.
- [166] Y. W. Teh and S. T. Roweis, “Automatic Alignment of Local Representations,” *undefined*, 2002.
- [167] S. Lafon and A. B. Lee, “Diffusion maps and coarse-graining: A unified framework for dimensionality reduction, graph partitioning, and data set parameterization,” *IEEE Trans. Pattern Anal. Mach. Intell.*, 2006.
- [168] K. Q. Weinberger, B. D. Packer, and L. K. Saul, “Nonlinear Dimensionality Reduction by Semidefinite Programming and Kernel Matrix Factorization,” in *Tenth International Workshop on Artificial Intelligence and Statistics*, 2005.
- [169] Xiaofei He, Deng Cai, Shuicheng Yan, and Hong-Jiang Zhang, “Neighborhood preserving embedding,” in *Tenth IEEE International Conference on Computer Vision (ICCV’05) Volume 1*, 2005.
- [170] L. Teng, H. Li, X. Fu, W. Chen, and I. F. Shen, “Dimension reduction of microarray data based on local tangent space alignment,” in *Fourth IEEE Conference on Cognitive Informatics 2005, ICCI 2005*, 2005.
- [171] G. E. Hinton and R. R. Salakhutdinov, “Reducing the dimensionality of data with neural networks,” *Science (80-.)*, 2006.
- [172] M. Balasubramanian and E. L. Schwartz, “The Isomap Algorithm and Topological Stability,” *Science (80-.)*, vol. 295, no. 5552, p. 7a–7, Jan. 2002.

- [173] T. Zhang, J. Yang, D. Zhao, and X. Ge, "Linear local tangent space alignment and application to face recognition," *Neurocomputing*, 2007.
- [174] V. De Silva and J. B. Tenenbaum, "Global Versus Local Methods in Nonlinear Dimensionality Reduction," *Adv. Neural Inf. Process. Syst.* 15, 2003.
- [175] F. Sha and L. K. Saul, "Analysis and extension of spectral methods for nonlinear dimensionality reduction," in *Proceedings of the 22nd international conference on Machine learning - ICML '05*, 2005, pp. 784–791.
- [176] D. K. Agrafiotis, "Stochastic proximity embedding," *J. Comput. Chem.*, 2003.
- [177] S. Roweis, "EM Algorithms for PCA and SPCA," *Computing*, 1997.
- [178] J. W. Sammon, "A Nonlinear Mapping for Data Structure Analysis," *IEEE Trans. Comput.*, 1969.
- [179] C. Spearman, "General Intelligence, Objectively Determined and Measured," *Am. J. Psychol.*, 1904.
- [180] X. He and P. Niyogi, "Locality preserving projections," *Neural Inf. Process. Syst.*, 2004.
- [181] K. Weinberger and L. Saul, "An introduction to nonlinear dimensionality reduction by maximum variance unfolding," *Aaai*, 2006.
- [182] K. Q. Weinberger, F. Sha, Q. Zhu, and L. K. Saul, "Graph Laplacian Regularization for Large-Scale Semidefinite Programming," in *Proceedings of the 19th Annual Conference on Neural Information Processing Systems*, 2006.
- [183] B. R. Kiran, B. Stanculescu, and J. Angulo, "Unsupervised clustering of hyperspectral images of brain tissues by hierarchical non-negative matrix factorization," in *BIOIMAGING 2016*, 2016, vol. 2, no. 77–84, p. 8.
- [184] H. Fabelo *et al.*, "An intraoperative visualization system using hyperspectral imaging to aid in brain tumor delineation," *Sensors*, vol. 18, no. 2, 2018.
- [185] R. Lazcano *et al.*, "Porting a PCA-based hyperspectral image dimensionality reduction algorithm for brain cancer detection on a manycore architecture," *J. Syst. Archit.*, vol. 77, pp. 101–111, 2017.
- [186] D. Madroñal *et al.*, "SVM-based real-time hyperspectral image classifier on a manycore architecture," *J. Syst. Archit.*, vol. 80, 2017.
- [187] D. Madroñal *et al.*, "Implementation of a spatial-spectral classification algorithm using medical hyperspectral images," in *2017 32nd Conference on Design of Circuits and Integrated Systems (DCIS)*, 2017.
- [188] D. Madronal *et al.*, "Energy consumption characterization of a Massively Parallel Processor Array (MPPA) platform running a hyperspectral SVM classifier," in *Conference on Design and Architectures for Signal and Image Processing, DASIP*, 2017, vol. 2017–Septe.
- [189] R. Lazcano *et al.*, "Parallel implementation of an iterative PCA algorithm for hyperspectral images on a manycore platform," in *Conference on Design and Architectures for Signal and Image Processing, DASIP*, 2017, vol. 2017–Septe.
- [190] D. Madroñal *et al.*, "Hyperspectral image classification using a parallel implementation of the linear SVM on a Massively Parallel Processor Array (MPPA) platform," in *Conference on Design and Architectures for Signal and Image Processing, DASIP*, 2017.
- [191] D. Madroñal, H. Fabelo, R. Lazcano, G. M. Callicó, E. Juárez, and C. Sanz, "Parallel implementation of a hyperspectral image linear SVM classifier using RVC-CAL," in *Proceedings of SPIE - The International Society for Optical Engineering*, 2016, vol. 10007.
- [192] R. Lazcano *et al.*, "Parallel exploitation of a spatial-spectral classification approach for hyperspectral images on RVC-CAL," in *Proceedings of SPIE - The International Society for Optical Engineering*, 2017, vol. 10430.
- [193] H. Fabelo *et al.*, "Deep Learning-Based Framework for In Vivo Identification of Glioblastoma Tumor using Hyperspectral Images of Human Brain," *Sensors*, vol. 19, no.

- 4, p. 920, Feb. 2019.
- [194] M. Abadi *et al.*, “TensorFlow: A System for Large-Scale Machine Learning TensorFlow: A system for large-scale machine learning,” in *12th USENIX Symposium on Operating Systems Design and Implementation (OSDI '16)*, 2016.
- [195] A. Krizhevsky and G. E. Hinton, “ImageNet Classification with Deep Convolutional Neural Networks,” *Neural Inf. Process. Syst.*, 2012.
- [196] Y. Song *et al.*, “Quantitative assessment of hemodynamic and structural characteristics of in vivo brain tissue using total diffuse reflectance spectrum measured in a non-contact fashion,” *Biomed. Opt. Express*, vol. 8, no. 1, p. 78, Jan. 2017.
- [197] G. Zonios, J. Bykowski, and N. Kollias, “Skin Melanin, Hemoglobin, and Light Scattering Properties can be Quantitatively Assessed In Vivo Using Diffuse Reflectance Spectroscopy,” *J. Invest. Dermatol.*, vol. 117, no. 6, pp. 1452–1457, Dec. 2001.
- [198] F. E. Robles, S. Chowdhury, and A. Wax, “Assessing hemoglobin concentration using spectroscopic optical coherence tomography for feasibility of tissue diagnostics.,” *Biomed. Opt. Express*, vol. 1, no. 1, pp. 310–317, Jul. 2010.
- [199] R. C. . Gonzalez and R. E. Woods, *Digital image processing*. 2008.
- [200] O. Ronneberger, P. Fischer, and T. Brox, “U-Net: Convolutional Networks for Biomedical Image Segmentation,” *Miccai*, 2015.
- [201] H. Fabelo *et al.*, “SVM Optimization for Brain Tumor Identification Using Infrared Spectroscopic Samples,” *Sensors*, vol. 18, no. 12, p. 4487, Dec. 2018.
- [202] E. Torti *et al.*, “The HELICoiD Project: Parallel SVM for Brain Cancer Classification,” in *Proceedings - 20th Euromicro Conference on Digital System Design, DSD 2017*, 2017.
- [203] “Accelerating the K-Nearest Neighbors Filtering Algorithm to Optimize the Real-Time Classification of Human Brain Tumor in Hyperspectral Images,” *Sensors*, Jul. 2018.
- [204] E. Torti *et al.*, “Acceleration of brain cancer detection algorithms during surgery procedures using GPUs,” *Microprocess. Microsyst.*, vol. 61, pp. 171–178, Sep. 2018.
- [205] A. Hernandez, H. Fabelo, S. Ortega, A. Baez, G. M. Callico, and R. Sarmiento, “Random forest training stage acceleration using graphics processing units,” in *2017 32nd Conference on Design of Circuits and Integrated Systems (DCIS)*, 2017, pp. 1–6.
- [206] S. Ortega, G. M. Callico, M. L. Plaza, R. Camacho, H. Fabelo, and R. Sarmiento, “Hyperspectral database of pathological in-vitro human brain samples to detect carcinogenic tissues,” in *Proceedings - International Symposium on Biomedical Imaging*, 2016, vol. 2016–June.
- [207] S. Ortega, H. Fabelo, R. Camacho, M. L. Plaza, G. M. Callicó, and R. Sarmiento, “Detecting brain tumor in pathological slides using hyperspectral imaging,” *Biomed. Opt. Express*, vol. 9, no. 2, 2018.
- [208] S. Ortega *et al.*, “PO3.18 Detection of human brain cancer in pathological slides using hyperspectral images,” *Neuro. Oncol.*, vol. 19, no. suppl\_3, p. iii37, 2017.
- [209] N. Corp., “CUDA Toolkit Documentation.” [Online]. Available: <http://docs.nvidia.com/cuda/cublas/>. [Accessed: 20-Aug-2001].
- [210] NVIDIA, “TESLA K40 GPU ACTIVE ACCELERATOR Board Specification.” [Online]. Available: [https://www.nvidia.com/content/PDF/kepler/Tesla-K40-Active-Board-Spec-BD-06949-001\\_v03.pdf](https://www.nvidia.com/content/PDF/kepler/Tesla-K40-Active-Board-Spec-BD-06949-001_v03.pdf). [Accessed: 09-May-2018].









